Breternitz, Joachim (2016) *A contribution towards the performance and structural understanding of copper and nickel salts as ammonia stores*. PhD thesis.

A Contribution Towards the Performance and Structural Understanding of Copper and Nickel Salts as Ammonia Stores

Joachim Breternitz

Master of Science

Submitted in fulfilment of the requirements for the
Degree of Doctor of Philosophy

School of Chemistry
College of Science and Engineering
University of Glasgow

May 2016

Abstract

The ongoing depletion of fossil fuels and the severe consequences of the greenhouse effect make the development of alternative energy systems crucially important. While hydrogen is, in principle, a promising alternative, releasing nothing but energy and pure water. Hydrogen storage is complicated and no completely viable technique has been proposed so far. This work is concerned with the study of one potential alternative to pure hydrogen: ammonia, and more specifically its storage in solids.

Ammonia, NH_3, can be regarded as a chemical hydrogen carrier with the advantages of strongly reduced flammability and explosiveness as compared to hydrogen. Furthermore, ammine metal salts presented here as promising ammonia stores easily store up to 50 wt.-% ammonia, giving them a volumetric energy density comparable to natural gas. The model system $\mathrm{Ni}X_2$–NH_3 (X = Cl, Br, I) is studied thoroughly with respect to ammine salt formation, thermal decomposition, air stability and structural effects. The system $\mathrm{Cu}X_2$–NH_3 (X = Cl,Br) has an adverse thermal decomposition behaviour, making it impractical for use as an ammonia store. This system is, however, most interesting from a structural point of view and some work concerning the study of the structural behaviour of this system is presented. Finally, close chemical relatives to the metal ammine halides, the metal ammine nitrates are studied. They exhibit interesting anion arrangements, which is an impressive showcase for the combination of diffraction and spectroscopic information.

The characterisation techniques in this thesis range from powder diffraction over single crystal diffraction, spectroscopy, computational modelling, thermal analyses to gravimetric uptake experiments. Further highlights are the structure solutions and refinements from powder data of $(NH_4)_2[NiCl_4(H_2O)(NH_3)]$ and $Ni(NH_3)_2(NO_3)_2$, the combination of crystallographic and chemical information for the elucidation of the $(NH_4)_2[NiCl_4(H_2O)(NH_3)]$ formation reaction and the growth of single crystals under ammonia flow, a technique allowing the first documented successful growth and single crystal diffraction measurement for $[Cu(NH_3)_6]Cl_2$.

Contents

List of Tables

List of Figures

Acknowledgements

The main trouble with acknowledgements is that I always forget those who are most important. I would therefore like to start with an apology and thank all those not mentioned below.

I am very grateful to Prof. Duncan H. Gregory for the opportunity and the research theme. I am grateful for his kindness and guidance during this thesis. I am very grateful to Dr Agata Godula-Jopek for her help and I would like to thank Airbus Group for funding this PhD project. I am indebted to Dr Justin Hargreaves for his great work and help as second supervisor. I am very grateful to Dr Christopher Syme, who helped when it was needed most. I am most thankful to Dr Peter McCabe for his kind help and great company throughout my time in Glasgow.

I would like to thank Prof Václav Petříček for his help with Jana2006; Prof Matteo Leoni for his help with pm2k; Peter Chung and Mauro Davide Cappelluti for their help with recording SEM images; Kim Wilson for measuring CHN-microanalysis; Michael Beglan for AAS and microtitration measurements; Dr Mario González for measuring far-infrared spectra; Dr Ron Smith for measuring powder neutron diffraction; Dr Pedro Duarte Vaz for inelastic neutron scattering experiments; Dr Louis Farrugia and Dr Claire Wilson for their help with single crystal measurement; Dr Stephen Thompson, Prof Chiu Tang, Dr Sina Saremi-Yarahmadi and Giandomenico Furnari for their help during the Synchrotron measurements, Finlay Walton is thanked for his help with proof-reading.

I would also like to thank the administrative, technical and academic staff of the School of Chemistry and the College of Science and Engineering for their help in chemical and administrative matters. In this instance, I would like to thank the members of the Gregory group for their help and company. It would be unjust to pick specific persons out, but I would like to mention one further name: Dr Tuan KA Hoang is especially thanked for his guidance at the beginning of this work.

Finally, I would like to thank my parents, my sisters and their families for just being who they are.

Author's Declaration

I declare that, except where explicit reference is made to the contribution of others, that this dissertation is the result of my own work and has not been submitted for any other degree at the University of Glasgow or any other institution.

Joachim Breternitz

1. Introduction

1.1. Energy

Life is driven by converting energies from one form to another. The electrical energy supplied to a light bulb for instance is transformed into light and heat, or the chemical energy of petrol is transformed into heat and mechanical energy using a motor. The energy required to maintain current standards of living is predominantly sourced from fossil fuels like oil, coal and natural gas. This primary energy source has two severe problems: 1) Fossil fuel reserves are limited and become more and more scarce, and 2) Burning fossil fuels releases CO_2 and therefore dramatically increases the levels of CO_2 in the atmosphere. An increased level of CO_2 in the atmosphere is the main cause for the greenhouse effect and hence could ultimately cause irreversible damage to our planet.

In the light of these dramatic scenarios, the pursuit of new forms of energy, storage and conversion has become one of the most important challenges for scientists in the 21^{st} century. Despite being commonly used terminology, I will not use the term *energy production* in this work. This is due to the fact that *energy production* is somewhat non-physical as energy can neither be produced nor destroyed. What is commonly described as *energy production* is the conversion of one form of energy into another and hence the term *energy conversion* shall be used instead. As energy cannot be produced, an energy source ought to be considered as the primary form of energy which can be transformed into another form during energy conversion.

An ultimate solution for an alternative to a carbon-based economy regarding the complete cycle of energy conversion and storage must address several important issues in order to overcome the intrinsic problems of the fossil fuel economy and still be usable in a normal environment:

- Sources of energy need to be unlimited or renewable
- The conversion of the source energy into a storage format or the desired form of energy needs to be feasible and efficient
- Energy conversion must not release supplementary CO_2 or other greenhouse gases
- The energy vector must be safe enough to handle

In order to organise the different processes and technologies, it is useful to look first at the different processes in a schematic way (Figure 1.1). The energy supplied by a primary source, e.g. light and heat from the sun, mechanic energy from running water or wind etc., is subsequently converted into a form of energy convenient for transport, mostly electrical energy but can also be converted into chemical energy. The energy is then used by the end consumer and is predominantly delivered as electricity but also in the form of chemical products (*e.g.* fuels). Electrical energy and chemical energy play the core role in the transport and storage of energy and their interconversion forms what can be understood as the *energy storage cycle*. While electrical energy is versatile in its use and can be transformed into other types of energy easily, it is very difficult to store.

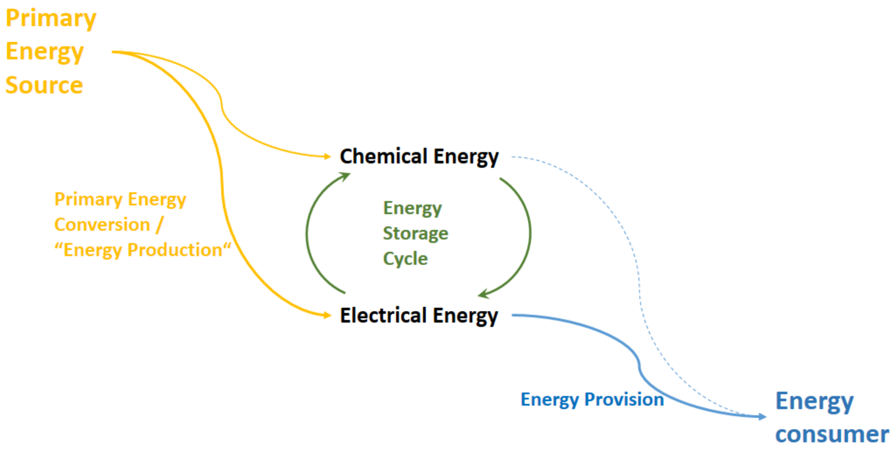

Figure 1.1.: Schematic representation of the energy conversion and storage in its way from the primary form of energy to the energy consumer.

The efficient transformation of electrical energy into chemical energy is therefore highly desirable for the storage of energy.

This work is primarily concerned with investigating one potential safe way of storing chemical energy, especially when it is used in mobile applications like cars or planes. This introduction will describe hydrogen storage and then summarise the research progress on ammonia storage as a potential safer alternative.

1.2. The Hydrogen Energy Cycle

From a chemical point of view, hydrogen is an ideal energy store. It can be directly produced through the splitting of water, and reacts readily with oxygen to deliver a huge amount of energy. This overall process can be described by the following reaction equation:

$$2\,H_{2(g)} + O_{2(g)} \longleftrightarrow 2\,H_2O_{(l/g)}$$

with a molar reaction enthalpy of $\Delta H = -569.4$ kJ/mol.[1] Despite the fact that hydrogen has a significantly higher energy per mass content than any other fuel,[2] there are some considerable problems to overcome, notably with storage. However, hydrogen production and use will be explained first, before some details on current storage technologies are reviewed.

1.2.1. Hydrogen production from water

Molecular hydrogen used nowadays is mostly made by steam-reforming natural gas:[3]

$$CH_{4(g)} + H_2O_{(g)} \xrightarrow[900\,^\circ C]{Ni} CO_{(g)} + 3\,H_{2(g)}$$

This process is however using fossil fuels and can therefore not be regarded as renewable. Given that water is the most abundant hydrogen containing compound, it is logical to design processes in which water is split into its elements.

Water splitting is a most interesting option for the production of hydrogen because it would allow the full integration of a closed cycle from water to the elements and back without production of further side products. Water splitting is indeed a natural process as plants split water during photosynthesis to produce oxygen and hydrocarbons and some microorganisms are able to split water and produce hydrogen gas.[4] Three general research directions in renewable water splitting are currently under research and shall be addressed briefly in this sections: 1) Biological processes using organisms to convert light into chemical energy, 2) Photochemical that mimic natural photosynthesis in the lab and 3) Electrochemical water splitting in the dark, in which the energy to split water molecules is not supplied by light but by electricity gained from renewable sources.

Biological Hydrogen Production

As natural organisms have developed methods to produce hydrogen at ambient conditions, it appears logical to employ natural organisms to produce hydrogen. Das and Veziroğlu classified hydrogen producing organisms according to their work principle into four categories:[5]

1. Biophotolysis of water
2. Photodecomposition of organic compounds
3. Fermentative hydrogen production
4. Hybrid systems with photosynthetic and fermentative organisms

Only biophotolysis works without the use of an organic feedstock. The other mechanisms have the degradation of hydrocarbon compounds in common, which needs to be delivered to the microorganisms, and involves a certain degree of CO_2 production as a consequence. These processes can be regarded as carbon-neutral in the best case but not as carbon-free, hence only biophotolysis will be explained here.

Biophotolysis employs the same mechanisms as photosynthesis, but instead of reducing CO_2 and forming hydrocarbons, hydrogen gas is produced on the reductive side of the reaction through hydrogenase and nitrogenase enzymes.[5] Both green algae and blue-green algae are capable of producing hydrogen and oxygen from light, but the overall process has yet to be demonstrated to work on a production scale.[6] The most limiting factors are the comparably low rate and the low efficiency of such biological processes.[7]

Photochemical Hydrogen Production

Instead of using biological processes in their natural environment, it is also possible to use artificial systems that convert photon energy into chemical energy, which is then transferred onto the water molecule to supply the energy necessary for bond breaking. Two main principles are used: 1) Homogeneous systems in which the charge separation is supplied by a molecule, and 2) Heterogeneous systems in which the charge separation is generated through a solid semiconductor. Both systems employ catalysts for the redox processes and facilitate electron transfers.[8]

Homogeneous systems rely heavily on transition metal complexes as photosensitisers, with $[Ru(bpy)_3]^{2+}$ being the most common example.[9] Photosensitisers capture photon energy in an energetic transition and is then quenched through the water splitting reaction by means of appropriate catalysts. Cobalt complexes and noble metal catalysts are widely used for water reduction (hydrogen synthesis)[10] and transition metal complexes based on light transition metals (most notably Co, Ni and Mn) and the "classical" water splitting element Ruthenium can be employed as water oxidation catalysts.[11,12] The most striking problem of molecular systems is photosensitiser deactivation through unintended complex degradation of the excited state complex.[13]

Heterogeneous systems overcome this problem through the replacement of the molecular photosensitiser by a solid that assumes the role of charge separator. This solid can be a classical semiconductor material[14] or a dye-sensitised photocell.[15] The latter can be regarded as a mixed form between a molecular and a semiconductor charge separator. Heterogeneous systems also use water splitting catalysts to favour the water splitting reaction over the charge recombination, with Ru oxides being the most widely used catalysts for the oxidation part.

Electrochemical Hydrogen Production

Instead of using light energy directly, water can be split by electrical energy through the process of electrolysis. Using electrical energy to split water has the great advantage that the source of electrical energy is not fixed and other renewable forms of energy, such as wind or tidal power may be preferred in areas without strong sun irradiation (*e.g.* Glasgow). The most important effect to overcome in order to yield the most efficient process is the overpotential of the electrolysis reaction.[16] While platinum is the most commonly used water splitting electrode material, many more transition metal based catalysts have been developed as well.[17–19]

1.2.2. Consumption of Hydrogen

The energy releasing reaction $2\,H_{2g} + O_{2g} \longrightarrow 2\,H_2O_{l/g}$ can be driven in two ways: 1) As a combustion process and 2) In a fuel cell reaction. Both processes have specific advantages and characteristics and shall therefore be explained briefly.

Hydrogen Combustion

Hydrogen reacts readily with oxygen and the stoichiometric ratio H_2:O_2 = 2:1 is known as *knallgas* or *oxhydrogen* because of its strong explosiveness. Hydrogen reacts readily with air in a range of 4–75 vol.-%[20] and such hydrogen-oxygen mixtures are used as propellants for space rockets.[21] Furthermore, the uses of hydrogen as sole combustive[22–24] as well as mixtures with other combustives such as natural gas[25–27] or diesel[28] are being researched. The use of hydrogen internal combustion engines has very similar characteristics to other internal combustion engines with the main advantages are a high power density output compared to fuel cells and the possibility of using modified petrol or diesel engines.[20] The most notable disadvantage is NOx formation during the hydrogen combustion process similar to that in fossil fuel internal combustion engines.[20]

Hydrogen Fuel Cells

Working principle: Fuel cells exploit the same overall reaction of hydrogen with oxygen to water as the combustion reaction. While combustions exploit the direct reaction of hydrogen and oxygen and use the thermal and mechanical energy released during the reaction, fuel cells proceed via the same reaction electrochemically and hence produce an electrical current directly out of chemical energy. In 1838, Christian Friedrich Schönbein and Sir William Grove invented the concept of fuel cells independently and understood their working principle as the reverse of electrolysis.[29] Accordingly, an anode and cathode reaction can be defined as where the anode is the place of oxidation and the cathode is the place of reduction. The reaction products at the anode and cathode depend on the fuel cell type (which is discussed below) but in all hydrogen fuel cells hydrogen is oxidised at the anode and oxygen is reduced at the cathode. In order to allow the reactions to happen, two transports must be possible; firstly the transport of material in the form of ions through the electrolyte and secondly the transport of electricity through the electric circuit (see Figure 1.2). In order to allow both transports to occur, some prerequisites are necessary for the different parts of a fuel cell; the anode and cathode need to conduct both ions and electricity to allow the reaction, but the electrolyte must only conduct ions as the electric conductivity of the electrolyte would short bypass the fuel cell and effectively impede the usability.

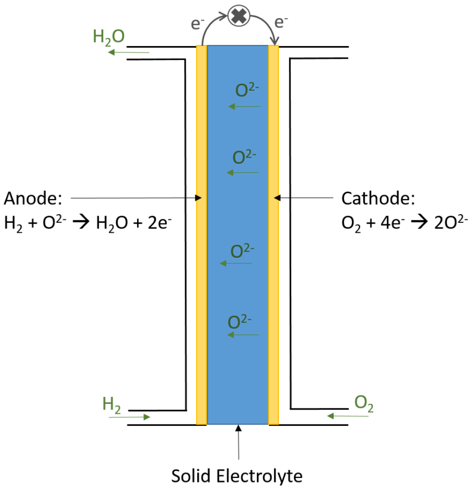

Figure 1.2.: Schematic representation of a solid oxide fuel cell (SOFC).

Types of hydrogen fuel cells: Fuel cells can be divided into different types according to their working principle and the electrolyte used, which defines the ionic species conducted and hence the oxidation and reduction reactions at the electrodes. As some fuel cell electrolytes (such as ceramic oxide conductors in solid oxide fuel cells) require higher temperatures for the effective conduction of ions, the electrodes may need to be adjusted accordingly. Characteristics of the main types of hydrogen fuel cells are presented in Table 1.1. It is noteworthy that MCFCs need a supplementary supply of CO_2 which is used as a chemical carrier of oxygen through the carbonate melt. Different fuel cell types have different working characteristics and are complementary to each other. While only PEMFCs are used in automotive applications due to their ability for cold starts and their power density,[30] SOFCs in particular have attracted a great amount of research in recent years due to their simple and robust working principle, their ability to consume natural gas directly and their large power output up to 100 MW.[31]

Table 1.1.: Main types of hydrogen fuel cells and their electrolyte characteristics.[31]

Fuel cell type	Electrolyte	Operation temperature	Transported ion
Alkaline fuel cell (AFC)	KOH(aq)	60–80 °C	OH^-
Proton exchange membrane fuel cell (PEMFC)	polymer membrane	60–200 °C	H^+
Phosphoric acid fuel cell (PAFC)	concentrated phosphoric acid	160–200 °C	H^+
Molten Carbonate fuel cell (MCFC)	molten carbonate salts	≈ 650 °C	CO_3^{2-}
Solid oxide fuel cell (SOFC)	doped zirconia	≈ 1000 °C	O^{2-}

1.2.3. Hydrogen storage

Storing hydrogen in a safe and convenient way has been widely recognised as the bottleneck of the hydrogen economy.[32] Three main problems impede the efficient storage of hydrogen: 1) It is explosive and highly flammable, 2) Its very low density and 3) It is highly mobile and diffusive. Three main storage techniques are being considered at the moment:

- Gaseous hydrogen under pressure
- Cryogenic liquid hydrogen
- Hydrogen storage in solids

The first two storage methods carry the unavoidable risk that a tank rupture or cooling interruption would cause the rapid release of great amounts of hydrogen gas into the surroundings. Such released hydrogen is prone to form explosive mixtures with air and hence bears a great danger. Furthermore, molecular hydrogen tends to absorb on and diffuse through metal walls and special storage system are therefore needed whose

Table 1.2.: Ultimate targets for hydrogen storage for light duty application as defined by DoE[34]

Parameter	Unit	Value
Gravimetric H_2 capacity	kg(H_2)/kg(system)	0.075
Volumetric H_2 capacity	kg(H_2)/L(system)	0.070
Operating Temperature	°C	–40 – 60
Gravimetric H_2 capacity	kg(H_2)/kg(system)	0.075
Onboard Efficiency	%	90

weight and volume lowers the possible gravimetric and volumetric storage density.[2] Liquid storage systems, as presented by BMW for instance,[2,32] have furthermore the problem that they constantly lose hydrogen through intake of thermal energy from the surroundings. This boil-off occurs at the rate of $\approx$1 %/day[32] to $\approx$1.5%/day[2] for automotive applications (meaning that around 20-30 % of a storage tank boil off during a two week period) but drop to far smaller numbers for much larger storage tanks (0.06% for 20,000 m^3 tanks)[33] as might be used for grid storage applications where neither volume nor weight of the storage system are a critical constraint. The U.S. Department of Energy (DoE) has defined a set of targets for a promising hydrogen store,[34] but which are not yet met by any hydrogen storage system available. The key targets are given in table 1.2. The following discussion shall concentrate on solid-state hydrogen storage systems, which profit from their increased level of safety and higher density yielding advantages in volumetric capacity.

Solid state hydrogen storage

In order to store hydrogen in a solid, it needs to interact with the solid matrix. This is possible through two possible approaches: 1) The storage of hydrogen through physical interaction with the surface of a material or 2) the formation of chemical bonds between hydrogen and the hosting compound.

Physical hydrogen stores rely on the adsorption of hydrogen on the surface and hence the main parameter determining their performance is the specific surface (surface area per mass) and to some extent the surface shape of the potential hydrogen store.[35] Eberle *et al.* rationalised the difference between physical (adsorption) storage and chemical storage depending on whether H_2 remains molecular (physical storage) or dissociates and forms chemical bonds with the storage material (chemical storage).[35] As the attractive field for adsorption diminishes very rapidly as a function of the surface distance,[2] their specific surface is crucial for high loadings. Porous solids, such as Metal Organic Frameworks (MOFs),[36–39] Covalent Organic Frameworks (COFs)[40,41] and high surface carbon structures[42–51] have a very favourable specific area and hence qualify as promising physical hydrogen stores.[52] Some overlap between physical adsorption and chemical phenomena such as spill-over[53–55] can exist in these materials. It should be noted that physical hydrogen stores only work conveniently at cryogenic temperatures and high pressures[56] which is the main hindrance to their applicability. While MOF 177 for instance has a hydrogen storage capacity of 7.5 w.-% at 77 K and 70 bar, its storage capacity drops below 1 wt.-% at ambient pressure.[57,58]

Chemical hydrogen storage, in contrast, profits from the formation of strong chemical bonds which make hydrogen incorporation more stable and hence adds a safety relevant feature. In a side-project during this thesis, we studied potential hydrogen storage materials on the basis of database deposited crystal structures.[59] As only some results will be included, the reader is referred to the original article for full details and computational methods. Looking at the ensemble of hydrogen containing compounds included in the Crystallographic Open Database (COD), 262,710 files at the time of the study,[59] it is interesting to see that the ratio of gravimetric and volumetric density does not follow a linear trend (figure 1.3). Instead, the volumetric capacity of the vast majority of materials does not lye over $\approx$ 130 g(H_2)/l, regardless of their gravimetric capacity. It is interesting

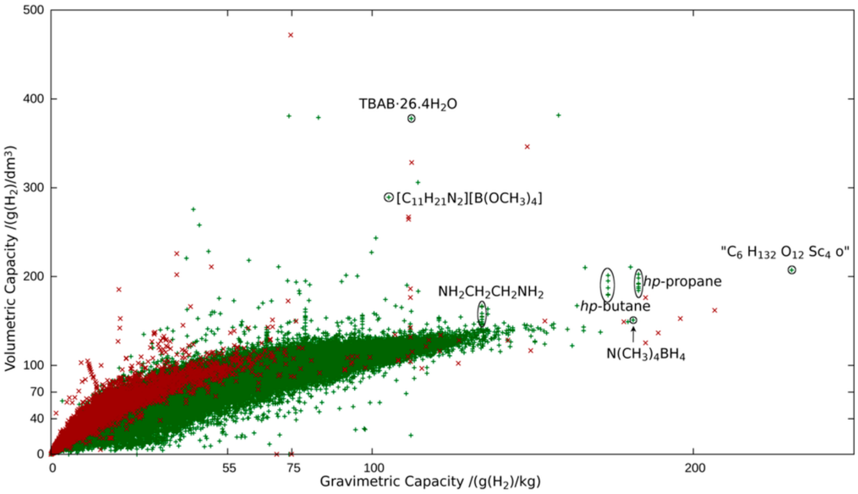

Figure 1.3.: Gravimetric and volumetric capacities of hydrogen containing compounds (inorganic: red crosses, organic: green plusses) from Crystallographic Open Database (COD).[59] Some notable organic compounds are highlighted.[60–65]

in this context that, even at the most extreme pressures, crystalline hydrogen does not possess much higher volumetric capacities (210 g(H_2)/l at 26.5 GPa) due to its very low density (0.210 g/ml at 26.5 GPa).[66]

As carbon content is part of the definition of an organic compound, this group of materials is prone to release the greenhouse gas CO_2* which is unfavourable for its use in a sustainable energy cycle. Inorganic materials, however, do not suffer from this constraint and are therefore most studied in the context of hydrogen storage. Amongst the hydrogen containing compounds, those containing hydrogen predominantly contained in water can be excluded as hydrogen stores, because the enthalpy to break the O–H bond would be in the same range as the energy profit from water formation (through combustion or fuel cell) and effectively no energy would hence be stored. Among solid-state hydrogen storage materials, three groups are currently most intensively investigated: a) Metal hydrides, b) Complex hydrides and c) Chemical hydrides. Within the vast amount of potential

---

*It should be mentioned that CO_2 is the most prominent greenhouse gas but others exist including CH_4, N_2O and H_2O.

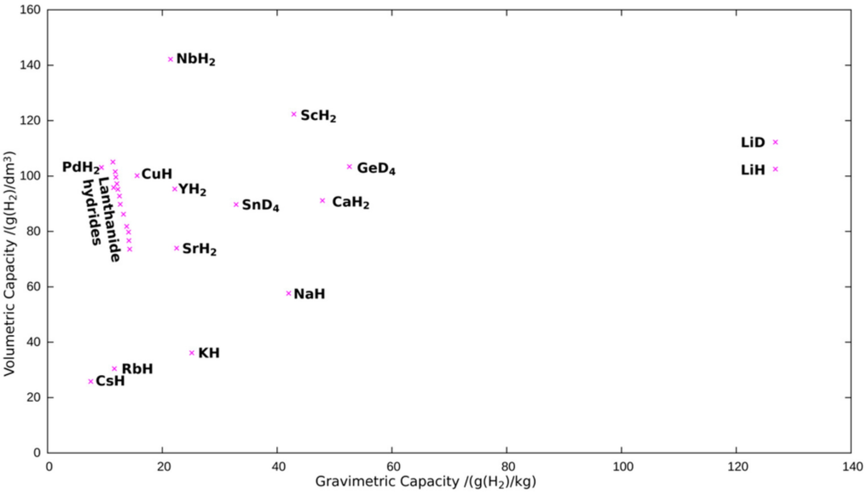

Figure 1.4.: Gravimetric and volumetric capacities of metal hydrides from COD.[59] The individual entries are labelled.[70–72]

hydrogen stores, some compounds have gained particular interest either on their own or as part of a mixture. As shown in Figure 1.4, LiH is clearly the metal hydride with the highest gravimetric hydrogen content, which is due to the low atomic weight of lithium. Also MgH_2 with its gravimetric hydrogen content of 7.7 wt.-% is considered one of the keystones in solid-state chemical hydrogen storage.[67] While the heavier metal hydrides suffer from the higher atomic weight of the metals and therefore drop significantly in gravimetric capacity as compared to the light metal hydrides, their higher density makes them promising stores for volume, but not mass constrained scenarios. In fact, the ternary hydride $LaNi_5H_6$ with a volumetric capacity of 115 $g(H_2)/l$[68] was already considered as a potential hydrogen store in the 1970s.[69]

Orimo *et al.* define complex hydrides as group I and II metal salts of alanates, borohydrides and amides.[73] On a more general level, complex hydrides could be understood as compounds containing hydrogen covalently bound inside the anion. Borohydrides have earned particular interest due to the low molecular weight of boron and its high hydrogen stoichiometry per boron atom. $LiBH_4$ further profits from the low atomic

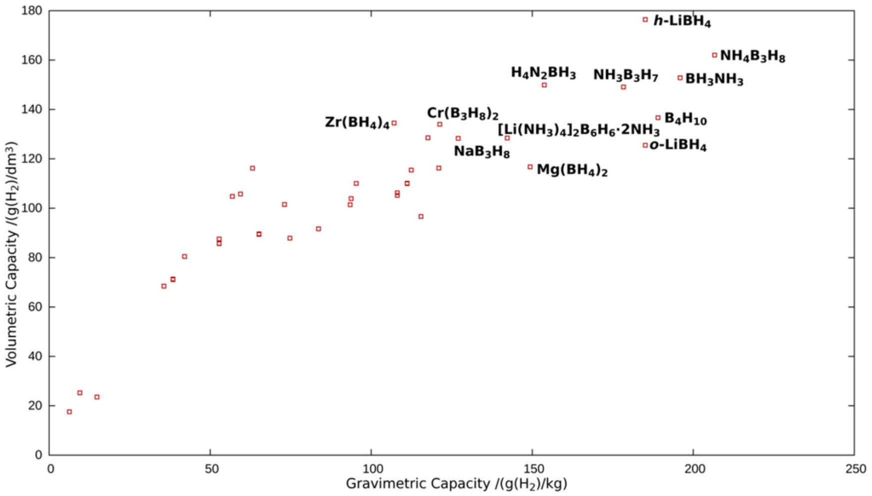

Figure 1.5.: Gravimetric and volumetric capacities of boron containing compounds (excluding those also containing C, O, P and/or S) from COD.[59] The individual entries are labelled.[75–85]

weight of Li and hence has a very high hydrogen content (Figure 1.5) and is probably the best studied complex hydride at the moment.[74] The gravimetric hydrogen content of complex hydrides can, however, be further increased when not only the anion but also the cation contains hydrogen, for instance in the case of $NH_4B_3H_8$ (Figure 1.5).

The combination of nitrogen and boron has been found to be particularly interesting as this group of compounds is stabilised through dative bonds of the strong Lewis base nitrogen and the strong Lewis acid boron.[86,87] It is also this difference in electron affinity which influences the covalently bound hydrogen atoms and leads to the formation of B–H$\cdots$H–N dihydrogen bonds in this class of compounds.[88] These dihydrogen bonds explain the high melting point of ammonia borane (377 K)[88] which goes along with its decomposition and therefore also allows one to obtain a major fraction of hydrogen below 383 K.[89] Furthermore, ionic derivatives of ammonia borane, namely sodium and lithium amidoboranes were considered by Xiong *et al.* in 2008.[90]

1.3. The Ammonia Energy Cycle

Given the considerable difficulties of hydrogen storage, alternative fuels, which effectively act as chemical hydrogen carriers have been considered for some time. Arguably the most promising systems for alternative energy vectors are methanol and ammonia. While methanol has the big advantage of being liquid at ambient conditions and hence usable within the known liquid combustive infrastructure, it contains carbon and would therefore be viable for CO_2 emissions, working CO_2 neutral at best. Ammonia on the other hand does not contain carbon and, if used in state-of-the-art fuel cells, emits nothing but water and nitrogen, the latter making up 78 % of the atmosphere already. Furthermore, ammonia is a widely used chemical and the production and transport infrastructure already exists. Ammonia, however, is toxic and corrosive and therefore needs to be contained in a safe store when being used in a mobile and safety critical environment. The following section shall give a brief overview of the current developments in ammonia production, consumption and storage to explain the environment for the research presented in this thesis.

1.3.1. Production of ammonia

As mentioned above, ammonia is a massively used product for the chemical industry and its world production for 2013 was 144 Mt.[91] Virtually all ammonia today is produced through the Haber-Bosch process, named after their inventors Fritz Haber and Carl Bosch. The Haber-Bosch process was named the most important invention of the 20th century by Nature due to its crucial importance for the supply of bioavailable nitrogen.[92] The increase in farming productivity is vital for nearly 50 % of today's world population.[93]

The Haber-Bosch process uses the direct reaction of molecular nitrogen and hydrogen gases,

$$N_{2(g)} + 3\,H_{2(g)} \longrightarrow 2\,NH_{3(g)}$$

over an iron-based catalysts for the production of ammonia.[93]. In fact, Haber and van Oordt published first considerations about the production of ammonia from its elements in 1905,[94] and were able to demonstrate a working process in 1909.[92] The Haber-Bosch process is however very energy intensive as it requires elevated temperatures and pressures, and accounts for $\approx$1.5 % of the world's energy consumption.[95] Furthermore, most hydrogen for the production of ammonia is obtained through steam-reforming of fossil fuels (see also section 1.2) and is therefore not renewable. The research efforts into green hydrogen production as discussed above are seconded by intensive research activity into more energy-efficient ways of producing ammonia through novel catalysts,[96] electrochemical processes,[97] and even light driven processes where ammonia is directly synthesised from water and nitrogen,[98] which promise sustainable ways of producing ammonia in the near future. The excellent review of Lan *et al.* dealing with all aspects of an ammonia driven economy shall be mentioned.[99]

1.3.2. Ammonia Consumption

Similarly to hydrogen, ammonia can be used in internal combustion engines as a supplement or replacement for conventional fuels. Both spark-ignited engines (like petrol motors)[100] and compression-igniting engines[101] (diesel motors) are being researched for their usability with ammonia. This is not a new development, and Kroch first considered ammonia as an alternative fuel as early as 1905.[102] Kroch also reported the use of ammonia to fuel a bus fleet in war-time Brussels in the 1940's as a response to the shortage of diesel.[102] The fleet reportedly drove "several tens of thousands of miles"[102] hence demonstrating the first larger-scale ammonia use for mobile applications. The uses of internal combustion engines for ammonia share the same advantages (high power rate, easy implementation in existing infrastructure) and disadvantages (comparably lower efficiency to fuel cells, no direct transfer in electrical energy) with internal combustion engines for hydrogen (see section 1.2).

Two possible ways to use ammonia in fuel cell applications exist: ammonia can either be catalytically split into the elements and the evolving hydrogen can be used in conventional fuel cells, or direct ammonia fuel cells (DAFCs) may be used. Classically, ammonia decomposition is catalysed using heterogeneous transition metal catalysts such as 1.3 wt.-% Ru/Al_2O_3[103] In 2004, Yin *et al.* pointed out, that Ru was the most active catalyst and carbon nanotubes were the best support,[104] which was still the state-of-the-art in 2012.[105] In 2014, however, David *et al.* presented a novel catalytic system exploiting sodium amide as catalyst to reach unprecedented conversion degrees at modest temperatures.[106] This work was then further expanded on lithium imide as catalyst[107] and further work was done on the mechanistic understanding of the catalytic process.[108] Lately, the same group extended their work on lithium calcium imide to further increase the activity at even lower temperatures as compared to the systems above.[109]

DAFCs were firstly presented in the early 1960s.[110] Rees and Compton gave a conclusive description of the development of DAFCs until 2011.[110] In fact, care has to be taken in the choice of the electrode material owing to the strongly basic behaviour of ammonia, which makes the use of alkaline fuel cells most promising. Furthermore, SOFCs are good candidates for use with ammonia[111–114] due to their chemical stability, but their high operation temperatures make them unsuitable for use in mobile applications.[110]

1.3.3. Ammonia Storage

Storage of ammonia is comparably simple with regards to hydrogen storage, as ammonia gas condenses into a liquid above ≈10 bar at room temperature or at –33.35 °C at ambient pressure. Although ammonia, in contrast to hydrogen, does not readily form explosive or flammable mixtures with air,[115] its toxicity and corrosive nature make storage as a pure compound under pressure or unfavourable as it bears the risk of releasing large amounts of toxic gas in short times and the low density of liquid ammonia, between 0.68 g/cm^3 at the boiling point and 0.60 g/cm^3 at room temperature further impedes this way of storage.[116,117] Zamfirescu and Dincer propose however that the risk of intoxication is comparably low as ammonia is self-alarming through its pungent odour.[115] Given that mobile applications necessitate an increased level of safety in a confined space, solid state storage materials were being discussed as potential alternative for a while with $[Mg(NH_3)_6]Cl_2$ being clearly the reference material in current research.

Physisorption Storages of ammonia in porous solids such as Metal-Organic Frameworks (MOFs)[118], Covalent-Organic Frameworks (COFs)[119] and zeolites[118,120,121] are being studied. The currently best performing material, COF-10, exhibits an ammonia uptake of 25.5 wt.-% at ambient pressure and room temperature.[119] This capacity is, however, only half of what is achievable with $[Mg(NH_3)_6]Cl_2$ (51 wt.-%).

Metal ammine salts are probably the most straightforward approach for storing ammonia in a solid. This is due to the fact that the lone electron pair of the nitrogen atom in ammonia readily forms complex bonds to metals. Christensen *et al.* were the first to consider the long known ammine complex salts as potential hydrogen stores and established the thermodynamical considerations for this ammonia store.[122–124]

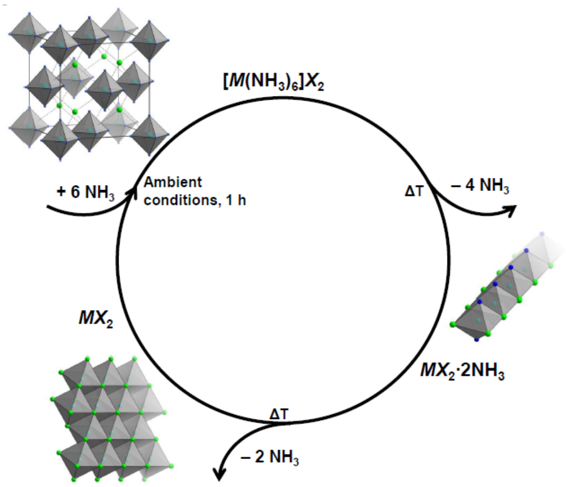

Figure 1.6.: Schematic of the loading-unloading cycle in the system MX_2–NH_3. The diammine phase is given as exemplary intermediate product present in all systems studied so far, but many systems exhibit further decomposition intermediates.

Hummelshøj *et al.* explored the possibility to reach a high packing density in $\mathbf{[Mg(NH_3)_6]Cl_2}$ based ammonia stores through the formation of nanopores within the material.[125] The same group also studied pore formation by SAXS[126] and explained the mobility of ammonia within the compound through computational methods and neutron scattering,[127] which was complemented by the work of Sørby *et al.* using powder neutron diffraction on $[Mg(ND_3)_6]Cl_2$.[128] Zhu *et al.* explored the large-scale production of $[Mg(NH_3)_6]Cl_2$ through the industrially used reaction of Mg_2Si with NH_4Cl.[129] Jones and coworkers elucidated the structures and desorption mechanisms in $[Mg(NH_3)_6]X_2$ X = Cl, Br, I using powder x-ray diffraction, thermal analysis and NMR in order to clarify the sometimes conflicting data presented in earlier studies.[130]

Additionally, $[Mg(NH_3)_6]Cl_2$, $[Ca(NH_3)_8]Cl_2$, $[Mn(NH_3)_6]Cl_2$ and $[Ni(NH_3)_6]Cl_2$ have been proposed as potential ammonia stores by Sørensen *et al.* in 2008.[131] The higher alkaline earth metal salts, and here particularly $SrCl_2$, gained further interest thereafter due to their capability of forming octammine complexes, hence increasing their potential storage density.[132–134] $[Mn(NH_3)_6]Cl_2$ was also studied by Reardon *et al.* in

2012.[135] The schematic absorption-desorption cycle in metal ammine salts is shown in Figure 1.6. Jensen *et al.* used computational methods to study mixed cation systems in order to tune the desorption behaviour[136,137] and presented experimental evidence for a mixed barium-strontium system which exhibits only one desorption step.[138]

Besides the divalent alkaline earth and transition metal salts, Johnson *et al.* proposed $Li(NH_3)BH_4$ as promising ammonia store by exploiting both a very light cation and anion.[139] Furthermore, lithium fullerides were assessed as ammonia stores in 2015.[140] Hartley recently demonstrated the use of microwave probes for the selective detection of the degree of ammonia uptake within the working system[141] and hence allowing for the exact monitoring of the degree of loading of a potential ammonia store.

1.4. On the Formation of Solid Metal Ammine Complex Salts

Metal ammine complexes are probably the best known complex compounds. In fact, the first scientific description of a complex formation was a copper ammine complex by Libavius in 1597.[142] Furthermore, Tassaert provided the first comprehensive description of an ammine formation for $[Co(NH_3)_6]Cl_3$ in 1798.[142–144] Tassaert described the dissolution of cobalt ore in nitric acid and aqua-regia and the appearance of a brown precipitate which re-dissolved when treating this solution with ammonia.[145] Despite the common interpretation, Tassaert only mentioned the reaction of cobalt chloride with ammonia briefly but the extensive part of his work, including the description of the typical brown colour which allows the identification of the product as an ammine complex, was done on nitrate or nitrate-chloride samples. It is hence *not* the formation of $[Co(NH_3)_6]Cl_3$, as commonly cited in the literature,[142,143] but most probably the formation of the nitrate that Tassaert observed.

It was, however, not until 1893 and the ground-breaking work of Alfred Werner[146] that the concept of complexes and their chemical and structural behaviour was understood. Werner was later awarded the Chemistry Nobel Prize in 1913:

> *"in recognition of his work on the linkage of atoms in molecules by which he has thrown new light on earlier investigations and opened up new fields of research especially in inorganic chemistry"*[147]

Metal complexes were thereafter understood as regular polyhedra with a defined shape depending on the number of coordinated ligands, *e.g.* octahedra for hexa-ligand complexes. This assumption was thereafter structurally proved by Wyckoff, who published a series of approximate crystal structure determinations on complex compounds including $(NH_4)_2[PtCl_6]$[148] and $[Ni(NH_3)_6]X_2$ (X=Cl, Br, I)[149]. Wyckoff was able to determine space group, cell parameters and the regular octahedral coordination of the central atoms but could not determine the ligand bond lengths reliably. Scherrer and Stoll, however, provided the concrete evidence, that these crystal structures were indeed the proof for Werner's theory in a very brief notification in 1922.[150]

The works above generally use aqueous solutions to obtain solid ammine complexes, but the direct reaction of ammonia gas with metal salts has been long known.[151] Wilhelm Biltz started a long lasting and extensive study of metal salt ammines in the series "Beiträge zur systematischen Verwandtschaftslehre",[152–180] to which he dedicated a good part of his work. The work of Fritz Ephraim and co-workers should also be mentioned who studied the thermal decomposition of ammine complexes extensively in the series

"Über die Natur der Nebenvalenzen" in order to determine the bond strengths of ligand bonds.[181–197] It is the ability of some metal salts to react with gaseous ammonia, which makes them directly usable as ammonia storage materials because no aqueous medium is needed and a solid metal salt tank could be directly filled with gaseous ammonia at ambient conditions.

1.5. Jahn-Teller Distortions in Solid Cu^{II} Complex Salts

Jahn and Teller provided an explanation for the apparent deviation of some complex compounds from the regular octahedral or tetrahedral coordination in 1937.[198] They postulated that a ligand field could only be stable for systems with a unique electronic ground state, *i.e.* an electron configuration without degenerate states. Taking the orbital splitting for a regular octahedron (Scheme 1.7) and filling it with the 8 *d*-electrons as for instance for Ni^{II} central atoms, one finds that the energetically favoured *d*-orbitals d_{xy}, d_{xz} and d_{yz} are fully occupied and the energetically disfavoured orbitals $d_{\mathrm{x^2-y^2}}$ and $d_{\mathrm{z^2}}$ are half occupied. If one now switched the central atom to Cu^{II} with its *d*9 configuration, the supplementary electron could be sitting in any of the higher energy orbitals, *i.e.* it would be electronically degenerate. However, As this state is unstable, the coordination must be different to lift the degeneracy (Scheme 1.7). This can be effectuated by lifting the structural degeneracy of the six ligand molecules in order to gain a lifting of the energetically equivalence of the $d_{\mathrm{x^2-y^2}}$ and $d_{\mathrm{z^2}}$ orbitals. Considering that the $d_{\mathrm{x^2-y^2}}$ orbital is aligned with the x and y axes and the $d_{\mathrm{z^2}}$ orbital is aligned with the z axis, the six ligands can be easily divided into two groups: a) Four ligands that are lying on the x and y axes (aligned with the $d_{\mathrm{x^2-y^2}}$ orbital) and b) Two ligands that lie on the z axis aligned with the $d_{\mathrm{z^2}}$ orbital.

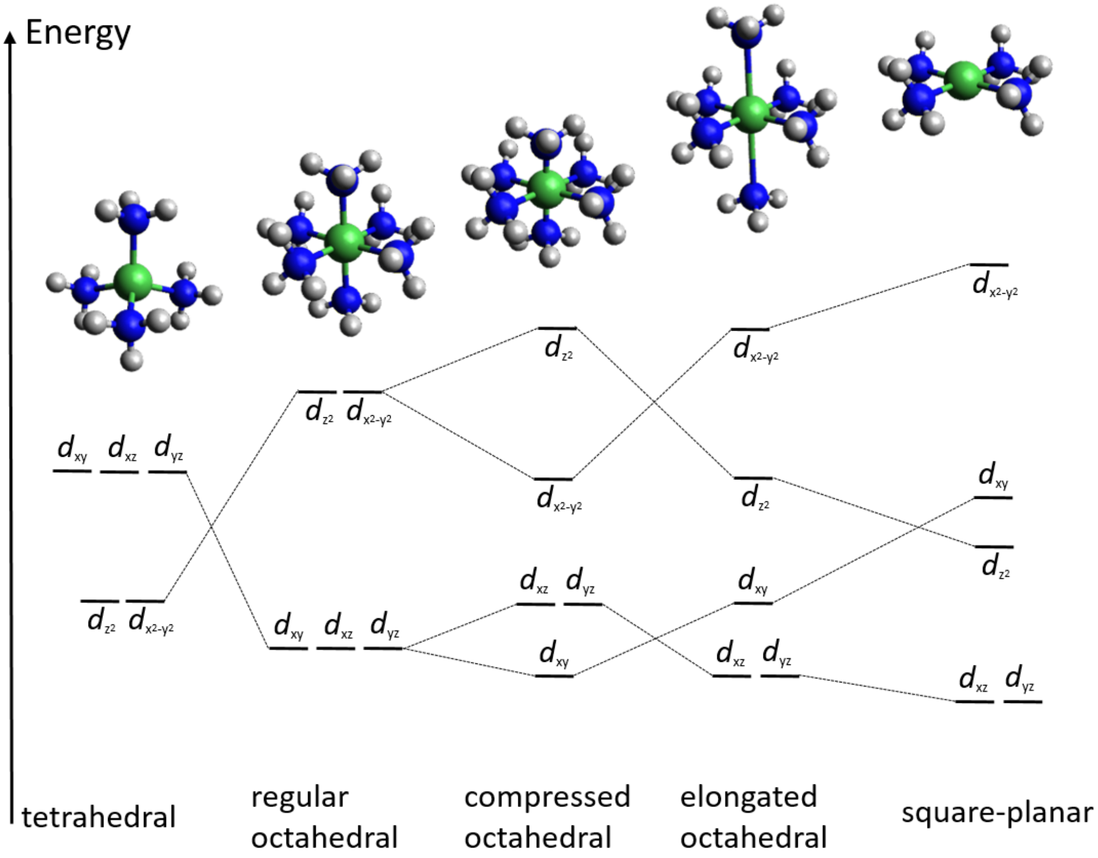

Scheme 1.7.: Schematic of the d-orbital splitting in different complex geometries.

The following nomenclature shall be used for the discussion of the two different ligand sites throughout this thesis: The four ligands of group a) Will be referred to as square-planar or equatorial ligands, while the two ligands of group b) Are referred to as overcapping or axial ligands.

Depending on which of the two orbitals is energetically preferred, the geometry of the complex arranges accordingly: $d_{x^2-y^2}$ is energetically preferred in the compressed octahedral configuration as the equatorial ligands shift further away from the metal center while the axial ligands come closer and hence disfavour d_{z^2}. This situation is inverted in the elongated octahedral configuration as the axial ligands are now further away from the metal center while the equatorial ligand-metal center distance is contracted. The case for the absence of axial ligands and hence a pure square-planar coordination follows the same trend as the elongated octahedral coordination but the energetic disfavouring is more extreme for $d_{x^2-y^2}$ and the favouring is equally stronger for d_{z^2} as it is no longer affected by the ligand arrangement. It should be noted that the energetically favoured orbitals d_{xy}, d_{xz} and d_{yz} are split in the event of a Jahn-Teller distortion into one orbital without spatial contribution in the z direction (d_{xy}) and two orbitals with spatial contributions in the z direction (d_{xz} and d_{yz}). This split however is unimportant for the case of Cu^{II} ions as all three orbitals would be filled entirely in both configurations and therefore no energy gain would be observed for one situation or the other. One important remark concerning Jahn-Teller distortions is the fact that it only strictly applies in systems with one unique ligand site, e.g. pure ammine complexes. The use of more than one inequivalent ligands is different, as different ligands cause different splittings in the ligand field and the degeneracy is therefore already lifted.[199] This effect, however, is normally superimposed with a further structural distortion and such an effect is hence called the pseudo-Jahn-Teller effect.

It has been found that elongated octahedral coordination is by far the most common for Cu^{II} complexes as opposed to the compressed octahedral coordination.[200] While the structural effects of the Jahn-Teller effect on the compounds analysed shall be discussed more in detail in Chapter 4, a general discussion of the effect of Jahn-Teller distortions in the solid shall be included here. While the rotational freedom of a complex in an isotropic environment (e.g. dissolved in a mobile solvent) means that the axial and equatorial ligands are only determined relative to each other, the same is not true for solid state systems. As the complexes are embedded into a defined structure, their orientation relative to the environment becomes important and two general cases could be envisaged: a) The Jahn-Teller distorted geometry is translated into the crystal symmetry and a defined orientation may be found, or b) The molecular symmetry of the complex clashes with the long range symmetry of the crystal structure and the distortion cannot be simply accounted for in the crystal structure. While the former case is trivial and is normally easily detected, the latter case can be less intuitive. Given the arrangement in space is important, one has to consider the case for the three crystal axes (x, y, z - note these are no longer the complex axes discussed above).[201] Again, three general cases would be possible: 1) The complex arranges along one of the three crystal directions predominantly (This case is equivalent with case a) above and hence is also trivial). 2) All three possible orientations are energetically equally favoured. The orientation of the distorted complex in such system would therefore be statistical and the complex appears crystallographically, which averages over space and time as regular octahedra because all positions are occupied by the same ratio of elongated and compressed sites and the average on all sites is therefore equal. 3) Two out of three possible orientations are preferred while the third is not. In this case, due to the 2:4 axial-to equatorial ratio, two out of three directions are statistically occupied by elongated and contracted ligands while the third direction is uniquely occupied by contracted ligands. The crystallographic image would therefore show two short ligand bonds and four longer ones, *i.e.* an apparent compressed octahedral coordination. Depending on the energy barrier between the orientation and whether the thermal motion is high enough to cross this barrier, the distortions above can be dynamic, *i.e.* the different forms constantly transform into each other in which case the positions are averaged over time, or static, *i.e.* the given statistical distribution is constant over time in which the crystallographic averaging over space is predominant. The structural consequence of both is, however, similar.[199]

1.6. Aims of this work

The exploration of novel storage materials forms the foundation of this work as well as its primary objective. It will be studied whether the systems under consideration are suitable for ammonia storage and can live to the standards of the state-of-the-art ammonia and hydrogen storage systems. Further objective of this work is the thorough study of structural effects in these material and to link these to the materials characteristics in order to allow direct and guided tuning of the parameters. This second objective also sets the starting point for the detailed studies on the Jahn-Teller distortion in the Cu system (chapter four) as well as the studies on the nitrate compounds (chapter five) as the characteristics of these systems may reveal precious information for promising ammonia stores such as the Ni system (chapter three).

1.7. References

[1] N. Kuhn, T. M. Klapötke, *Allgemeine und Anorganische Chemie: Eine Einführung*, Springer-Verlag, 2014.

[2] L. Schlapbach, A. Züttel, *Nature*, 2001, **414**, 353–358.

[3] H. P. Latscha, M. Mutz, *Chemie der Elemente: Chemie-Basiswissen IV*, Springer-Verlag, 2011.

[4] M. Rosenbaum, U. Schröder, *Electroanal.*, 2010, **22**, 844–855.

[5] D. Das, T. N. Veziroğlu, *Int. J. Hydrogen Energy*, 2001, **26**, 13–28.

[6] I. Dincer, C. Acar, *Int. J. Hydrogen Energy*, 2015, **40**, 11094–11111.

[7] F. Yilmaz, M. T. Balta, R. Selbaş, *Renewable Sustainable Energy Rev.*, 2016, **56**, 171–178.

[8] Y. Tachibana, L. Vayssieres, J. R. Durrant, *Nature Photonics*, 2012, **6**, 511–518.

[9] P. Du, R. Eisenberg, *Energy Env. Sci.*, 2012, **5**, 6012–6021.

[10] F. Gärtner, B. Sundararaju, A.-E. Surkus, A. Boddien, B. Loges, H. Junge, P. Dixneuf, M. Beller, *Angew. Chem. Int. Ed.*, 2009, **48**, 9962–9965.

[11] P.-E. Car, M. Guttentag, K. K. Baldridge, R. Alberto, G. R. Patzke, *Green Chem.*, 2012, **14**, 1680–1688.

[12] Q. Yin, J. M. Tan, C. Besson, Y. V. Geletii, D. G. Musaev, A. E. Kuznetsov, Z. Luo, K. I. Hardcastle, C. L. Hill, *Science*, 2010, **328**, 342–345.

[13] A. Juris, V. Balzani, F. Barigelletti, S. Campagna, P. l. Belser, A. Von Zelewsky, *Coord. Chem. Rev.*, 1988, **84**, 85–277.

[14] A. Currao, *CHIMIA Int. J. Chem.*, 2007, **61**, 815–819.

[15] W. J. Youngblood, S.-H. A. Lee, Y. Kobayashi, E. A. Hernandez-Pagan, P. G. Hoertz, T. A. Moore, A. L. Moore, D. Gust, T. E. Mallouk, *J. Am. Chem. Soc.*, 2009, **131**, 926–927.

[16] M. Wang, Z. Wang, X. Gong, Z. Guo, *Renewable Sustainable Energy Rev.*, 2014, **29**, 573–588.

[17] E. Rasten, G. Hagen, R. Tunold, *Electrochim. Acta*, 2003, **48**, 3945–3952.

[18] M. W. Kanan, D. G. Nocera, *Science*, 2008, **321**, 1072–1075.

[19] A. J. Esswein, M. J. McMurdo, P. N. Ross, A. T. Bell, T. D. Tilley, *J. Phys. Chem. C*, 2009, **113**, 15068–15072.

[20] C. M. White, R. R. Steeper, A. E. Lutz, *Int. J. Hydrogen Energy*, 2006, **31**, 1292–1305.

[21] J. J. Smith, G. Schneider, D. Suslov, M. Oschwald, O. Haidn, *Aerospace Science and Technology*, 2007, **11**, 39–47.

[22] L. M. Das, *Int. J. Hydrogen Energy*, 1996, **21**, 703–715.

[23] J. D. Naber, D. L. Siebers, *Int. J. Hydrogen Energy*, 1998, **23**, 363–371.

[24] S. Szwaja, K. Grab-Rogalinski, *Int. J. Hydrogen Energy*, 2009, **34**, 4413–4421.

[25] S. O. Akansu, Z. Dulger, N. Kahraman, T. N. Veziroğlu, *Int. J. Hydrogen Energy*, 2004, **29**, 1527–1539.

[26] J. Wang, Z. Huang, Y. Fang, B. Liu, K. Zeng, H. Miao, D. Jiang, *Int. J. Hydrogen Energy*, 2007, **32**, 3555–3564.

[27] Z. Huang, J. Wang, B. Liu, K. Zeng, J. Yu, D. Jiang, *Fuel*, 2007, **86**, 381–387.

[28] H. An, W. M. Yang, A. Maghbouli, J. Li, S. K. Chou, K. J. Chua, *Int. J. Hydrogen Energy*, 2013, **38**, 2919–2928.

[29] J. Lehmann, T. Luschtinetz in *Wasserstoff und Brennstoffzellen*, Springer, 2014, . 25–49.

[30] C. Mohrdieck, M. Venturi, K. Breitrück, H. Schulze in *Wasserstoff und Brennstoffzelle*, Springer, 2014, . 59–111.

[31] H. Eichlseder, M. Klell, *Wasserstoff in der Fahrzeugtechnik: Erzeugung, Speicherung, Anwendung*, Springer, 2012, chapter Brennstoffzellen, . 219–254.

[32] D. K. Ross, *Vacuum*, 2006, **80**, 1084–1089.

[33] A. Züttel, *Materials today*, 2003, **6**, 24–33.

[34] T. A. Semelsberger, K. P. Brooks, *J. Power Sources*, 2015, **279**, 593–609.

[35] U. Eberle, M. Felderhoff, F. Schueth, *Angew. Chem. Int. Ed.*, 2009, **48**, 6608–6630.

[36] N. L. Rosi, J. Eckert, M. Eddaoudi, D. T. Vodak, J. Kim, M. O'Keeffe, O. M. Yaghi, *Science*, 2003, **300**, 1127–1129.

[37] J. L. C. Rowsell, O. M. Yaghi, *Angew. Chem. Int. Ed.*, 2005, **44**, 4670–4679.

[38] L. J. Murray, M. Dincă, J. R. Long, *Chem. Soc. Rev.*, 2009, **38**, 1294–1314.

[39] D. J. Tranchemontagne, K. S. Park, H. Furukawa, J. Eckert, C. B. Knobler, O. M. Yaghi, *J. Phys. Chem. C*, 2012, **116**, 13143–13151.

[40] S. S. Han, H. Furukawa, O. M. Yaghi, W. A. Goddard iii, *J. Am. Chem. Soc.*, 2008, **130**, 11580–11581.

[41] D. Cao, J. Lan, W. Wang, B. Smit, *Angew. Chem. Int. Ed.*, 2009, **48**, 4730–4733.

[42] A. C. Dillon, K. M. Jones, T. A. Bekkedahl, C. H. Kiang, D. S. Bethune, M. J. Heben, *Nature*, 1997, **386**, 377–379.

[43] C. Liu, Y. Y. Fan, M. Liu, H. T. Cong, H. M. Cheng, M. S. Dresselhaus, *Science*, 1999, **286**, 1127–1129.

[44] S. M. Lee, Y. H. Lee, *Appl. Phys. Lett.*, 2000, **76**, 2877–2879.

[45] A. C. Dillon, M. J. Heben, *Appl. Phys. A*, 2001, **72**, 133–142.

[46] M. Hirscher, M. Becher, M. Haluska, U. Dettlaff-Weglikowska, A. Quintel, G. Duesberg, Y.-M. Choi, P. Downes, M. Hulman, S. Roth, I. Stepanek, P. Bernier, *Appl. Phys. A*, 2001, **72**, 129–132.

[47] H.-M. Cheng, Q.-H. Yang, C. Liu, *Carbon*, 2001, **39**, 1447–1454.

[48] M. Ritschel, M. Uhlemann, O. Gutfleisch, A. Leonhardt, A. Graff, C. Täschner, J. Fink, *Appl. Phys. Lett.*, 2002, **80**, 2985–2987.

[49] A. Züttel, P. Sudan, P. Mauron, T. Kiyobayashi, C. Emmenegger, L. Schlapbach, *Int. J. Hydrogen Energy*, 2002, **27**, 203–212.

[50] R. Ströbel, J. Garche, P. T. Moseley, L. Jörissen, G. Wolf, *J. Power Sources*, 2006, **159**, 781–801.

[51] H. Jin, Y. S. Lee, I. Hong, *Catal. Today*, 2007, **120**, 399–406.

[52] M. G. Nijkamp, J. E. M. J. Raaymakers, A. J. Van Dillen, K. P. De Jong, *Appl. Phys. A*, 2001, **72**, 619–623.

[53] P. A. Sermon, G. C. Bond, *Catal. Rev.*, 1974, **8**, 211–239.

[54] Y. Li, R. T. Yang, *J. Am. Chem. Soc.*, 2006, **128**, 726–727.

[55] L. Wang, R. T. Yang, *Energy Env. Sci.*, 2008, **1**, 268–279.

[56] K. M. Thomas, *Catal. Today*, 2007, **120**, 389–398.

[57] A. G. Wong-Foy, A. J. Matzger, O. M. Yaghi, *J. Am. Chem. Soc.*, 2006, **128**, 3494–3495.

[58] H. Reardon, J. M. Hanlon, R. W. Hughes, A. Godula-Jopek, T. K. Mandal, D. H. Gregory, *Energy Env. Sci.*, 2012, **5**, 5951–5979.

[59] J. Breternitz, D. H. Gregory, *Crystals*, 2015, **5**, 617–633.

[60] T. J. Boyle, L. A. M. Ottley, S. D. Daniel-Taylor, L. J. Tribby, S. D. Bunge, A. L. Costello, T. M. Alam, J. C. Gordon, T. M. McCleskey, *Inorg. Chem.*, 2007, **46**, 3705–3713.

[61] M. Podsiadło, A. Olejniczak, A. Katrusiak, *J. Phys. Chem. C*, 2013, **117**, 4759–4763.

[62] A. Budzianowski, A. Olejniczak, A. Katrusiak, *Acta Crystallogr. B*, 2006, **62**, 1078–1089.

[63] T. Jaroń, W. Grochala, *Acta Crystallogr. E*, 2011, **67**, o2171–o2171.

[64] N. Kuhn, M. Steimannand, G. Weyers, *Z. Kristallogr. - New Cryst. Struc.*, 2001, **216**, 325–327.

[65] T. V. Rodionova, V. Y. Komarov, G. V. Villevald, T. D. Karpova, N. V. Kuratieva, A. Y. Manakov, *J. Phys. Chem. B*, 2013, **117**, 10677–10685.

[66] H.-K. Mao, A. P. Jephcoat, R. J. Hemley, L. W. Finger, C. S. Zha, R. M. Hazen, D. E. Cox, *Science*, 1988, **239**, 1131–1134.

[67] I. P. Jain, C. Lal, A. Jain, *Int. J. Hydrogen Energy*, 2010, **35**, 5133–5144.

[68] P. Chen, M. Zhu, *Materials today*, 2008, **11**, 36–43.

[69] H. Ewe, E. W. Justi, K. Stephan, *Energy Convers.*, 1973, **13**, 109–113.

[70] R. W. G. Wyckoff, *Crystal structures 2nd ed.*, Interscience New York, 1963.

[71] D. A. Lang, J. V. Zaikina, D. D. Lovingood, T. E. Gedris, S. E. Latturner, *J. Am. Chem. Soc.*, 2010, **132**, 17523–17530.

[72] I. J. Maley, D. H. Brown, R. M. Ibberson, C. R. Pulham, *Acta Crystallogr. B*, 2008, **64**, 312–317.

[73] S.-i. Orimo, Y. Nakamori, J. R. Eliseo, A. Züttel, C. M. Jensen, *Chem. Rev.*, 2007, **107**, 4111–4132.

[74] A. Züttel, P. Wenger, S. Rentsch, P. Sudan, P. Mauron, C. Emmenegger, *J. Power Sources*, 2003, **118**, 1–7.

[75] Z. Huang, X. Chen, T. Yisgedu, E. A. Meyers, S. G. Shore, J.-C. Zhao, *Inorg. Chem.*, 2011, **50**, 3738–3742.

[76] Y. Filinchuk, D. Chernyshov, R. Cerny, *J. Phys. Chem. C*, 2008, **112**, 10579–10584.

[77] Y. Filinchuk, R. Cerny, H. Hagemann, *Chem. Mater.*, 2009, **21**, 925–933.

[78] L. H. Rude, M. Corno, P. Ugliengo, M. Baricco, Y.-S. Lee, Y. W. Cho, F. Besenbacher, J. Overgaard, T. R. Jensen, *J. Phys. Chem. C*, 2012, **116**, 20239–20245.

[79] A. C. Dunbar, J. A. Macor, G. S. Girolami, *Inorg. Chem.*, 2013, **53**, 822–826.

[80] D. M. Goedde, G. K. Windler, G. S. Girolami, *Inorg. Chem.*, 2007, **46**, 2814–2823.

[81] M. Panda, K. Hofmann, M. H. Prosenc, B. Albert, *Dalton Trans.*, 2008, 3956–3958.

[82] W. T. Klooster, T. F. Koetzle, P. E. Siegbahn, T. B. Richardson, R. H. Crabtree, *J. Am. Chem. Soc.*, 1999, **121**, 6337–6343.

[83] C. W. Yoon, P. J. Carroll, L. G. Sneddon, *J. Am. Chem. Soc.*, 2008, **131**, 855–864.

[84] S. Mebs, S. Grabowsky, D. Förster, R. Kickbusch, M. Hartl, L. L. Daemen, W. Morgenroth, P. Luger, B. Paulus, D. Lentz, *J. Phys. Chem. A*, 2010, **114**, 10185–10196.

[85] D. Förster, C. B. Hübschle, P. Luger, T. Hügle, D. Lentz, *Inorg. Chem.*, 2008, **47**, 1874–1876.

[86] F. H. Stephens, V. Pons, R. T. Baker, *Dalton Trans.*, 2007, 2613–2626.

[87] C. R. Miranda, G. Ceder, *J. Chem. Phys.*, 2007, **126**, 184703.

[88] T. Richardson, S. de Gala, R. H. Crabtree, P. E. Siegbahn, *J. Am. Chem. Soc.*, 1995, **117**, 12875–12876.

[89] Z. Huang, T. Autrey, *Energy Env. Sci.*, 2012, **5**, 9257–9268.

[90] Z. Xiong, C. K. Yong, G. Wu, P. Chen, W. Shaw, A. Karkamkar, T. Autrey, M. O. Jones, S. R. Johnson, P. P. Edwards, W. I. F. David, *Nat. Mater.*, 2008, **7**, 138–141.

[91] *U.S. Geological survey, Nitrogen*, 2013, accessed 02/04/2016. `http://minerals.usgs.gov/minerals/pubs/commodity/nitrogen/myb1-2013-nitro.pdf`.

[92] V. Smil, *Nature*, 1999, **400**, 415–415.

[93] J. W. Erisman, M. A. Sutton, J. Galloway, Z. Klimont, W. Winiwarter, *Nat. Geosci.*, 2008, **1**, 636–639.

[94] F. Haber, G. Van Oordt, *Z. Anorg. Chem.*, 1905, **44**, 341–378.

[95] E. C. Cocking, *European Rev.*, 2000, **8**, 193–200.

[96] D. Mckay, D. H. Gregory, J. S. Hargreaves, S. M. Hunter, X. Sun, *Chem. Commun.*, 2007, 3051–3053.

[97] S. Giddey, S. Badwal, A. Kulkarni, *Int. J. Hydrogen Energy*, 2013, **38**, 14576–14594.

[98] T. Oshikiri, K. Ueno, H. Misawa, *Angew. Chem.*, 2016.

[99] R. Lan, J. T. S. Irvine, S. Tao, *Int. J. Hydrogen Energy*, 2012, **37**, 1482–1494.

[100] S. M. Grannell, D. N. Assanis, S. V. Bohac, D. E. Gillespie, *J. Eng. Gas Turbines Power*, 2008, **130**, 042802.

[101] A. J. Reiter, S.-C. Kong, *Energy Fuels*, 2008, **22**, 2963–2971.

[102] E. Kroch, *J. Inst. Pet*, 1945, **31**, 213–223.

[103] R. Z. Sørensen, L. J. Nielsen, S. Jensen, O. Hansen, T. Johannessen, U. Quaade, C. H. Christensen, *Catal. Commun.*, 2005, **6**, 229–232.

[104] S. F. Yin, B. Q. Xu, X. P. Zhou, C. Au, *Appl. Catal., A*, 2004, **277**, 1–9.

[105] F. Schüth, R. Palkovits, R. Schlögl, D. S. Su, *Energy Env. Sci.*, 2012, **5**, 6278–6289.

[106] W. I. F. David, J. W. Makepeace, S. K. Callear, H. M. A. Hunter, J. D. Taylor, T. J. Wood, M. O. Jones, *J. Am. Chem. Soc.*, 2014, **136**, 13082–13085.

[107] J. W. Makepeace, T. J. Wood, H. M. Hunter, M. O. Jones, W. I. David, *Chem. Sci.*, 2015, **6**, 3805–3815.

[108] T. J. Wood, J. W. Makepeace, H. M. Hunter, M. O. Jones, W. I. David, *Phys. Chem. Chem. Phys.*, 2015, **17**, 22999–23006.

[109] J. W. Makepeace, H. M. Hunter, T. J. Wood, R. I. Smith, C. A. Murray, W. I. David, *Faraday Discuss.*, 2015.

[110] N. V. Rees, R. G. Compton, *Energy Env. Sci.*, 2011, **4**, 1255–1260.

[111] Q. Ma, R. Peng, Y. Lin, J. Gao, G. Meng, *J. Power Sources*, 2006, **161**, 95–98.

[112] A. Fuerte, R. Valenzuela, M. Escudero, L. Daza, *J. Power Sources*, 2009, **192**, 170–174.

[113] F. Ishak, I. Dincer, C. Zamfirescu, *J. Power Sources*, 2012, **202**, 157–165.

[114] A. Afif, N. Radenahmad, Q. Cheok, S. Shams, J. H. Kim, A. K. Azad, *Renewable Sustainable Energy Rev.*, 2016, **60**, 822–835.

[115] C. Zamfirescu, I. Dincer, *J. Power Sources*, 2008, **185**, 459–465.

[116] R. C. Weast, M. J. Astle (Eds.), *Handbook of Chemistry and Physics, 61st edition*, CRC Press, 1981.

[117] C. J. Plank, H. Hunt, *J. Am. Chem. Soc.*, 1939, **61**, 3590–3591.

[118] L. Ye, B. T. Lo, J. Qu, I. Wilkinson, T. Hughes, C. A. Murray, C. C. Tang, S. C. E. Tsang, *Chem. Commun.*, 2016, **52**, 3422–3425.

[119] C. J. Doonan, D. J. Tranchemontagne, T. G. Glover, J. R. Hunt, O. M. Yaghi, *Nat. Chem.*, 2010, **2**, 235–238.

[120] J. Helminen, J. Helenius, E. Paatero, I. Turunen, *J. Chem. Eng. Data*, 2001, **46**, 391–399.

[121] M. Dietrich, D. Rauch, U. Simon, A. Porch, R. Moos, *J. Sens. Sens. Syst.*, 2015, **4**, 263.

[122] C. H. Christensen, R. Z. Sorensen, T. Johannessen, U. J. Quaade, K. Honkala, T. D. Elmoe, R. Kohler, J. K. Norskov, *J. Mater. Chem.*, 2005, **15**, 4106–4108.

[123] C. H. Christensen, T. Johannessen, R. Z. Sørensen, J. K. Nørskov, *Catal. Today*, 2006, **111**, 140–144.

[124] A. Klerke, C. H. Christensen, J. K. Nørskov, T. Vegge, *J. Mater. Chem.*, 2008, **18**, 2304–2310.

[125] J. S. Hummelshøj, R. Z. Sørensen, M. Y. Kustova, T. Johannessen, J. K. Nørskov, C. H. Christensen, *J. Am. Chem. Soc.*, 2006, **128**, 16–17.

[126] H. S. Jacobsen, H. A. Hansen, J. W. Andreasen, Q. Shi, A. Andreasen, R. Feidenhans, M. M. Nielsen, K. Ståhl, T. Vegge, *Chem. Phys. Lett.*, 2007, **441**, 255–260.

[127] A. Tekin, J. S. Hummelshøj, H. S. Jacobsen, D. Sveinbjörnsson, D. Blanchard, J. K. Nørskov, T. Vegge, *Energy Env. Sci.*, 2010, **3**, 448–456.

[128] M. H. Sørby, O. M. Løvvik, M. Tsubota, T. Ichikawa, Y. Kojima, B. C. Hauback, *Phys. Chem. Chem. Phys.*, 2011, **13**, 7644–7648.

[129] H. Zhu, X. Gu, K. Yao, L. Gao, J. Chen, *Ind. Eng. Chem. Res.*, 2009, **48**, 5317–5320.

[130] M. O. Jones, D. M. Royse, P. P. Edwards, W. I. F. David, *Chem. Phys.*, 2013, **427**, 38–43.

[131] R. Z. Sørensen, J. S. Hummelshøj, A. Klerke, J. B. Reves, T. Vegge, J. K. Nørskov, C. H. Christensen, *J. Am. Chem. Soc.*, 2008, **130**, 8660–8668.

[132] S. Lysgaard, A. L. Ammitzbøll, R. E. Johnsen, P. Norby, U. J. Quaade, T. Vegge, *Int. J. Hydrogen Energy*, 2012, **37**, 18927–18936.

[133] A. L. Ammitzbøll, S. Lysgaard, A. Klukowska, T. Vegge, U. J. Quaade, *J. Chem. Phys.*, 2013, **138**, 164701.

[134] R. E. Johnsen, P. B. Jensen, P. Norby, T. Vegge, *J. Phys. Chem. C*, 2014, **118**, 24349–24356.

[135] H. Reardon, J. M. Hanlon, M. Grant, I. Fullbrook, D. H. Gregory, *Crystals*, 2012, **2**, 193–212.

[136] P. B. Jensen, S. Lysgaard, U. J. Quaade, T. Vegge, *Phys. Chem. Chem. Phys.*, 2014, **16**, 19732–19740.

[137] P. B. Jensen, A. Bialy, D. Blanchard, S. Lysgaard, A. K. Reumert, U. J. Quaade, T. Vegge, *Chem. Mater.*, 2015, **27**, 4552–4561.

[138] A. Bialy, P. B. Jensen, D. Blanchard, T. Vegge, U. J. Quaade, *J. Solid State Chem.*, 2015, **221**, 32–36.

[139] S. Johnson, W. I. David, D. Royse, M. Sommariva, C. Tang, F. P. Fabbiani, M. Jones, P. Edwards, *Chem. Asian J.*, 2009, **4**, 849–854.

[140] D. Pontiroli, D. D'Alessio, M. Gaboardi, G. Magnani, C. Milanese, S. Duyker, V. Peterson, N. Sharma, M. Riccò, *J. Mater. Chem. A*, 2015, **3**, 21099–21105.

[141] J. Hartley, A. Porch, M. Jones, *Sens. Actuators, B*, 2015, **210**, 726–730.

[142] B. Weber, *Koordinationschemie: Grundlagen und aktuelle Trends*, Springer-Verlag, 2014, chapter Was Sind Komplexe?, . 3 ff.

[143] V. Carunchio, *Polyhedron*, 2002, **21**, 1313–1318.

[144] L. Beyer, J. A. Cornejo, *Koordinationschemie: Grundlagen-Synthesen-Anwendungen*, Springer-Verlag, 2012.

[145] B. M. Tassaert, *Ann. Chim.*, 1798, **28**, 92–107.

[146] A. Werner, *Z. Anorg. Chem.*, 1893, **3**, 267–330.

[147] *The Nobel Prize in Chemistry 1913*, Nobelprize.org, 2016, accessed 15/02/2016. `http://www.nobelprize.org/nobel_prizes/chemistry/laureates/1913/`.

[148] R. W. G. Wyckoff, E. Posnjak, *J. Am. Chem. Soc.*, 1921, **43**, 2292–2309.

[149] R. W. G. Wyckoff, *J. Am. Chem. Soc.*, 1922, **44**, 1239–1245.

[150] P. Scherrer, P. Stoll, *Z. Anorg. Allg. Chem.*, 1922, **121**, 319–320.

[151] W. Biltz, E. Birk, *Z. Anorg. Allg. Chem.*, 1923, **127**, 34–42.

[152] W. Biltz, B. Fetkenheuer, *Z. Anorg. Chem.*, 1913, **83**, 163–176.

[153] W. Biltz, *Z. Anorg. Chem.*, 1913, **83**, 177–192.

[154] W. Biltz, B. Fetkenheuer, *Z. Anorg. Chem.*, 1914, **89**, 97–133.

[155] W. Biltz, B. Fetkenheuer, *Z. Anorg. Chem.*, 1914, **89**, 134–140.

[156] W. Biltz, *Z. Anorg. Chem.*, 1914, **89**, 141–163.

[157] W. Biltz, G. F. Hüttig, *Z. Anorg. Allg. Chem.*, 1919, **109**, 89–110.

[158] W. Biltz, *Z. Anorg. Allg. Chem.*, 1919, **109**, 132–144.

[159] W. Biltz, W. Stollenwerk, *Z. Anorg. Allg. Chem.*, 1920, **114**, 174–202.

[160] W. Biltz, G. F. Hüttig, *Z. Anorg. Allg. Chem.*, 1920, **114**, 241–265.

[161] W. Stollenwerk, W. Biltz, *Z. Anorg. Allg. Chem.*, 1921, **119**, 97–114.

[162] W. Biltz, G. F. Hüttig, *Z. Anorg. Allg. Chem.*, 1921, **119**, 115–131.

[163] G. F. Hüttig, *Z. Anorg. Allg. Chem.*, 1922, **123**, 31–42.

[164] W. Biltz, W. Fischer, *Z. Anorg. Allg. Chem.*, 1922, **124**, 230–247.

[165] G. F. Hüttig, *Z. Anorg. Allg. Chem.*, 1922, **124**, 322–332.

[166] G. F. Hüttig, W. Martin, *Z. Anorg. Allg. Chem.*, 1922, **125**, 269–280.

[167] W. Biltz, W. Hansen, *Z. Anorg. Allg. Chem.*, 1923, **127**, 1–33.

[168] W. Biltz, W. Fischer, *Z. Anorg. Allg. Chem.*, 1923, **129**, 1–14.

[169] W. Biltz, C. Messerknecht, *Z. Anorg. Allg. Chem.*, 1923, **129**, 161–175.

[170] W. Biltz, *Z. Anorg. Allg. Chem.*, 1923, **130**, 93–139.

[171] W. Biltz, E. Rahlfs, *Z. Anorg. Allg. Chem.*, 1925, **148**, 145–151.

[172] W. Biltz, C. Messerknecht, *Z. Anorg. Allg. Chem.*, 1925, **148**, 157–169.

[173] W. Biltz, C. Mau, *Z. Anorg. Allg. Chem.*, 1925, **148**, 170–191.

[174] W. Biltz, W. Wein, *Z. Anorg. Allg. Chem.*, 1925, **148**, 192–206.

[175] W. Biltz, H. Bröhan, W. Wein, *Z. Anorg. Allg. Chem.*, 1925, **148**, 207–216.

[176] W. Klemm, *Z. Anorg. Allg. Chem.*, 1927, **163**, 240–252.

[177] W. Biltz, K. A. Klatte, E. Rahlfs, *Z. Anorg. Allg. Chem.*, 1927, **166**, 339–350.

[178] W. Biltz, E. Rahlfs, *Z. Anorg. Allg. Chem.*, 1927, **166**, 351–376.

[179] W. Klemm, E. Tanke, *Z. Anorg. Allg. Chem.*, 1931, **200**, 343–366.

[180] W. Klemm, W. Tilk, H. Jacobi, *Z. Anorg. Allg. Chem.*, 1932, **207**, 187–203.

[181] F. Ephraim, *Ber. Dtsch. Chem. Ges.*, 1912, **45**, 1322–1331.

[182] F. Ephraim, *Z. Phys. Chem.*, 1913, **1**, 513.

[183] F. Ephraim, *Ber. Dtsch. Chem. Ges.*, 1913, **46**, 3103–3113.

[184] F. Ephraim, R. Linn, *Ber. Dtsch. Chem. Ges.*, 1913, **46**, 3742–3762.

[185] F. Ephraim, A. Jahnsen, *Ber. Dtsch. Chem. Ges.*, 1915, **48**, 41–56.

[186] F. Ephraim, *Ber. Dtsch. Chem. Ges.*, 1915, **48**, 624–629.

[187] F. Ephraim, E. Bolle, *Ber. Dtsch. Chem. Ges.*, 1915, **48**, 638–648.

[188] F. Ephraim, E. Bolle, *Ber. Dtsch. Chem. Ges.*, 1915, **48**, 1770–1777.

[189] F. Ephraim, S. Millmann, *Ber. Dtsch. Chem. Ges.*, 1917, **50**, 529–541.

[190] F. Ephraim, E. Rosenberg, *Ber. Dtsch. Chem. Ges.*, 1918, **51**, 130–136.

[191] F. Ephraim, *Ber. Dtsch. Chem. Ges.*, 1918, **51**, 644–669.

[192] F. Ephraim, *Ber. Dtsch. Chem. Ges.*, 1918, **51**, 706–710.

[193] F. Ephraim, *Ber. Dtsch. Chem. Ges. B*, 1919, **52**, 236–241.

[194] F. Ephraim, *Ber. Dtsch. Chem. Ges. B*, 1919, **52**, 241–254.

[195] F. Ephraim, *Ber. Dtsch. Chem. Ges. B*, 1919, **52**, 940–957.

[196] F. Ephraim, *Ber. Dtsch. Chem. Ges. B*, 1919, **52**, 957–964.

[197] F. Ephraim, F. Moser, *Ber. Dtsch. Chem. Ges. B*, 1920, **53**, 548–563.

[198] H. A. Jahn, E. Teller in *Proceedings of the Royal Society of London A: Mathematical, Physical and Engineering Sciences*, The Royal Society, . 220–235.

[199] L. R. Falvello, *J. Chem. Soc., Dalton Trans.*, 1997, 4463–4476.

[200] M. A. Halcrow, *Dalton Trans.*, 2003, 4375–4384.

[201] R. J. Deeth, L. J. Hearnshaw, *Dalton Trans.*, 2006, 1092–1100.

2. Experimental Section

2.1. Gravimetric Uptake Experiments

Two different setups were used for gas uptake experiments. The major part of the experiments were conducted using a commercial instrument (ISOSorp, Rubotherm), while the uptake into $CuCl_2$ was additionally measured using a self-built apparatus under flowing ammonia conditions.

Static Atmosphere Instrument

The use of a magnetic suspension balance (ISOSorp, Rubotherm) allows the direct study of the mass changes of the sample in a static atmosphere of ammonia at given pressures (figure 2.1). The instrument separates the sample environment from the balance by the use of a magnetic field to carry the sample in the sample environment.[1] The sample could therefore be exposed to corrosive ammonia while the balance was in air. Samples were filled in a quartz glass sample holder in the glovebox and transported to the instrument in a closed vial. A short contact of the sample with ambient air could not be avoided during the sample preparation but was minimised (ca. 1 min) in order to avoid larger

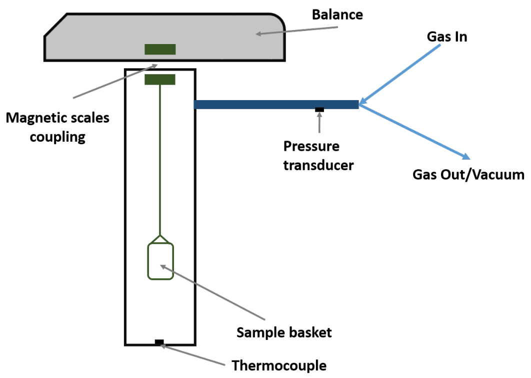

Figure 2.1.: Schematic of the static instrument used to measure the ammonia uptake.

water contents in the sample. During a typical experiment, the sample was left under vacuum at the beginning of the measurement and then exposed to ammonia gas at 1 bar. After this initial step, the sample was placed under different ammonia pressures according to the experimental conditions. The initial ammonia filling and pressure control had to be done manually as the software controlled process did not allow a quick pressurisation of the system. The temperature control was performed with an external heating mantle fed by a Julabo thermostat.

Ammonia Flow Measurements

Gravimetric measurements under dynamic atmospheres were conducted using a modified laboratory scales setup, where the balance was connected to a computer to measure the mass with a rate of $\approx$ 24 Hz. The sample and gas flow arrangement can be seen in Figure 2.2. in this setup, the sample could be weighed in the glovebox and transferred outside in a closed sample vial. This sample vial was also used as sample holder during the experiment; the vial cap was removed and the sample was exposed to ammonia atmosphere. A short contact of the sample with air could not be avoided during the measurement preparation but was kept to ca. 10 s to avoid sample contamination.

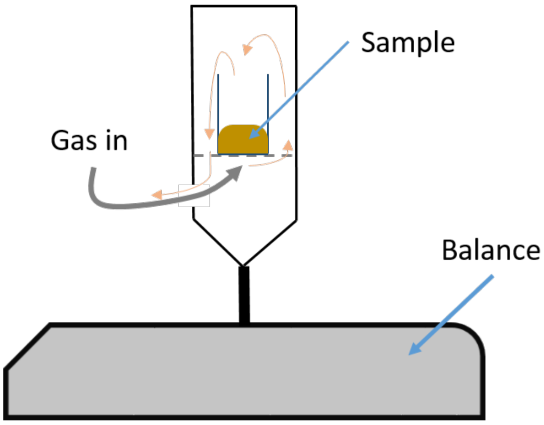

Figure 2.2.: Schematic of the dynamic scales setup used to measure the ammonia uptake. The orange arrows illustrate the gas flow within the measurement cell.

2.2. Thermal Analyses

The transformations of materials when heated up can give important information about their properties and composition. Three main techniques are used to study these transformations either simultaneously (henceforth referred to as simultaneous thermal analysis, STA) or independently from each other:

Thermo-gravimetry (TG) is used to follow the mass changes of the sample when heating. As the sample decomposes during heating, it commonly loses mass in the form of gaseous reaction products which will be carried away from the sample by the constant gas stream in the instrument. This mass loss is characteristic for the compound it is evolved from, and the comparison of the starting mass with the masses after the reaction steps allow the abstraction of chemical information of the sample. This shall be demonstrated for the hypothetical reaction:

$$\mathrm{A(s)} \xrightarrow{\Delta} x\mathrm{B(s)} + y\mathrm{C(g)}\uparrow$$

The direct observable is the mass of the sample at a given temperature (or time). Given that product C is gaseous, its mass is taken off the balance and hence the mass before the reaction can be fully attributed to product A ($m_{\text{start}} = m_{\text{A}}$), the mass at the end of the reaction fully to product B ($m_{\text{end}} = m_{\text{B}}$) and the mass difference to product C ($\Delta m = m_{\text{C}}$). This fulfils the general rule of constant masses as:

$$m_A = m_B + m_C \tag{2.1}$$

Hence the knowledge of two of the masses provides knowledge of the third. However, the direct observed mass losses do not allow the abstraction of the reaction formulae but the introduction of the number of moles (n) via the general relationship $m = n \cdot M$ (where M is the molar mass of the compound) allows the direct comparison of the observed results with the reaction equation through:

$$m_A = n_A \cdot M_A \tag{2.2}$$

$$m_B = n_B \cdot M_B \tag{2.3}$$

Further, the general relationship between n_A and n_B is determined through the stoichiometry of the reaction as:

$$n_A = x \cdot n_B \tag{2.4}$$

With the knowledge of this, the relative mass loss during the experiment $w = m_B/m_A$ can be determined solely on the basis of the reaction equation and the molar masses of compounds A and B as materials constants:

$$w = \frac{m_B}{m_A} = x \cdot \frac{M_B}{M_A} \tag{2.5}$$

which means that the mass loss is specific for a certain reaction and allows the determination of one parameter M_A, M_B or x if the other two are known.

Differential thermal analysis (DTA) is a complementary method in which the temperature change between two sample holders is measured. The empty reference sample holder serves to determine the temperature curve unaffected by effects from the sample. Given the sample in the other sample holder undergoes a reaction, it either releases heat (exothermic reaction) or it consumes heat from the surroundings (endothermic reaction). In the event of an exothermic reaction, the supplementary heat from the reaction heats the sample container further than the reference and a positive temperature difference can be observed. Conversely for an endothermic reaction, the sample consumes heat from the surrounding and the temperature of the sample drops below the temperature of the reference. In the simplest case employed here, the nature of the reactions can be detected very easily from the difference signal and a qualitative statement of the reaction behaviour can be drawn without further calibration. It would however be possible to determine the calorimetric capacity of the instrument by the measurement of a standard sample with known heat of reaction in order to obtain quantitative information on the heat of reactions, but this was not pursued during this work.

The knowledge of the thermodynamics of a reaction allows further assumptions on the reactions causing a weight loss as well as the detection of reactions without any weight changes, *i.e.* pure solid-solid reactions, as well as physical transformations in the solid like crystallisation, glass transitions or crystal phase changes.

Evolved Gas Analysis *via* mass spectrometry (MS) is the third complementary method to gain more information on the reaction, and more specifically on the gases released from the reaction. In cases where it is doubtful which reaction products evolve from the reaction or even on the nature of the starting material, equation (2.5) is of limited use. It can therefore be very helpful to identify the gaseous products from the reaction as a direct insight into one part of the reaction. The gas evolved from the reaction is carried by the gas stream from the reaction furnace towards the mass spectrometer and a small fraction of the gas stream is used to analyse the gas composition. In order to gain this information, the sample gas stream is first ionised to obtained charged particles, which are then driven through a magnetic field, where they are separated as a function of their mass-to-charge ratio m/z. The impact of the magnetic field on the flight pathway is a function of the field strength, the mass of the object and its electrical charge. The separated fractions are then directed to the detector, where an electrical current proportional to the number of charged objects is generated, proportional to the amount of ions per m/z ratio.

2.2.1. Kissinger analyses

While common activation energy determination using Arrhenius' law[2,3] $k = A \cdot \exp\left[-E_a/(RT)\right]$ necessitates the determination of *isothermal* reaction constants at different temperatures, Kissinger developed a special form of Arrhenius' law using non-isothermal DTA data at different heating rates.[4] Kissinger took the peak temperature of the DTA signal as the point of maximal reaction rate and was hence able to draw a quantitative comparison between the different heating rates and their respective reaction rate through this relationship. Through some simplification steps, Kissinger obtained a general relationship independent of the reaction order:[5]

$$\frac{d\left(\ln\frac{\beta}{T_m^2}\right)}{d\left(\frac{1}{T_m}\right)} = -\frac{E_a}{R} \tag{2.6}$$

where β is the heating rate, T_m is the peak temperature, $R = 8.314 \frac{\mathrm{J}}{\mathrm{K \cdot mol}}$ is the universal gas constant and E_a is the activation energy. Plotting $\ln \frac{\beta}{T_m^2}$ against $\frac{1}{T_m}$ therefore yields linear function with the slope of $-\frac{E_a}{R}$ and the activation energy may therefore be directly determined from non-isothermal DTA data.

Experimental

Thermal analyses were conducted on a Netzsch 409 PC STA instrument under flowing argon gas (BOC, 99.998 %) coupled to a Hiden Analytical HPR 20 mass spectrometer. Combined STA-MS studies were conducted at a heating rate of 5 K/min with sample sizes of $\approx$ 30 mg in order to obtain clear MS signals. Variable heating rate experiments were conducted without MS and with samples of 15 $\pm$2 mg. The STA instrument was positioned inside an Argon filled glove box (UNIlab, MBraun) with O_2 and H_2O levels below 3 ppm to avoid contamination of the samples and the samples were loaded into Al_2O_3 sample holders.

2.3. Vibrational Spectroscopy

Chemical bonds are not static like a rod but can be considered as an attractive force holding the atoms together much like a spring. By analogy to a spring, the atoms are able to vibrate about the bonds when they are excited with energy. Unlike a spring, however, the strength of excitement is not arbitrary but is determined by the quantum states of the system and can hence only take discrete values.[6] This fact allows for the identification of vibrational modes within a molecule by a variety of techniques as only discrete amounts of energy are absorbed or emitted and a direct attribution of these is possible. Two different techniques were used to conduct vibrational spectroscopy during this study: Fourier-transform infrared (FTIR) spectroscopy and inelastic neutron scattering. While both techniques observe the same fundamental phenomenon, their mode of interaction with matter is different and hence the signals obtained are different as well.

2.3.1. FTIR Spectroscopy

Infrared spectroscopy is undoubtedly the most prominent vibrational spectroscopy and also the most widely used. The principle is very simple and reveals information on vibrational energy transitions lying in the infrared region of the electromagnetic spectrum. When irradiating the sample with infrared light, vibrational transitions are excited and light of the corresponding wavelength is absorbed, yielding a drop in the measured intensity at characteristic wavelengths. It is important to point out that not all vibrational modes can be excited using IR spectroscopy. In order to observe an interaction of the infrared light with a specific mode its dipole moment must change during the vibrational mode. This point is important as it restricts the observable transitions in high symmetry systems and the absence or presence of different modes can be significant for the structural analysis of a sample.

The instruments used during this study were equipped with an Attenuated Total Reflection (ATR) sample stage. When an electromagnetic wave undergoes a total reflection at the interface of a medium, it interacts with the matter at the opposite side of the interface without penetrating it.[7] This allows therefore to record the IR spectrum of a sample, when it is brought closely to an interface used for total reflection of infrared light. In a common procedure, the samples are pressed on a crystal (a diamond in the sample stages used herein), which provides suitable IR transmission and a suitable surface for the total reflection.

Experimental

Infrared spectra were collected on an attenuated total reflection Fourier-transform infrared spectrometer (ATR-FTIR) in the wavenumber range of 4000–600 cm^{-1} on an FTIR-8400S (*Shimadzu*). 24 accumulated spectra were collected with a resolution of 2 cm^{-1}. A short contact of the sample with ambient air could not be avoided when loading the samples on the spectrometer. However, the time of the sample in air was reduced to a minimum (ca. 2 s) to avoid reaction with oxygen or water in air. Far Infrared spectra were collected on a Bruker Vertex 70 with ATR sample stage in the range of 150–400 cm^{-1}. 100 spectra were collected and summed to yield the final result. Samples were pressed on the diamond measurement window.

2.3.2. Inelastic Neutron Scattering Spectroscopy

When neutrons interact with matter, they can interact elastically or inelastically, *i.e.* energy is transferred from the neutrons to the sample. The amount of energy transferred can be measured by comparing the known energy of the incident beam with the energy of the scattered beam after the sample. Analogous to excitation with infrared light, vibrational modes can be excited by neutrons in inelastic scattering events. It is therefore possible to measure the energy of scattered neutrons and correlate the loss of energy with the vibrational modes in the matter. The use of inelastic neutron scattering has some key advantages: 1) Selection rules do not apply as the scattering arises from the nucleus,[8] meaning that more transitions are observable; 2) Hydrogen ^{1}H has a larger cross-section than any other element and is hence predominantly detected when present;[9] and 3) Neutron scattering is a comparably rare event making this technique largely insensitive for scattering in the gaseous phase. This means that direct spectroscopic observations under specific gas atmospheres are possible,[9] which would normally be impossible in infrared spectroscopy due to the absorption of IR light by the gas phase.

Experimental

A sample of $[Cu(NH_3)_{6\text{-}x}]Cl_2$ was measured at the Tosca instrument at the ISIS pulsed neutron source (see section 2.8.8 for a brief description of the facility). TOSCA is an indirect neutron spectrometer,[10] i.e. the sample is irradiated with polychromatic neutrons while scattered neutrons are detected at a fixed energy by using graphite analysers.[11] TOSCA makes use of a gadolinium poisoned water moderator, which is 17 m far away from the sample and ^{3}He squashed tubes as detectors.[11] Ten detector banks are arranged around the sample and allow to measure both front scattering and back scattering.[11] The prepared sample (see chapter 4 for details of sample preparation) was sent to the facility and measurements were conducted there at 30 K.

2.4. UV-VIS Spectroscopy

When the energy of excitement is raised above the level of vibrational excitations, it is possible to provoke changes in the electronic structure of the matter and to lift electrons from their ground state into an excited state. The transitions observed in this work arise from transition metal complexes and are therefore closely linked to the formation of complexes. During the complex formation, the *d* orbitals of the transition metal central atom loose their degeneracy and lower/higher their energy level according to the coordination environment (see section 1.5). Such transitions are observable in the visible and UV region of light as the energy of this light corresponds to the energy differences between ground- and excited state, *i.e.* the energy an electron needs to jump from a lower energy orbital into a higher energy orbital. The observation of electronic transitions in metal complexes is particularly beneficial as the observed excitations are commonly those of split *d*-orbitals of the complex and hence are characteristic of a specific complex.

Experimental

UV-Vis spectra were obtained using a Shimadzu UV-2600 spectrometer with a diffuse reflectance sample holder. When light is hitting a rough surface, e.g. a powder sample, a fraction of the light gets reflected but while an even surface reflects the light in one direction (for instance in a mirror), a rough surface scatters in many directions. The diffuse reflectance sample stage is therefore built in a way, that the light reflected diffusely from the sample is collected. Herein, the detector sits in the middle of a spherical arrangement of parabolic mirrors, so that all scattered light is reflected towards the detector, an arrangement known as integrating sphere. Light with the energy of electronic transitions, will however be absorbed by the sample and the wavelength dispersive measurement of diffuse reflectance allows to probe the electronic spectra of the compounds. The instrument scanned through the wavelength range (1100 nm – 400 nm) with a slit width of 5 nm and a sampling interval of 0.5 nm. The sample was prepared in the glovebox and held between the sample holder and a quartz glass window to avoid decomposition in air.

A small further peak can be detected at the detector change wavelength (830 nm) but is instrumental rather than sample induced.

2.5. SEM/EDX experiments

Microscopy with radiation is ordinarily limited to a lower resolution limit, the Abbe limit, depending on the wavelength of the light used.[12,13] It should be noted that groundbreaking work on fluorescence microscopy in recent years has yielded in a method to overcome this limit.[14] Another way to overcome the Abbe limit for visible light microscopy is the use of smaller wavelengths, such as those encountered for electron beams. As electrons are charged, a stream of electrons can be accelerated and redirected through the use of electric and magnetic fields. Multiple physical processes happen when such an electron beam hits a sample. Those most important for SEM are: 1) Secondary electrons and 2) Characteristic X-ray emission. 1) Secondary electrons are emitted from the atoms of the sample when they are bombarded with an electron beam. These electrons can be conveniently detected as they have energy an order of magnitude smaller than the energy of the incident beam. There distribution is characteristic for the sample surface and therefore allows the imaging of the sample. 2) Characteristic X-ray emission is caused by removal of a lower shell electron through the high energy incident beam electrons. The hole in the lower shell is filled with an electron from a higher shell and the energy difference between the two electron states is emitted as an X-ray photon. The energy of these photons are characteristic of the elements and their amount is a direct function of the count of an atom species in the sample. Energy dispersive X-ray (EDX) spectroscopy is another technique for the qualitative and quantitative chemical analysis.

Experimental

SEM images for $[Ni(NH_3)_6](NO_3)_2$ were collected using an XL 30 ESEM (Philips) SEM with a tungsten filament and an accelerating voltage of 10 kV. The same instrument was used to collect the EDX spectra with a 10 mm^2 silicon drifted X-act EDX detector (Oxford Instruments) using 15 kV acceleration voltage. The SEM images of $[Ni(NH_3)_6]Cl_2$ were obtained on a ΣIGMA field emission SEM (Carl Zeiss) using an acceleration voltage of 15 kV and a target-to-sample distance of 8.5 mm. The samples were sputtered with gold prior to the experiments and the unavoidable contact of the samples with air was kept to a minimum (less than one minute).

2.6. Elemental Analyses

Chemical analysis of the samples proves vital for some of the experiments and three main techniques, according to the elements analysed were used:

Combustion analysis[15] was used to analyse the nitrogen and hydrogen content of the samples. For this, a small amount of sample (typically 2 mg) was burnt in a pure oxygen atmosphere to produce water from the hydrogen in the sample and nitrogen gas from the nitrogen content of the sample. The gas stream was then analysed using a series of thermal conductivity detectors between which specific parts of the gases were removed. The difference allows for the quantification of those specific elements in the sample.

Experimental

Hydrogen and nitrogen contents were determined using an Exeter Analytical CE-440 combustion analyser with samples of ≈ 2 mg. The samples were weighed into silver crucibles and automatically processed in the instrument.

Titrimetric Analysis[16] served to determine the Cl^- content.* The analysis is based on the simple precipitation reaction $Ag^+ + Cl^- \longrightarrow AgCl\downarrow$. The silver ions for the analysis are generated *in situ* by passing a defined current through a silver anode which therefore produces Ag^+ ions controllably. The end point of the reaction is determined through the increase of conductivity caused by free Ag^+ ions.

Experimental

The decomposition product of $[Ni(NH_3)_6]Cl_2$ in air was analysed for its Cl^- content using a Sherwood chloride analyser. The aqueous sample was prepared by dissolving 6.2 mg sample in 25 ml 0.01 M HNO_3.

Atomic Absorption Spectroscopy (AAS) was used to analyse the Ni content. AAS is based on the absorption of light by specific element at specific wavelengths through atomic excitations. These are characteristic for an element and the amount of extinction is proportional to the amount of the type of atomic species in the sample.

---

*It should be noted that this method is not specific for Cl^- but would work equally on the higher halides.

Experimental

The same solution as above was used to determine the Ni content using a AAnalyst 400 AAS (Perkin Elmer) with a wavelength of 232 nm, an external Ni standard and an automatic instrument background correction.

2.7. Quantum Chemical Calculations

Theoretical work on atomic structure and the development of quantum theory has facilitated detailed predictions of the atomic and electronic structure of chemical compounds and to derive further materials from these. Due to the fact that a multi-particle problem is not directly solvable, however, two main techniques to circumvent this problem have been developed: 1) The Hartree-Fock (HF) method makes use of the discretely solvable atom orbital function and combines them to approximate for the whole molecule. This has the disadvantage that the obtained energy of a molecule is unavoidably higher than the real energy due to the fact that electron-electron interactions are not considered. This energy difference between the ideal Hartree-Fock energy and the real energy is called the correlation energy or Hartree-Fock limit.[17] 2) This limitation does not exist in Density-Functional theory (DFT) based on the work of Kohn and Sham. Instead, DFT starts from the observable electron density and models the system's electron density as a function of Coulombic repulsions and attractions in this system. Although this theory is in principle exact, the so-called exchange-correlation potential can not be calculated directly and has to be modelled using more or less numerical solutions.

Both HF and DFT have intrinsic weaknesses and known shortfalls but both have advantages as well which makes both techniques suitable for special problems. Furthermore, two different practical approaches were chosen throughout this work. Calculations in molecules are made *in vacuo*, *i.e.* the calculations were performed for exactly one molecule in an otherwise entirely empty space. This means that the boundary conditions of the system are zero. The same is not true for calculations in the solid state where an extended structure is considered. As the Coulombic interactions are in principle of infinitely long range, interactions with particles further away in the structure have to be taken into account, *i.e.* non-zero boundary conditions. Calculations in the solid state are hence more demanding, since more atoms have to be included in the calculation, and their number is in theory infinitely large. The trick in solid state calculations lies in the use of the unit cell as a repeating unit. Because all unit cells are equivalent in an ideal case, their boundary conditions have to be as well. This means that the electronic state of one cell face can be used as boundary condition of the opposite face, very much as if the next unit cell would follow.

Ab-initio **solid-state computations**

Solid state computations in the system $CuCl_2$–NH_3 were performed using the ABINIT 7.8.1 suite[18,19] on density functional theory level general gradient approximation with a Perdew-Burke-Enzerhoff exchange-correlation potential.[20] Troullier-Martins valence electron pseudo-potential generated with fhi98pp were used for the elements.[21] The *k*-point grid size and cutoff energy were converged and the optimal values used for the calculations.

Molecular *ab-initio* calculations

Structural optimisations for copper ammine complexes were performed using NWChem 6.6.[22] The structure optimisation was performed as unrestricted Hartree-Fock self consistent calculation with defined doublet spin state. A preliminary structure optimisation was performed using a STO-3G basis set and a final structure optimisation using a 6-31G* basis set.

2.8. Crystallographic methods

2.8.1. X-ray diffraction — A double discovery

The field of crystallography did not begin with the first diffraction experiment. In fact, the translational nature of crystals was assumed much earlier, for instance through the observation on the morphologies of minerals. Furthermore, mathematical group theory including the 230 3-dimensional space-groups (detailed in the next section) were derived before the first diffraction experiment.[23,24] There was, however, no experimental evidence for this theory of crystals. This evidence was finally produced by Max von Laue, Walter Friedrich and Paul Knipping in 1912,[25] when they observed the diffraction of X-rays by a crystal lattice. Knipping and Friedrich irradiated a crystal with X-rays and observed sharp peaks coming from the scattering of the X-rays at the repeating motifs in the crystal, correctly interpreted by Laue.[26] This experiment was also remarkable from another point of view: Laue proved not only that crystals are composed of repeating motifs but also that X-rays do in fact have the characteristics of waves. This is due to the fact that scattering is a fundamental characteristic of waves which occurs upon the interaction of waves with repeating units of a size similar to its wavelength. This experiment therefore proved that X-rays are electromagnetic waves because they are scattered on crystal lattices which in return proved that crystals are built from lattices of similar dimensions to the wavelengths of the X-rays.

This ground-breaking discovery earned the Nobel Prize in Physics in 1914 and gave rise to the field of crystal structure determination. Very soon after the Laue experiment, the Australian born scientist William Lawrence Bragg developed, in collaboration with his father William Henry Bragg, the most ground-breaking equation in the field of crystallography, which linked the angle of the observed reflections to the distance between the layers at which they are scattered:[27]

$$n \cdot \lambda = 2d \cdot \sin(\theta) \tag{2.7}$$

where n is a natural number (which signifies the order of scattering as will be discussed subsequently), λ is the wavelength of the X-rays used, d is the distance between the scattering layers and θ is the angle of the observed scattering. With this equation, the metrics of the cell could be determined and therefore the size of the repeating unit determined. It is not surprising that this discovery lead to the second Nobel prize in Physics in a row attributed to crystallographers, awarded to both Braggs together in 1915.

2.8.2. Symmetry in the crystal structure

Atoms and molecules that make up the crystal structure often arrange in a particular way which is characterised by special symmetrical relationships between atoms of the same type. Contrary to molecular symmetry, one does not consider isolated molecules,

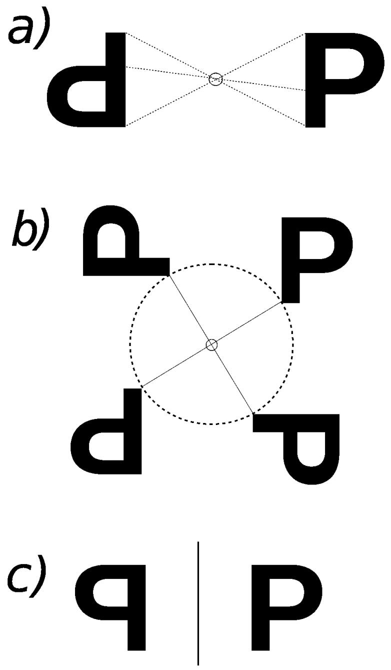

Figure 2.3.: Representation of Point symmetries in 2D of a model motif (P). a) Inversion, b) 4-fold rotation, c) mirror plane.

but a 3-dimensional arrangement of molecules. Only a limited number of molecular symmetries are compatible with the translation symmetry of the crystal structure. These are namely inversions, 2-, 3-, 4- and 6-fold rotation axes and mirror planes.

In addition to these Point symmetries and the pure translational symmetries along the axes, crystals can contain a special type of symmetry that is made up of both translational and point symmetry. The two symmetry elements fulfilling these requirements are the glide-plane and the screw-axis. The different symmetry elements discussed in the following sections are ordered in Point and translational symmetry elements and the standard notation for the symmetries in crystal structures is then explained more in detail.

Point symmetries

Inversion is the complete inflection of the motif in a single point (Figure2.3 a). Inversion symmetry is the most common type of symmetry encountered in crystal structures. The absence of inversion symmetry can be problematic in crystal structure analysis. Friedel discovered that all observed diffraction patterns exhibit an inversion symmetry as a consequence of the intensity being the square of the structure factor.[28]

2,3,4 and 6-fold rotations signify the rotation of the structure around a one-dimensional axis which will therefore be called the rotation axis (Figure 2.3 b). The order of the rotation signifies the number of equivalent positions within a rotation around 360°. The angle between the equivalent positions is therefore defined as 360° divided by the order of the rotation as they need to be equally spaced in order to be equivalent. It is important to bear in mind, that the rotation does not only affect a single molecule or unit cell, but it affects the whole structure and the rotation therefore must be in line with the translational symmetry of the neighbouring cells. This relationship will become of significant importance for the cell metrics as they are determined by symmetry.

Reflections are symmetry operations in which the motif is flipped on a plane, the mirror plane (Figure 2.3 c). Due to the restriction mentioned above that the symmetry elements must be reflected within the entire crystal structure, mirror planes can only exist for certain unit cell metrics, namely with 90° angles.

Translational symmetry

Screw axes are a combination of a rotation around an axis (all 2,3,4 and 6-fold rotations are possible) together with a translation along the rotation axis. The translation distance along the rotation axis depends on the length of the cell vectors and the order of the rotation.

Glide reflections combine the Point reflection on a mirror plane with the translation parallel to the mirror plane (or glide plane as it is consequently called for glide reflections). As multiple translations parallel to the mirror plane could be thought, the direction of the translation therefore has to be given in the crystal symmetry notation.

2.8.3. Arrangement of symmetries: The space groups and crystal systems

As shown by Schönflies and Fedorov,[23,24] all possible arrangements of the different symmetry elements in 3 dimensions can be described by 230 unique sets. These 230 unique sets form the most important basis for the rationalisation of crystallographic arrangements and each individual arrangement is called a *space group*. It is useful to organise the space groups further, which is practical to do as a function of the highest point symmetry elements (the non-translational parts of screw axes and glide planes can take the same role here) into the following categories:

1. Inversion symmetry as the highest element
2. Highest symmetry is 2-fold (2-fold rotation or mirror plane) in one direction
3. Three two-fold symmetry elements perpendicular to each other
4. Three-fold symmetry as the highest symmetry element

Table 2.1.: Defining directions for Hermann-Mauguin Notation[29]

Crystal system	primary	secondary	tertiary
Triclinic		None	
Monoclinic	[010]		
Orthorhombic	[100]	[010]	[001]
Hexagonal*	[001]	$\{100\}$	$\{1\bar{1}0\}$
Tetragonal	[001]	$\{100\}$	$\{110\}$
Cubic	$\{100\}$	$\{111\}$	$\{110\}$

* applies to Hexagonal and Trigonal

5. Six-fold symmetry as the highest symmetry element

6. Four-fold symmetry as the highest symmetry element

7. Four three-fold symmetry elements separated by the tetrahedral angle

The above-mentioned categories define the seven different crystal systems with their different basis cells. This is because the defining symmetry of the crystal systems defines, together with the necessity of a translational reproduction of the cell, how the metrics of the cell have to look like. This is probably most easily described in the tetragonal crystal system where the basis vectors $a = b$. The four fold rotation defining the tetragonal cell dictates that the cell has to have 90° angles and that at least two out of three cell vectors have to have the same length as no proper four-fold rotation would otherwise be possible. Following this principle through, the crystal systems above have the following metric requirements:

Crystal system	Defining symmetry element	Cell metrics requirements
Triclinic	None or inversion symmetry only	None
Monoclinic	One 2-fold axis or mirror plane	$a \neq b \neq c$ $\alpha = \gamma = 90°$ $\beta \neq 90°$
Orthorhombic	Three 2-fold axes	$a \neq b \neq c$ $\alpha = \beta = \gamma = 90°$
Trigonal	One 3-fold axis	$a = b \neq c$ $\alpha = \gamma = 90°$ $\beta \neq 120°$
Hexagonal	One 6-fold axis	$a = b \neq c$ $\alpha = \gamma = 90°$ $\beta \neq 120°$
Tetragonal	One 4-fold axis	$a = b \neq c$ $\alpha = \beta = \gamma = 90°$
Cubic	Four 3-fold axes	$a = b = c$ $\alpha = \beta = \gamma = 90°$

It is important to point out that the cell metrics are not a sufficient parameter to determine the crystal system. While an orthorhombic system, for instance, does not need to have equally long cell parameters, it may have them. This case happens comparably often for two of the three cell parameters and care has to be taken not to mistake the cell as tetragonal in such a case.

Hermann-Mauguin Notation of Crystal Symmetries

The Hermann-Mauguin (H-M) notation is used to specify the space groups through their different symmetry elements. An H-M sign is composed out of two parts: a capital letter to signify the centering of the space group and the defining symmetry elements along three unique directions. These unique directions are a function of the crystal system (Table 2.1). The different elements are noted with numbers for rotation and screw-axes and letters for mirror and glide planes. The details of the different symmetry elements and their distributions throughout the different space groups is conclusively described in the International tables of Crystallography Volume A.[29]

2.8.4. Solving crystal structures: The phase problem

The main difficulty in determining crystal structures is the phase problem. The observed peak intensity of crystal diffraction is proportional to the square of the diffracted wave amplitude, but no direct measurement of the wave phase is possible.[30] This lack of information makes it impossible to solve structures directly from the measured data and different methods have been developed to reconstruct the phases.

Molecular replacement is probably the simplest way of solving the phase problem. Instead of starting from scratch, this method relies on the use of the phase of a known, similar, structure and uses this as a starting model.

The Patterson method uses the intensity instead of the structure factors in the Fourier synthesis of the diffraction data. Instead of atomic positions, this methods yields vectors between atoms as result and therefore allows to solve crystal structures.[30] This method is particularly useful if the structure contains atom sorts with large differences in electron density as the peak intensity in the Patterson Fourier synthesis is proportional to the factor of the electron counts of the two atom sorts.[30]

Direct Methods use systematic relationships between intensities within peak groups to abstract the phases directly. Different relationships are used and it is referred to specialised literature for more detail.[30] The Patterson method and direct methods are implemented in SHELXS,[31] probably the most popular software for the solution of small molecule single crystal data.

Charge Flipping is a recent method first proposed by Ozlani and Sütö in 2004.[32] As it is the method used for most structure solutions herein, it will be briefly explained. It is surprisingly simple and starts from a random model to attribute the (unknown) phase to the structure factors. An inverse Fourier transformation is performed to yield the electron density of this model. Based on the physical principle that the electron density cannot be negative, those areas with negative electron density are multiplied with –1, *i.e.* “flipped”. The so obtained electron density is then Fourier transformed into structure factors and the phase of these structure factors is used with the observed amplitudes (square root of the observed intensities) for a second iteration. This process is repeated until no significant changes in the model can be detected any more. The program used to solve the structures herein was Superflip, which performs the charge flipping algorithm in arbitrary dimensional space.[33]

2.8.5. Structure Refinement

The refinement procedure is, in principle, an iterative process in which the difference between the Intensity observed and the intensity calculated from the model is minimised through adjustments of the model. While this method is easily usable for single crystal structures, for instance using the program SHELXL[31], the case for powder patterns is more complicated. This is due to the fact that the diffraction information is merged into one dimension making the deconvolution more difficult. Hugo Rietveld therefore introduced a method, using not only the structure factors as basis for the refinements but the whole pattern profile.[34,35] This method proved to be hugely successful for the structure refinement from powder data and over 7000 scientific publications relied on Rietveld refinements in 2013.[35]

2.8.6. Laboratory Powder X-ray Diffraction

Two different instruments were available for the measurements of powder X-ray patterns. Non air-sensitive materials were measured on a X'Pert MPD Pro (*PANalytical*, Cu-$K_{\alpha 1}$-radiation) instrument in para-focussing reflection Bragg-Brentano geometry for flat plate samples. Non-ambient *in situ* measurements were also conducted on the X'Pert Pro using a furnace HTK-1200N (*Anton Parr*) flushed with argon (ca. 50 ml/min) in order to guarantee air-free thermal decompositions. A short contact with air during sample loading could not be avoided but was kept to a minimum of ca. 10 s. As a consequence of the sample environment, the measurement range was restricted to 10° – 90° .

Air-sensitive samples were measured in capillaries using a D8 Advance diffractometer (*Bruker*) with Cu-$K_{\alpha 1}$-radiation in transmission Debye-Scherrer geometry. The capillaries (special glass, *Hilgenberg*) were prepared in the glovebox and then sealed to avoid any contact of the sample with air. The collection strategies were adapted to sample and time constraints with step-sizes between 0.016° and 0.025° and collection angles between 5° and 108° .

2.8.7. *In-situ* Synchrotron X-ray Experiments

In-Situ experiments were conducted at the I11 beamline[36,37] at the Diamond Synchrotron facility. A monochromatised beam (Si (111) monochromator, $\lambda = 0.82562$ Å) was used for *in situ* diffraction. A position sensitive detector (PSD) of Mythen-2 Si-strip detectors over a range of 90° was used during the experiments. Patterns measured for one second were collected and the detector was shifted by 0.5° to measure a second pattern. The two patterns were than summed to account for the detector bank edges and to obtain a complete pattern in the range of 2-92°. A whole pattern collection cycle took ca. 10 seconds. The sample was oscillated around the omega angle in an angular range of 10° during the measurements.

Sample Environment

The samples were exposed to ammonia *in-situ* on the diffractometer using a specialised gas-dosing system developed on the beamline.[38] The samples were filled into quartz-capillaries in a glovebox and the quartz capillaries were held in an angled Swagelok fitting equipped with a sequence valve making sure that the sample has no contact with air when taken out of the glovebox. The fitting was then brought onto the goniometer head of the diffractometer and the no-return valve was connected to the gas line. The inherent difference between these experiments and the synthesis setup in the lab is, that no constant flow of ammonia could be used in these experiments due to the architecture of the experimental cell. This has the consequence that the diffusion of ammonia through the argon filled cell is the rate determining step at the start of the uptake. For safety reasons, the gas dosing system was positioned outside of the experimental hall which had to be evacuated before opening the beam shutter. The connecting line was therefore ca. 5 m long and was evacuated up to the no-return valve before starting the experiment in order to minimise the ammonia diffusion length. The ammonia pressure was set between 1.42 and 1.45 bar to allow sufficient contact between ammonia gas and the pure dihalides.

2.8.8. Powder Neutron Diffraction

A sample of $[Cu(ND_3)_{6-x}]Cl_2$ was measured by powder neutron diffraction on the GEM instrument at the ISIS pulsed neutron source. The sample was filled into a vanadium sample can with 5 mm diameter in the glovebox in Glasgow, closed and sealed using indium wire and then sent to ISIS. The sample was measured for 2 hours at room temperature in order to achieve a refineable dataset. ISIS is a pulsed neutron source, *i.e.* neutrons are produced by spallation. For this, bundles of protons are accelerated in a proton synchrotron and then collided with a Tungsten target, where they liberate neutrons.[39] These intense neutron pulses are slowed through hydrogenous moderators and then distributed on the different instruments.[39] The neutrons in a pulse have different energies (and wavelengths) and their scattering angles for the same reflections are hence different. Instead of measuring at variable angle as for powder X-Ray diffraction, the incoming neutrons at different set angles are counted as a function of the flight time (hence the name “time-of-flight” measurement), and therefore of their specific energy.

2.8.9. Single-crystal X-ray diffraction

Single crystal data was recorded on a APEX-II (Bruker) four circle diffractometer with Kappa geometry and Mo-K_α radiation (λ = 0.7097 Å). The data acquisition strategy was determined based on the tentative crystal system and the achievable resolution of the pattern using the APEX2 software.[40] The raw-data were integrated using SAINT[41] and corrected for absorption using SADABS[42] (all Bruker). Data reduction, space-group assignment and file preparation were performed using Bigxprep (Bruker).[40] The structure solution was performed using direct methods using SHELXS-2013 and the structure refinement was done with SHELXL-2013.[31]

Air sensitive crystals were chosen under paraffin oil and coated in superglue in order to avoid decomposition in air. The low temperature measurements were performed using a cryostream (Oxford Cryosystems) and the samples were cooled to the target temperature as quickly as possible.

2.9. References

[1] Y. Zhong, R. E. Critoph, R. Thorpe, Z. Tamainot-Telto, Y. I. Aristov, *Appl. Therm. Eng.*, 2007, **27**, 2455–2462.

[2] J. H. Van't Hoff, *Etudes de dynamique chimique*, F. Muller & Company, 1884.

[3] S. Arrhenius, *Z. Phys. Chem.*, 1889, **4**, 226–248.

[4] H. E. Kissinger, *J. Res. Natl. Bureau Stand.*, 1956, **57**, 217–221.

[5] H. E. Kissinger, *Anal. Chem.*, 1957, **29**, 1702–1706.

[6] C. Czeslik, H. Seemann, R. Winter, *Basiswissen Physikalische Chemie 4th ed.*, Springer, 2010.

[7] J. Fahrenfort, *Spectrochim. Acta*, 1961, **17**, 698–709.

[8] S. F. Parker, J. W. Taylor, P. Albers, M. Lopez, G. Sextl, D. Lennon, A. R. McInroy, I. W. Sutherland, *Vib. Spectrosc.*, 2004, **35**, 179–182.

[9] G. J. Kearley, M. R. Johnson, *Vib. Spectrosc.*, 2010, **53**, 54–59.

[10] S. F. Parker, A. J. Ramirez-Cuesta, P. W. Albers, D. Lennon in *Journal of Physics: Conference Series*, IOP Publishing, . 012004.

[11] D. Colognesi, M. Celli, F. Cilloco, R. J. Newport, S. Parker, V. Rossi-Albertini, F. Sacchetti, J. Tomkinson, M. Zoppi, *Appl. Phys. A*, 2002, **74**, s64–s66.

[12] E. Abbe, *Arch. Mikr. Anat.*, 1873, **9**, 413–468.

[13] C. Cremer, *Phys. Unserer Zeit*, 2011, **42**, 21–29.

[14] M. Dyba, S. W. Hell, *Phys. Rev. Lett.*, 2002, **88**, 163901.

[15] Exeter Analytical (UK) Ltd, accessed 17/02/2016. `http://www.exeteranalytical.co.uk/ce440_theory.htm`.

[16] Sherwood Scientific, Ltd, accessed 04/05/16. `http://www.sherwood-scientific.com/chloride/chloridemeters.html`.

[17] H. Haken, H. C. Wolf, *Molekülphysik und Quantenchemie: Einführung in die experimentellen und theoretischen Grundlagen*, Springer-Verlag, 2006.

[18] X. Gonze, B. Amadon, P.-M. Anglade, J.-M. Beuken, F. Bottin, P. Boulanger, F. Bruneval, D. Caliste, R. Caracas, M. Cote, et al., *Comput. Phys. Commun.*, 2009, **180**, 2582–2615.

[19] X. Gonze, G.-M. Rignanese, R. Caracas, *Z. Kristallogr.*, 2005, **220**, 458–472.

[20] J. P. Perdew, K. Burke, M. Ernzerhof, *Phys. Rev. Lett.*, 1996, **77**, 3865.

[21] M. Fuchs, M. Scheffler, *Comput. Phys. Commun.*, 1999, **119**, 67–98.

[22] M. Valiev, E. J. Bylaska, N. Govind, K. Kowalski, T. P. Straatsma, H. J. Van Dam, D. Wang, J. Nieplocha, E. Apra, T. L. Windus, et al., *Comput. Phys. Commun.*, 2010, **181**, 1477–1489.

[23] J. J. Burckhardt, *Arch. Hist. Exact Sci.*, 1967, **4**, 235–246.

[24] J. J. Burckhardt, *Arch. Hist. Exact Sci.*, 1971, **7**, 91–141.

[25] M. Eckert, *Ann. Phys.*, 2012, **524**, A83–A85.

[26] W. Friedrich, P. Knipping, M. Laue, *Ann. Phys.*, 1913, **346**, 971–988.

[27] W. H. Bragg, W. L. Bragg, *Proc R. Soc. Lond. A*, 1913, **88**, 428–438.

[28] L. Spieß, G. Teichert, R. Schwarzer, H. Behnken, C. Genzel, *Moderne Röntgenbeugung: Röntgendiffraktometrie für Materialwissenschaftler, Physiker und Chemiker*, Springer-Verlag, 2009.

[29] T. Hahn (Ed.), *International Tables for Crystallography, Volume A: Space-Group Symmetry 5th ed.*, 2005.

[30] W. Massa, *Kristallstrukturbestimmung 4th ed.*, Springer, 2011.

[31] G. M. Sheldrick, *Acta Crystallogr. A*, 2007, **64**, 112–122.

[32] G. Oszlányi, A. Sütő, *Acta Crystallogr. A*, 2004, **60**, 134–141.

[33] L. Palatinus, G. Chapuis, *J. Appl. Crystallogr.*, 2007, **40**, 786–790.

[34] H. M. Rietveld, *Z. Kristallogr. Cryst. Mat.*, 2010, **225**, 545–547.

[35] H. M. Rietveld, *Phys. Scr.*, 2014, **89**, 098002.

[36] S. P. Thompson, J. E. Parker, J. Potter, T. P. Hill, A. Birt, T. M. Cobb, F. Yuan, C. C. Tang, *Rev. Sci. Instrum.*, 2009, **80**, 075107.

[37] S. P. Thompson, J. E. Parker, J. Marchal, J. Potter, A. Birt, F. Yuan, R. D. Fearn, A. R. Lennie, S. R. Street, C. C. Tang, *J. Synchrotron Radiat.*, 2011, **18**, 637–648.

[38] J. E. Parker, J. Potter, S. P. Thompson, A. R. Lennie, C. C. Tang, *Mater. Sci. Forum*, 2012, **706**, 1707–1712.

[39] accessed 15/02/2016. `http://www.isis.stfc.ac.uk/about/how-isis-works6313.html`.

[40] W. U. Bruker APEX2 (Version 2012.10-0) BrukerAXS Inc, Madison.

[41] W. U. Bruker SAINT (version 8.27B) BrukerAXS Inc, Madison.

[42] M. W. U. Bruker SADABS (version 2012/1), BrukerAXS Inc.

3. Nickel Halides as Promising Ammonia Stores

3.1. Introduction

The first and most elementary process of a storage material is the charge of the material. In the case of ammonia stores, it is the ammonia gas uptake process. The fact that ammonia gas is absorbed into metal salts has been known for a long time but is nevertheless a fascinating process. The work presented in this chapter shines a light on the kinetics of the reaction and elucidates the reaction mechanism in the system $NiCl_2$–NH_3. This system is also subject to thorough crystallographic studies, both *in situ* and *ex situ*.

The second integral part of a promising ammonia store besides its ammonia uptake is the study of the release from the store upon activation. The most straightforward form of activation of the hexammine metal halides as ammonia stores is upon their thermal activation. This is why the thermal decomposition of these compounds is of great interest and was studied to some detail. The studies of the compounds were using two principal approaches: Firstly the direct study of the thermal decomposition *via* their mass change, thermal profile and analysis of the effluent gas stream and secondly the observation of the structural changes upon heating to different temperatures. Due to the different nature of the methods, it will be shown that the decomposition temperatures between the different methods differ slightly but this can be attributed to the differences in partial pressure and sample preparation. Another emphasis of this chapter is drawn on the stability of the promising ammonia store $[Ni(NH_3)_6]Cl_2$ when it is exposed to air, a scenario thinkable for a car accident with a tank rupture. The knowledge of this stability is of integral importance for the safety of a realistic application and is therefore is great interest in a study of new ammonia storage materials.

3.2. Experimental

Syntheses of hexammine metal halides

$[Ni(H_2O)_6]Cl_2$ (99.9 %, Aldrich) was dehydrated at 250 °C for 12 hours before use. $NiBr_2$ (99 %, Aldrich), NiI_2 (synth. grade, Aldrich) and NH_3 (99.98 %, Premium Grade, anhydrous, BOC) were used without further purification. Ammonia was supplied in a low pressure cylinder ($\leq$ 10 bar) and a specific low-pressure regulator suitable for the work with ammonia was fitted. The regulator was made from stainless steel only and it had to be made sure that neither the regulator nor the gas tubing contain brass parts commonly used for inert gases, as copper corrodes under ammonia atmosphere. The hexammine halides were produced by exposing the respective halide salts to a stream of ammonia gas ($\approx$ 50 ml/min) for one hour at ambient conditions. In order to avoid contamination, starting materials and reaction products were handled in a glove box (O_2, $H_2O \leq 10$ ppm).

The gravimetric uptake experiments and Synchrotron experiments were conducted using commercial $NiCl_2$ (98 %, Aldrich) and NiI_2 (synth. grade, Aldrich, Synchrotron only) without further purification.

3.3. Uptake of Ammonia into $NiCl_2$

It was in fact in 1926, when Paul Stoll published his doctoral thesis under Paul Scherrer, that the crystal structure of $[Ni(NH_3)_6]Cl_2$ was first determined.[1] With a cubic cell and a cell parameter of 10.15 Å, Stoll determined the correct structure but the cell parameters do differ from the recent re-determination by Eßmann and co-workers.[2] Between these two measurements, a lot of research energy has been invested in understanding the unique structural arrangements which arise from the fast rotation of the ammonia molecules which occupy a crystallographic site with higher symmetry than the point symmetry of the ammonia molecule. This research extended from specific heat analyses[3,4] through electron paramagnetic resonance spectroscopy[5,6] to inelastic neutron scattering[7,8], along also with neutron diffraction[9].

Yet, the aim for the work in this section was not to re-perform the same studies on the same materials but **1)** To examine the structures of the nickel products obtained from the reactions described herein, **2)** To investigate the structure of hexammine nickel iodide which has not been previously reported and **3)** To study the mechanism of the ammonia uptake reaction by means of time-resolved X-ray diffraction.

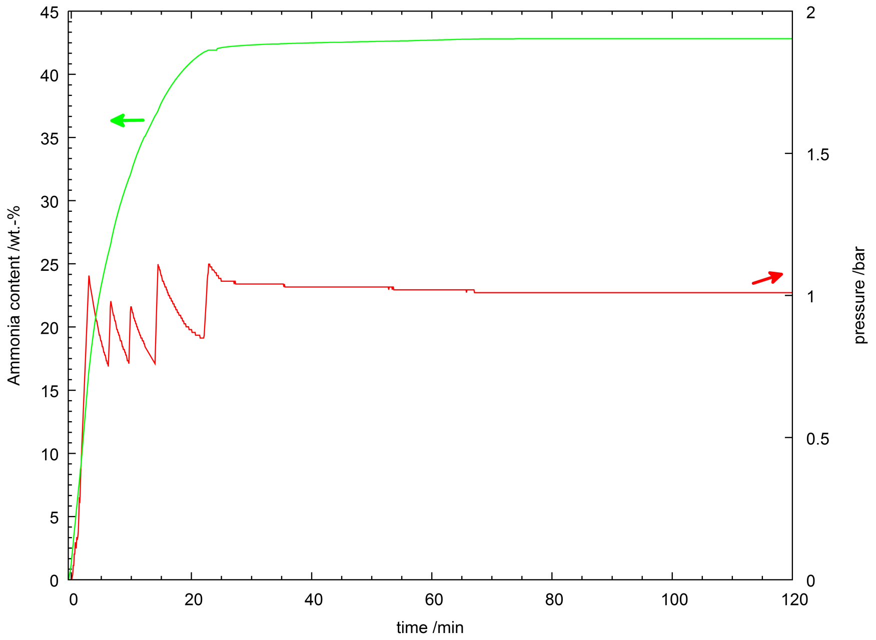

Figure 3.1.: Gravimetric measurement of the ammonia uptake into $NiCl_2$ at 20 °C (green line) and the used pressure profile (red line).

3.3.1. Gravimetric measurements

In order to study the kinetics of the ammonia uptake reactions $M\mathrm{Cl}_2 + 6\,\mathrm{NH}_3 \longrightarrow [M(\mathrm{NH}_3)_6]\mathrm{Cl}_2$ in a more quantitative way, one has to be able to follow the reaction propagation by means of a suitable physical parameter which changes during the reaction accordingly. Probably the most straightforward parameter to measure is the mass of the sample, since the uptake of ammonia increases the weight of the sample accordingly. Such an experiment is however not so simple to set up as the reaction affords a defined ammonia atmosphere which is not compatible with common balances and furthermore demands safety precautions such as a closed or vented space. The setup used in this study circumvents these problems by separating the balance from the sample containing space, which in itself is hermetically closed to prevent ammonia leakage, by means of a magnetic system. The details of the setup may be found in section 2.1.

A first glance at the mass development over time during the uptake reaction of ammonia into $NiCl_2$ (figure 3.1) unveils a rapid uptake of ammonia which is virtually finished after 25 minutes of reaction time. Also, the mass increase starts instantly with the introduction of ammonia into the reaction chamber (which is set to $t = 0$ in the series of experiments). This behaviour is indicative of thermodynamically driven reaction kinetics. It is important to mention that the kink in the uptake curve at ≈ 90 % loading is a feature of the instrument which conducts regular zero-point measurements during which no mass data is taken. It is not entirely clear why the uptake of ammonia into the material does not reach 100 % of the theoretical loading (maximising at ≈ 95 %) but this can most probably be attributed, besides a buoyancy effect discussed in the next paragraph, to traces of humidity in the starting material which could not be avoided during the sample preparation and could not be otherwise detected analytically. Given the sample size used in this experiment, the amount of water necessary for such a deviation would be very small.

Buoyancy effect on the measured weight

In order to study the mass reaction of the sample under the influence of different ammonia pressures, the fully loaded sample was exposed to 3 bar ammonia and to vacuum ($p \leq$ 4 mbar). When regarding the gravimetric uptake as measured (figure 3.2, green curve), it appears that the mass of the sample drops when exposed to 3 bar NH_3 and suddenly increases when exposed to vacuum. This behaviour is however not intrinsic to the sample but is an influence of the buoyancy on the apparent mass of the sample. According to Archimedes' principle, the buoyancy acting on a solid body is just as large as the gravimetric force for the fluid (ammonia gas in our case) it is immersed in.[10] As the pressure rises, the gas becomes compressed and increases its density which also increases

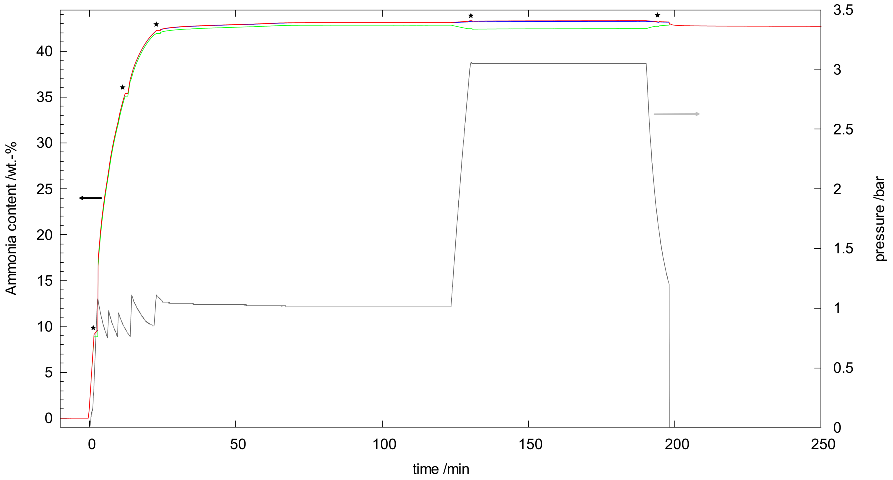

Figure 3.2.: Gravimetric measurement of the ammonia uptake into $NiCl_2$ at 20 °C without buoyancy correction (green line), applying sample buoyancy correction only (blue line), applying buoyancy correction for sample holder and sample (red line) and the used pressure profile (grey line). The sample corrections contributes little and the red line hence nearly supersedes the blue line. Instrument zero phases are signified by stars.

the buoyancy force applied to the sample container and the same product would therefore appear lighter. Vacuum does not possess any buoyancy and the sample therefore appears heavier than at ambient pressure. The common technique for buoyancy correction in gravimetric measurement is *via* the measurement of an external standard which is known to be inert against the gas. Such a correction is however difficult in this case as the sample increases its volume strongly during the reaction (over 4 times based on the bulk densities of starting material and product: $NiCl_2$, ρ = 3.53 g/ml[11]), $[Ni(NH_3)_6]Cl_2$, ρ = 1.50 g/ml – see also section 3.4), which is impossible to account for when using an external standard. Instead, a fully analytical buoyancy correction based on the ideal gas law was developed. This function was split into two parts, one for the sample container and one for the sample itself. The knowledge of the sample container volume is indispensable to account for the first and a blank measurement of the sample container only was used to determine the sample container volume. Starting from the ideal gas law[12]:

$$p \cdot V = n \cdot R \cdot T \tag{3.1}$$

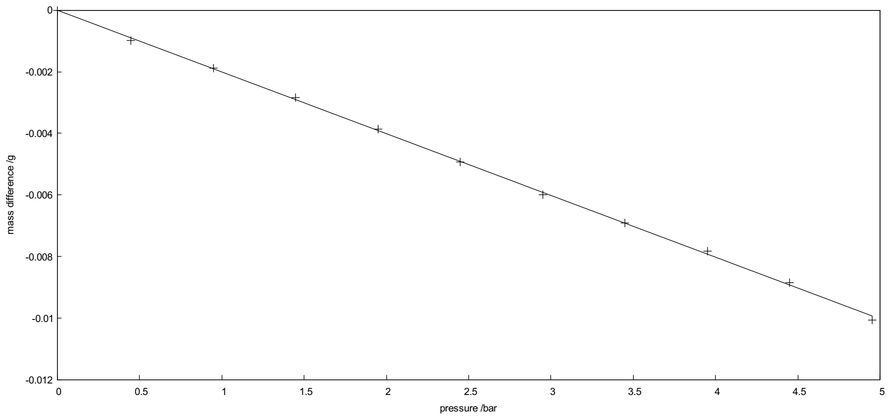

Figure 3.3.: Linear regression of the sample holder buoyancy effect at 20 °C (black line) with the observed masses (black plusses)

and replacing the number of moles by its conversion in mass $n = m/M$, one can establish the relationship between mass and pressure of a gas under the regime of an ideal gas as:

$$m = \left(\frac{V \cdot M_{\text{gas}}}{R \cdot T} \right) \cdot p \qquad (3.2)$$

Under isothermal condition and assuming that the sample holder does not change its volume during the blank measurement, the observed mass loss as a function of the pressure should yield a linear function where the slope can be directly linked to the sample holder volume. The linear regression of the blank measurement fits very well (Figure 3.3) and yields a slope of –0.002005 g/bar. This slope is equivalent to a sample holder volume of 2.8788 ml. Taking this volume and the sample holder mass, one can calculate the sample holder density as ρ = 2.2 g/ml, which is in excellent agreement with the tabled density of fused silica of which the sample holder is made.

The density correction for the sample is not as easily possible, given the aforementioned volume change. The mass uptake however allows to determine how much of the starting product has reacted and the overall volume of the sample can therefore be calculated using the starting material-to-product ratio and the known bulk densities of starting material and product. It has to be mentioned that the densities used here are crystal structure densities and do not take packing densities into account and also other possible sample effects such as surface adsorption are not taken into account and the buoyancy value calculated this way is a minimal value and may be higher in reality but it appears to be the best compromise for the volume changing system (also bearing in mind that the sample volume is about ten times smaller than the sample holder volume).

Temperature effect of the ammonia uptake

The buoyancy effect on the sample mass becomes very clear when regarding the 3 bar NH_3 region a little closer (Figure 3.4). It is already evident that the apparent mass drop upon pressure increase is a purely buoyancy inflicted feature when the buoyancy correction for the sample holder only is applied. When adding the buoyancy correction for the sample in addition, this phenomenon is even stronger and the sample clearly takes up a small amount of ammonia when brought under higher pressures. This amount is, however, negligible compared to the amount of ammonia picked up at ambient pressure. Also, the system loses a small amount of ammonia when brought in dynamic vacuum, but again, this amount is under 1 % of the overall ammonia amount in the sample.

A similar behaviour can be observed at 45 °C , where the overall uptake curve is largely comparable to the measurement at 20 °C (Figure 3.5). The final ammonia uptake at 1 bar of 43 wt.-% (buoyancy corrected) is only 0.1 wt.-% lower than the value observed for 20 °C and a major temperature influence is not ostensible in this range. The same image is also valid for the 3 bar region, where the difference is again in the range of 0.1 wt.-%. The overall profile is also preserved at 65 °C (Figure 3.6) but the ammonia uptake value is circa 0.5 wt.-% lower than for the lower temperatures, signifying a starting significance

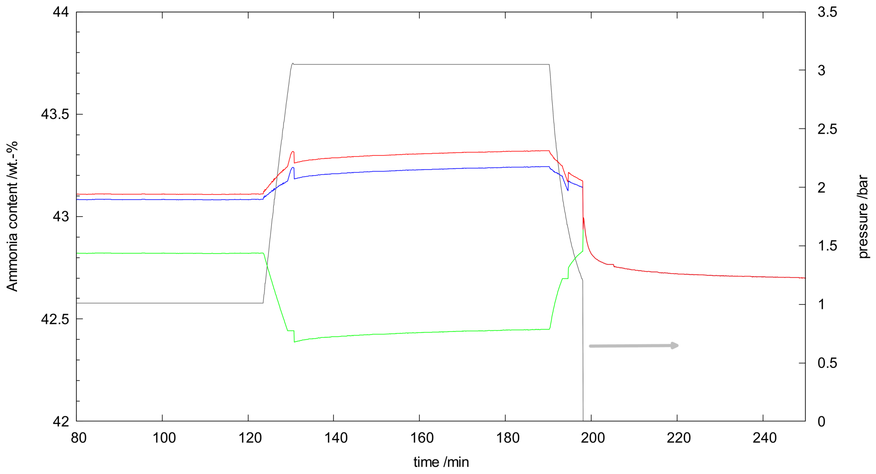

Figure 3.4.: Zoom into the gravimetric measurement of the ammonia uptake into $NiCl_2$ at 20 °C without buoyancy correction (green line), applying sample buoyancy correction only (blue line), applying buoyancy correction for sample holder and sample (red line) and the used pressure profile (grey line).

of the temperature on the storage material. Also, the mass loss when exposing the sample to dynamic vacuum is larger (in the range of 1 wt.-%) compared to the lower temperature experiments, which speaks for a significant weakening of the Ni–NH_3 bond strength.

Kinetic considerations

The question of an appropriate rate law for the use with this kind of gas-solid reaction is not straightforward to answer. First and foremost, the derived rate law can only be regarded as a pseudo-rate law which depends solely on the amount of $NiCl_2$ in the system, because the amount of ammonia surrounding the sample in this setup is by orders of magnitude higher and regulated to a constant pressure and can therefore be regarded as a non-rate determining constant. Given the dramatic sample volume increase during the reaction discussed above together with the dramatic crystal structure change during the reaction, it is unlikely that the particle morphology remains unchanged (as would be the case in a pseudomorphic reaction). The particle size would, in contrast, be expected

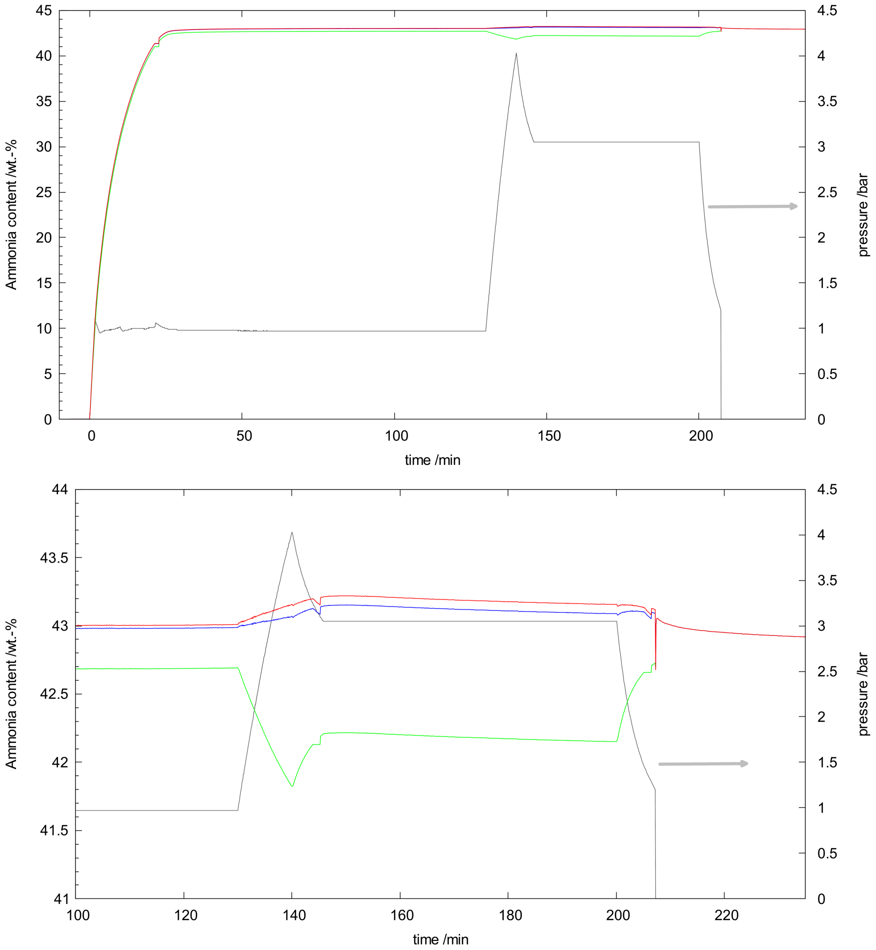

Figure 3.5.: Top: Gravimetric measurement of the ammonia uptake into $NiCl_2$ at 45 °C without buoyancy correction (green line), applying sample buoyancy correction only (blue line), applying buoyancy correction for sample holder and sample (red line) and the used pressure profile (grey line). Bottom: Zoom into the high pressure region.

to decrease and this assumption is in line with the small particle sizes of the reaction products as observed by SEM (Figure 3.7) and full profile matching of the diffraction pattern (see section 3.3.5). Based on the reaction equation — one equivalent of $NiCl_2$ is needed to form one equivalent of $[Ni(NH_3)_6]Cl_2$ — one could argue that the pseudo-rate law with respect to the solid starting material has to be of first order. A first order reaction hand would have a slowing of the reaction rate towards the end of the reaction anyway as the starting material gets increasingly scarce. This interpretation would also be in line

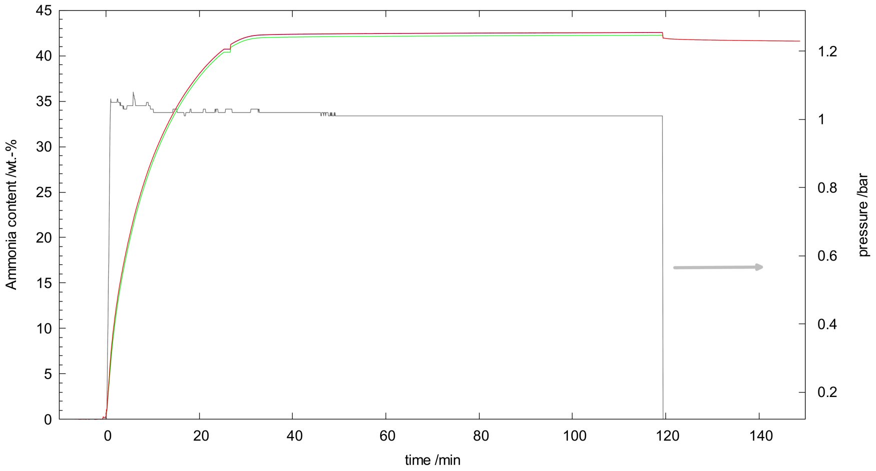

Figure 3.6.: Gravimetric measurement of the ammonia uptake into $NiCl_2$ at 65 °C without buoyancy correction (green line), applying sample buoyancy correction only (blue line), applying buoyancy correction for sample holder and sample (red line) and the used pressure profile (grey line).

with the interpretation by Hartley *et al.*, who studied the uptake of ammonia gas into CaI_2.[13]

Given the complexity of gas-solid reaction kinetics and the number of different kinetic models,[14,15] it was not possible to derive an analytical expression for the rate law. When qualitatively comparing the reaction curves for the different temperatures (Figure 3.8), however, it is evident that the reaction propagation at lower temperatures is quicker than at higher temperatures. Considering Arrhenius law:

$$k = A \cdot \exp(-\frac{E_A}{R \cdot T}) \tag{3.3}$$

such a behaviour should not happen for a simple reaction of the type

$$\mathrm{n\,A} + \mathrm{B} \xrightarrow{k_1} \mathrm{C}$$

but the reaction rate should continuously increase with increasing temperature. Such a behaviour is however explainable when introducing a second reaction into the system in

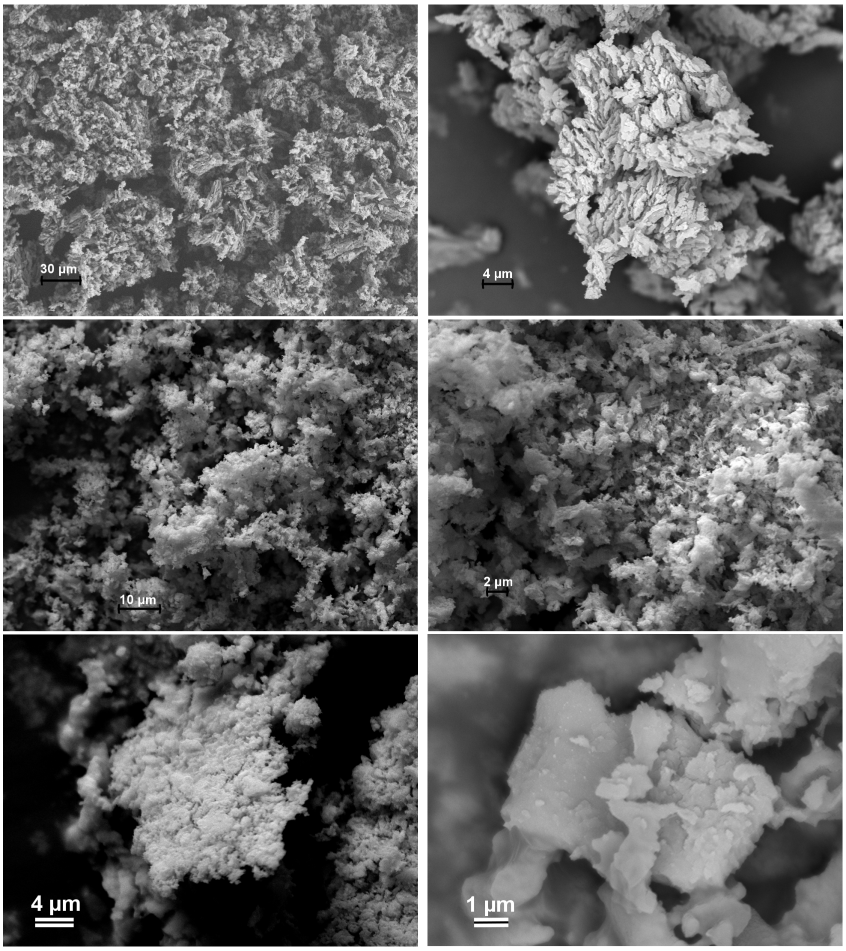

Figure 3.7.: SEM images for $[Ni(NH_3)_6]X_2$ X = Cl, top; X = Br, middle; X = I, bottom

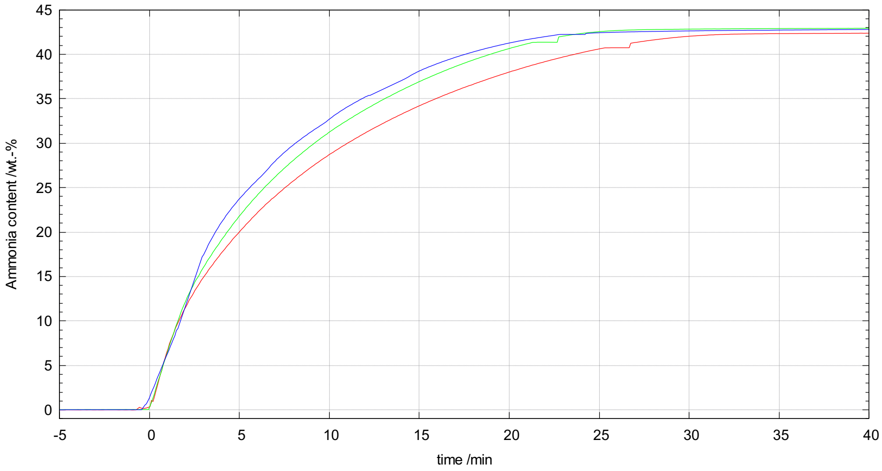

Figure 3.8.: Comparison of the ammonia uptake profile into $NiCl_2$ at 20 °C (blue line), 45 °C (green line) and 65 °C (red line).

the form:

$$\mathrm{n\,A + B \xrightarrow{k_1} C \underset{k_3}{\overset{k_2}{\rightleftharpoons}} D + m\,E}$$

where the activation energy for the second reaction has a larger activation energy and therefore shows a stronger temperature dependence. This would mean that reaction 2 would be negligibly slow at lower temperatures but gains increasing influence at higher temperatures until it outnumbers reaction 1. Such a second reaction in the metal halide ammine system could simply be the back reaction to metal halide and ammonia (in this case $k_1 = k_3$) or the formation of lower ammines, which becomes dominant. It is evident that the reaction kinetics and mechanics are of crucial importance for the loading and storage process, loading of an ammonia store in the tropical region as opposed to the polar region for instance. The thorough study of these processes is therefore an important future direction for the work on metal ammine salt based ammonia stores.

3.3.2. *In situ* powder XRD observations

The uptake of ammonia into the pure nickel dihalides was studied by X-ray diffraction at the synchrotron beamline I11 at the Diamond light source[16] in order to learn more about the uptake mechanism in the formation of the hexammine complexes. This beamline provides both a position sensitive detector system for the collection of time-resolved patterns[17] and a unique gas cell which allows the observation of crystallographic changes during the reaction of the solid phase with gas.[18] Also, the phase behaviour of the ammonia complexes of nickel chloride at variable temperature and under ammonia pressure were studied.

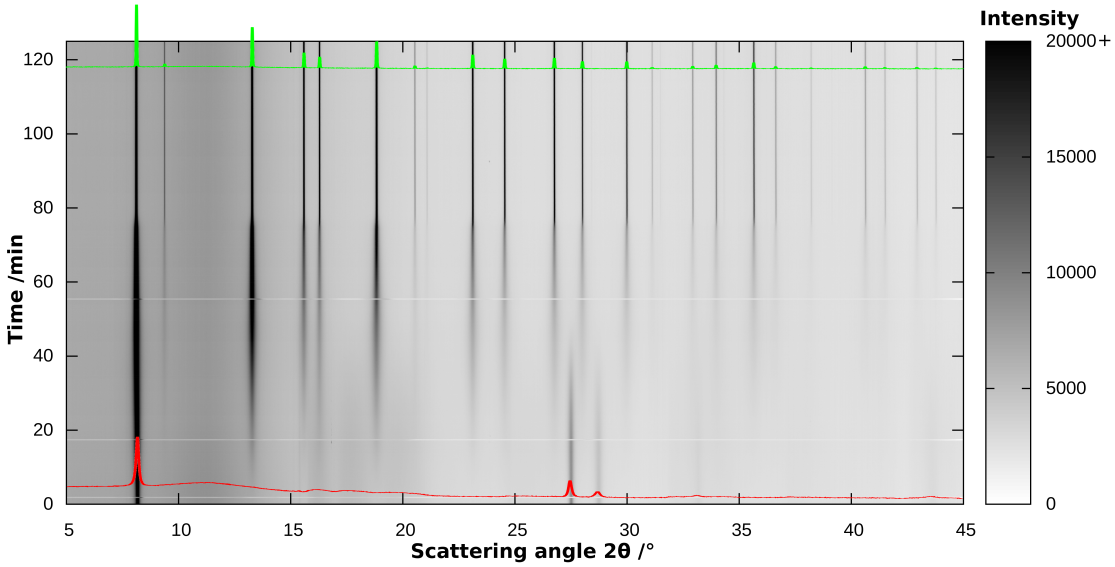

Figure 3.9.: Time resolved ammonia uptake in $NiCl_2$ at RT. The patterns of the starting material (red) and the reaction product (green) are given as patterns over the data.

3.3.3. Ammonia uptake by the pure dihalides

A consequence of the experimental setup provided at I11 is the fact that the true dynamics of the reaction can unfortunately not be clarified. This is due to the fact that we were working in a static system together with the use of a sequence valve which protected the sample in the capillary after preparing it in the glovebox and later provided the connection to the ammonia line in the experimental setup. However, this sequence valve also prevented the complete evacuation of the sample environment and the sample environment remained filled with argon gas used to protect the sample during the preparation until NH_3 with the trigger pressure was connected. Consequently, the kinetics of the reaction are influenced by the diffusion of ammonia gas in this system unlike the magnetic suspension balance setup presented above in which the sample was set in a large excess of ammonia gas. Pressures slightly higher than ambient pressure (1.44–1.45 bar) were used throughout the experiments in order to minimise the diffusion time by providing a greater (partial) pressure gradient. The mechanistic reaction pathway of the ammonia

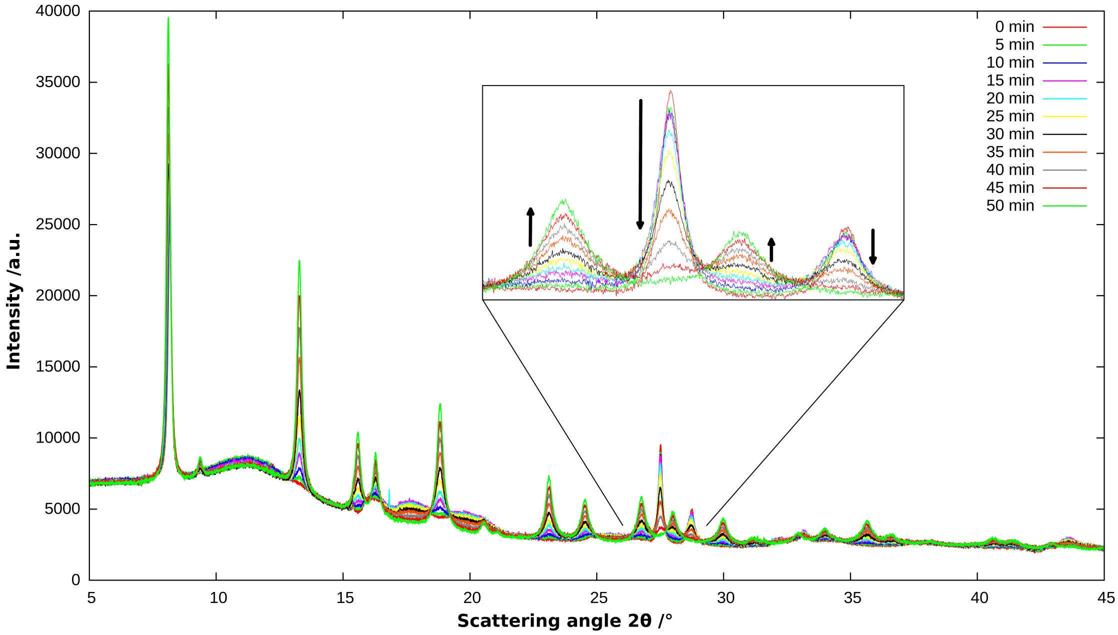

Figure 3.10.: Overlay of the patterns during the reaction propagation of $NiCl_2 + NH_3$ (Each pattern is taken at an interval of 5 minutes). The inset gives a close-up of the region at $\approx 28°$ where the arrows show the propagation direction with time.

uptake should remain unaffected by this and, moreover, intermediate products should be clearer to identify as the reaction rate is reduced. It was however not possible to obtain presentable data for the bromide analogue as bromine showed strong fluorescence due to the wavelength of X-ray radiation used.

Ammonia Uptake by $NiCl_2$

The fact that no intermediate phases could be observed (Figure 3.9) during uptake indicates that the ammine formation, in contrary to the decomposition, is a one-step process. This assumption is limited to the formation of intermediate products that are crystalline but the formation of one or more non-crystalline intermediate product could not be detected directly using this method and a multi-step process could essentially be masked by this. It is notable that the background changes during the reaction (Figures

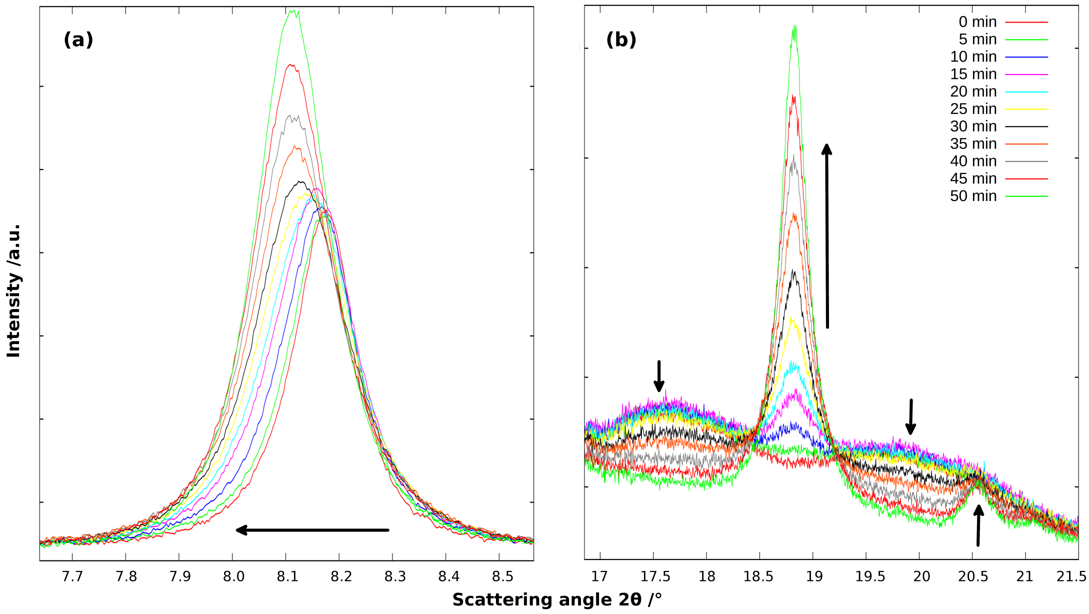

Figure 3.11.: Detail of the peaks at $2\theta \approx 8^\circ$ (a) and $2\theta \approx 19^\circ$ (b) as the reaction of $NiCl_2 + NH_3$ propagates.

3.10 and 3.11) but remains constant afterwards (compare next paragraph) indicating that an amorphous phase other than the poorly crystalline starting material could be involved. Such a behaviour would be indicated in the kinetic data of the reaction, the results of which are presented in section 3.3.4. A further limitation of this purely observation based approach is the possible multiple-step process in which the formation of a hypothetical intermediate phase is the rate determining step. One could envisage a pseudo steady-state case in which the rate constant for the formation of the intermediate is by orders of magnitude smaller than the rate constant of its destruction. This consequently means that the hypothetical intermediate product would be consumed far more quickly than it is produced and its concentration would therefore remain very small, possibly below the detection limits of the characterisation methods, in this case PXD. However, it has been demonstrated that the complex formation constants* of ammine nickel(II) complexes in aqueous solutions are by 2 order of magnitude larger for the incorporation of the

---

*It shall be noted that these are equilibrium constants not kinetic constants first equivalent of ammonia than they are for the sixth equivalent.[19] Although these equilibrium constants do not allow a direct assumption on the rate constants, they can be seen as a general tendency to the complex formation, which is by far higher for the first molecule than for the sixth one. Given this behaviour, it appears unlikely that the ammonia uptake by the pure dihalides or a potential lower ammine intermediate could be the rate determining step while its further reaction to the hexammine is by orders of magnitude faster and it is hence unlikely that such a behaviour would happen in this reaction.

Despite the fact that the starting material $NiCl_2$ is poorly crystalline (Figure 3.10), the formation of $[Ni(NH_3)_6]Cl_2$ can be followed *via* the evolution of its characteristic peaks in the powder pattern. From the detailed examination of some of the growing peaks (figures 3.10-inset and 3.11), it can be observed that the formation is steady and does not show any derivations or remarkable plateaus during the reaction. This is particularly noticeable for the region ca. $2\theta = 8^\circ$ (Figure 3.11, a) where the strongest peaks in both starting material and reaction product are located. Although both peaks are close together, a clear shift in the peak position can be observed with the propagation of the reaction. The same peak growth can be observed in the region at ca. 19° (Figure 3.11, b) where two peaks of $[Ni(NH_3)_6]Cl_2$ are evolving over time. However, as interesting as the growing peaks are the broad contributions from the starting material. that vanish over time leaving the full pattern with a lower level of background. Although the reflections of $NiCl_2$ in this region are so broad that they are hardly distinguishable as individual peaks, their disappearance upon ammoniation is clearly observed despite the low crystallinity of the starting material. The possibility of these peaks being an amorphous intermediate product can be ruled out as the decrease of background appears monotone and in alignment with the disappearance of the larger $NiCl_2$ peaks.

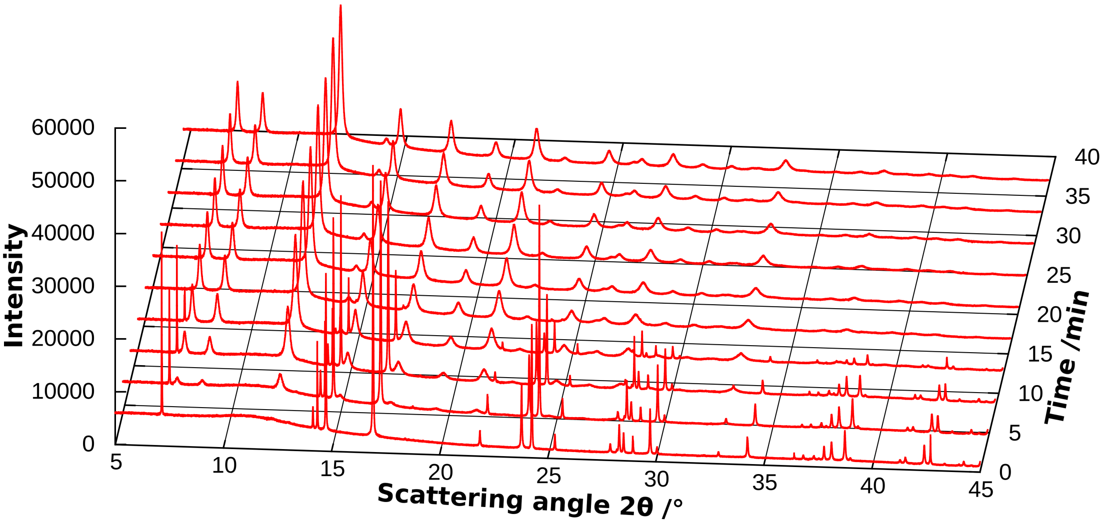

Figure 3.12.: Time resolved ammonia uptake in NiI_2 at room temperature. Patterns are shown every 4 minutes.

Ammonia Uptake by NiI_2

A similar trend to the above can be observed for the formation *in situ* of the iodide analogue $[Ni(NH_3)_6]I_2$ (Figure 3.12). It is worth noting that NiI_2 is much more crystalline than the chloride analogue. Nevertheless, the reaction with ammonia takes place very rapidly and forms a single phase of $[Ni(NH_3)_6]I_2$ within ≈15 min. Again, no intermediate phases can be detected during the reaction which further underlines the assumption that the reaction of the pure nickel dihalides with ammonia forms the according hexammine structures directly without the formation of lower ammines as intermediate phases (or a transformation below the detectable time range).

3.3.4. Kinetic studies of the NH_3 uptake in $NiCl_2$

The devolution of the kinetics of the different reaction parts, consumption of $NiCl_2$ and evolution of $[Ni(NH_3)_6]Cl_2$ in the reaction may yield more reliable and more detailed information of the mechanisms involved in the ammonia uptake reaction. Bearing the observations and conclusions noted in the section above in mind (no observed crystalline intermediate and no steady-state type intermediate), the uptake reaction could consist of multiple steps. Two potential reaction mechanisms could be thought of: On the one hand, the two reaction components ($NiCl_2$ consumption, ammine formation) could have a similar reaction rate and the intermediate products would be non-crystalline. The complete disappearance of the starting material and the appearance of the final reaction product in this case would be separated with respect to each other leaving a period of time in which the intermediate products would be formed in a significant amount. On the other hand, both hypothetical reactions (intermediate formation and intermediate disappearance) could have largely different reaction constants making one step effectively rate determining. The ideal way of determining the reaction constant from the *in situ* powder data would be to analyse the phase fractions in each pattern based on the Rietveld method as this would take the whole pattern into account. This is extremely challenging in this case as the starting material $NiCl_2$ exhibits a very low crystallinity making the Rietveld refinement of the pattern all but impossible. Instead, it was decided to restrict the analysis to the range between $25.5^\circ \leq 2\theta \leq 30.6^\circ$ in which two peaks from the starting material ($2\bar{1}0$ and $2\bar{1}3$) diminish and three peaks of the final product (404, 315 and 206) evolve. The area under the individual peaks was monitored as a function of time because it is proportional to the phase fraction.

Some assumptions were taken as a measure to simplify the problem: Firstly, in order to de-convolute the strongly overlapping peaks successfully, the position of the $NiCl_2$ reflections were determined using a single phase $NiCl_2$ pattern before the beginning of the reaction and those for $[Ni(NH_3)_6]Cl_2$ were determined using a phase pure $[Ni(NH_3)_6]Cl_2$ patter at the end of the reaction (as the analysis was performed on an *in situ* sample, it is safe to assume that systematic erros such as zero-point error are negligible in this

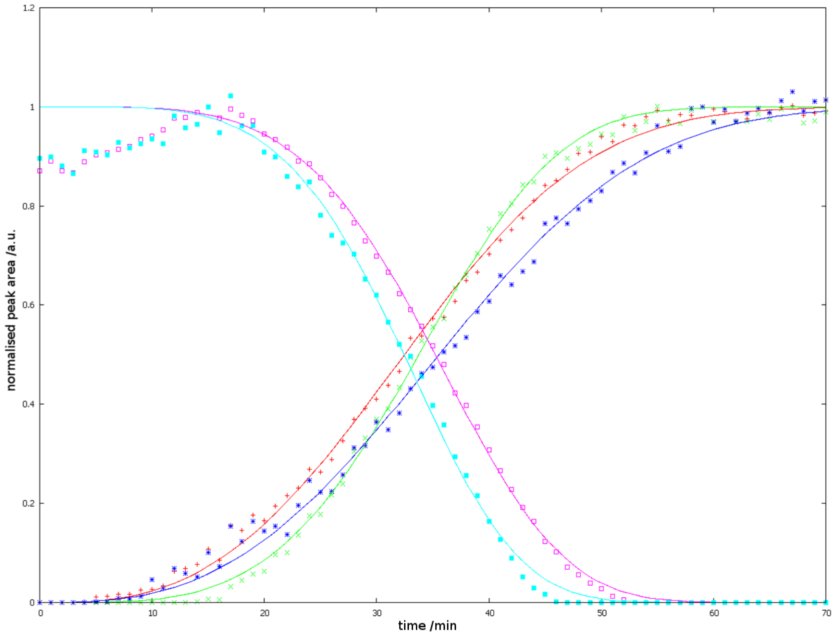

Figure 3.13.: Development of the relative peak area for the peaks of $NiCl_2$ ($2\bar{1}0$: magenta filled squares; $2\bar{1}3$: turquoise open squares) and $[Ni(NH_3)_6]Cl_2$ (404: red plusses; 315: green crosses; 206: blue asterisks) with time and their fitting with an Avrami type function (lines, compare equations (3.4) and (3.5)).

treatment). The positions of the peaks were fixed as determined above during the peak deconvolutions of the individual patterns and those peaks with negligible area were set to zero to avoid physically unreasonable results (e.g. negative peaks). Furthermore, the peak shapes were described by a pure Lorentzian function as the use of a pseudo-Voigt function with generically refined mixing variables proved inconsistent. Secondly, without the exact knowledge of a strict physical link between the areas of the different peaks as defined by the scattering powers from a crystal structure, the largest areas within the series were set to a value of "one" and the other areas normalised with respect to this value.

Some important points can be noted regarding the development of the peak areas with time (Figure 3.13). *Firstly*, the peak areas from $NiCl_2$ at the beginning of the experiment are not constant although they should remain constant before a reaction takes place. This can be explained in the context of the arrangement of the experiment. As the powder expands in volume when it starts to react with ammonia, the capillaries had to be filled with a small amount of starting material, which was forming a small layer in the horizontally arranged capillary. Once ammonia gas was allowed to enter the capillary, it started to react with the $NiCl_2$ powder at the entrance of the capillary, probably pushing more of the $NiCl_2$ powder into the area irradiated by the X-ray beam which increased the absolute intensities of the peaks during the initial period. This explanation is supported by the observation that the relative peak area of the two $NiCl_2$ reflections changed simultaneously and with the same relative rate (Figure 3.13).

The kinetics observed in these experiments, especially the relatively slow initiation period, are in stark contrast to what was observed in the gravimetric experiments presented in section 3.3.1. This initiation period is again a consequence of the experimental setup used. As discussed in the previous section, the sample environment could not be evacuated before the experiment and the sample was kept under argon gas at ambient pressure. Consequently, the initial reaction rate is limited by the ammonia diffusion through the argon atmosphere in the capillary and hence is different from the situation observed in the gravimetric experiments where ammonia is entering an evacuated chamber in large excess. This difference means that the reaction kinetics in this experiment are not only dependent on inherent gas-solid reaction rate but are also limited by the ammonia supply during the reaction. Therefore, the data are not directly comparable with the results in section 3.3.1.

This difference in the initial reaction rate is also the main reason for the different kinetic model used in the two experiments. While the uptake in the gravimetric experiment appears to be best described with a pseudo-first order reaction model, the kinetic profile in the X-ray experiment exhibits a clearly sigmoidal shape (s-shape). This s-shape is explainable with an initial slow step, a high rate at intermediate times and a slowing of the rate at the later stages of the reaction. A suitable model has been developed for the primary crystallisation and growth in solids from Johnson-Mehl-Avrami-Kolmogorov (JMAK) theory.[20–24] In this model, the slow initial rate is attributed to the slow nucleation, a fast intermediate step to the rapid crystal growth and the last slow step to influences like grain boundary and defect formations which impede further subsequent crystal growth.[25] Although this model is not directly applicable to the reaction process in the formation of hexammine nickel halides, where one might propose crystal growth at the gas-solid interface, the kinetic profile is very comparable to those of JMAK crystal growth and the model has been applied successfully to solid-gas reactions.[26,27] It should however be noted that the work by Jensen *et al.* consisted of the gas evolving MgH_2 decomposition rather than a gas uptake reaction.

While the fast intermediate crystal growth and later stage defect formation kinetics of the JMAK model are directly applicable to the ammonia uptake studied here, an initial slow nucleation step is not evident from gravimetric data (see section 3.3.4). The slow initiation period in the *in situ* X-ray experiment caused by the diffusion of ammonia gas through the argon atmosphere gives this process kinetics comparable to a JMAK model. Due to the similarity of the two kinetic processes, the JMAK theory kinetics were applied to the curves in this model in order to extract kinetic information for the comparison of the $NiCl_2$ consumption and the $[Ni(NH_3)_6]Cl_2$ evolution.

The peaks were therefore fitted with an Avrami-type function for the reaction rate r(t):[28]

$$r(t) = 1 - \exp(-(k \cdot t)^n) \tag{3.4}$$

for the evolving phase, with the reaction constant K and the Avrami exponent n, and:

$$r(t) = \exp(-(k \cdot t)^n) \tag{3.5}$$

for the diminishing phase. The values for the reaction constants for both the consumption of $NiCl_2$ and the evolution of $[Ni(NH_3)_6]Cl_2$ (Table 3.1) are similar (average for consumption: k = 0.027 /min and for evolution: k = 0.0263 /min). Together with the fact that no time shift between the appearance of $[Ni(NH_3)_6]Cl_2$ and the disappearance of $NiCl_2$ can be observed (easily recognisable through the fact that the sigmoidals cut each other at 50 % relative peak area), the matching rate constants prove that appearance and disappearance are kinetically linked and therefore must belong to the same process. This strongly suggests that no intermediate phases are formed during the reaction and that the reaction of gaseous NH_3 with $[Ni(NH_3)_6Cl_2$ is a one-step process. It is however important to have a closer look at the Avrami exponents of the fits to the peak areas (Table 3.1). The physical meaning of the Avrami exponents[26] has been discussed in the literature and it is generally agreed that it is attributed to the degrees of freedom of the reaction (generally: one degree of freedom for the diffusion and one for each space dimension in which the reaction takes place) and therefore the underlying reaction mechanism. The first observation is, that the exponents for the peaks of $NiCl_2$ and $[Ni(NH_3)_6]Cl_2$ are consistent within the data series apart from the value of the (315) peak of $[Ni(NH_3)_6]Cl_2$. This latter discrepancy, however, can be attributed to the (315) peak position which is located between the two $NiCl_2$ peaks and the peak deconvolution for this peak is especially prone to errors, given that some component peaks are small at the beginning and the end of the reaction. The fact that the Avrami exponent for the $NiCl_2$ component is however larger than for the $[Ni(NH_3)_6]Cl_2$ may be attributed to differences in the reaction mechanisms, e.g. different crystallite sizes and preferentially reactive crystal faces. It can nevertheless

Table 3.1.: Overview of the reaction constants k and the exponent n in the Avrami fitting with estimated uncertainties for the reaction of $NiCl_2$ with NH_3.

Peak Position /°	hkl index	k /min^{-1}	n
$NiCl_2$			
27.51	$2\bar{1}0$	0.026(5)	4.4(5)
28.74	$2\bar{1}3$	0.028(5)	4.5(5)
$[Ni(NH_3)_6]Cl_2$			
26.77	404	0.027(5)	2.9(5)
28.00	315	0.027(5)	3.9(5)
29.97	206	0.025(5)	2.9(5)

be assumed that the difference of the Avrami exponents is not affecting the conclusive nature of the one-step process extracted from the information.

3.3.5. Development of the crystallinity with time

It is commonly agreed that pure solid state reactions require effective diffusion in the solid to work, which is normally only reached over $\approx$ 2/3 of the the melting point, an empirical rule known as Tammann's rule.[29] Following this rule of thumb, one would not normally expect a solid state reaction at room temperature. It is therefore surprising that the peak shape of $[Ni(NH_3)_6]Cl_2$ changes considerably after the reaction with NH_3 appears to be finished (based on the complete disappearance of $NiCl_2$; Figure 3.14). The peaks of $[Ni(NH_3)_6]Cl_2$ narrow with time and increase their maximal intensity, which suggests a change in the texture of the crystallites. The peak width is in fact influenced by many parameters, most notably the crystallite size, the crystallite shape and microstrain. Strong anisotropy in the crystallite shapes can be detected. Strongly anisotropic crystallites produce non-uniformly broadened groups of peaks (of certain hkl values). It was assumed

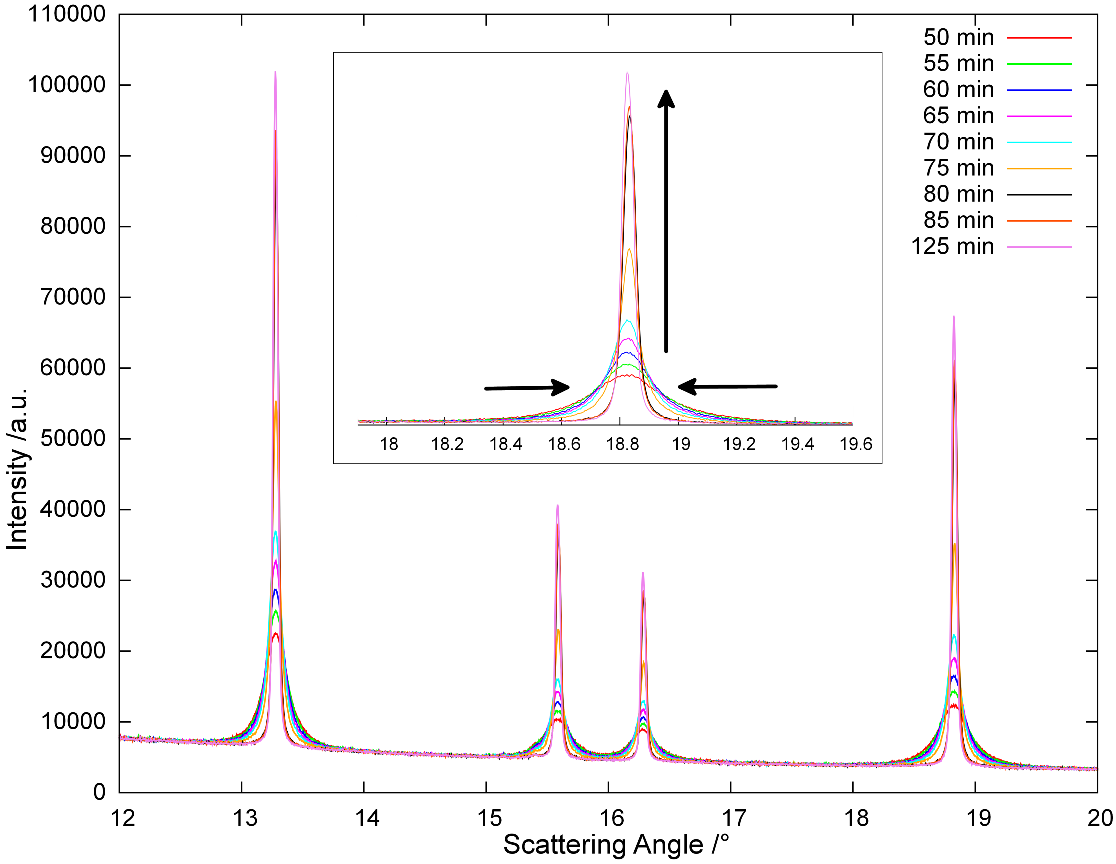

Figure 3.14.: Overlay of the patterns of $[Ni(NH_3)_6]Cl_2$ in the system $NiCl_2 + NH_3$ under constant NH_3 pressure (patterns are given in intervals of 5 min). The arrows in the inset signify the direction of propagation during the reaction.

for this analysis that the main contributions to the peak broadening are from the crystallite size and size distribution rather than the microstrain, which was was neglected.

In order to gain some more insight into the mechanisms behind the formation of sharper reflections over time, an analysis using the whole pattern profile modelling (wppm)[30] method was performed with the program PM2K.[31] Common size and strain analyses such as Scherrer's equation,[32] Williamson-Hall analyses[33] and Warren-Averbach analyses,[34] are based on the extraction of the peak width with an arbitrary function and the further extraction of the size and strain analysis from this. Wppm, however, aims to reconstruct the whole diffraction profile from physically correct descriptions of the broadening effects directly.[30] For this, the experimentally determined powder pattern is directly fitted to a function containing terms for the different peak broadening effects, which are convoluted in Fourier space.[31] Unfortunately as it was not expected to observe these effects at the time of the measurements, the retrospective treatment of the data was problematic. The profile of the PSD detector used for the measurement is not ideal for refinements and therefore resulted in relatively high residuals for the best fits. Furthermore, no standard was measured at the time of the experiment, which would have been necessary to obtain realistic values for the instrumental peak broadening over the whole 2θ range. However, as the peaks in the later patterns in the experiment are much narrower than those in the initial pattern, it can be assumed that the size contribution to the peak shape in the earlier measurements is much more significant than the instrumental broadening and it was therefore chosen to use the last pattern measured as an internal standard to approximate the effect of the instrumental broadening. This approach thus introduces an intrinsic error that the peak broadening from size effects in the internal standard is negligible and therefore leads to a systematic underestimation of the peak width causing a systematic overestimation of the crystallite sizes.[†] While the absolute values for the crystallite size in this treatment are therefore to be treated with some prudence, the relative trends in crystallite size and size distribution can be regarded with a much higher degree of certainty.

Instrumental profile fitting

The instrumental broadening was fitted with a Caglioti type function[35] using a pseudo-Voigt bell-shaped function where the peak broadening with 2θ is described by the six

---

[†] The level of systematic overestimation is solely dependent on the size of the crystallites in the last measurement but as the peak width between the earlier and the later patterns does differ significantly, this effect should be small in comparison.

parameters U,V,W,a,b and c in:[36]

$$pV(2\theta) = (1-\eta_{Lorentz})\sqrt{\pi \ln 2} \exp\left(-\ln 2 \frac{2\theta - 2\theta_B}{\sigma}\right)^2 + \frac{\eta_{Lorentz}}{\pi\sigma} \frac{1}{1+\left(\frac{2\theta-2\theta_B}{\sigma}\right)^2} \tag{3.6}$$

where θ_B is the Bragg angle and $\sigma = \frac{FWHM}{2}$ with the paramters defined as follows.

$$FWHM^2 = W + V \cdot \tan(\theta) + U \cdot \tan^2(\theta) \tag{3.7}$$

$$\eta_{Lorentz} = a + b \cdot \theta + c \cdot \theta^2 \tag{3.8}$$

During the instrumental profile fitting, the cell parameter was fixed to 10.08 Å as determined in the prior Rietveld refinements of $[Ni(NH_3)_6]Cl_2$ (section 3.4) and the zero error was taken as determined by the instrument scientist at the beamline through the measurement of a standard. In addition to the instrumental profile, shifts in the pattern were corrected with a tangent polynomial sample displacement as described by Wilson[36,37] with:

$$\Delta(2\theta) = a_{-1} \tan^{-1}(\theta) + a_0 + a_1 \tan(\theta) + a_3 \tan^3(\theta) \tag{3.9}$$

Applying these two instrumental corrections, the profile can be fitted conveniently and leads to a stable refinement. It should be noted that the some of the resulting refinement parameters, namely the Goodness of fit, are relatively high due to the problematic profile arising from the use of the PSD detectors.

Crystallite size fitting

The crystallite size effect in the patterns may be determined after defining the instrumental broadening as above. This treatment works provided that the peak profiles of the refined patterns are considerably broader than the pattern chosen as the standard. This is certainly the case for the earlier patterns as can be judged by simple visual examination (Figure 3.14). Two major assumptions have to be made when using the size function provided by the program: the shape of the domains must be described and the distribution must follow a log-normal distribution function, the latter has been shown to be suitable for crystallite size descriptions.[38,39] It was decided to describe the domain particle shape as spherical particles ad hence isotropic given the high (cubic) crystal symmetry. This treatment allowed to fit patterns measured up to $\approx$ 70 minutes after the start of the ammonia uptake because their peak width was sufficiently different from pattern used as standard. While the fitting for the pattern after 75 minutes converged as well, the results from this fitting are much less reliable as the assumption of much smaller crystallites compared to the standard is no longer true. Although the average crystallite size was still rising in this analysis, the size distribution does not follow the general trend sfter 75 minutes. This is a consequence of the less reliable fitting and arises from the definition of the log-normal function which has to start at zero.

The sequential refinement of the different patterns collected for $t \leq 75$ min then led to the distributions as seen in Figure 3.15. The size distribution broadens as the peaks narrow and the average size of the crystallites increases. The data suggest that the amount of smaller crystallites decreases and the amount of larger crystallites increases. An alternative explanation of the crystal growth could be the encapsulation of $NiCl_2$ starting material within a shell of $[Ni(NH_3)_6]Cl_2$. The crystal growth could be caused by the subsequent reaction of the core inside the particle. The amount of encapsulated starting material could however only be very small as it is not detectable in the PXD patterns (neither as peaks nor as an amorphous background).

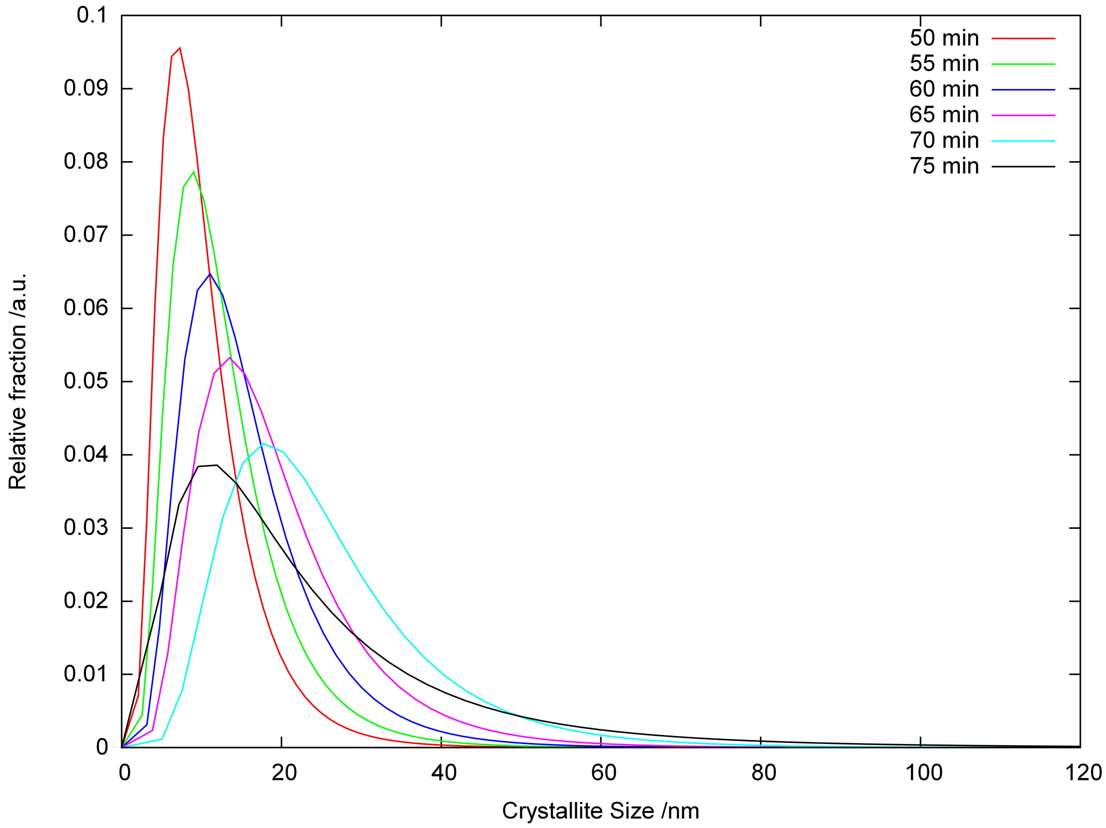

Figure 3.15.: Crystallite size distributions evolving with time as refined from synchrotron data of $[Ni(NH_3)_6]Cl_2$ with the wppm method.

3.4. Structures of the hexaammines $[Ni(NH_3)_6]X_2$

The crystal structures of the hexaammines of the nickel halides had been determined before this work with the exception of the hexaammine nickel iodide.[2,40] Nevertheless, the full structural characterisation of our ammonia storage materials is crucial in order to be able to detect any structural anomalies as a function of ammonia partial pressure and/or time. The structures were refined with the programme Jana2006.[41]

3.4.1. Structural refinements of $[Ni(NH_3)_6]X_2$

The powder patterns recorded for ammoniated nickel halides (X = Cl, Br) were compared with theoretical powder patterns calculated from cif files in the literature.[2,40] The hexaammine iodide pattern could nevertheless be indexed with a cell isostructural to the other halides (with bigger cell parameters; Table 3.2). The patterns were subsequently treated with a structure-less Le Bail fitting using Jana2006 in order to extract the intensities of the different reflections. The latter were used for structure solutions using Superflip.[42] All non-hydrogen atoms could be located during the structure solution. The position of the hydrogen atoms in these structures are particularly difficult to locate due to the low scattering power of the hydrogen atoms in combination with a strong crystallographic distortion of the hydrogen atoms which smears the electron density on a circle with respect to the nitrogen position. It is however crucial to include a treatment for the hydrogen atoms. This is due to the relative electron density of the hydrogen atoms in ammonia that account for 30 % of the electron density of the whole ammonia molecule. A failure to include the hydrogen atoms in the model would therefore lead to a systematic overestimation of the nickel – ammonia distance. In order to treat this problem appropriately, a model was chosen in which the hydrogen atoms and the Ni atoms form the corners of a tetrahedron around the nitrogen atom. Although realistic nitrogen – hydrogen distances in ammonia are of the order of 1.01 Å, the nitrogen and hydrogen distance was generically set to a value of 0.87 Å which has been shown to correspond to the apparent bond length in X-ray structures.[43] The latter apparent contraction is caused by the strong polarisation of the sole electron of hydrogen towards the covalent bond vector which shifts the centre of the electron density of the hydrogen atoms from the physical hydrogen position towards its bonding partner. This treatment led to a heavily distorted hydrogen arrangement on a circular position due to the clash of the molecular three-fold symmetry and the crystallographic four-fold symmetry of the site as has been observed in numerous studies in the past.[2–9] Nonetheless, the refinements of $[Ni(NH_3)_6]Cl_2$, $[Ni(NH_3)_6]Br_2$ and $[Ni(NH_3)_6]I_2$ (Figure 3.17) using this model refined smoothly and resulted in very good refinement values (Table 3.2). The structural models are in good agreement with prior measurements and comparable structures.[2,44,45]

Table 3.2.: Refinement results for the Nickel hexa-ammine halides.

Formula	**$[Ni(NH_3)_6]Cl_2$**	**$[Ni(NH_3)_6]Br_2$**	**$[Ni(NH_3)_6]I_2$**
Crystal system	Cubic		
Space group	$Fm\bar{3}m$		
a /**Å**	10.0800(1)	10.3830(1)	10.9053(2)
Volume /Å^3	1024.20(2)	1119.34(2)	1296.92(4)
Z	4		
Calculated Density, ρ_x /g·cm^{-3}	1.5027	1.9023	2.1231
R_p; wR_p	0.028; 0.036	0.029; 0.037	0.018; 0.023
Goof; X^2	0.99; 0.98	1.16; 1.35	1.24; 1.54
R_{obs} ; wR_2 **(all)**	0.016; 0.023	0.016; 0.020	0.044; 0.038
Ni–N distance /Å	2.142(2)	2.155(2)	2.167(5)

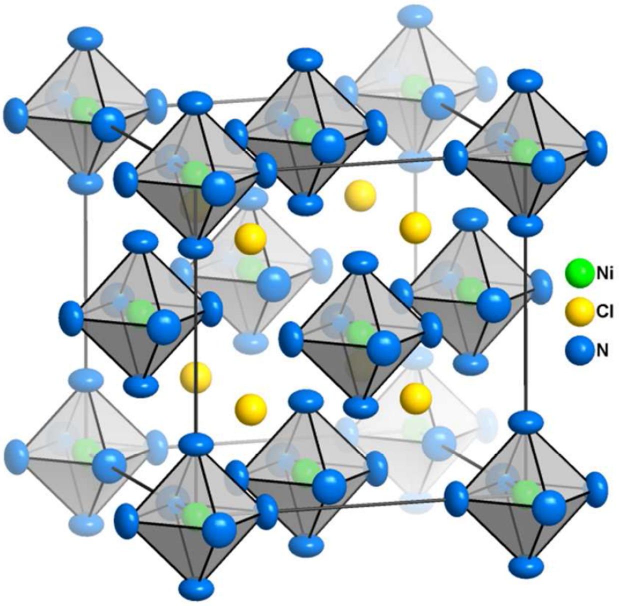

Figure 3.16.: Representation of the cell for $[Ni(NH_3)_6]Cl_2$. The atoms (Ni, green; Cl, gold; N, blue) are represented by their thermal ellipsoids of 90 % probability. The ammonia molecules are only represented by their nitrogen atoms and the hydrogen atoms are omitted for clarity.

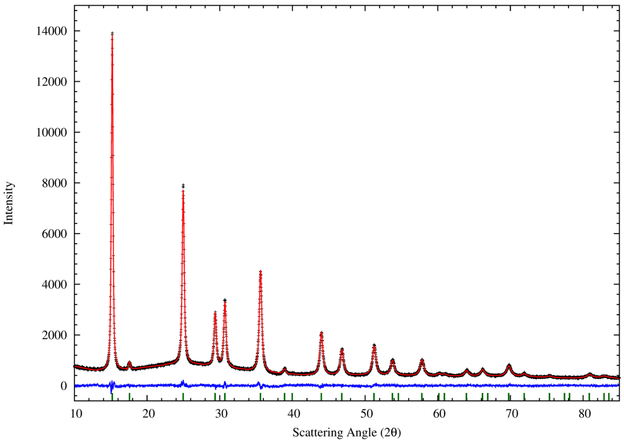

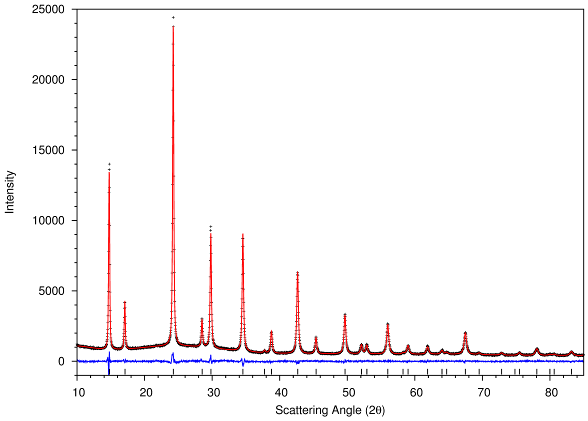

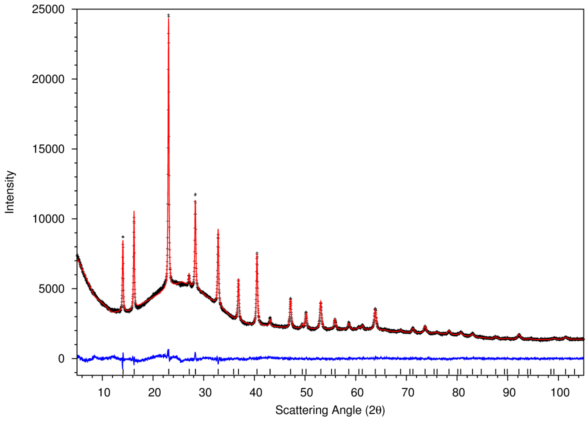

Figure 3.17.: Measured powder patterns of $[Ni(NH_3)_6]X_2$ X = Cl, top; X = Br, middle; X = I, bottom (black crosses) compared with the refined profile (red line). The difference $I_{obs} - I_{calc}$ is given as blue line and the theoretical peak positions are given as dashes.

Description of the Structures

The compounds are composed of octahedral $[Ni(NH_3)_6]^{2+}$ complex cations with eight nearest-neighbour anions arranged in a cube-shape as well as simple halide anions that are surrounded tetrahedrally by the complex cations (Figure 3.16). The long distances between the Ni atom and the halide anion (Ni–Cl = 4.3648(1) Å, Ni–Br = 4.4960(1) Å, Ni–I = 4.7221(1) Å) allows the assumptions that the bonding between the complex cation and the anion is essentially ionic and the ion arrangement can be understood as a fluorite type arrangement.

The very high symmetry of the cell only allows the refinement of a limited number of parameters. Besides the cell parameter a and the isotropic displacement parameters of the atoms U_{iso}, only the distance between nickel and the nitrogen atom in the ammonia molecule and the anisotropic displacement parameters for nitrogen (expansion along and perpendicular to the Ni–N bond vector) are free to refine. The Ni–N bond distances in the complexes are very similar throughout the different halides, but a variation exists from 2.142(2) Å for $[Ni(NH_3)_6]Cl_2$ to 2.167(5) Å for $[Ni(NH_3)_6]I_2$. Due to the general semi-quantitative relationship between bond length and bond strength,[46–48] it can therefore be assumed that the complex cations show a general trend towards weaker bonds in the series Cl $>$ Br $>$ I. This correlates well with the findings from FTIR (Figure 3.18, Table 3.4.1). The IR mode frequencies generally decrease in the series Cl $>$ Br $>$ I with one notable exception. The symmetric deformation mode δ_s exhibits a blue-shift with increasing anion mass. As remarked previously by Eßmann, the symmetric deformation band is most sensitive to the $\sphericalangle$Ni–N–H bonding angle.[49] The blue-shift in these complexes is consequently also a sign of the decreasing bond strength in the complex cation because a weaker Ni–N bond polarises the nitrogen lone pair less and therefore decreases the degree of freedom for the N–H bond. This effect is most pronounced when changing the metal centre, as has been previously demonstrated by Fujita *et al.*[50]

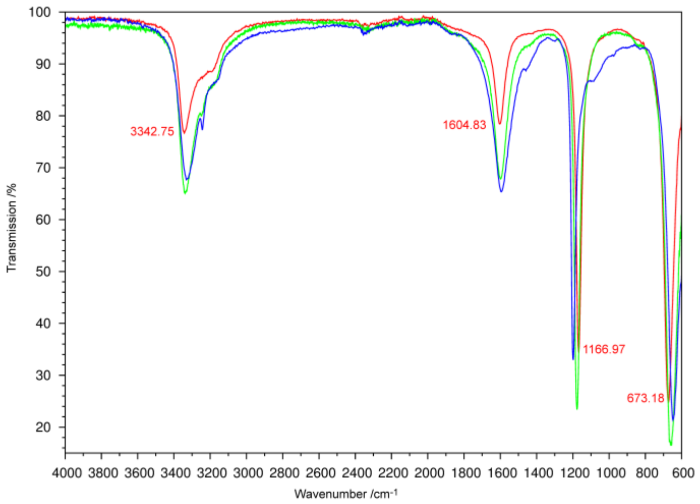

Figure 3.18.: FTIR spectra for $[Ni(NH_3)_6]X_2$ with X = Cl (red), X = Br (green) and X = I (blue). The wavenumbers of the absorption maxima given in the figure are those for the chloride

Table 3.3.: FTIR spectrum band assignment for $[Ni(NH_3)_6]X_2$. Wavenumbers are given in cm^{-1}
.

Band	$[Ni(NH_3)_6]Cl_2$	$[Ni(NH_3)_6]Br_2$	$[Ni(NH_3)_6]I_2$	$[Ni(NH_3)_6]Cl_2$ [51]
$\nu_{as}(NH_3)$	3343(2)	3338(2)	3331(2)	3345
$\nu_s(NH_3)$	3193(2)	3177(2)	3173(2)	3190
$\delta_a(HNH)$	1605(2)	1598(2)	1595(2)	1605
$\delta_s(HNH)$	1167(2)	1177(2)	1198(2)	1186
$\rho(NH_3)$	673(2)	661(2)	648(2)	684

Hydrogen bonding N–H$\cdots$Cl

The distances between the distorted hydrogen position described as a circle with respect to the nitrogen position of the ammonia molecules and their closest halide atoms give rise to the assumption that hydrogen bonding could play an important role in the stabilisation of the compound structure. Each ammonia molecule is surrounded by four equidistant halide atoms which are arranged in a square. The closest distances between the ring of hydrogen positions and each individual halide atom therefore exist in a range $-45° \leq \omega \leq +45°$ around the closest H$\cdots X$. The H$\cdots X$ distance can be described as a function $d(\omega)$ of the rotation angle of the ammonia molecule around the cell axis parallel to the Ni–N bond (in this case the *c*-axis, see Figure 3.19):

$$d(\omega) = a \cdot \sqrt{[x(\mathrm{Cl}) - r(\mathrm{H}) \cdot \cos\omega]^2 + [y(\mathrm{Cl}) - r(\mathrm{H}) \cdot \sin\omega]^2 + [z(\mathrm{Cl}) - z(\mathrm{H})]^2} \quad (3.10)$$

Where a is the cell edge length, ω is the rotation angle of the circle of H-atoms and r its radius, i.e. the hydrogen distance from the rotation axis.

The situation in $[\mathrm{Ni(NH_3)_6}]\mathrm{Cl_2}$ is described as an exemplary case. The position, where the hydrogen atom is equidistant to two neighbouring chlorine atoms (+45° relative to

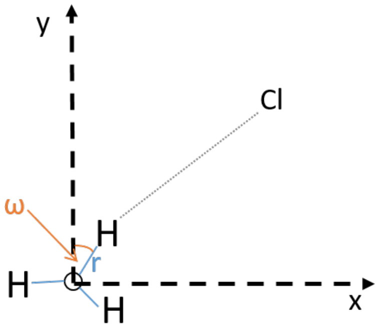

Figure 3.19.: Schematic view along the z-axis of the N–H$\cdots$Cl hydrogen bonding arrangement in $[\mathrm{Ni(NH_3)_6}]\mathrm{Cl_2}$.

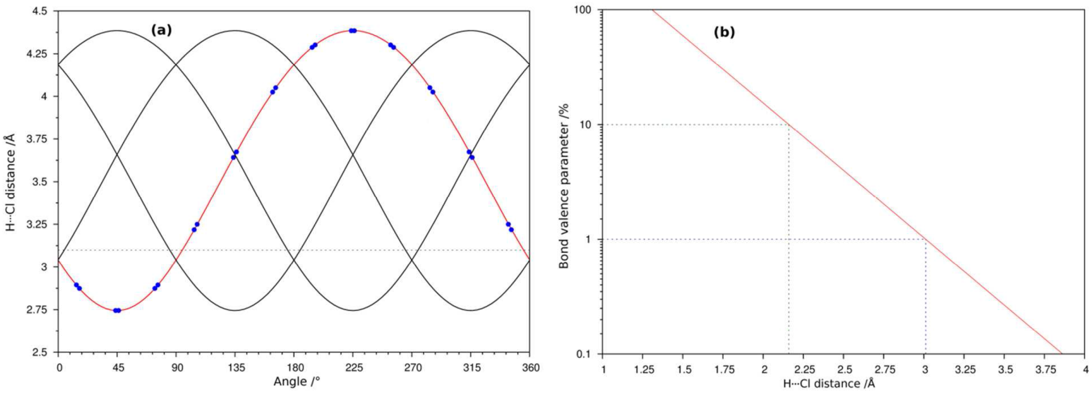

Figure 3.20.: **(a)** Plot of all possible H–Cl distances in $[Ni(NH_3)_6]Cl_2$ for the four chlorine atoms surrounding each ammonia molecule (red and black lines). The curve for one atom is highlighted (red line) and all distances used in the refinement are given as blue circles. The green dashed line marks a bond distance of 3.1 Å corresponding to a bond valence parameter of ≈ 0.01. **(b)** Bond valence parameter for H–Cl as a function of the distance (red line). The green and blue dashed lines correspond to a bond valence of 10 % and 1 % .
The discrepancy between the cut off value of 3.1 Å in (a) and the theoretical value for 1 % bonding in (b) takes account of the systematic overestimation of the H–Cl distance from X-ray data.

one chlorine atom and −45° relative to its neighbouring chlorine atom) is ca. 3 Å away from both chlorine atoms and signifies the furthest distance possible for hydrogen and chlorine in the hydrogen bonding region of $[Ni(NH_3)_6]Cl_2$. The closest distances between hydrogen and chlorine is the bonding for which the angle ∢N–H–Cl reaches a maximum and can be calculated to be 2.7443(1) Å(Figure 3.20, a).

The bond-valence method can be used to estimate the maximum length for which interactions can be considered as hydrogen bonding. A region of a bond valence parameter between 1 % and 10 % of a single bond can be commonly considered as such a region.[52] Therefore, a H···Cl distance of ≈ 3 Å marks the limit for hydrogen bonding (Figure 3.20, b). Taking the systematic overestimation of the H···Cl distance from X-rays into account, it should be noted that hydrogen bonding to a chlorine atom can be observed in *any* rotational position of the hydrogen circle. Furthermore, due to the three-fold symmetry of the ammonia molecule and the four-fold symmetry of the surrounding chlorine environment, no significant energetic minimum can be reached for any particular rotational position of the ammonia molecule, because an approach of one hydrogen atom to its neighbouring chlorine atom would unavoidably lead to a elongation of the bonding distance for the other hydrogen atoms. This fact explains the low energetic barrier to rotation and hence the fast rotation of the ammonia molecules around the Ni–N bond axis as has been shown previously by inelastic neutron scattering and diffraction experiments.[7,9,53–56]

It has to be remarked though, that the sophisticated models employed to explain the rotational disorder of the ammonia molecules applied by Hoser and co-workers[53] could not be applied to data from lab powder X-ray diffraction experiments, which are too quality-limited for this treatment. The nearly homogeneous electron density distribution on the hydrogen positions in our model has therefore to be assumed as an approximation.

Cell parameter variations with the counter-anion

The hexa-ammine nickel halides $[Ni(NH_3)_6]X_2$ (X = Cl, Br, I) crystallise isostructurally in the spacegroup type $Fm\bar{3}m$. Their cell parameters increase accordingly with the increasing size of the anion ($r_{Cl} = 1.67$ Å, $r_{Br} = 1.82$ Å, $r_I = 2.06$ Å)[57,58] from a = 10.0800(1) Å for $[Ni(NH_3)_6]Cl_2$, to a = 10.3830(1) Å for $Ni(NH_3)_6]Br_2$ and a = 10.9053(2) Å for $[Ni(NH_3)_6]I_2$ (Table 3.2). This is very much in line with a linear relationship between the ionic radii and the cell parameters (Figure 3.21) according to Vegard's law.[59]

Fitting the the values with a linear function yields in the following equation ($R^2 =$ 99.96%):

$$a = 2.12174 \cdot r_{\text{anion}} + 6.53087 \tag{3.11}$$

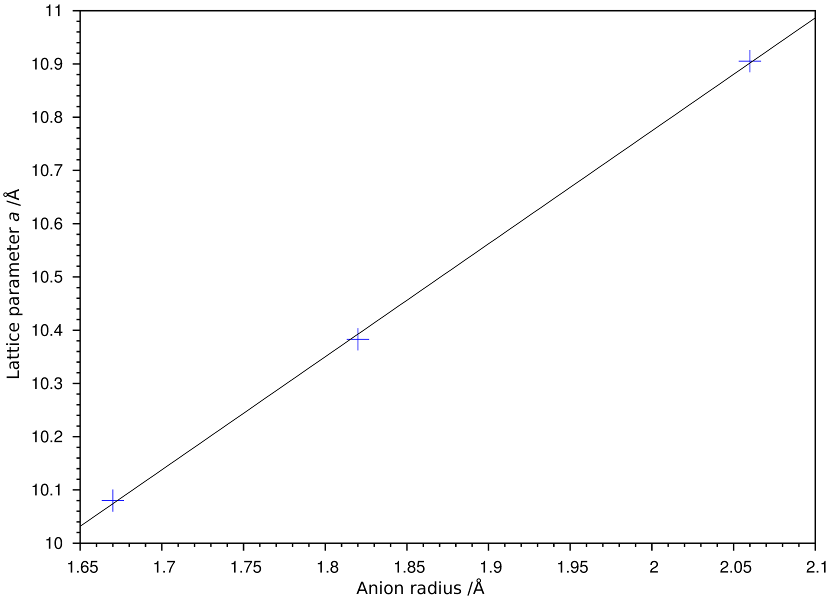

Figure 3.21.: Plot of the cell parameters of $[Ni(NH_3)_6]X_2$ (X = Cl, Br, I) against the respective ionic crystal radii after Shannon[57] (blue crosses) together with the least-square linear fit of these values (black line).

where a is the cell parameter and r_{anion} is the respective anion radius. These values can be further rationalised when looking at the arrangement of the anions and cations in the cell (see also Figure 3.16). In a first thought model, one could assume that the distances defining the size of the unit cell are the ones between the halide atoms and the complex cation octahedra. Their relationship should hence define the slope of equation (3.11). Due to the tetrahedral arrangement of the complex cations around the halide anions, the angle $\sphericalangle X - Ni - X = 70.529°$ is predefined by the symmetry (as 180° minus the tetrahedral angle). These considerations therefore leave to the following equation:

$$a = 4 \cdot \sin\left(\frac{70.529°}{2}\right) \cdot r_{\text{anion}} + d_{\text{cation}} = 2.30932 \cdot r_{\text{anion}} + d_{\text{cation}} \qquad (3.12)$$

The slope of this equation fits very well with the measured ones indicating that the model used to derive equation (3.12) is most likely defining the closest contacts between the ions and therefore is determining the cell size. Also, the successful use of Vegard's law for the series of different halide compounds indicates no change in bonding nature within the series.

3.5. Thermal Decomposition of $[Ni(NH_3)_6]X_2$ (X = Cl, Br, I)

3.5.1. Thermal analyses

The targets for the thermal analysis of the hexammine nickel halides were to **a)** Define the decomposition steps and evaluate the gases released at each stage of the reaction and **b)** Extract the activation energies of the different decomposition steps *via* a Kissinger analysis at different heating rates. Two different strategies were used to achieve the two different goals; Qualitative understanding of the deammoniation required large samples (ca. 30 mg) in order to optimise the mass spectra of the evolved gas. The Kissinger analyses, however, were mainly performed with smaller samples of $\approx$ 15 mg in order to circumvent problems related to any potential partial pressure dependence of the decomposition steps.

Previous discussion of the thermal decomposition of hexammine nickel chloride in the literature[40,60–63] concerned whether the thermal decomposition of $[Ni(NH_3)_6]Cl_2$ is a pure two-step process with the diammine as sole intermediate or whether it is a three-step process with both the diammine and the monoammine as intermediates prior to complete deammoniation to $NiCl_2$. The initial results of the TG-DTA-MS analysis and the *in situ* XRD analysis did not suggest a three-step process but a more complex behaviour could be observed using thermal analysis at different heating rates, which is discussed below.

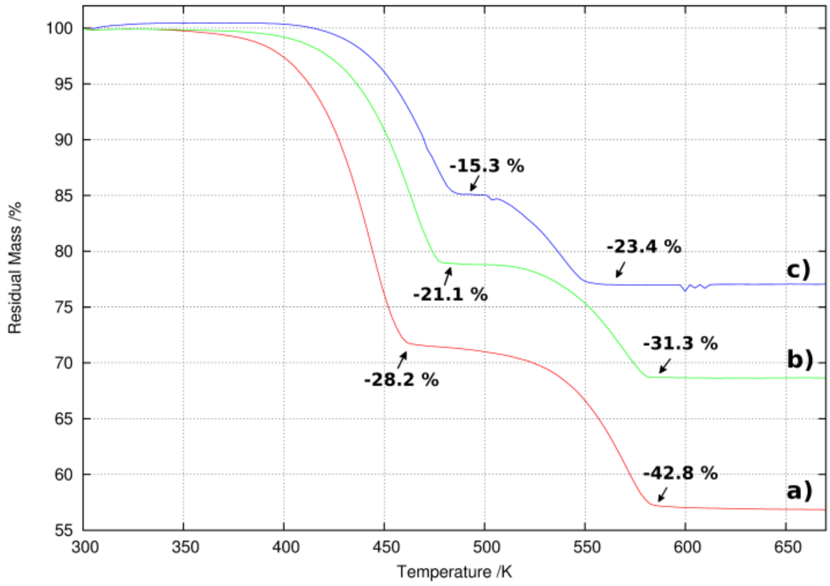

Figure 3.22.: TGA profiles of $[Ni(NH_3)_6]X_2$ where X = (a) Cl, (b) Br and (c) I. The observed mass loss steps are given as relative values in the figure.[64]

TG-DTA-MS analysis

Regarding the thermogravimetric curves for the different hexammine nickel halides (Figure 3.22) it is notable that decomposition is complete below 600 K. The mass losses of the respective steps are close to those calculated for the decomposition of the stoichiometric hexammine nickel halides to the diammines and the pure dihalides (Table 3.4) and hence allow the abstraction of the apparent two-step mechanism *via* the corresponding diammine nickel halide. Another interesting factor when comparing the different halides is the fact that the onset of the first decomposition step is shifted to lower values for the lighter halides while the complete decomposition, *i.e.* the end of the second step, is observed at lower temperatures for the heavier halides.

The chloride compound is discussed in detail with regards to the ambiguities of the decomposition pathway, while the thermal decomposition of the bromide and iodide are included as part of the Kissinger analyses below. The observation of a two-step process in these experiments is also confirmed by the corrsponding differential thermal analyses curves showing only two strong endothermic events correlating with the mass losses in the TG curve (Figure 3.23). The mass spectra of the evolving gas (Figure 3.24) showed that the evolved gas is predominantly ammonia with some traces of nitrogen and hydrogen, but the signals of the latter are almost negligible within the instrument detection limit. Bearing in mind that one viable consumption process for ammonia could be *in situ* cracking at the anode of a solid oxide direct ammonia fuel cell, small impurities of hydrogen and nitrogen, if not avoidable by further tuning of the decomposition process, would not poison the fuel cell. None of the TG-DTA analyses showed any trace of a three-step deammoniation mechanism as suggested in the literature.[60–63] Each could be described as a two-step process in line with the more recent report by Rejitha *et al.*[40] By considering the thermal decomposition curves at a higher temperature ramp (20 K/min) for $[Ni(NH_3)_6]Cl_2$ however (Figure A.4), a further decomposition step becomes evident which appears to be hidden under the second decomposition step at lower heating rates. A study of the thermal decompositions at different heating rates was performed in order to gain further insight and to derive the activation energies of the different steps by applying the Kissinger method.

Table 3.4.: Thermal decomposition (STA)results for $[Ni(NH_3)_6]X_2$ (X = Cl, Br, I) with a heating ramp of 5 K·min^{-1}.

Sample	$n(NH_3)$ final	Mass changes obs.(calc.) /wt.-% Total	Stepwise	TG (STA) Temperatures /K Onset	Final	Peak Temperatures /K DTA	MS
$[Ni(NH_3)_6]Cl_2$	2	28.2 (29.4)	28.2 (29.4)	400	456	448	485
	0	42.8 (44.0)	14.6 (14.6)	547	580	575	587
$[Ni(NH_3)_6]Br_2$	2	21.1 (21.2)	21.1 (21.2)	416	475	468	466
	0	31.3 (31.7)	10.2 (10.5)	532	579	575	588
$[Ni(NH_3)_6]I_2$	2	15.3 (16.4)	15.3 (16.4)	427	482	477	494
	0	23.4 (24.6)	8.1 (8.2)	514	549	543	555

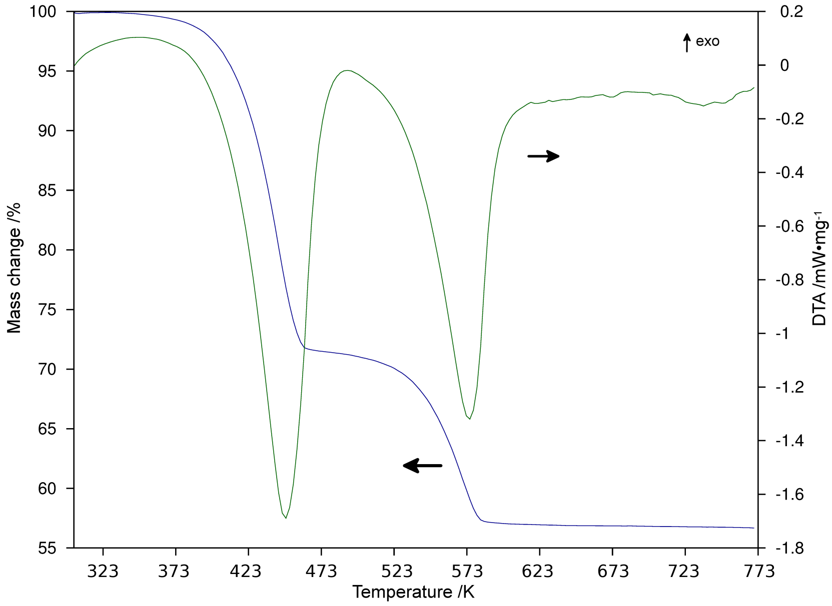

Figure 3.23.: TG-DTA profile for $[Ni(NH_3)_6]Cl_2$ with TG (blue) and DTA (green).[64]

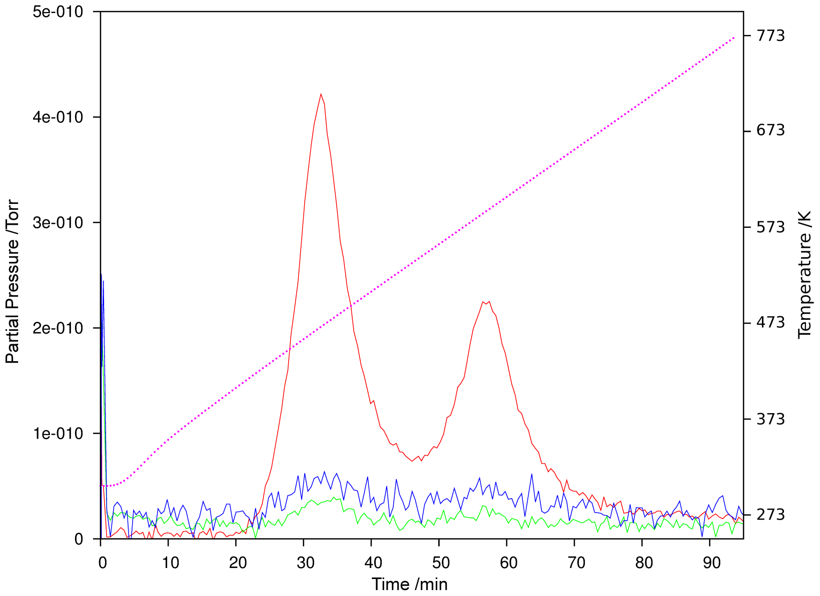

Figure 3.24.: Partial MS spectrum for the evolved gas from the TG-DTA experiment for $[Ni(NH_3)_6]Cl_2$ with m/z = 2 (H_2^+, blue), 17 (NH_3^+, red) and 28 (N_2^+, green). The TG-DTA temperature profile is given by the dotted line (magenta).[64]

Kissinger analyses

When comparing the stepwise decomposition of the different halides, it becomes obvious that their kinetics is slightly different from one another. While the third step in the chloride becomes more and more obvious as a function of increasing heating rates (Figures A.1–A.4), the same is not true for the bromides and iodides (Figures A.5–A.12). No evidence for a third step could be found in these latter cases. It is therefore useful to separate discussion of the results on $[Ni(NH_3)_6]Cl_2$ from the higher halide analogues.

$[Ni(NH_3)_6]Cl_2$ exhibits an apparent two-step decomposition process at lower heating rates (2 K/min and 5 K/min in our experiments) and a three-step process at higher heating rates (10 K/min, 15 K/min and 20 K/min in the experiments presented herein). This behaviour is caused by the merging of the last two steps at the lower heating rates and their greater separation at higher heating rates. Great care has therefore to be taken when treating the results in order to make sure that only those steps with the correct kinetics are used for the calculation of the results. For this reason, the kinetic energies of the two latter steps could only be derived with confidence from the DTA curves at the higher heating rates. The resulting activation energies for the decomposition of the hexammine, the diammine and the monoammine chloride are 77 kJ/mol, 245 kJ/mol and 137 kJ/mol respectively (Figure 3.25, Table 3.5). With the knowledge of these numbers, the reason for the merging of the latter two steps at lower heating rates becomes obvious. Due to the lower activation energy of the monoammine decomposition, its reaction rate is effectively less temperature dependent than that of the diammine decomposition. The deammoniation of the diammine is therefore rate determining at lower heating rates and an instant decomposition of the monoammine to the dihalide follows, as this step is much quicker. It is consequently only at higher heating rates, when the reaction rates of the

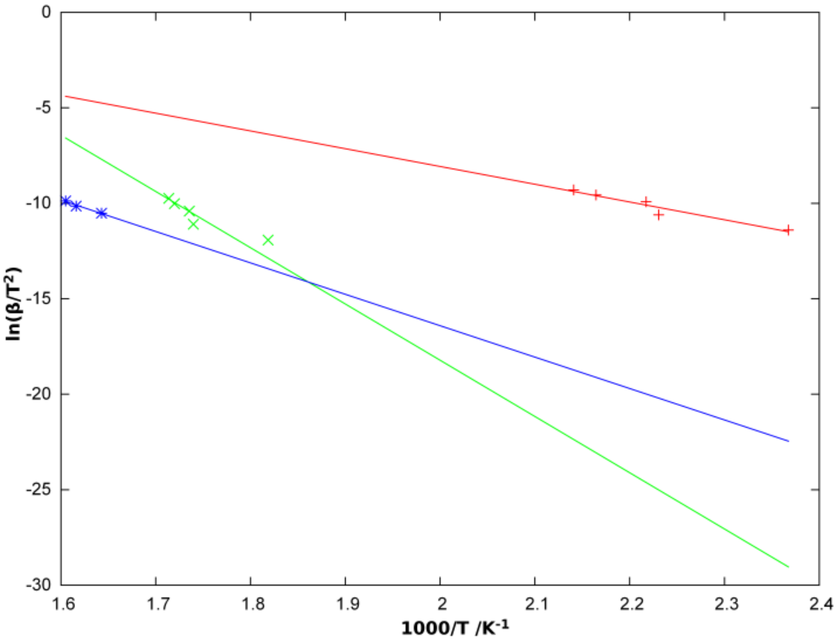

Figure 3.25.: Kissinger plots for the 3 steps in the decomposition of $[Ni(NH_3)_6]Cl_2$ with the hexaammine – diammine step in red (plusses), the diammine – monoammine step in green (crosses) and the monoammine - dihalide decomposition in blue (asterisks). The linear fit is given as a solid line in each case.

diammine and monoammine decomposition become comparable, that the third reaction step becomes visible. This is in fact consistent with the results of prior analyses,[40,61,62] since those identifying a two-step process employed low heating rates[40] and/or large sample sizes (*i.e.* a potential supplementary diffusion control in the kinetics),[62] while the observations of three-step processes were made on small samples at higher heating rates.[61]

Table 3.5.: Analysis of the DTA data for $[Ni(NH_3)_6]Cl_2$ obtained at varied heating rates. The temperatures are the peak temperatures of the DTA signal (Peak 1: hexammine decomposition, peak 2: diammine decomposition and peak 3: monoammine decomposition).[64]

Heating rate /(K/min)	Peak 1 /K	Peak 2 /K	Peak 3 /K
2	422.4	549.9	
5	448.3	574.8	
10	451.0	576.2	608.7
15	462.0	581.5	618.8
20	467.1	583.5	623.1

$[Ni(NH_3)_6]Br_2$ and $[Ni(NH_3)_6]I_2$ decompose in only two steps over the whole range of heating rates probed in this experiment (2 K/min – 20 K/min). One feature was observed for the iodide samples, where a small supplementary weight loss is observed following the complete decomposition of the hexammine to the pure iodide. The corresponding weight loss is too small for a stoichiometric loss of any other molecule and the most likely explanation is a small loss of iodine from the complex. This is reflected in the small constant mass loss after the last decomposition step. Alongside, a sample of the diammine and of the reaction product were stored in a sample vial under argon atmosphere at ambient conditions and a dark colouring of the plastic sample lid (not in physical contact with the sample) after some time further suggests the evolution of some iodine from the samples. The small weight loss (ca. 1 wt.-%) can only be correlated with a small shoulder in the DTA curve at the lowest heating rate. It is therefore unlikely that the overall decomposiion process is strongly influenced by this side process.

The discrepancy in the decomposition pathways between the chloride on the one hand and the bromide and iodide on the other hand can be rationalised when regarding the activation energies of the decomposition steps in the latter. While the activation energies of the hexammine decompositions (Br: 77 kJ/mol; I: 81 kJ/mol) are very much in the range of that of the chloride (77 kJ/mol), the activation energies of the diammine

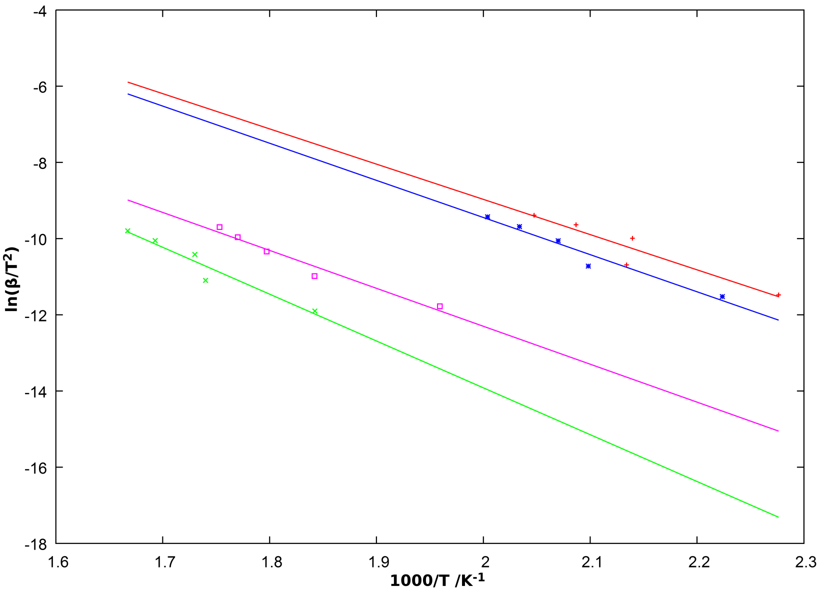

Figure 3.26.: Kissinger plots for the decomposition of $[Ni(NH_3)_6]Br_2$ and $[Ni(NH_3)_6]I_2$ with the hexaammine – diammine step (Br: red plusses; I: blue asterisks), the diammine - dihalide decomposition (Br: green crosses; I: magenta squares). The linear fit is given as a solid line in each case.

decompositions (Br: 102 kJ/mol; I: 83 kJ/mol) are consistently lower than those observed for $[Ni(NH_3)_6]Cl_2$ (Figure 3.26, Table 3.6). Furthermore, no sign of a supplementary intermediate decomposition step could be observed at higher heating rates for the heavier halide analogues (Figures A.5–A.12). It can therefore be concluded that the mechanism in the decomposition of $[Ni(NH_3)_6]Br_2$ and $[Ni(NH_3)_6]I_2$ does in fact only consist of two steps at a heating rate of 20 K/min or below.

Table 3.6.: Analysis of the DTA data for $[Ni(NH_3)_6]Br_2$ and $[Ni(NH_3)_6]I_2$ obtained at varied heating rates. The temperatures are the peak temperatures of the DTA signal (Peak 1: hexammine decomposition, Peak 2: diammine decomposition).

Heating rate /(K/min)	$[Ni(NH_3)_6]Br_2$		$[Ni(NH_3)_6]I_2$	
	Peak 1 /K	Peak 2 /K	Peak 1 /K	Peak 2 /K
2	439.3	542.8	449.7	510.4
5	468.6	574.7	476.6	542.9
10	467.4	578.0	483.1	556.4
15	479.2	590.7	491.7	564.9
20	488.4	599.8	499.0	570.4

3.5.2. *In situ* study of the Decomposition of $[Ni(NH_3)_6]Cl_2$

Two sets of experiments allowed further insight into the thermal decomposition of the hexammine nickel halides upon thermal activation: A complete study of the thermal decomposition while heating under a flow of argon was obtained using a heating chamber on a laboratory X-ray diffractometer and information on the decomposition under pure ammonia atmosphere was obtained as part of the *in situ* ammonia uptake studies at the synchrotron.

Decomposition followed by temperature-programmed XRD

While higher heating rates provoked the formation of monoammine nickel chloride as an intermediate phase (see previous section), no such intermediate could be observed during the *in situ* XRD studies. Also, the temperatures of the decomposition steps are lower compared to the thermal decomposition measurements presented in the previous section. While the thermal analyses presented earlier are measured non-isothermally, *i.e.* the temperature was raised with a constant rate, the *in situ* XRD results presented herein represent a pseudo-isothermal decomposition process. The temperature was raised

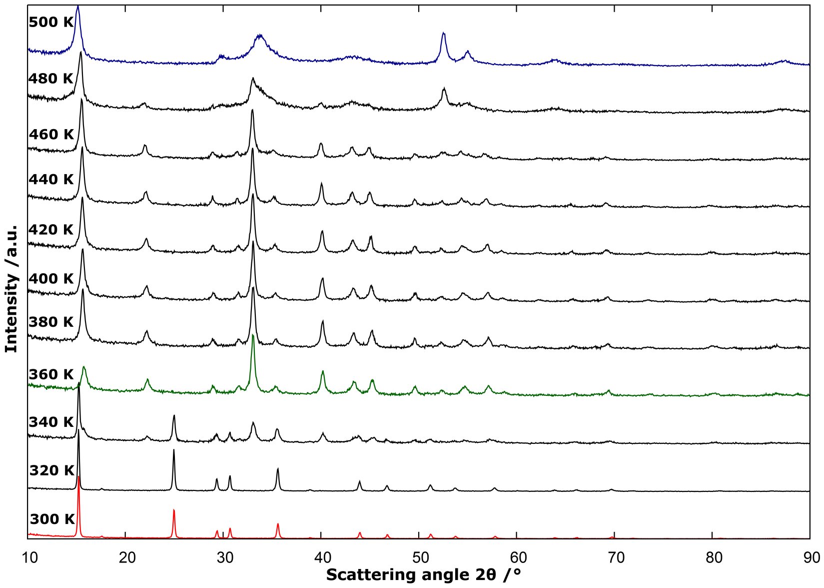

Figure 3.27.: Variable temperature *in-situ* PXD patterns of the thermal decomposition of $[Ni(NH_3)_6]Cl_2$. The measured temperature steps are given. The patterns with the first single phase appearance of each phase are highlighted in colour: $[Ni(NH_3)_6]Cl_2$ (300 K, red), $Ni(NH_3)_2Cl_2$ (360 K, green) and $NiCl_2$ (500 K, blue).

between the individual pattern collections (10 K/min) and kept constant during the measurement of each individual pattern. This resulted in isothermal steps far longer in duration than the heating periods.

The decomposition behaviour observed by *in situ* XRD of the halide samples are very similar (Figures 3.27, A.13 and A.14) and only significantly differ by their decomposition temperatures. None of the three compounds showed evidence for the formation of any other phases but the hexammine, diammine and pure dihalide of the different halides. The decomposition of $[Ni(NH_3)_6]Cl_2$ is discussed as an example (Figure 3.27). As far as $[Ni(NH_3)_6]Cl_2$ is concerned, the hexammine phase remains stable (*i.e.* giving a single phase pattern) until 320 K, while the mass loss onset in the TG profile is observed at 400 K (Table 3.4). The conversion into the diammine phase (the structure of which will be the subject of the next section) is however not completed until 360 K (TG: 456 K) with the pattern at 340 K exhibiting peaks both from the hexammine and the diammine phase.

It is important to note the decrease in crystallinity when approaching the hexammine-diammine phase transition temperature and the restitution of the crystallinity after this transition (as manifested through narrower peaks at higher temperatures). One could assume that the decomposition reaction proceeds during the measurement of the 340 K pattern. This reaction would have to cause significant changes in the relative intensity of the different phases at different measurement angles as the recording of one pattern took ca. 1 hour. Such a behaviour can, however, not be observed. It should therefore be assumed that the reaction at such low temperatures (60 K below the observed onset point in the TG analysis) is relatively slow. This is in line with the rather large activation energy (77 kJ/mol) causing a strong temperature dependence of the reaction rate. The diammine phase remains stable until 460 K and continues to transform into the pure dihalide until 500 K with the pattern at 480 K showing peaks of the diammine phase and the pure dihalide. The pattern of $NiCl_2$ shows a strongly anisotropic peak broadening. While the reflections from planes perpendicular (or nearly perpendicular) to the crystallographic *c*-axis are narrow, the other reflections are much broader, signifying a pronounced stacking disorder of the $[NiCl_{6/3}]$ layers which are parallel to the *ab*-plane.

Decomposition under NH_3 pressure

In contrast to the comparably low decomposition temperatures observed above when heating the sample under a stream of argon, the decomposition temperatures are raised significantly when the surrounding atmosphere is changed to ammonia. Under mild ammonia pressure (1.45 bar) used during the synchrotron *in situ* measurements (at a heating rate of 4 K/min), no decomposition of the hexammine is observed up to 473 K at which point the transformation to the diammine phase starts during a short isothermal step and is completed upon further heating to 483 K (Figure 3.28). The heating limit

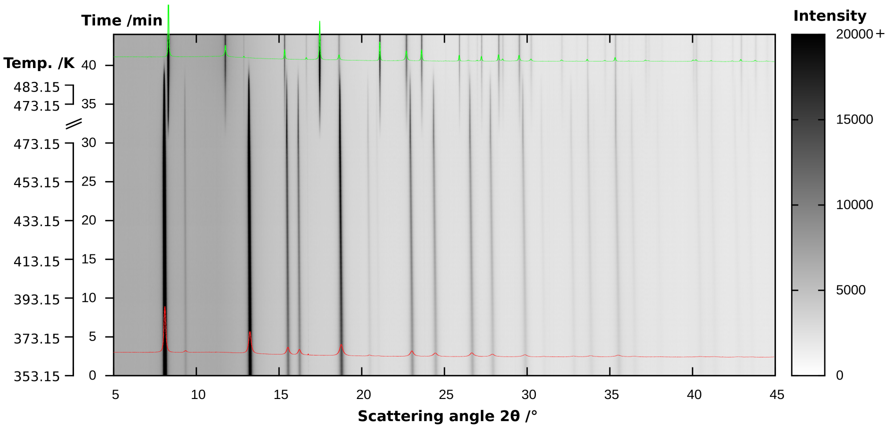

Figure 3.28.: Thermal behaviour of the system $NiCl_2 + NH_3$ under constant ammonia pressure (1.4 bar) followed by in-situ PXD. The patterns of $[Ni(NH_3)_6]Cl_2$ (red) at the start and $Ni(NH_3)_2Cl_2$ (green) at the end are given in the pattern.

of the synchrotron setup used (500 K) did not allow to study further decomposition of the diammine could be probed under the given conditions. This upwards shift of the decomposition temperature under ammonia atmosphere is important for the storage characteristics and has to be taken into account at the design of an ammonia store.

3.5.3. Structures of $Ni(NH_3)_2X_2$ (X = Cl, Br, I)

Although the patterns obtained from the *in-situ* studies of the decomposition of the hexammine structures (see section 3.5.2) are of relatively low quality and therefore not ideal for structural refinement with the Rietveld method, an attempt was made to fit the prior known structures to the obtained patterns. One of the main purposes for this analysis was to determine which form of diammine nickel halide formed under the given conditions. The literature reports two different structures which differ by the internal arrangement of the 1-dimensional $[NiX_{4/2}(NH_3)_2]$ chains. While the β-polymorph is built of chains that are all oriented in the same direction, the chains in the α-polymorph are partly turned by 90° resulting in a situation with two orientations. As a consequence of the

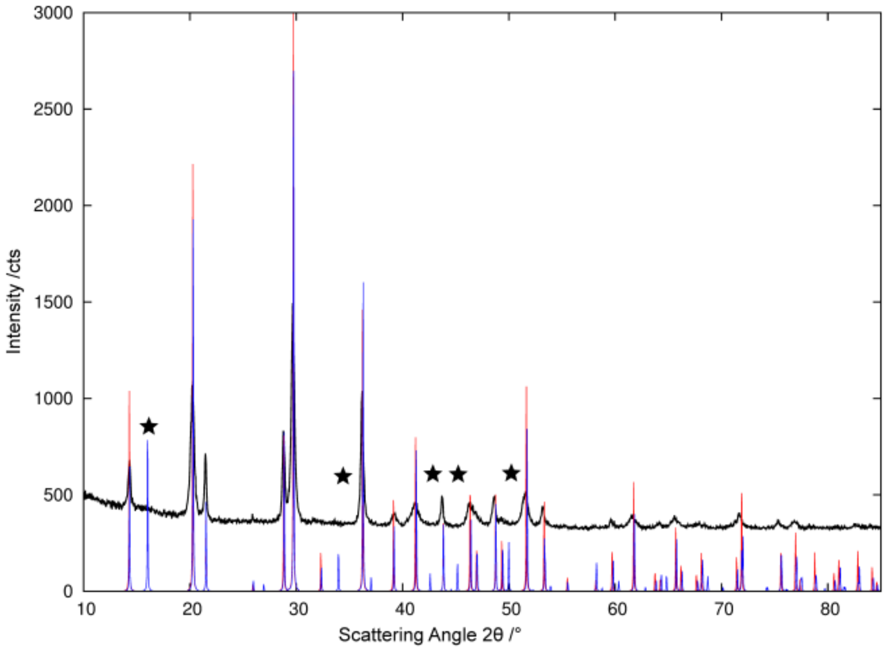

Figure 3.29.: Comparison of the powder pattern of $Ni(NH_3)_2I_2$ with the calculated patterns for α–$Ni(NH_3)_2I_2$ (blue) and β–$Ni(NH_3)_2I_2$ (red). The supplementary peaks of the α-phase (*i.e.* absent in the experimental pattern) are marked with stars.[64]

different packing of chains in the two polymorphs, the distances between the chains and consequently the inter-chain hydrogen bonding are different in the two polymorphs. The α-polymorph has only 2 nearest-neighbour chains (d(Ni–Ni) = 5.8650 Å, all values in this discussion are taken from $Ni(NH_3)_2Br_2$ described by Leineweber and Jacobs[65]) while the β-polymorph has 4 nearest neighbour chains (d(Ni–Ni) = 5.8584 Å). However when looking at the next-nearest neighbour distances, it becomes obvious that the α-polymorph has 4 shortest distances (d(Ni–Ni) = 6.5541 Å) which are significantly shorter than the 2 next-nearest neighbour contacts in β-$Ni(NH_3)_2X_2$ (d(Ni–Ni) = 8.2970 Å). This internal arrangement stabilises the α-polymorph at higher temperatures.

Table 3.7.: Refinement results for the diammine nickel halides.

Formula	**$Ni(NH_3)_2Cl_2$**	**$Ni(NH_3)_2Br_2$**	**$Ni(NH_3)_2I_2$**
Crystal system		Orthorhombic	
Space group		*Cmmm*	
Measurement Temperature /K	373	373	393
***a* /Å**	8.016(3)	8.298(2)	8.726(3)
***b* /Å**	8.030(3)	8.324(2)	8.800(2)
***c* /Å**	3.678(2)	3.8684(7)	4.142(2)
Volume /$Å^3$	236.7(2)	267.20(9)	318.0(2)
Z		2	
Calculated Density, ρ_x /g·cm^{-3}	2.295	3.138	3.618
R_p; wR_p	0.100; 0.134	0.104; 0.126	0.105; 0.134
Goof; X^2	1.67; 2.79	1.56; 2.43	1.21; 1.46
R_{obs} ; wR_2 (all)	0.083; 0.106	0.058; 0.066	0.072; 0.068

Refinement against *in-situ* data

When having a closer look at the powder pattern of the diammine structures, only reflections of the β-phase are appearing in the *in-situ* experiments. Although the calculated patterns of both polymorphs are very similar (Figure 3.29), there are several supplementary reflections, that only exist in the α-phase. None of these additional reflections exist in the experimental patterns of the diammine phases from the *in-situ* experiments (Figure 3.31).

One of the main consequences of the low data quality was the fact that it was impossible to fit a full model to the pattern of the diammine phase and no convergence could be reached when refining the profile function and atomic parameters in the case of $Ni(NH_3)_2Cl_2$. It was therefore chosen to fix the thermal displacement parameters of the atoms in the cell to generic values in order to obtain a reasonable structural model. The

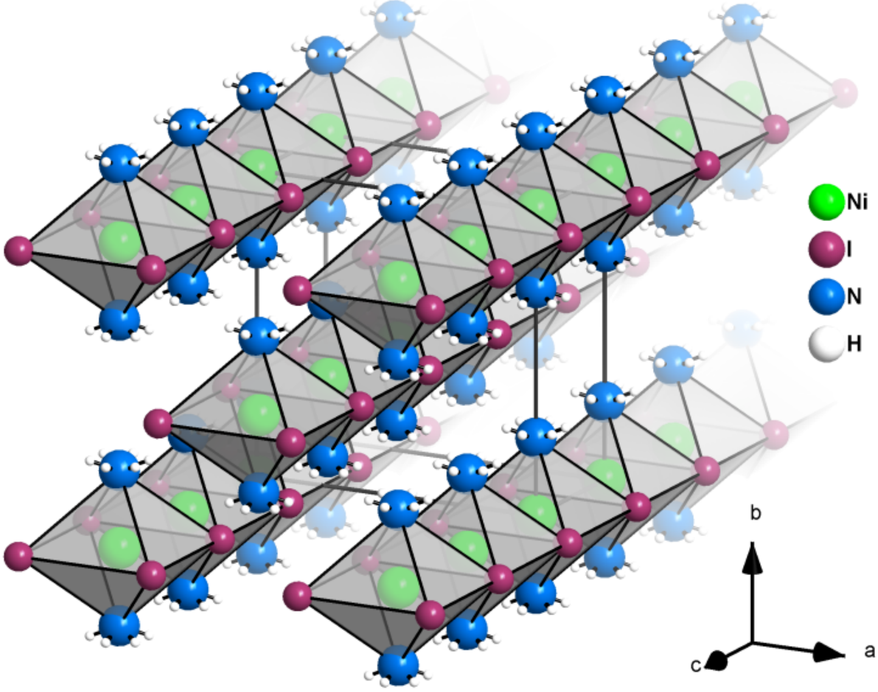

Figure 3.30.: Structure representation for β–Ni(NH$_3$)$_2$I$_2$. The atoms are represented by thermal ellipsoids at the 90 % probability level apart from H which is shown as generic spheres.

structural parameters converged in this model while a remaining shift in parameters was observed for the peak profile functions. The fact that a full refinement converged for the bromide and iodide analogues could be attributed to the stronger anisotropy in electron density (*i.e.* greater differences in the electron counts of the atoms in the unit cell) in these compounds or a more favourable crystallisation of the compounds. This coincides with the fact that heavier atoms contribute stronger to the phase than light atoms and a reasonable estimation of the phase can be obtained when locating the heavy atoms in the structure (as is used for instance in protein crystallography, where heavy cation salts are crystallised to facilitate phasing). Given the difficulties noted, the structural description of Ni(NH$_3$)$_2$Cl$_2$ herein is only a partial model and should not be regarded with the same confidence as a fully refined (and converged) structure. The structure of

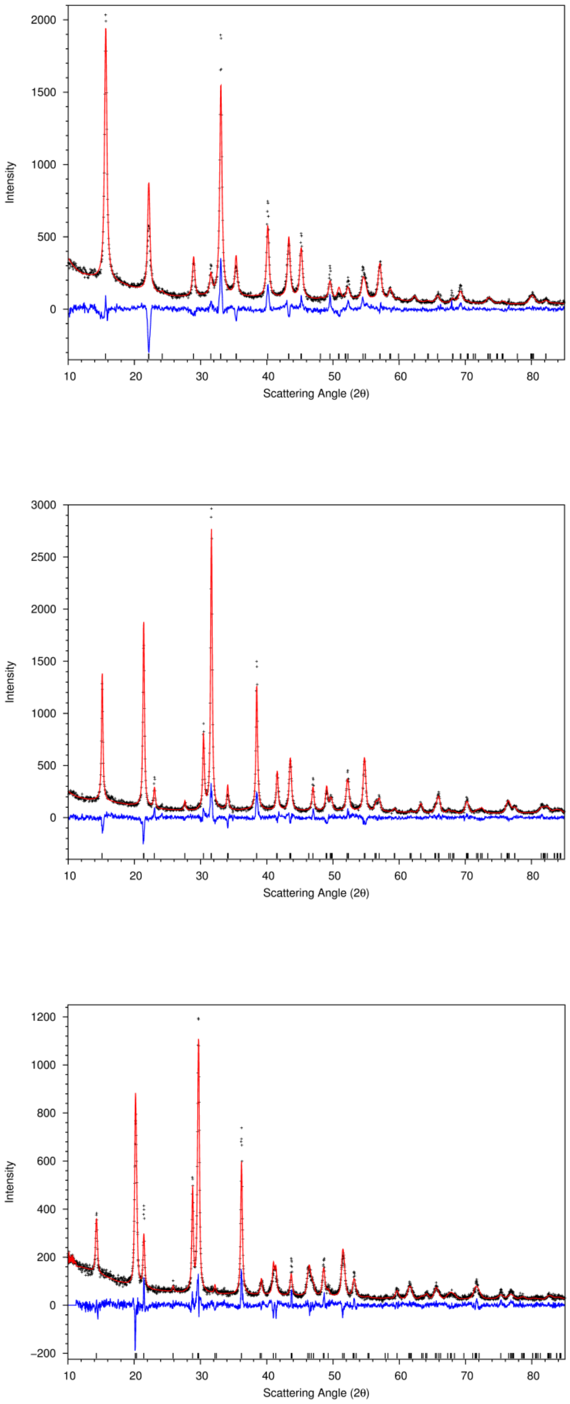

Figure 3.31.: Plot of the Rietveld refinement profiles for $Ni(NH_3)_2X_2$ (X = Cl: top, X = Br: middle, X = I: bottom). Shown are the observed profile (black crosses), the calculated profile (red line), the difference $I_{obs} - I_{calc}$ (blue line) and the calculated peak positions (black ticks).

Table 3.8.: Atom positions and displacement parameters in $Ni(NH_3)_2I_2$ at 393 K.

Atom Site	X	Y	Z	$U_{\mathrm{iso}}/U_{\mathrm{eq}}$ /Å^2
Ni1	0	0	0	0.056(6)
I1	0.2374(5)	0	0.5	0.028(2)
N1	0	0.254(4)	0	0.053(9)
H1n1	-0.000671	0.28655	0.198043	0.0639
H2n1	0.081745	0.28655	-0.097797	0.0639
H3n1	-0.081073	0.28655	-0.100246	0.0639

$Ni(NH_3)_2I_2$ is discussed in some detail here as this is the first full structural refinement of diammine nickel iodide as opposed to the chloride and bromide analogues that have been reported before.[65] The halides are however isostructural to each other and the characteristics presented for the iodide structure apply equally to the other compounds. Where appropriate, the distances in all the halide structures will be discussed and the full details of the refinements can be found in the appendix, sections A.1.8 ff.

Description of $Ni(NH_3)_2I_2$

The structure of $Ni(NH_3)_2I_2$ is composed of 1-dimensional chains ${}^{1}_{\infty}[NiI_{4/2}(NH_3)_2]$ which are arranged parallel to each other in the same orientation (see previous section) and aligned in the [001] direction. The chains themselves are composed of edge-sharing

Table 3.9.: Atomic distances in $Ni(NH_3)_2I_2$ at 393 K.

Atom Site 1	Atom Site 2	Distance /Å
Ni1	I1	2.929(3)
Ni1	N1	2.23(3)
N1	H1n1	0.87

octahedra with iodine atoms located in the equatorial plane and ammonia molecules in the axial positions (Figure 3.30).

The distances between the central nickel atom and the nitrogen atom of the ammonia molecule (d(Ni–N) = 2.23(3) Å, Table A.20) is nearly 0.1 Å longer than in the equivalent hexammine structure (Table 3.2), but this difference is mainly attributable to the different temperatures of the measurements which causes an expansion of the diammine structure measured at 120 °C as opposed to the structure of $Ni(NH_3)_6I_2$ determined at room temperature. A similar behaviour is observed in the bromide analogue (d(Ni–N) = 2.23(2) Å). Leineweber and Jacobs reported Ni–N distances of only 2.091 Å for this compound[65] but these measurements were performed *ex situ* at room temperature and a structural comparison has to consider thermal expansion effects. The structural model of $Ni(NH_3)_2Cl_2$ shows much shorter Ni–N distances of only 2.04(1) Å. This behaviour however is most likely attribuable to the use of generic rather than refined thermal parameters which can slightly influence the atom positions. While the cell size depends mainly on the Ni–X distances since the Ni and X atoms are restricted by symmetry (Table 3.8), the nitrogen position on the c-axis has a high degree of freedom in the refinement and is therefore probably the most sensible indicator for a problematic model. The nickel halide distances in the refinements presented herein (d(Ni–Cl) = 2.562(4) Å, d(Ni–Br) = 2.716(3) Å, d(Ni–I) = 2.929(3) Å, Table A.20) are, again taking thermal expansion into account, consistent with the values reported by Leineweber and Jacobs for the chloride and bromide compounds (d(Ni–Cl) = 2.513(1) Å, d(Ni–Br) = 2.690(1) Å).[65] The general trend of the Ni–X distances and cell parameters in the diammines is comparable to the trend in the hexammine nickel halides (see section 3.4.1).

Infrared spectra

All the bands in the three diammine halides (*ex situ* at room temperature, Figure 3.32) can be assigned to those of the diammine halides as given in the literature (Table 3.5.3). Due to the fact that all bands are caused by NH_3 vibration modes, their position is similar to those in the hexammine compounds, indicating similar bonding environments within the ammonia molecule. The symmetric scissoring mode forms a notable exception for the similarity of the hexammine and diammine IR spectra and is also the strongest band in the diammine compounds. As stated by Eßmann[49], this mode is the most sensitive to the complex bonding of the ammonia molecule. The upshift of over 50 cm^{-1} can therefore be interpreted as a result of the more rigid complex environment both through the inclusion of the heavier chloride anions in the coordination sphere as well as the formation of polymeric chains of complex octahedra. It is furthermore interesting to observe the development of the rocking intensity from the hexammine to the diammine. While the rocking mode is the most intense band in the hexammine, its relative intensity is strongly decreased in the diammine compound. This is an indicator of the impact of the respective coordination environments on the ammonia rotation. The ammonia molecules have a very small barrier to rotation in the hexammine compounds and hence strongly degenerate rocking and stretching modes. In the diammines, however, the rocking modes are less distinct and the stretching bands are narrower.

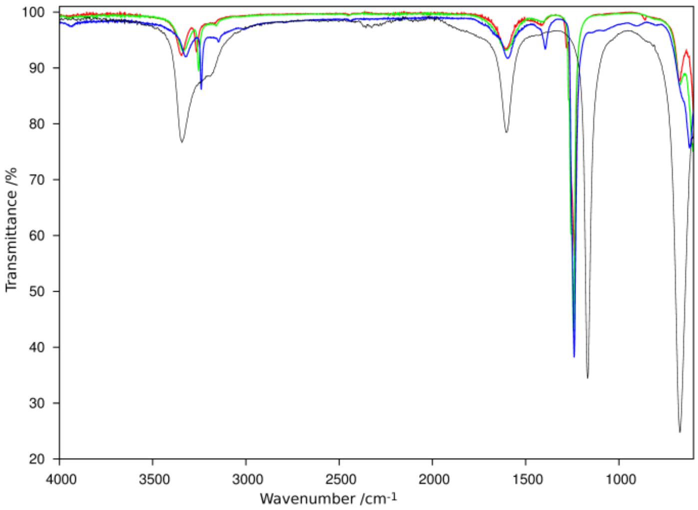

Figure 3.32.: ATR-FTIR spectra for $Ni(NH_3)_2X_2$ where X = Cl (red), Br (green) and I (blue) compared to the spectrum for $[Ni(NH_3)_6]Cl_2$ (black).

Table 3.10.: Maxima and relative intensities of the IR bands for $Ni(NH_3)_2X_2$ compared with the literature values. Wavenumbers are given in cm^{-1}

.

	$Ni(NH_3)_2Cl_2$ [66]	$Ni(NH_3)_2Cl_2$	$Ni(NH_3)_2Br_2$	$Ni(NH_3)_2I_2$
$\nu_a(NH_3)$	3347	3346(2) (m)	3336(2) (m)	3323(2) (m)
$\nu_s(NH_3)$	3264	3265(2) (m)	3254(2)(m)	3239(2) (m)
$2\delta_a(HNH)$	3171	3167(2) (w)	3161(2) (w)	3146(2) (w)
$\delta_a(HNH)$	1611	1607(2) (m)	1604(2) (m)	1596(2)(m)
$\delta_s(HNH)$	1405	1406(2) (w)	1411(2) (w)	1395(2)(m)
$\delta_s(HNH)$	1282	1281(2) (w)	1270/1257(2) (w)	not observed
$\delta_s(HNH)$	1246	1239(2) (vs)	1244(2) (vs)	1240(2) (vs)
$\rho(NH_3)$	675	675(2) (m)	673(2) (m)	660(2) (sh)

vs: very strong, s: strong, m: medium, sh: shoulder, w: weak

3.6. Decomposition of $[Ni(NH_3)_6]Cl_2$ in moist air

The stability of ammonia storage materials in moist air is particularly important in case of accidental contact of the storage material with moist air, *e.g.* through a tank rupture. One could imagine such a situation to happen for instance in the event of a car accident. It would be important in such a case that the lowest amount of NH_3 possible is released into the atmosphere while recovery and safety work are conducted. As can be deduced from Figure 3.33, $[Ni(NH_3)_6]Cl_2$ only decomposes considerably after 5-10 hours making such a recovery easily possible within that time frame. This aspect is a point of crucial importance for the safety aspect when using nickel based ammonia stores as compared to magnesium based ammines. Hanlon showed that $[Mg(ND_3)_6]I_2$ for instance decomposes completely within $\approx$ 120 minutes.[45]

After 10 days of exposure to air, no presence of $Ni(NH_3)_6]Cl_2$ in the sample could be detected by powder X-ray diffraction. Instead, a new phase had formed which could be indexed with the approximate cell parameters $a = 7.70(1)$ Å $b = 7.90(1)$ Å and $c = 7.70(1)$ Å using the three indexing programmes Dicvol[67], Ito[68] and Treor[69]. Further treatments were then made using Jana2006[41]. Firstly, a structureless Le Bail fitting without symmetry constraints (spacegroup $P1$) was performed. However, the angles were fixed to 90 degrees within the refinement. After the initial Le Bail fitting, the spacegroup determination algorithm of Jana2006 was used to determine a tentative spacegroup. Although the cell parameters a and c were very similar to each others and therefore could indicate a tetragonal symmetry, it was chosen not to restrain the system too strongly and the spacegroup was chosen within the Laue-symmetry *mmm*. Together with the fact that the centering algorithm gave a very good fit for a body-centered symmetry, the preliminary spacegroup for the structure solution was set to *Immm*. It

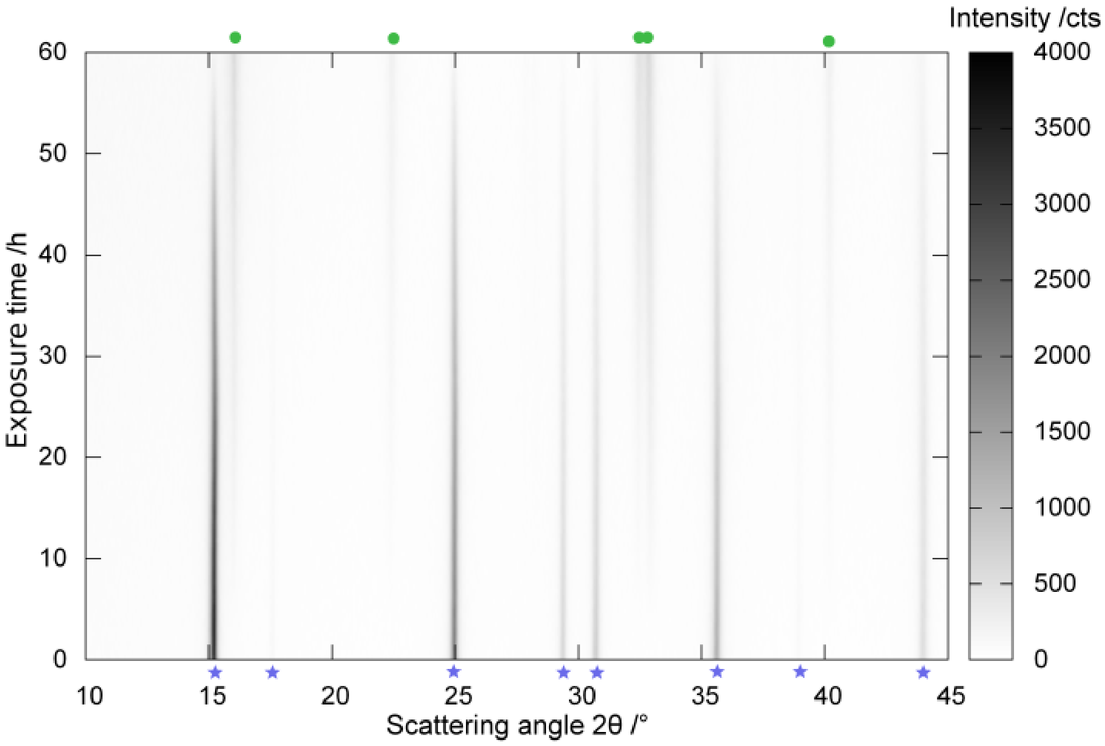

Figure 3.33.: Exposure of $[Ni(NH_3)_6]Cl_2$ to air under ambient conditions followed by time-resolved PXD. The blue stars (bottom) mark $[Ni(NH_3)_6]Cl_2$ and the green circles (top) the phase formed following air exposure.[64]

is to be noted that Superflip[42], used for the structure solution, does not use symmetry information during the crystal structure solution but Jana2006 determines the symmetry elements derived from the structure solution when building up a structure model based on the peak positions from Superflip. This allows a comparison between the space group determination from the structureless Le Bail fitting to the one from the structure solution. Both resulted in the orthorhombic spacegroup *Immm*. The fact that the charge flipping method works with electron density directly rather than an atomic model and attributes atoms to the peaks after the solution proved to be particularly beneficial for the solution of this structure as the composition of the crystal was unknown. Through the assignment of the heaviest atom position as nickel and the second heaviest atom position as chlorine through their relative scattering powers, the identification of the oxygen/nitrogen sites was straightforward, giving the overall contents of the cell. Most important, however, during the structural solution is a continuing assessment of the the chemical sensibility of the structure. The ammonium ion for instance could be refined as a water molecule or even an OH^{-} anion (especially with the limited resolution of a powder pattern) but the nickel atom would have to carry a charge of +4 or even +6 to maintain charge balance in the compound.

As refinement progressed, a supplementary 4-fold symmetry became obvious and the cell was changed to the standard setting in $I4/mmm$ using the following matrix determined with Addsym/Platon[70]:

$$P_{\text{tetragonal}} = \begin{pmatrix} 0 & 0 & -1 \\ 1 & 0 & 0 \\ 0 & -1 & 0 \end{pmatrix} \cdot P_{\text{orthorhombic}} \tag{3.13}$$

with P being any point in the cell. Furthermore, some shoulders and small peaks indicated the existence of a minor phase. This second phase could be identified as NH_4Cl and was subsequently introduced in the refinement. However, the low relative intensity of the “impurity” phase (12(3) vol-%, 10(2) wt.-%) did not allow the stable refinement of a full peak profile function for NH_4Cl and therefore only the Gaussian angle independent broadening width parameter G_w was refined. This overall treatment resulted in the stable refinement of the biphasic system with very reasonable refinement indices and atomic parameters (Figure 3.34, tables 3.11, 3.12, A.25).

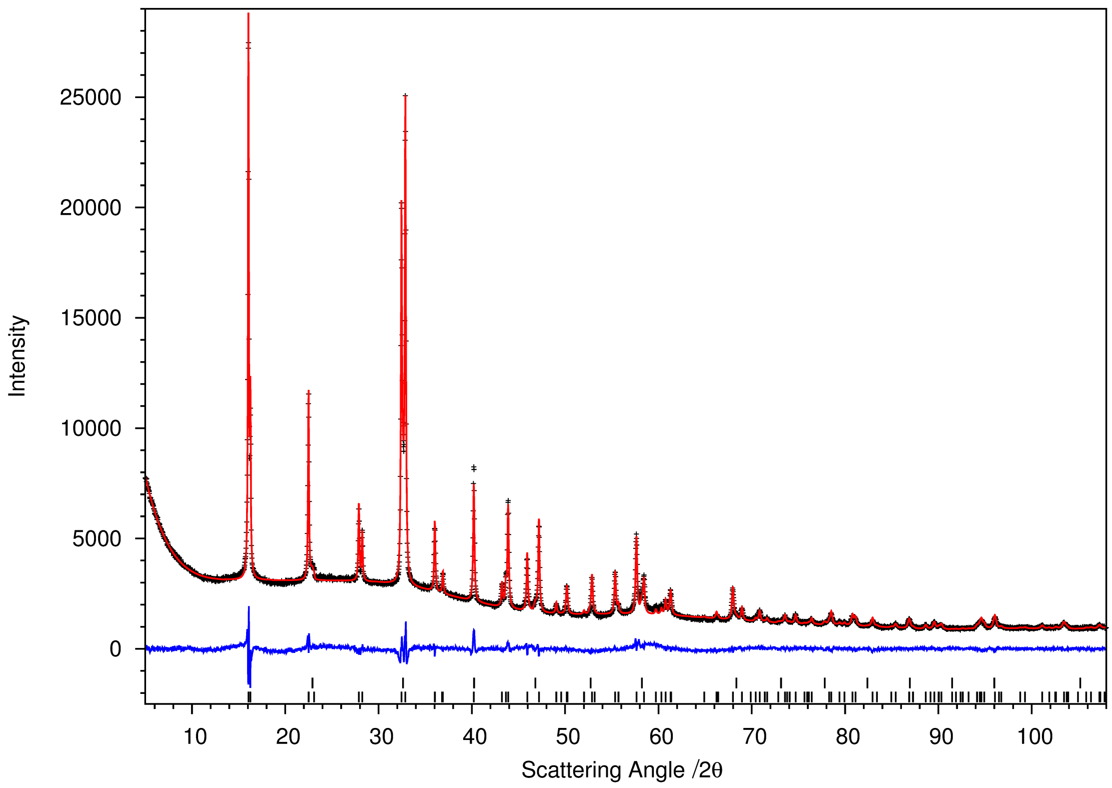

Figure 3.34.: Plot of the Rietveld refinement profile for $(NH_4)_2[NiCl_4(NH_3,H_2O)_2]$. Shown are the observed profile (black crosses), the calculated profile (red line), the difference $I_{\mathrm{obs}} - I_{\mathrm{calc}}$ (blue line) and the peak positions for $(NH_4)_2[NiCl_4(NH_3,H_2O)_2]$ (black ticks, bottom) NH_4Cl (black ticks, top).

Table 3.11.: Results for the refinement of the decomposition products $(NH_4)_2[NiCl_4(NH_3,H_2O)_2]$ and NH_4Cl.

Formula	**$(NH_4)_2[NiCl_4(NH_3,H_2O)_2]$**	**NH_4Cl**
Crystal system	Tetragonal	Cubic
Space group	$I4/mmm$	$Fm\bar{3}m$
a **/Å**	7.6981(5)	3.878(2)
c **/Å**	7.8961(8)	3.878(2)
Volume /Å^3	467.93(7)	58.32(5)
Z	2	1
Calculated Density, ρ_x /g·cm^{-3}	1.9348	1.5231
R_p; wR_p	0.028; 0.039	
Goof; $\mathscr{X}^2$	1.84; 3.39	
R_{obs} ; wR_2 **(all)**	0.045; 0.054	0.038; 0.048

Table 3.12.: Atom positions and displacement parameters in $(NH_4)_2[NiCl_4(NH_3,H_2O)_2]$

Atom Site	X	Y	Z	U_{iso}/U_{eq} /Å^2
Ni1	0	0	0	0.016(6)
Cl1	0.2303(8)	0.2303(8)	0	0.014(4)
O1	0	0	0.260(4)	0.046(15)
N1	0	0.5	0.25	0.027(18)
H1o1	–0.077639	0.049818	0.31527	0.0554
H1n1	0.408(15)	0	0.186(10)	0.04(3)

3.6.1. Description of the structure of ammonium di(ammine/aqua)-tetrachloro-nickelate(II)

The structure of $(NH_4)_2[NiCl_4(NH_3,H_2O)_2]$ consists of NH_4^+ cations and complex $[NiCl_4(NH_3,H_2O)_2]^{2-}$ anions (Figure 3.35). While the cations are surrounded tetrahedrally by complex anions, the latter are themselves surrounded by eight cations in a cubic arrangement. This cation-anion arrange can be understood as an anti-fluorite type[71] which is distorted from the cubic fluorite type (respectively anti-fluorite type, $Fm\bar{3}m$) to a tetragonal substructure ($I4/mmm$) due to the different bonding lengths in the complex anion and the therefore anisotropic ligand environment. The octahedral anion is distorted from the ideal structure due to the square-planar arrangement of the Cl^- ligands which have a longer bonding distance (d(Ni–Cl) = 2.513(1) Å) than the capping (NH_3,H_2O) ligands (d(Ni–O) = 2.06(3) Å). These distances are very similar to those refined in the prior structure determination of $(NH_4)_{2\text{-}2z}[Ni(NH_3)_2]_z[NiCl_4(NH_3)_2]$ (d(Ni–Cl) = 2.4981(7) Å, d(Ni–O) = 2.055(3) Å) reported by Leineweber.[71] The hydrogen positions of the aqua-ligand were generically set to yield a value of d(O–H) = 0.82 Å as suggested by the refinement programme Jana2006.[41] In contrast, the hydrogen position of the ammonium ions was found from the difference Fourier-map and could be varied in the latter stages of the refinement using a constraint for the thermal displacement parameter of the hydrogen atom, which was fixed as:

$$U_{\text{iso}}(\text{H}) = 1.5 \cdot U_{\text{iso}}(\text{N}) \tag{3.14}$$

where $U_{\text{iso}}(\text{H})$ is the thermal displacement of the hydrogen atom of the ammonium ion and $U_{\text{iso}}(\text{N})$ the displacement parameter of the corresponding nitrogen atom. Constraining the thermal parameter for hydrogen is common practice as its scattering power does not

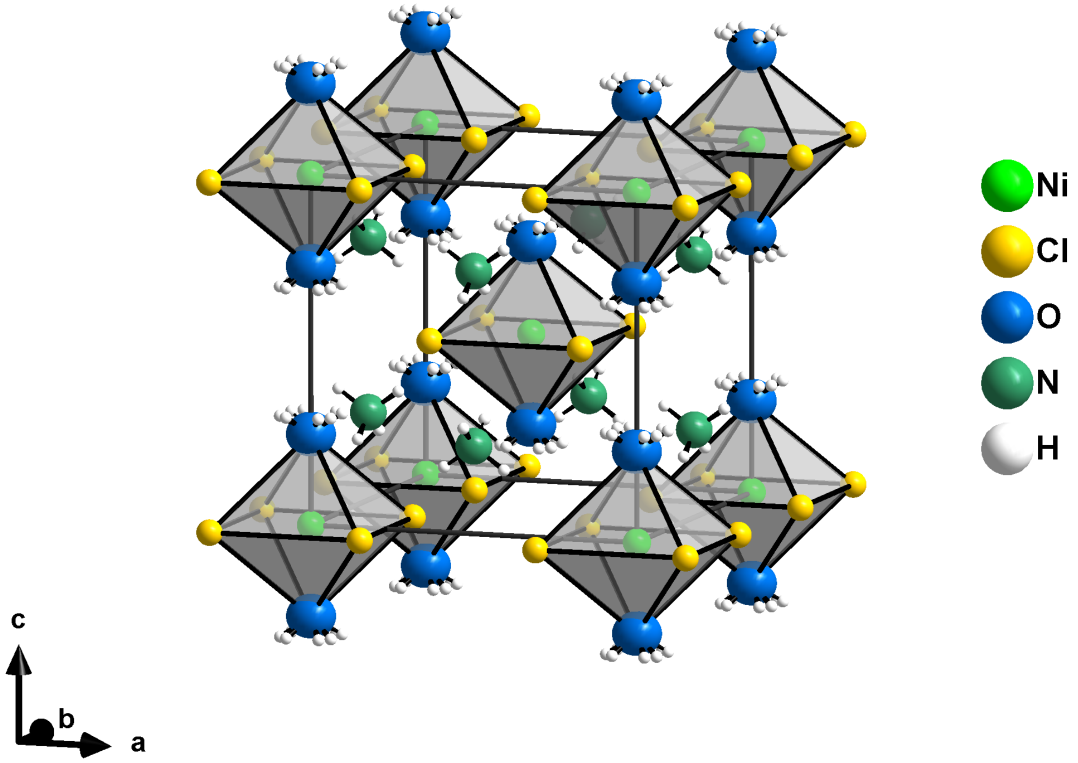

Figure 3.35.: Representation of the cell of $(NH_4)_2[NiCl_4(NH_3,H_2O)_2]$. The atoms of Ni (green), Cl (gold), O (blue) and N (green) are represented by 90 % of their spatial probability. The H atoms (white) are given as generic balls.

suffice for the exact determination of the thermal displacement parameters. The factor of 1.5 was taken as it is the standard value in SHELXL for the expansion of hydrogen atoms and was preferred over the standard value in Jana2006 (1.2) to account for the greater degree of rotational freedom of the ionic ammonium atoms as opposed to a bound ligand molecule.

It is important compare the result above with the refinements of an apparently similar compound $(NH_4)_2(NH_3)_x[Ni(NH_3)_2Cl_4]$ by Meyer and Nockemann[72], leter reinterpreted as $(NH_4)_{2-2z}[Ni(NH_3)_2]_z[Ni(NH_3)_2Cl_4]$ by Leineweber.[71] The structure determinations of the nickel ammonia chloro compounds as given in the literature, contained supplementary electron density on $(0,\frac{1}{2},0)$, which cannot be found in the structure described here (Figure 3.36). Meyer and Nockemann interpreted this electron density as interstitial ammonia molecules that are not bound as ligands.[72] The distance to the neighbouring ammonium ions is however very short (d(N–N) = 1.99 Å) and provided the motivation for the re-interpretation by Leineweber[71] who attributed the supplementary electron density to a partial occupation of Ni. The placement of the supplementary nickel atom at $(0,\frac{1}{2},0)$ was rationalised with an exchange of the neighbouring ammonium ions (above and below) for ammonia molecules to maintain charge balance. The consequence of this supplementary nickel atom is therefore the formation of a three-membered chain of $[NiCl_4(NH_3)_2]$ octahedra connected through common chlorine edges. Considering the structure of $Ni(NH_3)_2Cl_2$ which is composed of 1-dimensional chains $^1_\infty[NiCl_{4/2}(NH_3)_2]$, the compound described by Leineweber can be understood as a partial intermediate between the purely anionic complexes found herein and the polymeric chains in $Ni(NH_3)_2Cl_2$.

3.6.2. Considerations of the sample composition and the reaction pathway

One of the major issues with the reaction products as refined from the powder pattern of the product is the refined Ni:Cl ratio in $(NH_4)_2[NiCl_4(NH_3,H_2O)_2]$ (1:4) as compared to the ratio in the starting material $[Ni(NH_3)_6]Cl_2$ (1:2). This deviation is even stronger when taking the ammonium chloride phase into account, which increases the Cl:Ni ratio to >4. It is, however, difficult to envisage a gaseous Ni-compound which could evaporate from the sample to account for the “loss of nickel”. Also, the molar ratio as determined by

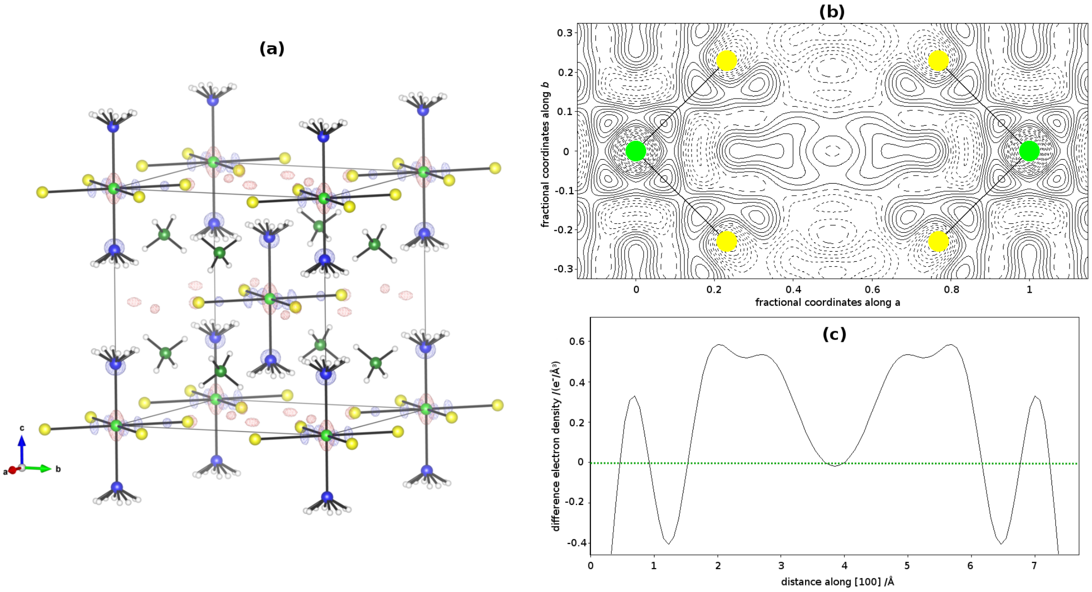

Figure 3.36.: **(a)** Difference electron density iso-surfaces (±0.6 e$^-$/Å^3) in the unit cell of $(NH_4)_2[NiCl_4(NH_3,H_2O)_2]$(blue: positive, red: negative); **(b)** Difference electron density map in the (110) plane (±0.1 e$^-$/Å^3 isolines, solid: positive, dashed: negative); **(c)** Difference electron density plot from the origin along [100]. The atoms are given as balls-and-sticks; Ni in green, Cl in yellow, O in blue, N in green and H in white.

elemental analysis (1:1.98, Table 3.14)), is more consistent with the stoichiometry of the starting material than of the crystalline products as identified from PXD. It must therefore be concluded that some X-ray amorphous Ni compounds were formed most likely nickel hydroxides and/or nickel oxides. Hydroxide formation is perhaps most likely given that the reaction of the ammonia ligand in the starting hexammine to form ammonium ions in the reaction product requires a proton-donor for the proton transfer. Water (from air) is the most likely candidate for this as no other proton donor could be identified in the reaction mixture and because $[Ni(NH_3)_6]Cl_2$ remains stable in the inert atmosphere of the glovebox over long periods of time.

The presence of hydroxides can also be presumed from the characteristic shoulder at 3640 cm^{-1} in the FTIR spectrum of the product (Figure 3.37, Table 3.13). Also, the notable background in the region 3000–3600 cm^{-1} may be due to a broad water peak.

Table 3.13.: FTIR spectrum band assignment of the end product of the decomposition of $[Ni(NH_3)_6]Cl_2$ in moist air.

Wavenumber /cm^{-1}	$Ni(NH_3)_2Cl_2$ [64]	NH_4Cl [73]	$Ni(OH)_2$ [74]	$NiCl_2 \cdot 6\,H_2O$ [75]
3641(2) (sh)			3635 $\nu(OH)$	
3350(2) (w)	3346 $\nu_{as}(NH_3)$			
3259(2) (w)	3265 $\nu_s(NH_3)$			
3133(2) (m)		3138 $\nu_3(NH_4^+)$		
3046(2) (m)		3041 $\nu_1(NH_4^+)$		
2819(2) (w)		1400·2 2·ν_4		
1624(2) (m)	1607 $\delta_a(HNH)$			1624, 1656 ν_2
1410(2) (s)		1400 ν_4		
1247(2) (s)	1239 $\delta_s(HNH)$			

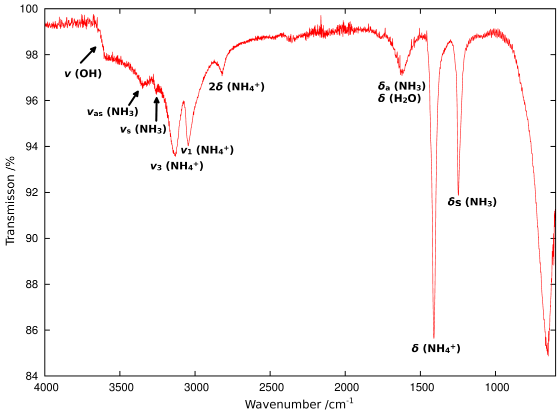

Figure 3.37.: FTIR spectrum of the end product of the decomposition of $[Ni(NH_3)_6]Cl_2$ in moist air.

In order to determine the overall composition of the sample, elemental analyses of the reaction mixture were performed on the elements Ni, Cl, N and H (Table 3.14). While the

Table 3.14.: Results of the elemental analyses of the decomposition product of $[Ni(NH_3)_6]Cl_2$ in moist air.

Element	content /wt.-%	Determination method
Ni	29.62±0.4	Atomic absorption spectroscopy
Cl	35.48±0.4	Microtitration
N	10.75±0.3	CHN combustion analysis
H	3.74±0.3	CHN combustion analysis

microanalyses for N and H were done in the solid state and directly determined the weight fraction in the title compound, the analyses for Ni and Cl were performed in solution. For this, 6.2 mg of the reaction product were dissolved in 25 ml 0.01 M HNO_3. The concentrations determined by atomic absorption spectrometry (for Ni) and coulometric Ag titration (for Cl^-) could therefore be re-calculated directly as weight fractions in the solid product. A way to estimate the phase fractions from the overall composition of the reaction mixture is to employ a system of equations that relate the elemental content of the individual compounds to the elemental contents in the reaction mixture. A model with five variables can be established where:

- a is the weight fraction of $(NH_4)_2[NiCl_4(NH_3)_2]$;
- b is the weight fraction of $(NH_4)_2[NiCl_4(H_2O)_2]$[‡];
- c is the weight fraction of NH_4Cl;
- d is the weight fraction of residual Ni;
- e is the weight fraction of residual H.

With these variables, four equations can be established from the elemental contents of Ni, Cl, N, and H:

$$w_{Ni,a} \cdot a + w_{Ni,b} \cdot b + w_{Ni,c} \cdot c + w_{Ni,d} \cdot d + w_{Ni,e} \cdot e = w_{Ni} \tag{3.15}$$

$$w_{Cl,a} \cdot a + w_{Cl,b} \cdot b + w_{Ni,c} \cdot c + w_{Cl,d} \cdot d + w_{Cl,e} \cdot e = w_{Cl} \tag{3.16}$$

$$w_{N,a} \cdot a + w_{N,b} \cdot b + w_{Ni,c} \cdot c + w_{N,d} \cdot d + w_{N,e} \cdot e = w_N \tag{3.17}$$

$$w_{H,a} \cdot a + w_{H,b} \cdot b + w_{Ni,c} \cdot c + w_{H,d} \cdot d + w_{H,e} \cdot e = w_H \tag{3.18}$$

[‡] The ammine and the aqua complexes are treated as individual paramaters in the system of equations in order to be able to determine the relative ratio of ammonia and water in the ligand sphere, while they are indistinguishable from X-ray diffraction, they are different in their elemental composition and therefore can be determined on this way

where $w_{Element}$ are the observed weight fractions for the four measured elements and $w_{Element,letter}$ are the calculated weight fractions for the individual component compounds. Substituting the known values therefore leads to the following system of equations:

$$0.21697 \cdot a + 0.21538 \cdot b + 0 \qquad + d + 0 = 0.2962 \tag{3.19}$$

$$0.52423 \cdot a + 0.52038 \cdot b + 0.66323 \cdot c + 0 + 0 = 0.3548 \tag{3.20}$$

$$0.20703 \cdot a + 0.10276 \cdot b + 0.26193 \cdot c + 0 + 0 = 0.1075 \tag{3.21}$$

$$0.05176 \cdot a + 0.04404 \cdot b + 0.07484 \cdot c + 0 + e = 0.0374 \tag{3.22}$$

A system of four linear equations with four equations and five variables is not exactly solvable. Two ways are possible to tackle this problem: The number of variables could be reduced to four by combining d and e into one variable for a fixed compound, *i.e.* by fixing the Ni:H ratio to 1:2 as in $Ni(OH)_2$. This inflexible assumption does not allow for the existence of NiO or non-stoichiometric (O,OH) mixtures or compounds. A better solution is to add more data equations derived from chemical and crystallographic knowledge of the sample to the system of equations.. The first assumption is based on the knowledge that the Ni:Cl molar ratio in the reaction mixture remains stable at 1:2 and therefore the following equation must be valid providing no other Cl containing compound is present in the product:

$$2 \cdot \left(\frac{1}{M_a} \cdot a + \frac{1}{M_b} \cdot b + \frac{1}{M_d} \cdot d \right) = \frac{4}{M_a} \cdot a + \frac{4}{M_b} \cdot b + \frac{1}{M_c} \cdot c \tag{3.23}$$

$$2 \cdot \left(\frac{1}{270.49} \cdot a + \frac{1}{272.49} \cdot b + \frac{1}{58.69} \cdot d \right) = \frac{4}{270.49} \cdot a + \frac{4}{272.49} \cdot b + \frac{1}{53.45} \cdot c \tag{3.24}$$

The division by the molar mass is necessary to convert the weight fractions of the compounds into a molar quantity. Although this quantity is still in units of mol/g, the overall mass in the denominator is constant for all of the values and therefore constant in the calculations. Although five equations would be sufficient for five variables to determine one exact solution, the use of more than five equations can be beneficial. Instead of solving the system of equations exactly, it is fitted using a least-squares algorithm and the more equations that are used, the better is the potential precision of the model and the validity of all equations can be assessed through the residual sum of squares.

Using the crystallographic data obtained from the Rietveld refinement, the phase ratio refined in volume fractions and converted in weight fractions by Jana2006 of $(NH_4)_2[NiCl_4(NH_3/H_2O)_2]$ to NH_4Cl can be taken into account as:

$$a + b = 9 \cdot c \tag{3.25}$$

The final assumption for the system of equations is, that the elements Ni, Cl, N and H should not be contained in any other compounds but the five compounds under consideration. The sum of weight fractions of those five compounds must therefore add up to the overall sum of the elemental weight fractions ($w_{Ni} + w_{Cl} + w_N + w_H = 0.7959$). A factor has to be introduced, though that accounts for the fact that $(NH_4)_2[NiCl_4(H_2O)_2]$ contains oxygen, namely the ratio between the molar weight and the sum of Ni, Cl, N and H in the compound ($\frac{M_{Ni}+4\cdot M_{Cl}+2\cdot M_N+12\cdot w_H}{M_b} = 0.8826$) to yield the overall formula:

$$a + 0.8826 \cdot b + c + d + e = 0.7959 \tag{3.26}$$

Taking the equations (3.19)–(3.22), (3.24), (3.25) and (3.26), the system was fitted with a least-squares fit with the Python numpy module.[76] This contains a linear matrix least-square fit (numpy.linalg.lstsq) for the solution of linear equation systems which was fed with the linear equation system in matrix form:

$$\begin{bmatrix} 0.21697 & 0.21538 & 0 & 1 & 0 \\ 0.52423 & 0.52038 & 0.66323 & 0 & 0 \\ 0.20703 & 0.10276 & 0.26193 & 0 & 0 \\ 0.05176 & 0.04404 & 0.07484 & 0 & 1 \\ \frac{2}{270.49} & \frac{2}{272.49} & \frac{1}{53.45} & -\frac{2}{58.69} & 0 \\ 1 & 1 & -9 & 0 & 0 \\ 1 & 0.88256 & 1 & 1 & 1 \end{bmatrix} \cdot \begin{bmatrix} a \\ b \\ c \\ d \\ e \end{bmatrix} = \begin{bmatrix} 0.2962 \\ 0.3548 \\ 0.1075 \\ 0.0374 \\ 0 \\ 0 \\ 0.7959 \end{bmatrix} \tag{3.27}$$

The very low residual sum of squares (RSS $= 7.256 \cdot 10^{-9}$) shows that the found solution is in close agreement to the chemical and crystallographic information used to establish the system of equation and makes the result reliable. The solution of the equation system is as follows, giving the weight fractions of the different products:

$$\begin{bmatrix} a \\ b \\ c \\ d \\ e \end{bmatrix} = \begin{bmatrix} 0.27797 \\ 0.31747 \\ 0.06616 \\ 0.16751 \\ 0.00408 \end{bmatrix} \tag{3.28}$$

The knowledge of the weight fractions in isolation however is of limited use as it does not allow the comparison of the stoichiometries directly. It is further impossible to convert the weight fractions into molar fractions directly as the overall molar mass of the mixture needed for the conversion is unknown. Given that the mass of the mixture is constant, however, allows the conversion of the weight fractions in a molar quantity that is similar to the molality in solutions. In analogy to the definition of molality as $b = \frac{n_{\text{compound}}}{m_{\text{solvent}}}$, the quantity F shall be defined as the number of moles of the component per mass of mixture, $F = \frac{n_{\text{compound}}}{m_{\text{mixture}}}$. F is of great help, because it allows calculation of the molar ratio of the different compounds in the reaction mixture and is easily derived by dividing the weight fraction by the molar masses of the respective pure compounds:

$$F = \begin{bmatrix} w_i \end{bmatrix} \frac{\text{g}}{\text{g}} \cdot \begin{bmatrix} \frac{1}{M_i} \end{bmatrix} \frac{\text{mol}}{\text{g}} \tag{3.29}$$

$$F = \begin{bmatrix} 0.27797 \\ 0.31747 \\ 0.06616 \\ 0.16751 \\ 0.00408 \end{bmatrix} \frac{\text{g}}{\text{g}} \cdot \begin{bmatrix} \frac{1}{270.49} \\ \frac{1}{272.49} \\ \frac{1}{53.45} \\ \frac{1}{58.69} \\ \frac{1}{1.01} \end{bmatrix} \frac{\text{mol}}{\text{g}} = \begin{bmatrix} 1.028 \cdot 10^{-3} \\ 1.165 \cdot 10^{-3} \\ 1.238 \cdot 10^{-3} \\ 2.854 \cdot 10^{-3} \\ 4.040 \cdot 10^{-3} \end{bmatrix} \frac{\text{mol}}{\text{g}} \tag{3.30}$$

This finally allows the establishment of the molar ratios of the different compounds (with $a + b \overset{!}{=} 1$):

$$\begin{array}{ccccccccc} (NH_4)_2[NiCl_4(NH_3)_2] & : & (NH_4)_2[NiCl_4(H_2O)_2] & : & NH_4Cl & : & Ni & : & H \\ 0.469 & : & 0.531 & : & 0.565 & : & 1.301 & : & 1.842 \end{array}$$

The primary information to get from these calculations is the molar ratio of ammonia to water ligands in $(NH_4)_2[NiCl_4(NH_3/H_2O)_2]$. The NH_3-to-H_2O ratio in $(NH_4)_2[NiCl_4(NH_3/H_2O)_2]$ is nearly 1:1 allowing the formulation of the overall equation of the main decomposition product derived from crystallographic and elemental analysis information as

$(NH_4)_2[NiCl_4(H_2O)_{1.06}(NH_3)_{0.94}]$. Furrthermore the ratio of the residual Ni content and the residual H content of 1:1.416 would be consistent with a non-stoichiometric hydroxide/oxide mixture as the Ni:H ratio is smaller than in stoichiometric nickel hydroxide $Ni(OH)_2$ (1:2) alone. The molar ratios permit an equation for the reaction of $[Ni(NH_3)_6]Cl_2$ in humid air to be formulated. Based only on the molar ratio of $(NH_4)_2[NiCl_4(H_2O)_{1.06}(NH_3)_{0.94}]$ to NH_4Cl (7.08:4, rounded to 7:4 for the further calculations) as a reference,[§] the following reaction formula can be derived:[¶]

$$16[Ni(NH_3)_6]Cl_2 + 25H_2O \longrightarrow 7(NH_4)_2[NiCl_4(H_2O)(NH_3)] + 4NH_4Cl + 9Ni(OH)_2 + 59NH_3\uparrow$$

It is notable, that the $(NH_4)_2[NiCl_4(H_2O)_{1.06}(NH_3)_{0.94}]$:$Ni(OH)_2$ ratio derived from this equation (1:1.286) is very much in agreement with that solved from the equation system (1:1.301). This is a clear evidence for the consistency of the calculations and shows therefore that the calculations based on the elemental analyses can be taken as a trustworthy source of information for the overall reaction. Also the weight fractions calculated from this derived equation are in strong agreement with the values measured and only differ by ≤ 3 % for the different elements (Table 3.15). This is particularly interesting as the derived values are calculated for stoichiometric $Ni(OH)_2$ and therefore introduce a small systematic error on the hydrogen content as compared to the presumably non-stoichiometric mixture of $NiO/Ni(OH)_2$ assumed from the system of equations.

Concerning the reaction mechanism and most importantly the proton transfer from the water molecules to the ammonia molecules, it is unlikely that this would happen in

---

[§] This ratio was preferred as reference as it is based on chemical analysis and Rietveld refinement and therefore most reliable.

[¶] The NH_3:H_2O ratio in the complex compound is set to 1:1 instead of 0.94:1.06) and the remaining Ni content was expressed as $Ni(OH)_2$ for reasons of simplicity

Table 3.15.: Comparison of measured and calculated elemental weight fractions of the decomposition product of $[Ni(NH_3)_6]Cl_2$ in moist air.

Element	Content /wt.-% (meas)	Content /wt.-% (from reaction equation)
Ni	29.62	31.86
Cl	35.48	38.49
N	10.75	11.87
H	3.74	3.77

a pure gas-solid reaction. It is instead most likely that the reaction process involves an intermediate solution stage. The reaction pathway can in this case be imagined as follows: Water initially entering the complex will replace some of the ammonia ligand simply due to its higher partial pressure in the gas phase. The leaving ammonia molecules, however, will remain in the proximity and, due to the high hygroscopicity of ammonia, will attract some water molecules to form highly alkaline droplets of $NH_3/H_2O/NH_4OH$ which can act as *in situ* solvent for the formation of the ammonium and hydroxide ions in the reaction mixture. Such a behaviour may be detectable in a long-term spectroscopic experiment where one could observe the appearance/disappearance of water related vibration bands as a function of time.

3.7. Conclusions

Ammonia and nickel halides react readily at ambient conditions yielding the hexammine nickel halides as sole product. The uptake reaction is quick and a loading of 50 % is reaching within little more than two minutes. Full loading is reached at ambient pressure making the use of high pressures unnecessary. The crystal structures of the hexammine nickel halides have been re-assessed and the prior known structure could be validated by Rietveld refinements. The use of *in situ* data allowed the mechanistic study of the ammonia uptake and proved that it is a pure one step reaction. The *in situ* data furthermore allowed the study of the development of the crystallite sizes after the reaction and showed that grain boundaries vanish yielding in larger crystallite sizes after a ripening time. The data presented herein proves that this system is likely to be a promising ammonia store and further studies in the next chapter should underline this.

The thermal decomposition of the nickel halide hexammines in this study show a clean release behaviour from the hexammine in a two-step process (for X = Br, I) or a three-step process (X = Cl) *via* the diammine compound (and the monoammine for X = Cl) to the pure dihalide making the products perfectly recyclable. The diammine-monoammine transition in the chloride system is however on observable at higher heating rates, because the diammine-monoammine and monoammine-dihalide transitions happen at once for lower heating rates. This is due to the differences in activation energies between the different decomposition steps. While the structure of the monoammine nickel chloride could not be isolated for further studies due to its relative instability, the diammines could be observed *in situ* by PXD and their structures could be elucidated. This study indicates that $[Ni(NH_3)_6]Cl_2$ possesses all the necessary characteristics of a promising ammonia store and is therefore an interesting subject for further work in the field.

It could be shown that $[Ni(NH_3)_6]Cl_2$ possesses an extraordinarily high stability in moist air again underlining its suitability as an ammonia store. The reaction product of the decomposition in air could be identified by PXD and the structure of the main product was solved and refined from powder data. The combination of chemical information and crystallographic information in a mathematical way allowed the further analysis of the final product composition and an elucidation of the reaction pathway of the decomposition. This information is important as it proves the crucial role of water in the decomposition process and the elimination of water would hence make the material completely stable in air.

3.8. References

[1] P. Stoll, Ph.D. thesis, ETH Zürich, 1926.

[2] R. Eßmann, G. Kreiner, A. Niemann, D. Rechenbach, A. Schmieding, T. Sichla, U. Zachwieja, H. Jacobs, *Z. Anorg. Allg. Chem.*, 1996, **622**, 1161–1166.

[3] H. van Kempen, W. T. Duffy Jr., A. R. Miedema, W. J. Huiskamp, *Physica*, 1964, **30**, 1131 – 1140.

[4] A. Elgsaeter, I. Svare, *J Phys. Chem. Solids*, 1970, **31**, 1405 – 1408.

[5] A. R. Bates, K. W. H. Stevens, *J. Phys. C: Solid State Phys.*, 1969, **2**, 1573.

[6] A. R. Bates, *J. Phys. C: Solid State Phys.*, 1970, **3**, 1825.

[7] W. Press, M. Prager, *J. Chem. Phys.*, 1977, **67**, 5752–5754.

[8] H. Blank, G. J. Kearley, *J. Chem. Phys.*, 1987, **87**, 6809–6815.

[9] J. Eckert, W. Press, *J. Chem. Phys.*, 1980, **73**, 451–460.

[10] R. W. Pohl, K. Lüders, R. O. Pohl, *Pohls Einführung in die Physik: Band 1: Mechanik, Akustik und Wärmelehre*, *Vol. 1*, Springer-Verlag, 2009, chapter IX, . 128.

[11] A. Ferrari, A. Braibanti, G. Bigliardi, *Acta Crystallogr.*, 1963, **16**, 846–847.

[12] H. Niedrig, M. Sternberg, *Das Ingenieurwissen: Physik*, Springer, 2013, chapter 8, . 69–70.

[13] J. Hartley, A. Porch, M. Jones, *Sens. Actuators, B*, 2015, **210**, 726–730.

[14] R. E. Carter, *J. Chem. Phys.*, 1961, **34**, 2010–2015.

[15] M. Ishida, C. Y. Wen, *AIChE J.*, 1968, **14**, 311–317.

[16] S. P. Thompson, J. E. Parker, J. Potter, T. P. Hill, A. Birt, T. M. Cobb, F. Yuan, C. C. Tang, *Rev. Sci. Instrum.*, 2009, **80**, 075107.

[17] S. P. Thompson, J. E. Parker, J. Marchal, J. Potter, A. Birt, F. Yuan, R. D. Fearn, A. R. Lennie, S. R. Street, C. C. Tang, *J. Synchrotron Radiat.*, 2011, **18**, 637–648.

[18] J. E. Parker, J. Potter, S. P. Thompson, A. R. Lennie, C. C. Tang, *Mater. Sci. Forum*, 2012, **706**, 1707–1712.

[19] B. J. Hathaway, A. A. G. Tomlinson, *Coord. Chem. Rev.*, 1970, **5**, 1–43.

[20] A. N. Kolmogorov, *Akad. Nauk SSSR, Ser. Matem*, 1937, **3**, 355.

[21] W. A. Johnson, R. F. Mehl, *Trans. Am. Inst. Min. Metall. Eng.*, 1939, **135**, 396–415.

[22] M. Avrami, *J. Chem. Phys.*, 1939, **7**, 1103–1112.

[23] M. Avrami, *J. Chem. Phys.*, 1940, **8**, 212–224.

[24] M. Avrami, *J. Chem. Phys.*, 1941, **9**, 177–184.

[25] M. Fanfoni, M. Tomellini, *Il Nuovo Cimento D*, 1998, **20**, 1171–1182.

[26] T. R. Jensen, A. Andreasen, T. Vegge, J. W. Andreasen, K. Ståhl, A. S. Pedersen, M. M. Nielsen, A. M. Molenbroek, F. Besenbacher, *Int. J. Hydrogen Energy*, 2006, **31**, 2052–2062.

[27] T. R. Jensen, T. K. Nielsen, Y. Filinchuk, J.-E. Jørgensen, Y. Cerenius, E. M. Gray, C. J. Webb, *J. Appl. Crystallogr.*, 2010, **43**, 1456–1463.

[28] E. Woldt, *J. Phys. Chem. Solids*, 1992, **53**, 521–527.

[29] R. Merkle, J. Maier, *Z. Anorg. Allg. Chem.*, 2005, **631**, 1163–1166.

[30] P. Scardi, M. Leoni, *Acta Crystallogr. A*, 2002, **58**, 190–200.

[31] M. Leoni, T. Confente, P. Scardi, *Z. Kristallogr. Suppl*, 2006, **23**, 249–254.

[32] P. Scherrer, *Nachr. Ges. Wiss. Goettingen, Math.-Phys. Kl.*, 1918.

[33] G. K. Williamson, W. H. Hall, *Acta Metall.*, 1953, **1**, 22–31.

[34] B. E. Warren, B. L. Averbach, *J. Appl. Phys.*, 1950, **21**, 595–599.

[35] G. Caglioti, A. T. Paoletti, F. P. Ricci, *Nucl. Instrum. Meth.*, 1958, **3**, 223–228.

[36] P. Scardi, M. Ortolani, M. Leoni, *Mater. Sci. Forum*, 2010, **651**, 155–171.

[37] A. J. C. Wilson, *Mathematical theory of X-ray powder diffractometry*, Centrex Publishing Company Eindhoven, 1963.

[38] C. D. Terwilliger, Y.-M. Chiang, *Acta Metall. Mater.*, 1995, **43**, 319–328.

[39] T. Ungár, J. Gubicza, G. Ribárik, A. Borbély, *J. Appl. Crystallogr.*, 2001, **34**, 298–310.

[40] K. S. Rejitha, T. Ichikawa, S. Mathew, *J. Therm. Anal. Calorim.*, 2011, **103**, 515–523.

[41] V. Petříček, M. Dušek, L. Palatinus, *Z. Kristallogr. - Cryst. Mater.*, 2014, **229**, 345–352.

[42] L. Palatinus, G. Chapuis, *J. Appl. Crystallogr.*, 2007, **40**, 786–790.

[43] M. R. Churchill, *Inorg. Chem.*, 1973, **12**, 1213–1214.

[44] H. Reardon, J. M. Hanlon, M. Grant, I. Fullbrook, D. H. Gregory, *Crystals*, 2012, **2**, 193–212.

[45] J. M. Hanlon, Ph.D. thesis, University of Glasgow, 2013.

[46] L. Pauling, *J. Am. Chem. Soc.*, 1929, **51**, 1010–1026.

[47] L. Pauling, *J. Am. Chem. Soc.*, 1947, **69**, 542–553.

[48] N. E. Brese, M. O'keeffe, *Acta Crystallogr. B*, 1991, **47**, 192–197.

[49] R. Eßmann, *J. Mol. Struct.*, 1995, **356**, 201 – 206.

[50] J. Fujita, K. Nakamoto, M. Kobayashi, *J. Am. Chem. Soc.*, 1956, **78**, 3295–3297.

[51] A. Müller, K. H. Schmidt, G. Vandrish, *Spectrochim. Acta, Part A*, 1974, **30**, 651–663.

[52] T. Malcherek, J. Schlüter, *Acta Crystallogr. B*, 2007, **63**, 157–160.

[53] A. Hoser, W. Joswig, W. Prandl, K. Vogt, *Mol. Phys.*, 1985, **56**, 853–869.

[54] A. Hoser, W. Prandl, P. Schiebel, G. Heger, *Z. Phys. B: Condens. Matter*, 1990, **81**, 259–263.

[55] J. M. Janik, J. Janik, A. Migdał-Mikuli, E. Mikuli, K. Otnes, *Physica B: Condens. Matter*, 1991, **168**, 45–52.

[56] P. Schiebel, A. Hoser, W. Prandl, G. Heger, W. Paulus, P. Schweiss, *J. Phys.: Condens. Matter*, 1994, **6**, 10989.

[57] R. D. Shannon, *Acta Crystallogr. A*, 1976, **32**, 751–767.

[58] F. G. Fumi, M. P. Tosi, *J. Phys. Chem. Solids*, 1964, **25**, 31–43.

[59] L. Vegard, *Z. Phys.*, 1921, **5**, 17–26.

[60] K. Kido, T. Watanabe, *J. Phys. Soc. Jpn.*, 1959, **14**, 1217–1224.

[61] T. D. George, W. W. Wendlandt, *J. Inorg. Nucl. Chem.*, 1963, **25**, 395–405.

[62] N. Tanaka, M. Kagawa, M. Kamada, *Bull. Chem. Soc. Jpn.*, 1968, **41**, 2908–2913.

[63] G. Kenessey, G. Liptay, *J. Therm. Anal. Calorim.*, 1993, **39**, 333–349.

[64] J. Breternitz, E. Giraud, H. Reardon, T. K. A. Hoang, A. Godula-Jopek, D. H. Gregory, *ChemSusChem*, 2016, **accepted.**

[65] A. Leineweber, H. Jacobs, *J. Solid State Chem.*, 2000, **152**, 381 – 387.

[66] R. Eßmann, C. Mockenhaupt, *Spectrochim. Acta*, 1996, **A52**, 1897–1901.

[67] A. Boultif, D. Louër, *J. Appl. Crystallogr.*, 1991, **24**, 987–993.

[68] J. W. Visser, *J. Appl. Crystallogr.*, 1969, **2**, 89–95.

[69] P.-E. Werner, L. Eriksson, M. Westdahl, *J. Appl. Crystallogr.*, 1985, **18**, 367–370.

[70] A. L. Spek, *J. Appl. Crystallogr.*, 2003, **36**, 7–13.

[71] A. Leineweber, *J. Solid State Chem.*, 2003, **176**, 198–202.

[72] G. Meyer, P. Nockemann, *J. Solid State Chem.*, 2001, **162**, 254–259.

[73] N. E. Schumaker, C. W. Garland, *J. Chem. Phys.*, 1970, **53**, 392–407.

[74] E. F. De Oliveira, Y. Hase, *Vib. Spectrosc.*, 2003, **31**, 19–24.

[75] F. Agulló-Rueda, J. M. Calleja, M. Martini, G. Spinolo, F. Cariati, *J. Raman Spectrosc.*, 1987, **18**, 485–491.

[76] T. E. Oliphant, *A guide to NumPy*, *Vol. 1*, Trelgol Publishing USA, 2006.

4. Structural Effects Copper Halide Ammines

4.1. Introduction

The first part of this chapter will establish that $CuCl_2$ behaves differently from the nickel halide analogue and bears some chemical consequences from the Jahn-Teller distortion of the copper-(II)-ion. The rest of this chapter is dedicated to the in-depth analysis and discussion of the chemical and structural effects of the Jahn-Teller distortion. In order to gain more information about the structure of the hexammine salts, a method for the crystallisation of single crystals of these was developed and the first single crystal analysis of $[Cu(NH_3)_{6-x}]Cl_2$ is presented herein. A more detailed insight on the arrangement of the hydrogen atoms in these compounds was obtained through neutron diffraction of the deuterated analogue of the hexammine salt and the local coordination environment of the Cu^{II} ions was probed by different spectroscopic techniques.

Heating the tetragonal $[Cu(NH_3)_{6-x}]Cl_2$ has the surprising effect of an apparent loss of the Jahn-Teller distortion in this compound. This fully reversible effect is observed by *in* *situ* PXD and the structure of the cubic undistorted phase is refined from PXD. The nature of the coordination environment herein is further probed by *ab-initio* calculations and the alternative stabilisation of regular octahedrally coordinated $[Cu(NH_3)_6]^{2+}$ through a chemical way is discussed.

4.2. Experimental

4.2.1. Syntheses of hexammine copper halides

$CuCl_2$ (99 %, Aldrich), $CuBr_2$ (99 %, Aldrich), $MgCl_2$ (98 %, Sigma) and NH_3 (anhydrous, BOC) were used without further purification. The hexammine halides were produced by exposing the respective halide salts to a stream of ammonia gas ($\approx$ 50 ml/min) for one hour at ambient conditions. In order to avoid contamination, starting materials and reaction products were handled in a glove box (O_2, $H_2O \leq 10$ ppm). Mixed Cu,Mg hexammine chloride was synthesised by ball-milling $MgCl_2$ and $CuCl_2$ in a planetary ball mill (Retsch PW100, ball-to-powder ratio 35:1) for 15 hours in 5 min cycles at 450 /min and further resting time of 30 s after each cycle. The mixed dihalide was exposed to ammonia gas for one hour under similar conditions to the pure dihalides.

The gravimetric uptake experiments and Synchrotron experiments were conducted using commercial $CuCl_2$ (99 %, Aldrich) without further purification.

4.2.2. Synthesis of $[Cu(ND_3)_{6-x}]Cl_2$

The reaction pattern above was modified for the preparation of the deuterated sample $[Cu(ND_3)_{6-x}]Cl_2$ in order to minimise the losses of expensive ND_3. Herein, pure $CuCl_2$

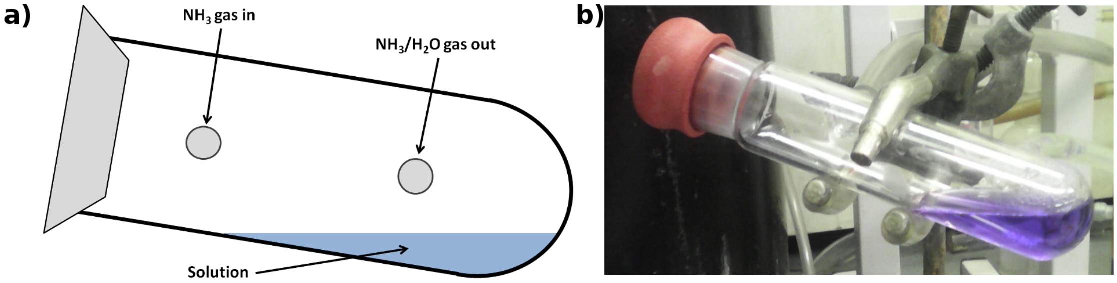

Figure 4.1.: a) Schematic view of the reactor used for the crystallisation under NH_3 flow. b) Photograph of the reactor used for the crystallisation under controlled atmosphere.

was exposed to an atmosphere of ND_3 for ≈8 hours. A very small stream of ND_3 guaranteed the saturation of the atmosphere in ND_3.

4.2.3. Crystal growth from aqueous solution under NH_3 atmosphere

The starting materials ($CuCl_2 \cdot 2\,H_2O$: 99 %, BDH; $[Ni(H_2O)_6](NO_3)_2$: 99 %, BDH; $Cu(NO_3)_2 \cdot 2.5\,H_2O$: 99.99 %, Aldrich) were dissolved in ≈ 5 ml de-mineralised water until saturation has been reached. The solution was then exposed to a stream of ammonia and agitated to facilitate the saturation of the solution with ammonia. To remove impurities and precipitated material in cases where the ammine salt is less soluble than the hydrate (i.e. for nickel nitrate), the solution was filtered before further exposure to an ammonia stream. The so prepared solutions were allowed to slowly evaporate water in a special reactor to control the atmosphere (Figure 4.1). To elicit the crystal growth, a constant stream of ammonia over the water reservoir was assuring saturation in ammonia and the retention of water from the vapour phase. Within several days, crystals of the desired products were formed in the solution. The crystals were manually separated from the mother liquor and were stored under paraffin oil during the crystal picking process.

4.3. Uptake of Ammonia into $CuCl_2$

4.3.1. Study of the Ammonia Deficiency under Working Conditions

Gravimetic uptake study under ammonia flow

Two different methods for determining the deficiency were combined on order to determine the ammonia deficiency. Firstly, the reaction propagation was followed using a bespoke gravimetric setup working under a flow of ammonia and secondly, the deficiency in the final product was determined by Rietveld refinement. The gravimetric setup used consisted of a pan balance, on which a special sample holder was fitted. This sample holder was built of a large tube in which a sample vial with the starting product could be placed. An ammonia flow entered the sample holder below the sample. Ammonia has a lower density than air and so this configuration ensured the sample was under an ammonia atmosphere. In earlier prototypes, where the ammonia flow was directed from above, the gas did not reach the sample. The mass values were recorded at a rate of ≈ 24 Hz to a PC. Details of the setup are discussed in section 2.1.

Assuming that the stoichiometric hexammine $[Cu(NH_3)_6]Cl_2$ represents full loading, the implication from the experimental values (Figure 4.2) is that the uptake does not reach 100 % conversion. The setup was benchmarked using the Ni analogue compounds, where an equivalent conversion of 100 % was found. It can be assumed that the experimental values indicate an under-stoichiometric uptake of ammonia into the copper chloride phase. While the stoichiometry of the product can be proposed with some confidence, the same is not necessarily true for the real kinetics of the reaction. This latter is influenced by the crude setup of the gravimetric experiment as compared to those in section 3.3.1. Further,

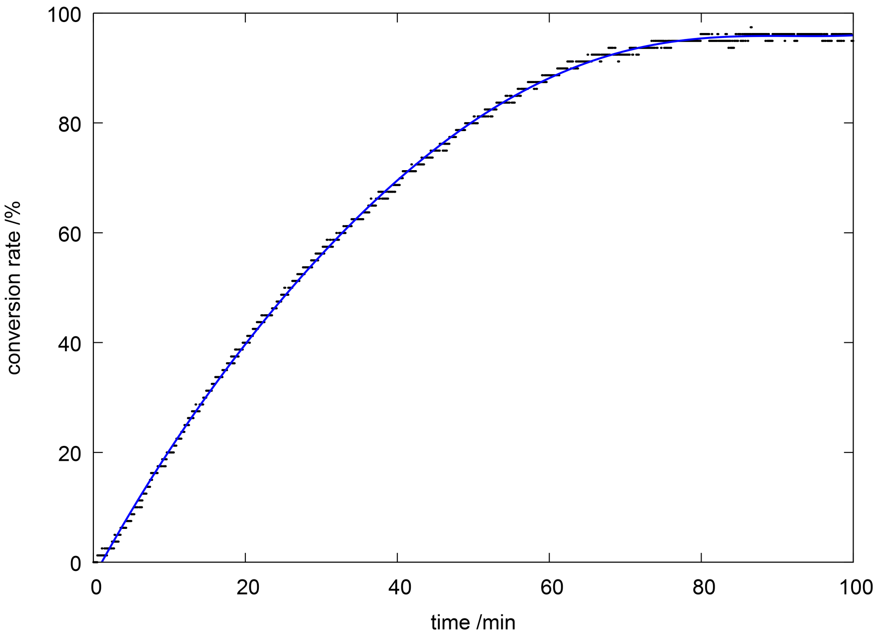

Figure 4.2.: Gravimetric measurement of the ammonia uptake into $CuCl_2$ under dynamic NH_3 flow conditions (1 l/min). The conversion rate is normalised to the full conversion into stoichiometric $[Cu(NH_3)_6]Cl_2$. The black dots mark the measured values and the blue line is a 5^{th} order polynomial fit.

the precision and sensitivity of the balance was low (±10 mg). In order to minimise systematic errors, dihalide samples of ca. 1 g were used. The mass of the final product was obtained as an average of the values over a 25 minute period at the conclusion of each experiment, once effectively constant. This led to a conversion of 95.6(7) % of the theoretical uptake for $[Cu(NH_3)_6]Cl_2$, corresponding to a product stoichiometry of $[Cu(NH_3)_{5.74(4)}]Cl_2$. This value is in fact very close to what was obtained from single crystal analysis (see section 4.6).

Rietveld Refinement of "$[Cu(NH_3)_6]Cl_2$"

A capillary of the sample from the gravimetric experiments above was prepared, sealed instantly after the end of the uptake and mounted on the diffractometer immediately. The powder X-ray pattern obtained from this sample did not show traces of any impurities but instead confirmed the formation of single phase “hexammine” copper chloride. The structure and phase behaviour of the $CuCl_2$–NH_3 system is discussed in greater detail in due course of the chapter and the discussion of the structure and refinement here is limited to the determination of the ammonia occupancy within the compound. The full details of the refinement may be found in tables A.26–A.28 in the appendix. The cell parameters found during the refinement (Table 4.1) with Jana2006[1] are in line with the values obtained during the analysis of the *in-situ* powder patterns (see next section) and reinforce the premise that the compound forms a tetragonal distortion of the K_2PtCl_6 structure type. The Jahn-Teller effect of the Cu^{II} ions causes a deviation of the coordination arrangement around the Cu^{2+} ions from a regular octahedral coordination towards an elongated square-planar bipyramid. The change in point symmetry of the complex ion invokes a change in the crystal structure from the $Fm\bar{3}m$ aristotype structure adopted for instance by$[Ni(NH_3)_6]Cl_2$ to a $I4/mmm$ subgroup structure in which the equatorial and axial ammonia molecules occupy two different crystallographic sites: The equatorial site has a multiplicity of 8 and represents all ammonia molecules in the contracted square-plane, while the axial site has a multiplicity of 2 and represents the elongated capping ammonia molecules. As a consequence of the symmetry reduction, all atoms could be refined anisotropically. This however led to unstable refinements and some physically unreasonable anisotropic thermal ellipsoids along with only a small improvement in the goodness of fit, and it was hence decided to refine only isotropic displacement parameters together with the refinement of the non-stoichiometry of the ammonia molecule on the axial site. The occupancy on the square-planar site was also explored but the value deviated within error of full occupancy and so was fixed. Furthermore, the zero-shift correlated strongly with the asymmetry correction and the cell parameters leading to diverging results. It was therefore decided to fix the zero shift in the later stages of the refinement but to allow the refinement of the other components, because this combination proved to be best converging. The refinement is summarised in Table 4.1 and the data fit is plotted in Figure 4.3.

Regarding the occupancy of the elongated site, one finds a standard occupation factor of 0.68(2) which translates to a loading of 5.35(3) eq. of ammonia (to one eq. of $CuCl_2$) and therefore the overall composition of the reaction product is $[Cu(NH_3)_{5.35(3)}]Cl_2$. This value is smaller but comparable to those found in the gravimetric experiments: 5.73(4) eq. in the dynamic measurement (see above). Although the values and errors depend to some extend on the configuration of the uptake experiments, an ammonia deficiency is consistently found throughout these measurements such that the $n = 6$ hexammine is never obtained. The nature and possible explanation for this effect is further discussed in section 4.9 also including further results from thermal and spectroscopic analyses.

Table 4.1.: Crystallographic data for $[Cu(NH_3)_{5.35(3)}]Cl_2$

Sum formula	$Cl_2CuH_{16.06}N_{5.35(3)}$
Crystal System	Tetragonal
Space Group	$I4/mmm$
a / Å	7.2930(1)
b / Å	9.4274(3)
V /Å^3	501.42(2)
Z	2
Calculated Density, ρ_x /g·cm^{-3}	1.4942
R_p; wR_p	0.070; 0.094
Goof; X^2	1.00; 1.00
R_{obs}; wR_2(all)	0.049; 0.052
$\Delta\rho$ [max, min] /(e^-/Å^3)	0.47; –0.54

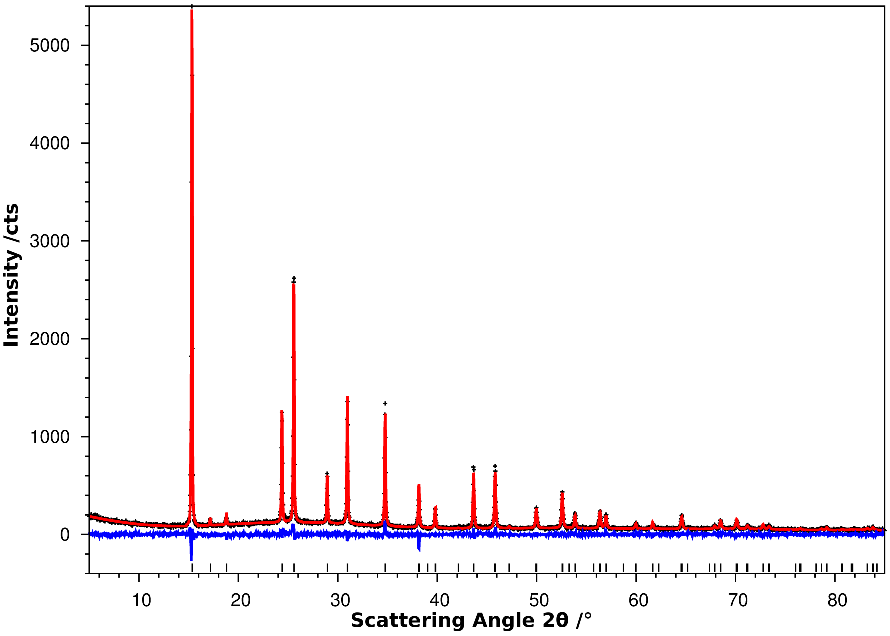

Figure 4.3.: Comparison of the observed (black crosses) and calculated patterns (red line) from the Rietveld refinement against PXD data for $[Cu(NH_3)_{5.35(3)}]Cl_2$ at room temperature. The blue line represents the difference profile ($I_{obs} - I_{calc}$) and the black tick marks indicate the theoretical reflection positions.

4.3.2. *In situ* XRD studies

Similar to $[Ni(NH_3)_6]Cl_2$ (section 3.3.2), the copper analogue forms readily during the reaction of $CuCl_2$ with NH_3. In order to quantify this effect more in detail, the reaction was followed by time resolved X-ray diffraction (Figure 4.4). It is apparent that the reaction under the given conditions is extraordinarily quick and the period of time in which peaks of $CuCl_2$ and the hexammine phase can be found simultaneously is very small ($<$ 1 min). Although no intermediate phases could be detected during the reaction and only peaks from either the starting material or the reaction product can be found, one observation in this experiment is of great importance: The peaks of the hexammine phase shift very strongly during the formation of the hexammine phase and, in fact, still shift after the complete disappearance of the $CuCl_2$ peaks in the diffractograms. This behaviour shows that the cell parameters of “$[Cu(NH_3)_6]Cl_2$” exhibit some variability over the course of ammoniation. This behaviour is in fact in line with the observations during single crystal measurements, where especially the *c*-parameter showed an important degree of freedom and was hard to pin (see section 4.5). Analogous behaviour was not observed for the hexammine nickel compounds and is consistent wit the premise of a variable ammonia stoichiometry (n = 6-x).

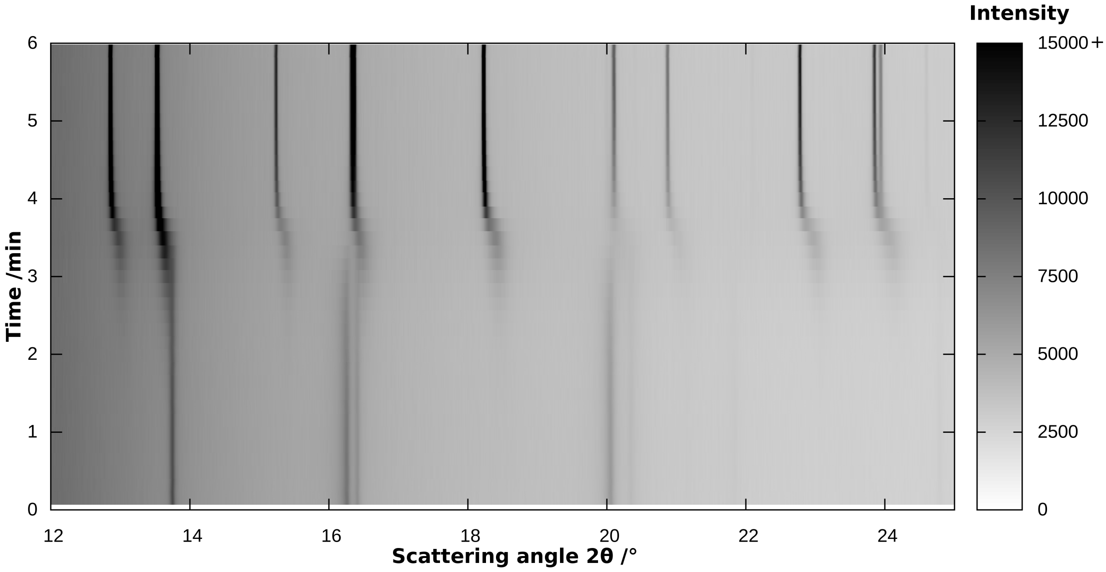

Figure 4.4.: Time resolved powder diffraction of the formation of $[Cu(NH_3)_6]Cl_2$ (top) from $CuCl_2$ (bottom) at room temperature.

Development of the cell parameters

In order to quantify the shifting of the cell parameters during the formation of hexammine copper chloride, the individual patterns were decomposed using a Le Bail fitting procedure. Strong overlap with the peaks from the $CuCl_2$ structure coupled with the problematic peak profiles from the area detectors used during the refinement necessitated a particular procedure for the fitting. Firstly, the cell from $CuCl_2$ was fitted using one of the earlier patterns in which $CuCl_2$ was a single phase. The cell parameters obtained in this way (a = 6.903(5) Å, b = 3.308(5) Å, c = 6.813(6) Å, β = 122.14(8)°) were fixed in the subsequent refinements (at later time points) and only the cell parameters of $[Cu(NH_3)_6]Cl_2$, the profile parameters and the background function (12-term Legendre type polynomial) were refined. In order to lower the number of overlapping peaks between the two phases, the refinement was only performed up to an angle of $2\theta = 35°$ beyond which large areas of peak overlap occured. The deconvolution of the two phases remained non-trivial and the cell parameters obtained before the complete removal of the starting material (< 1 min,

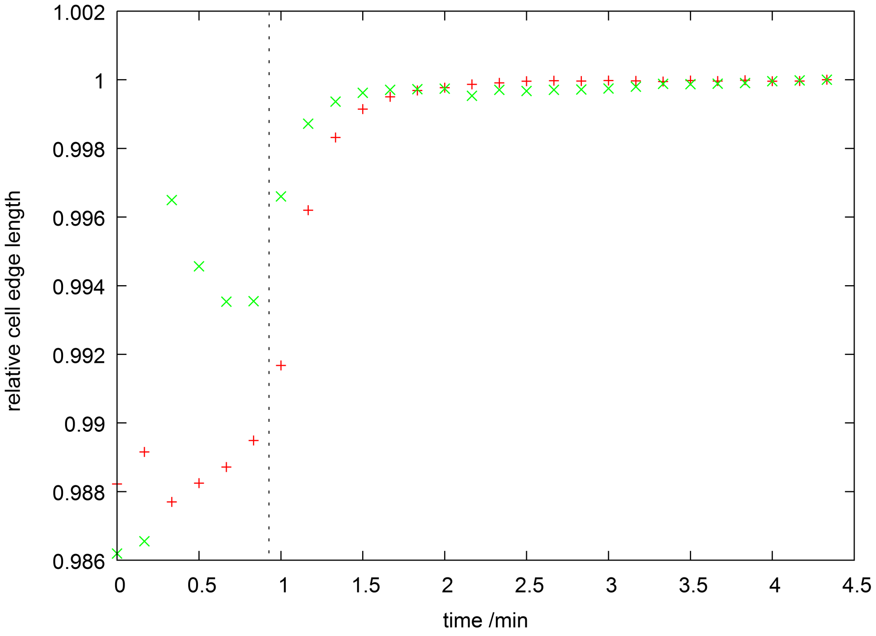

Figure 4.5.: Relative shift of the cell edge lengths of $[Cu(NH_3)_6]Cl_2$ (red plusses: *a*; green crosses: *c*) during the reaction of $CuCl_2$ with NH_3 at room temperature. The vertical dotted line marks the limit between the patterns containing peaks of $CuCl_2$ (left) and those with only $[Cu(NH_3)_6]Cl_2$. The highest value of the respective cell edge was normalised to 1.

Figure 4.5) are prone to a large error arising from the overlap of the two phases and the low intensity of the “hexammine” phase. This also explains the outlier values in this time range in Figure 4.5.

While the *a*-parameter during this analysis varies by 0.0867 Å (or 1.18 % of the maximum value, from 7.2821 Å to 7.3688 Å), the *c* parameter changes by 0.1305 Å (1.38 % of the maximum value, from 9.3319 Å to 9.4624 Å; Figure 4.5 for the development of the relative cell parameters over time). It is notable that these cell parameter values differ from other values in the different analyses within this report. This is mainly due to the fact that the peak profile used in this analysis neglected further shape effects (including asymmetry, zero point shift etc.) due to the limited quality of the patterns. This treatment was nevertheless chosen as it allowed the treatment of the low intensity patterns in the beginning of the uptake as well as the high intensity patterns at the end with one consistent set of parameters and therefore allows the direct comparison of the values obtained. Consequently, the absolute values of the cell parameters should not be compared to other experimental data herein, but the relative ratio of the different values in the set can be regarded with a higher degree of certainty. These numbers suggest a relatively isotropic growth of the cell in the course of the reaction with the *c*-parameter expanding slightly more than the *a*-parameter. This finding can be explained in terms of the ammonia deficiency being predominantly located on the on the axial site of the square-bipyramidal $[Cu(NH_3)_6]^{2+}$ complex cations, and hence a preferred filling of the square-planar site. It has to be remarked though that the values at the lower end of the analysis cannot be treated with high confidence and when one restricts the consideration to those values that can be determined with some certainty (the patterns after the complete disappearance of $CuCl_2$ after one minute) the situation is in fact inverted and the growth of the *a*-parameter appears to be larger than that of the *c*-parameter. It therefore has to be assumed that the transformations in the structure and chemical behaviour during the formation of the hexammine phase are somewhat more complex than a simple model of a step-wise inclusion of ammonia into the structure and an ultimate answer to this question cannot be obtained from the data presented herein. In order to determine the nature of this variability in the cell parameters, further time resolved experiments, especially those probing the Cu coordination environment directly like EXAFS.

4.4. Thermal Decomposition of $[Cu(NH_3)_6]X_2$ (X = Cl, Br)

4.4.1. Thermal Analyses

The thermal decomposition of $[Cu(NH_3)_6]X_2$ (X = Cl, Br) is of high importance for the usability of the material for ammonia storage, *i.e.* decomposition temperatures that are too high or too low would impede the usability. Yet, only one crude study of the thermal decomposition behaviour of an ammine copper halide has been reported in the literature.[2,3] Similar to the thermal analyses work on the hexammine nickel halides, the thermal analyses were performed here in two ways: Initially, a medium heating rate of 5 K/min was used. Secondly, Kissinger analyses for the thermal decompositions of the two compounds were conducted in order to extract the activation energies of the different thermal decomposition steps. It will become obvious during the analysis of the thermal decomposition data, that the decomposition of the hexammine copper halides does not produce the dihalide material, a fact which made the use of the XRD hot-stage equipment for *in situ* observations difficult if a potential damage by halogens was to be avoided. Such an analysis was further hindered given the higher ais-sensitivity of the hexammine copper halides compared to the nickel analogues.

TG-DTA-MS analysis

The main difference between the two analyses in this section is the use of the evolved gas flow mass spectrometer for the decomposition of $[Cu(NH_3)_6]Br_2$ in order to elucidate the gaseous species in the gas stream. The decomposition of both samples follows the same general pattern (Table 4.2) and shall be explained a bit more in detail taking the bromide as an example.

Table 4.2.: Thermal decomposition (STA) results for $[Cu(NH_3)_6]X_2$ (X = Cl, Br) with a heating ramp of 5 K·min^{-1}.

Sample	Step	Mass changes obs. /wt.-%		TG (STA) Temperatures /K		Peak Temperatures /K
	final	Total	Stepwise	Onset	Final	DTA
$[Cu(NH_3)_6]Cl_2$	1	11.4	11.4	349	376	372
	2	22.1	11.0	393	413	409
	3	55.0*	32.9*	547		555, 585, 678, 691
$[Cu(NH_3)_6]Br_2$	1	8.6	8.6	352	380	375
	2	16.5	7.9	412	432	430
	3	53.4*	36.9*	523		541, 621

* from the Diammine step to the end of the measurement

$[Cu(NH_3)_6]Br_2$ does not start to decompose considerably until 350 K (Figure 4.6, Table 4.2). This fact may be surprising at first sight, considering the high instability in air.[3,4] The STA sample, however, was not exposed to air and in analogy to Ni (section 3.6), one would expect water (in air) to play an important role in the room temperature decomposition. The first decomposition step is immediately followed by a second at 420 K which then leads to a plateau of stability of approx. 90 K. The intermediate products in these two steps are most likely the tetrammine copper bromide and the diammine copper bromide respectively. Further decomposition from the diammine clearly proceeds as a multi-step process, as can be deduced from the DTA signal very clearly, which shows two endothermal events at 541 K and 621 K. These steps do, however hardly correspond to the TG signal, where (at least) 2 weak intermediate steps can be identified. The final mass loss further does not correspond to the formation of $CuBr_2$ but suggests towards the formation of the reduced halide, CuBr by loss of one equivalent of bromine. These results do in fact correlate well with the report from Tomlinson and Hathaway,[2,3] who mentioned the thermal decomposition of $[Cu(NH_3)_5]Cl_2$ briefly if one regards the last multi-step mass loss as one combined step. They also describe a 3-step process with the overall mass loss way too large for the decomposition pathway into the pure dihalide.

The four main steps as found in the DTA signal are also reflected in the MS data for NH_3^+ (Figure 4.7), which exhibits four peaks at 403 K, 448 K, 562 K and 638 K. The temperature difference in the maxima in the STA of ≈ 20 K is caused by the retention time of the evolved gas flow between the STA furnace and the MS instrument. A possible explanation for the multi-step reaction and the potential reduction of Cu^{II} could be the formation of ammonium bromide during the thermal decomposition. This latter would also explain the distinct shoulder in the NH_3^+ curve to higher temperatures as this could correspond to the further sublimation of NH_4Br from the reaction because is decomposes into the molecular compounds NH_3 and HBr in the gas phase.[5] Such a mechanism

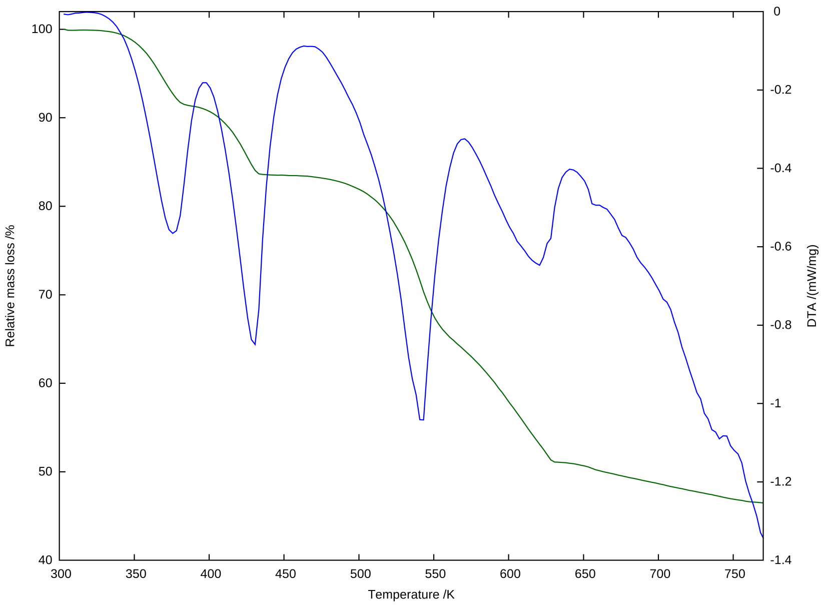

Figure 4.6.: TG-DTA profile for $[Cu(NH_3)_6]Br_2$ with TG (green) and DTA (blue) at 5 K/min.

could be concluded in one of the following formulae, depending on whether ammonium bromide is formed or not:

$$6\,CuBr_2 \cdot 2\,NH_3 \longrightarrow 6\,CuBr + 6\,HBr + 10\,NH_3 + N_2$$

$$6\,CuBr_2 \cdot 2\,NH_3 \longrightarrow 6\,CuBr + 6\,NH_4Br + 4\,NH_3 + N_2$$

$[Cu(NH_3)_6]Cl_2$ shows a very similar decomposition behaviour (Figure 4.8) to the bromide analogue with little shift in the decomposition temperatures (Table 4.2). While the decomposition starts nearly at the same temperature for the two analogues (349 K for the chloride against 352 K for the bromide), the diammine copper chloride is more stable and decomposes at a temperature over 20 K higher (onset: 547 K) than the diammine copper bromide (onset: 523 K), by analogy to the hexammine nickel halides. The DTA profile for $[Cu(NH_3)_6]Cl_2$ shows a strong endothermic signal with a double peak at around 700 K. It is unclear what process this peak corresponds to, but the TG signal at this temperature signifies, by analogy to the copper bromide system, that thermal treatment leads to mass losses higher than those attributable to the formation of copper dihalide. The direct

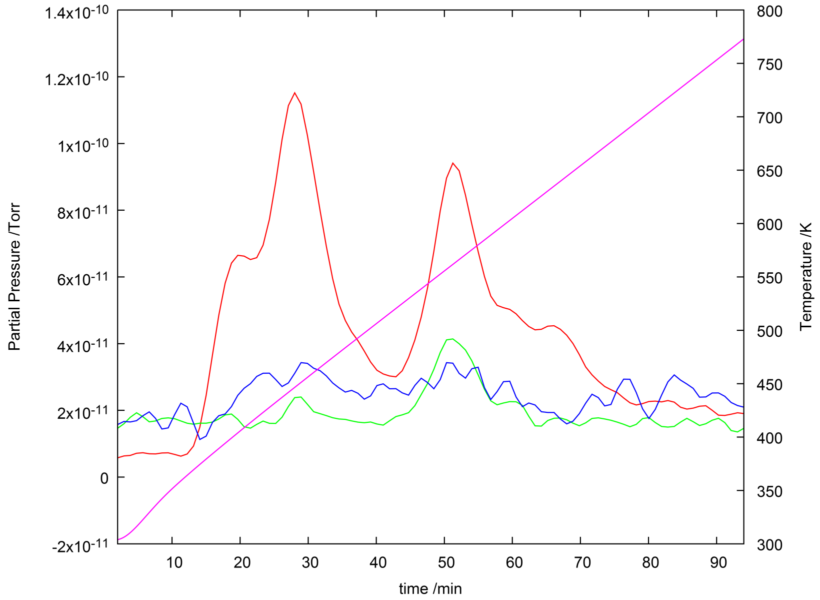

Figure 4.7.: MS profile for $[Cu(NH_3)_6]Br_2$ for NH_3^+ (red), N_2^+ (green) and H_2^+ (blue). The curves were smoothed using a *via* an averaging splines function. The magenta line gives the temperature profile in the STA furnace.

decomposition of this material into the reduced copper monochloride greatly impedes the use of $CuCl_2$ as ammonia storage material as complete ammonia release would make the material non-recyclable. Using the diammine as discharged material instead, one could still envisage a recyclable storage material but at the expense of a significantly lower storage capacity. Given this obvious disadvantage compared to the nickel halide system, the copper halide system cannot be regarded as a promising ammonia store. The structural study of the material is however of great interest due to the influence of the Jahn-Teller effect in the crystal structure and the resulting chemical behaviour of the material.

One of the principal reasons for the thermal analysis however was to study the possible non-stoichiometric behaviour in this system. As can be easily deduced from the weight loss steps (Table 4.3), the observed weight losses are consistently lower than the expected values for stoichiometric hexammine copper chloride. Comparing the observed weight

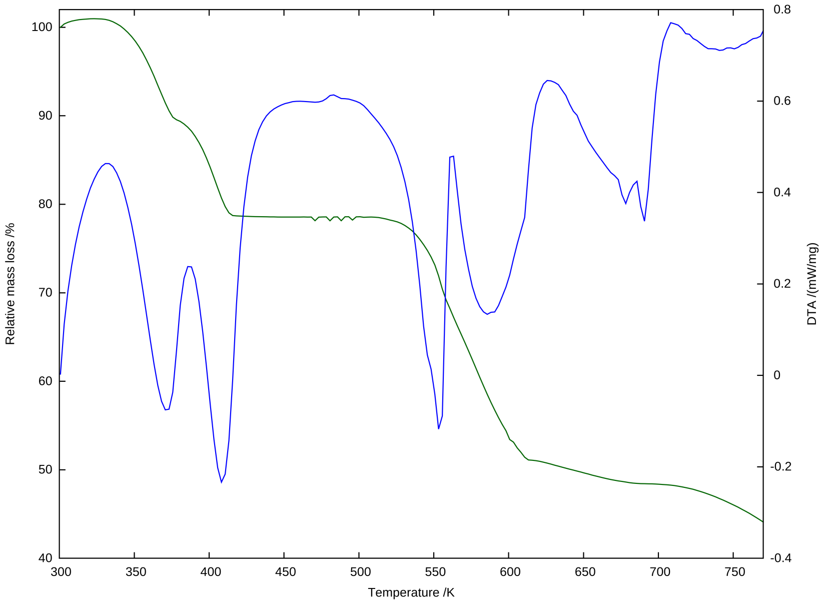

Figure 4.8.: TG-DTA profile for $[Cu(NH_3)_6]Cl_2$ with TG (green) and DTA (blue) at 5 K/min.

losses with those calculated on the basis of hexammine copper chloride and the deficient stoichiometries as obtained from gravimetric ($[Cu(NH_3)_{5.74(4)}]Cl_2$) and diffraction ($[Cu(NH_3)_{5.35}]Cl_2$) experiments (Table4.3),it can be stated that the deficient structures explain the observed data better than stoichiometric hexammine copper chloride. Based on the calculation of the residual weight through:

$$\Delta w = \frac{M_{final}}{M_{initial}} \tag{4.1}$$

where Δw is the relative residual mass and $M_{initial}$ and M_{final} are the molecular masses of starting material and product, one can in fact link the number of ammonia ligands in the fully ammoniated ammine (n) to the observed weight loss by substituting the molar mass of the starting material with the molar masses of its components, i.e. $CuCl_2$ and n equivalents of NH_3. The so obtained formula:

$$n = \left(\frac{M_{product}}{\Delta w} - M_{CuCl_2} \right) / M_{NH_3} \tag{4.2}$$

yields values of n = 5.5, 4.9 and 5.0 for the three steps of the reaction respectively. One has to note that this calculation assumes stoichiometric products at each intermediate step. This assumption is probably the largest potential source of error in this calculation and one could argue that one or another step could be better defined than the others. Nevertheless, the values are consistently below the stoichiometric number of ligands (n = 6) and lie within the range of the values obtained by gravimetric uptake and Rietveld refinement. It is worth mentioning that the weight loss values obtained by Tomlinson and Hathaway from the product they identified as stoichiometric "pentaammine copper chloride"[2,3] yield similar values using this analysis method. Tomlinson and Hathaway reported a first weight loss of 13 wt.-% and a second weight loss of 9 wt.-% which they interpreted as:

$$[Cu(NH_3)_5]Cl_2 \longrightarrow [Cu(NH_3)_{3.3}]Cl_2 \longrightarrow [Cu(NH_3)_2]Cl_2$$

with the theoretical weight losses of 13.2 wt.-% and 10 wt.-% respectively. If one assumes the first intermediate to be the tetrammine, however and then applies the formula stated above, ammonia contents of n = 5.8 and 4.8 eq. can be calculated. It is not possible to evaluate the results given by Tomlinson and Hathaway over 45 years ago fully, as crucial parameters like the atmosphere during sample handling and measurement are missing and it is therefore not discernible whether these similarities are coincidental or systematic. Nevertheless, applying the same calculation to the bromide analogue results in similar values for the ligand number (n = 5.6, 5.0, 5.0 for the three main decomposition steps). These results demonstrate once again that the product of the reaction of ammonia with cooper halides at room temperature is in fact not the stoichiometric hexammine copper chloride but a sub-stoichiometric phase which contains a variable amount of ammonia in the range between five and six equivalents of ammonia. It has to be noted that such deviations in the gravimetric experiments (uptake and thermal decomposition)

Table 4.3.: TG analysis of $[Cu(NH_3)_6]Cl_2$ as compared to the stoichiometric compound $[Cu(NH_3)_6]Cl_2$ and the non-stoichiometric compositions $[Cu(NH_3)_{5.74}]Cl_2$ and $[Cu(NH_3)_{5.35}]Cl_2$ as found in section 4.3.1.

Compound	Weight loss /wt.-%			
	obs.	$[Cu(NH_3)_6]Cl_2$	$[Cu(NH_3)_{5.74}]Cl_2$	$[Cu(NH_3)_{5.35}]Cl_2$
$[Cu(NH_3)_4]Cl_2$	11.4	14.4	12.7	10.1
$[Cu(NH_3)_2]Cl_2$	22.1	28.8	27.4	25.3
CuCl	55.0	58.1	57.3	56.1

could also be caused by other reasons, such as an inert impurity phase. They do, however, coincide well with the diffraction experiment, where the copper ammine phase is probed directly.

Kissinger Analyses

The Kissinger analysis (Figure 4.9 and A.15–A.21, Table 4.4) of the first four peaks in the DTA curve of $\mathbf{[Cu(NH_3)_6]Cl_2}$ are of some importance for the clarification of the decomposition process. While the first two steps can be clearly associated with the ammonia losses of the compound, the latter two are somewhat less certain, due to the superposition of ammonia desorption and reduction of the Cu^{II} ion along with a loss of one equivalent of the halide. The derived activation energies for the first two steps: 58 kJ/mol and 73 kJ/mol respectively do compare very well with the activation energy for the hexammine decomposition of $[Ni(NH_3)_6]Cl_2$ (77 kJ/mol). This probably implies that, despite the chemical differences in the Ni and Cu system, the ammonia removal mechanism is similar in both systems.

The third decomposition step has an activation energy of 189 kJ/mol and takes a value between the activation energies for the diammine decomposition (245 kJ/mol) and

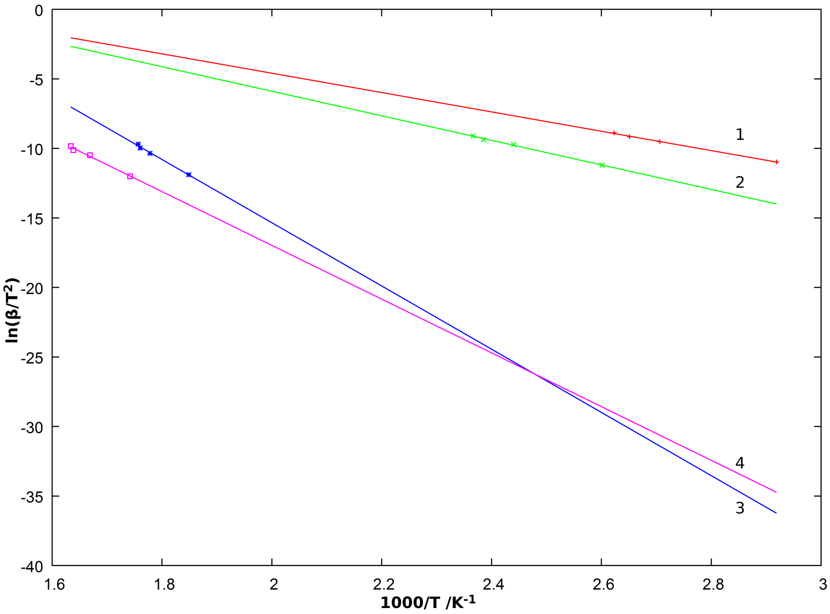

Figure 4.9.: Kissinger plots for the 4 steps in the decomposition of $[Cu(NH_3)_6]Cl_2$ with the hexaammine decomposition in red (1, plusses), the tetrammine decomposition in green (2,crosses), the diammine decomposition in blue (3,asterisks) and the further decomposition step in magenta (4, squares). The linear fit is given as a solid line in each case.

monoammine decomposition (137 kJ/mol) in the nickel chloride system. The activation energy of the fourth decomposition step is with 161 kJ/mol only slightly higher and a definitive attribution to distinct reaction steps is not possible on the basis of these experiments. Assignment of the fourth peak to a pure ammonium chloride sublimation, as would be possible if ammonium chloride was formed during the reaction, can be

Table 4.4.: Analysis of the DTA data for $[Cu(NH_3)_6]Cl_2$ obtained at varied heating rates. The temperatures are the peak temperatures of the DTA signal (Peak 1: hexammine decomposition, peak 2: tetrammine decomposition, peak 3: diammine decomposition, peak 4: further decomposition).

Heating rate /(K/min)	Peak 1 /K	Peak 2 /K	Peak 3 /K	Peak 4 /K
2	342.6	384.4	540.9	574.1
10	369.5	409.8	562.4	599.2
15	377.2	419.2	568.1	610.3
20	381.2	422.5	569.3	612.1

neglected because the activation energy for the sublimation of ammonium chloride has been determined as 55.2 kJ/mol.[5] The double peak observed in the 5 K/min measurement (Figure 4.8, at ca. 700 K) does also appear in the 2 K/min measurement, while it is merged into a single peak in the 10 K/min measurement and vanishes at higher heating rates. The interpretation of this complex decomposition behaviour requires careful evaluation of further data. This is beyond the scope of this thesis but would be valuable in future work. None of the different heating rate experiments, however, gives hint to the formation of the pure copper dihalide.

$[Cu(NH_3)_6]Br_2$ (Figure 4.10) behaves very similar to $[Cu(NH_3)_6]Cl_2$ and the activation energies of the hexammine decomposition and tetrammine decomposition (58 kJ/mol and 76 kJ/mol) are in close agreement to those of $[Cu(NH_3)_6]Cl_2$ (58 kJ/mol and 75 kJ/mol) showing the similarity between the different halide analogues.

The activation energy of the third decomposition step (158 kJ/mol) is somewhat lower than its chloride analogue (189 kJ/mol). This may be an influence of the halide anion entering into the complex coordination sphere at lower ammonia contents. Such an influence would at first sight also be expected for the decomposition of the tetrammine complex, where the halide ion is likely to enter into the coordination sphere, but as consequence of the Jahn-Teller effect, the halides anions are most likely coordinated in

Table 4.5.: Analysis of the DTA data for $[Cu(NH_3)_6]Br_2$ obtained at varied heating rates. The temperatures are the peak temperatures of the DTA signal (Peak 1: hexammine decomposition, peak 2: tetrammine decomposition, peak 3: diammine decomposition, peak 4: further decomposition).

Heating rate /(K/min)	Peak 1 /K	Peak 2 /K	Peak 3 /K	Peak 4 /K
2	355.7	406.5	521.1	582.0
10	386.7	435.8	544.8	631.9
20	396.6	447.7	553.8	644.7

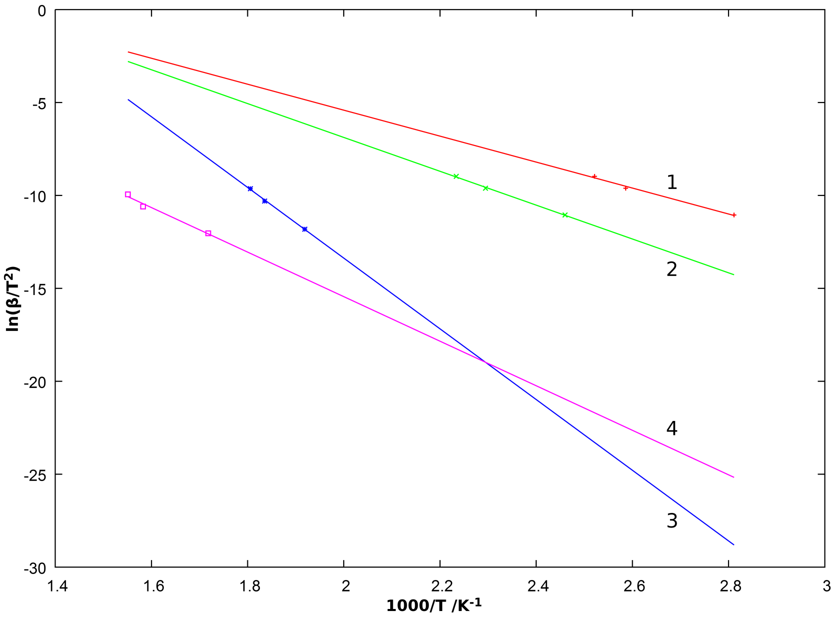

Figure 4.10.: Kissinger plots for the 4 steps in the decomposition of $[Cu(NH_3)_6]Br_2$ with the hexaammine decomposition in red (1, plusses), the tetrammine decomposition in green (2, crosses), the diammine decomposition in blue (3, asterisks) and the further decomposition step magenta (4, squares). The linear fit is given as a solid line in each case.

the axial positions and the strength of the Cu–*X* interaction is therefore much less than for an undistorted complex. It has to be noted that no tetrammine copper halide structure is known and despite efforts, it was not possible to determine the structure, either. The fourth decomposition step, however, exhibits a considerably smaller activation energy for the bromide (100 kJ/mol) as compared to the chloride (161 kJ/mol). It is due to the difference in activation energies of the third and fourth step, that a small plateau at 556 K at a residual mass of 73.5 wt.-% becomes visible for higher heating rates (Figures A.19–A.21). This value does fit very well to the theoretical residual mass for the monoammine (73.9 wt.-%) when starting from the stoichiometric hexammine copper bromide. If one was to assume the decomposition product was the pure dihalide, however, then calculating the number of ammonia molecules in the starting materials as above, then this would result in a number of $n = 4.7$. The appearance of nitrogen in the evolved gas analysis does however coincide with the third peak and therefore the identity of the sample as one pure compound of known composition is dubious, especially as the 1:1 mixture of CuBr and NH_4Br that would arise from the reaction discussed above would have a similar molecular weight to the monoammine compound (different by only one mass unit).

4.5. Single Crystal Growth Under controlled atmosphere

While complexes are easily observed in solution and have been extensively studied,[6] solid state structures are more difficult to obtain in some cases. This is partly due to the fact that crystals of ammine complexes suitable for single crystal diffraction experiments are not straightforward to obtain and often require the use of super-critical ammonia[7] as a solvent which makes the reaction difficult and potentially dangerous. The most common ways to prepare solid ammine complex salts are either by the reaction of gaseous ammonia with a transition metal salt dissolved in an non-aqueous solvent[8,9] or by the direct reaction of the transition metal salt with gaseous or liquid ammonia.[2,10,11] Obtaining crystals from aqueous solutions is only possible when the crystal growth is fast enough to avoid the evaporation of dissolved ammonia from the mother liquor.[12] One such example is the growth of $[Ni(NH_3)_6](NO_3)_2$ from $[Ni(H_2O)_6](NO_3)_2$ and $NH_{3(g)}$ in an *in situ* crystal growth presented in section 5.3. Such fast reactions however normally result in the formation of polycrystalline samples. The following section describes a novel technique to grow crystals of ammine metal salts from aqueous solution that are suitable for single crystal diffraction analysis. A small but constant flow of ammonia gas over the mother liquor was introduced to saturate the mother liquor at all times and to remove evaporated water from the gas phase to allow further evaporation and concentration of the solution. Three compounds obtained in this way will be presented in this thesis:

$[Cu(NH_3)_{6\text{-x}}]Cl_2$ in this chapter and $[Ni(NH_3)_6](NO_3)_2$ and $Cu(NH_3)_4(NO_3)_2$ in chapter 5. The general procedure that was used for all three samples is discussed in the first section of this chapter.

The motivation for investigation of these three compounds chosen was different: The crystal structure of $[Cu(NH_3)_{6\text{-x}}]Cl_2$ had only been determined by Rietveld refinement from powder data[9] and classical crystal growth techniques had proved unsuccessful. Given the structural ambiguities in the system caused by the Jahn-Teller distortion and the non-stoichiometric behaviour, the application of the growth of crystals under ammonia atmosphere allowed the first single crystal analysis of the compound. The system $Cu(NO_3)_2$–NH_3 was chosen because no hexammine or pentammine structure is known in this system and the highest ammine determined so far is tetrammine copper nitrate.[13,14] The aim of this study was therefore to test whether a higher ammine in the system could be obtained by controlling the atmosphere. The study was further extended to the synthesis of $[Ni(NH_3)_6](NO_3)_2$ to test a different metal cation and to determine the low temperature structure of $[Ni(NH_3)_6](NO_3)_2$ by single crystal diffraction.

4.5.1. Growth of single crystals

As mentioned above, no single crystal growth for $[Cu(NH_3)_{6\text{-x}}]Cl_2$ has been reported previously and common methods (e.g. slow evaporation from aqueous solution, crystal growth from liquid ammonia) failed when they were tested during this work. Although $CuCl_2$ reacts very quickly in liquid ammonia, yielding a blue product, this reaction product is virtually insoluble in liquid ammonia as might be deduced from the fact that the liquid phase remains colourless during the experiment. This behaviour has already been observed in earlier experiments.[15] The same situation is the case in organic solvents, such as ethyl acetate, in which $CuCl_2$ is soluble but in which the ammine complex is insoluble. This then leads to quick precipitation upon introduction of NH_3.[9] Secondly, crystallisation by slow evaporation from an aqueous solution is not directly possible because of the higher evaporation rate of NH_3 from such solutions. The higher partial pressure of NH_3 renders classical techniques such as the cooling of warm saturated solutions or the slow evaporation of water almost impossible because NH_3 evaporates quicker than water under such circumstances. Nevertheless, an excess of NH_3 is crucial for the formation of ammine complexes to prevent competing formation of $Cu(OH)_2$ in alkaline solutions. The introduction of a pure ammonia atmosphere over the mother liquor circumvents this problem as it saturates the solution at all times. A flow of ammonia is necessary to remove evaporated water from the vapour phase to allow further evaporation.

The high concentrations of NH_3 in the solutions introduced through the control of atmosphere lower the evaporation rate of H_2O significantly as, according to Raoult's law,[16] the H_2O fraction in the gas phase is much lower than for pure water. The crystallisation process can be modified in three crucial ways to take account of this slower evaporation: Firstly, the reaction was performed in a bespoke reactor designed in house which allowed, by rotation from a vertical to a nearly horizontal position, the modification of the area of the liquid-gas interface and therefore the evaporation rate. Secondly, the evaporation rate could be modified by altering the ammonia flow rate, which directly influences the composition of the gas phase and avoids saturation with water vapour. As long as the ammonia flow rate is high enough to avoid full saturation of the gas phase with water vapour, it proved beneficial to raise the temperature of the reaction slightly above room temperature. This allows quicker evaporation of water from the mother liquor and can therefore significantly increase the reaction time. A temperature of 35-40 °C provided a good balance between evaporation and crystal growth. It is important to point out that if the solution is heated, it has to be guaranteed that the evaporated water

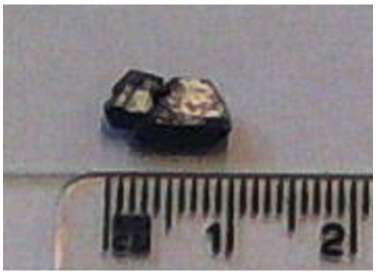

Figure 4.11.: Photograph of a crystal of $[Cu(NH_4)_4](NO_3)_2$.

does not condense on the walls of the reaction vessel and drains back into the solution because this would provoke re-dissolution. This can be avoided by heating the entire reaction vessel (including the gas outlet) rather than heating only the solution itself (e.g. by placing the reaction vessel in a drying oven). Alternatively the gas outlet can be engineered to be located near the solution surface so that any water that condenses does so in the outlet gas line rather than in the reaction vessel itself. This led to the formation of crystals of sizes sufficient for single crystal analyses, sometimes remarkably bigger. An impressive case is shown for $[Cu(NH_4)_4](NO_3)_2$ in Figure 4.11. The quality of the crystals obtained by this process is not ideal, however, and twinning or intergrown crystals are often observed. Nevertheless, we were able to determine and refine the single-crystal structures to an acceptable level and most notably were able to obtain single-crystal data for $[Cu(NH_3)_{6\text{-}x}]Cl_2$ for the first time.

4.6. Structure of $[Cu(NH_3)_{6\text{-}x}]Cl_2$

It is to some extent surprising that neither the structure of $[Cu(NH_3)_{6\text{-}x}]Cl_2$ nor of any other hexammine copper halide has been determined by single crystal methods. All preceding work was performed using Rietveld techniques on powders obtained from salts precipitated from organic solutions.[9] This is mainly due to the difficulties discussed

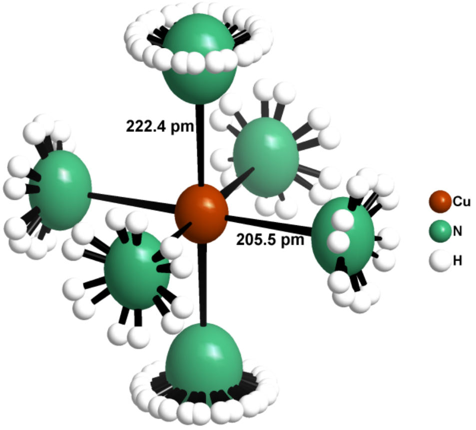

Figure 4.12.: Representation of one $[Cu(NH_3)_{6-x}]^{2+}$ pseudo-octahedron. The atoms are being represented by their ellipsoids at the 50 % probability level and the Cu–N distances are given in pm.

above and the low equilibrium constants for the uptake of a fifth and sixth ammonia molecule,[17] making the hexammine formation unfavourable when the ammonia content in the mother liquor is not sufficiently high. Using crystal growth under ammonia atmosphere leads to the formation of blue single crystals within several days of water evaporation. These crystals are of mediocre quality and all crystals tested consisted of at least two intergrown individua. This made the crystal choice particularly difficult and uncovered a relatively wide spread of possible cell parameters, especially on the crystallographic *c*-axis, which also displayed high e.s.d.s. It was however possible to obtain data suitable for refinement by single crystal analysis by using the Cell_Now software for indexing.[18] The dataset chosen for further analysis was obtained from a crystal agglomeration with one predominant individuum. The integration of this individuum only yielded a usable dataset, which was then used to refine the structure (Table 4.8). The low precision of the cell parameters is believed to correlate with the ammonia deficiency, also observed by Rietveld refinements (see also section 4.3.1).

Table 4.6.: Atomic positions, isotropic displacement parameters and occupancy factors in $[Cu(NH_3)_{6\text{-}x}]Cl_2$ as refined from single crystal data

Atom Site	X	Y	Z	U_{iso}/U_{eq} /Å^2	SOF
Cu1	0	0	0	0.0594(7)	1
N1	0.2014(7)	0.2014(7)	0	0.095(3)	0.97(2)
H1A	0.2935	0.1674	0.0556	0.114	0.243(5)
H1B	0.1532	0.3077	0.0298	0.114	0.243(5)
H1C	0.2446	0.2163	–0.0854	0.114	0.243(5)
N2	0	0	0.230(2)	0.128(7)	0.89(3)
H2A	0.0482	0.1058	0.2603	0.154	0.112(4)
H2B	0.0675	–0.0947	0.2603	0.154	0.112(4)
H2C	−0.1157	–0.0112	0.2603	0.154	0.223(7)
Cl2	0.5	0.5	0.25	0.0792(9)	1

$[Cu(NH_3)_{6\text{-}x}]Cl_2$ crystallises in the tetragonal space group $I4/mmm$ as previously shown by Distler and Vaughan.[9] It consists of $[Cu(NH_3)_{6\text{-}x}]^{2+}$ pseudo-octahedra surrounded by isolated Cl^- anions (Figure 4.13) in a distorted fluorite-type structure, otherwise similar to that of the nickel hexammine salts (see chapter 4). The most eye-catching feature of these complexes is the Jahn-Teller distortion, which is expressed by a symmetry reduction from the parent K_2PtCl_6 structure-type ($Fm\bar{3}m$) into the $t3$ *translationengleiche* sub-group $I4/mmm$[19] provoking the splitting of the unique ammonia position (Wyckoff position 24e) in the cubic parent structure into two crystallographically independent ammonia positions. The equatorial four-fold ammonia position (Wyckoff position 8h) herein describes the contracted square-plane, while the two-fold position (Wyckoff position 4e) describes the elongated axial environment that completes the pseudo-octahedron (Figure 4.12). Interestingly, these two crystallographically independent positions also show distinctive differences in their chemical behaviour. The axial site is only 80 % occupied, while the equatorial site does not show significant deviation from unity. This leads to an overall formula of $[Cu(NH_3)_{5.7(2)}]Cl_2$ (*i.e.* $x = 0.3(2)$). In line with many other hexammine salts, the hydrogen atoms within the ammonia ligands show a great

Table 4.7.: Anisotropic displacement parameters in $[Cu(NH_3)_{6-x}]Cl_2$ as refined from single crystal data in Å^2

Atom Site	U^{11}	U^{22}	U^{33}	U^{12}	U^{13}	U^{23}
Cu1	0.0542(7)	0.0542(7)	0.0699(11)	0	0	0
N1	0.079(3)	0.079(3)	0.127(6)	–0.004(4)	0	0
N2	0.111(7)	0.111(7)	0.162(15)	0.000	0	0
Cl2	0.0800(12)	0.0800(12)	0.0775(17)	0.000	0	0

Table 4.8.: Refinement summary for the single crystal analysis of $[Cu(NH_3)_{6-x}]Cl_2$ at 295 K.

Sum formula	$Cl_2CuH_{17.1}N_{5.7}$
Space Group	$I4/mmm$
a /Å	7.2161(9)
c /Å	9.685(2)
V /Å^3	504.3(2)
Measurement range	$-6 \leq h \leq 7$
	$-7 \leq k \leq 8$
	$-10 \leq l \leq 11$
Measured Reflections	769
Independent Reflections ($I > 2\sigma$)	156(143)
R_{int}	0.071
R_1 [$F_o^2 > 2\sigma$]	0.048
wR_2 all F_o^2	0.130
Parameters	14
$Goof$	1.19
$\Delta\rho$ [max, min] /(e^-/Å^3)	0.63;–0.36

rotational freedom perpendicular to the Cu–N bond.[20–22] This makes the determination of the hydrogen positions impossible and a rigid body model with typical apparent N–H distances set through SHELXL was used to describe the electron density attributed to the ammonia molecules.

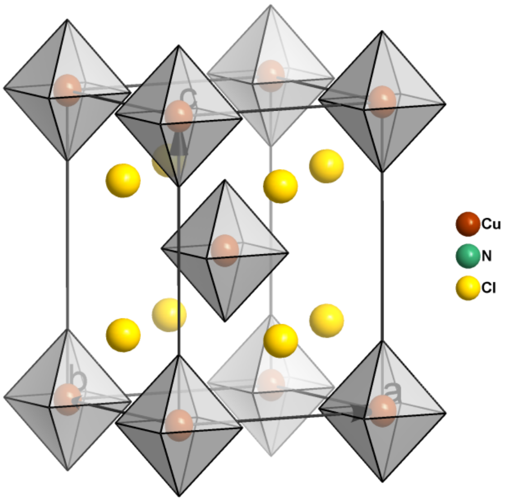

Figure 4.13.: Representation of a unit cell of $[Cu(NH_3)_{6-x}]Cl_2$ with Cl and Cu atoms being represented by their ellipsoids of 70 % probability. The ammonia molecules on the corners of the distorted octahedra are omitted in the image.

4.7. Neutron refinement of $[Cu(ND_3)_6]Cl_2$

The unique advantage of neutron diffraction is its different way of interaction with matter. While X-rays mainly interact with the electron cloud of the atoms, and the atom's scattering power is therefore proportional to its atomic mass, neutrons only interact with the nuclei of the atoms. This has the consequence that the scattering power of atoms is not dependent on their mass but rather on their particular nucleus. This extends to the fact that different isotopes of the same element can have dramatically different scattering lengths, as is the case for hydrogen. Normal ^1H hydrogen has a coherent scattering length of –3.7406 fm, while Deuterium (^2H) has a dramatically different scattering length of 6.671 fm.[23] It is this particularity which allows the exact determination of hydrogen (or more precisely deuterium positions) in a diffraction experiment and this principle was used for this experiment. The main aim of this experiment was to be able to verify the ammonia non-stoichiometry on the axial site by two independent parameters. While the main scattering component of the ammonia molecule using X-rays arises from the nitrogen atoms, the scattering lengths of deuterium and nitrogen (9.36 fm)[23] are in the same range but different enough model the exact contributions. In order to do so, a sample of $[Cu(ND_3)_6]Cl_2$ was prepared in very much in the same way as the conventional samples, by the reaction of anhydrous $CuCl_2$ with gaseous deutero-ammonia ND_3 at ambient conditions. In order to limit the losses of the expensive isotope gas, the reaction was not conducted with a large stream of deutero-ammonia but rather with such small amounts that a constant atmosphere of ND_3 that ambient pressure was maintained. This was guaranteed by regulating the incoming ND_3 flow so that the liquid level in the connected outstream bubbler remained at a constant level.

As for the other refinements throughout this work, Jana2006 was chosen as refinement program, due to its very effective way of applying constraints and restraints, which was of much use during the refinement. The initial peak fitting procedure however proved non-trivial using Jana2006, because the program does not use the Ikeda-Carpenter type rise-and-decay function and a new profile had therefore to be fitted from scratch (see chapter 3). It was however possible to refine the profile using a simple rise-and-decay function and a converging structural model could be developed and refined (Table 4.9, figures 4.14 and A.22–A.25). It is important to mention that the fitting between model and data is somewhat non-ideal. This is mainly due to the fact that, despite the large d-spacing range covered in the experiment, only isotropic displacement parameters were refined. This is on the one hand beneficial for the comparison with the refinement from X-ray powder data presented earlier, but is also a consequence of the complications in the model explained employed in the refinement. The free refinement of the anisotropic displacement parameters led to a better fit, but some of the displacement parameters took unreasonable values. One of the most striking unreasonable values, the strong elongation of the Cu-atom along the crystallographic c-axis, did give rise to the speculation that the space group attribution $I4/mmm$ may be wrong and that the Cu atom was in reality shifted away from the (then no longer existent) inversion centre. This however could not be verified after transforming the space group to the non-centrosymmetric subgroup $I4$ and it is hence assumed that this effect, which can be observed in the X-ray patterns as well, is mostly due to the higher degree of freedom of the central atom in the direction of the weaker bound axial ligands and a more detailed discussion will be made in the following section. All these considerations however resulted in the decision to use the isotropically refined model fir the further discussion.

Table 4.9.: Crystallographic data for $[Cu(NH_3)_{5.35(3)}]Cl_2$

Sum formula	$Cl_2CuD_{15.145}N_{5.421}$
Crystal System	tetragonal
Space Group	$I4/mmm$
a / Å	7.2670(2)
b / Å	9.3838(3)
V /Å^3	495.56(3)
Z	2
Calculated Density, ρ_x /g·cm^{-3}	1.6143
All Detector Banks	
R_p; wR_p	0.033; 0.042
Goof	3.08

4.7.1. Deuterium arrangement in $[Cu(ND_3)_6]Cl_2$

The first and foremost observation that can be made when regarding the neutron data as opposed to the X-ray data is the significant contribution of the deuterium scattering power to the overall model. By contrast to the model employed in the X-ray refinement, where the hydrogen position was set by the position of the nitrogen atoms, the positions of the deuterium atoms can be determined independently from the neutron diffraction data. Due to the strong overlap of several deuterium positions and the relatively high degree of rotational freedom of these groups, a set of constraints and restraints derived from chemical knowledge was used to improve the physical meaning of the model.

The first and probably most important restraint used in the model was to define that all N–D distances within the molecule shall be approximately equal. This is due to the fact that the ammonia molecules in the coordination sphere, although being chemically distinct, should share the same overall shape and the N–D bonding distance should remain largely unaffected by the different coordinations. It furthermore was set in place to guarantee a physically sound bonding situation where more than one deuterium position

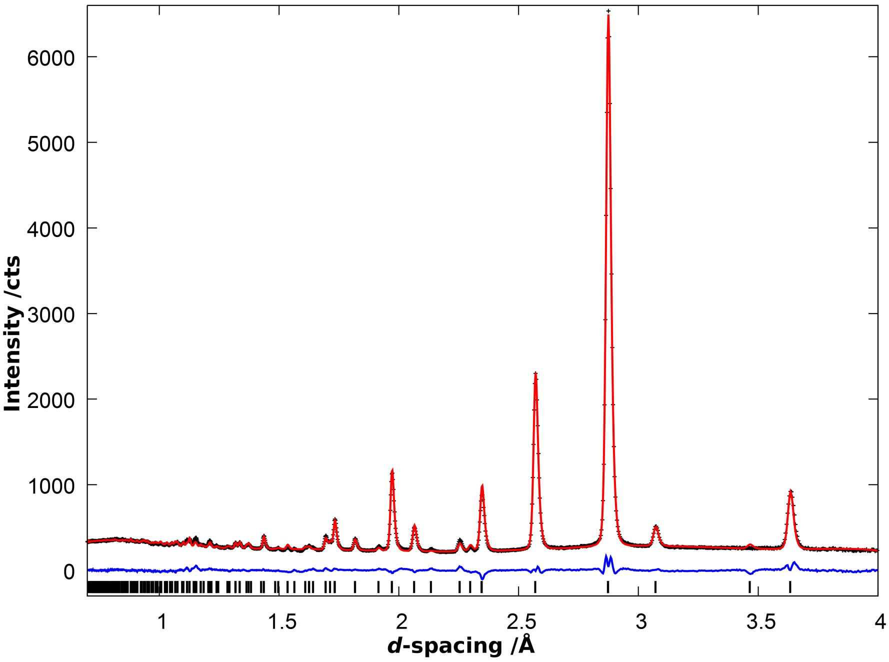

Figure 4.14.: Comparison of the observed (black crosses) and calculated patterns (red line) from the Rietveld refinement against PND (detector bank 4) data for $[Cu(NH_3)_{5.35(3)}]Cl_2$ at room temperature. The blue line represents the difference profile ($I_{obs} - I_{calc}$) and the black tick marks indicate the theoretical reflection positions.

was used to describe the ammonia orientation and to avoid the situation where one deuterium position was refined to a model where the remaining nuclear density of the other was “lost”. From similar considerations, it was also stipulated that those deuterium atoms bound to the same nitrogen atom should have the same displacement parameters, again ensuring that distinct sites rather than diffuse density was considered in the model.

The ammonia arrangement on the equatorial site about the Cu could be described with two deuterium positions (Figure 4.15 a). The loss of the 4-fold axis in the transformation from the $Fm\bar{3}m$ aristotype to the $I4/mmm$ structure allows a more distinct description of the molecule and the predominant pseudo four-fold hydrogen position observed in cubic hexammine structures[22] is distorted from the exact four-fold symmetry (site D1_2 in Figure 4.15 a). Besides this, a second deuterium position (D1_1) lying on the mirror plane perpendicular to (002) was found in the difference Fourier map. These two positions together allow two opposite arrangements of the nearly tetrahedral ammonia molecule shape (with the Cu central atom as the fourth corner of the tetrahedron). As can be easily deduced from the molecular shape, each of the two possible arrangements of the ammonia molecule will occupy two of the D1_2 sites and one of the D1_1 sites. As the multiplicity of the D1_1 is exactly half of the multiplicity of the D1_2 site, the overall occupancy of both sites should hence be equal (and in theory exactly 0.5 of the full occupancy) and this relationship was constrained, as well as the displacement parameters, in order to yield more realistic refinements. This treatment allowed to extract important information from the model as to whether the nitrogen occupancy (which was fixed to unity during the refinement) and the combined deuterium occupancy would match. This information is important due to the fact that even small traces of hydrogen would cause big shifts in the deuterium occupancy, because hydrogen has a negative scattering length whereas that of deuterium is positive. The refinement yielded an occupancy of 95.4(6) % of the deuterium site, suggesting a small contamination of the sample with hydrogen. This is also supported by the IR spectrum of the deuterated sample (Figure 4.16), which shows a small band at 3260 $\mathrm{cm^{-1}}$ corresponding to N–H stretching modes. The refined angle D1_2–N1–D1_1 is 115.1(2)° and therefore slightly larger than that in molecular ammonia (107.3°). This can be partly explained by the polarisation of the nitrogen lone-pair through the ligand bonding but it is nevertheless important to emphasise that this angle is prone to some error resulting from the heavily distorted ammonia arrangement. In addition, this particular arrangement has the consequence that the deuterium atoms on the D1_2 site point in the direction of the chlorine anions indicating hydrogen bonding. The deuterium atom on the D1_1 site is not in a position to form any hydrogen bonds and this particular situation can distort the molecule further.

While the deuterium positions associated with the equatorial N site do contain nearly perfectly shaped ammonia arrangements, the same is not true for those associated with the

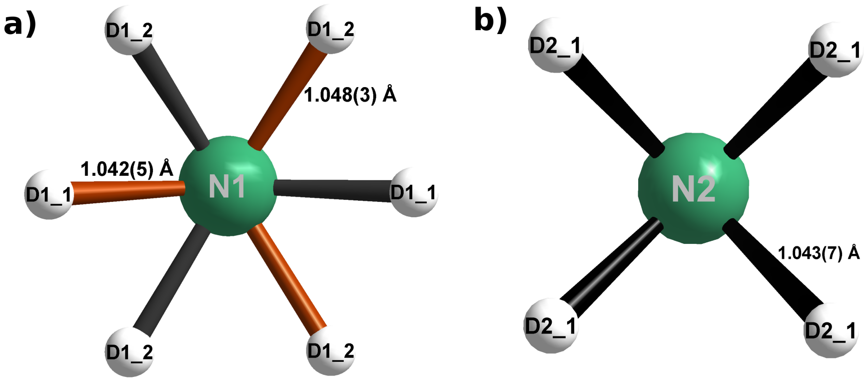

Figure 4.15.: Representation of the refined shapes of the ammonia molecules in $[Cu(ND_3)_6]Cl_2$. The equatorial site about the Cu (a) is defined with two deuterium positions allowing two opposite arrangements of ND_3 molecules marked with grey and brown bonds respectively. The axial N site (b) is only associated with one deuterium site.

N axial site. Only one deuterium position could be located during the refinements (Figure 4.15 b) which, due to the crystallographic four-fold axis running through the principal axis of the molecule, forms a square of ammonia positions. Despite the fact that this arrangement cannot explain the tetrahedral shape of the ammonia molecule, no obvious density contribution could be located in the difference Fourier map. This particular arrangement is consistent with observations in non-distorted ammine structures[22] and is therefore likely to describe the major contributions of the nuclear density.

4.7.2. Refinement of the ammonia deficiency

Instead of simply refining nitrogen and deuterium deficiency, which could lead to strong overlap of the density distribution between the atoms and may yield incorrect values, the system was constrained using the deuterium deficiency as refined on the equatorial site using the following equation:

$$a_i[\mathrm{D2\_1}] = 3.a_i[\mathrm{N2}] - a_i[\mathrm{N1}] + a_i[\mathrm{D1\_1}] \tag{4.3}$$

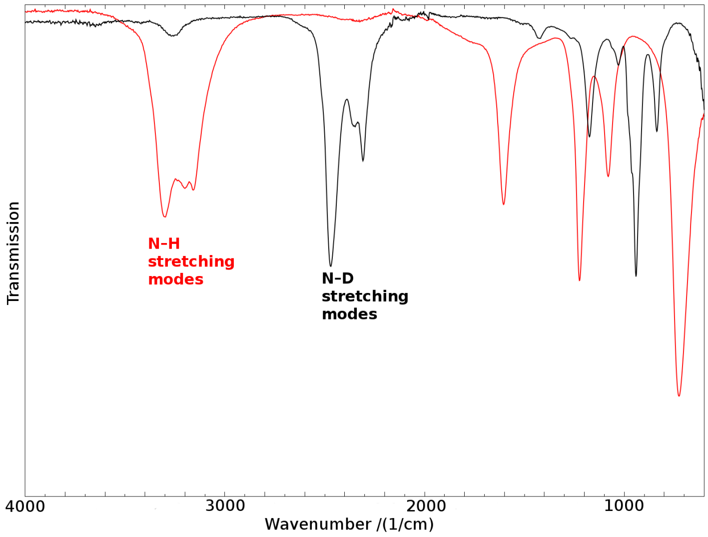

Figure 4.16.: Comparison of the mid IR of $[Cu(NH_3)_{6\text{-}x}]Cl_2$ (red) and $[Cu(ND_3)_{6\text{-}x}]Cl_2$ (black).

with a_i being the respective atom site occupation. It is important to note here that a_i is not defined as the fractional occupancy but as the occupancy divided by the multiplicity of the site. Hence, a_i is 1 on the general site but smaller on a special position. While the deuterium positions could lie on sites with different multiplicities, a_i will always retain the same value and the formula implication is hence much simpler as compared to a refinement where occupancies are used. The first term $3.a_i[\text{N2}]$ accounts for ammonia occupancy while the second term $-a_i[\text{N1}] + a_i[\text{D1\_1}]$ accounts for the D/H partial occupancy as refined on the equatorial site. This leads to a stable refinement of the structure, giving an occupation of 67.3(3) % on the axial ammonia site.

Table 4.10.: Comparison of the Cu–N bond lengths refined by different methods.

Refinement	$a_i(NH_3)$	d(Cu–N$_1$) /Å	d(Cu–N$_2$) /Å
Powder X-ray	0.68(2)	2.026(9)	2.404(1)
Powder Neutron	0.67(1)	2.112(2)	2.267(8)
Single Crystal	0.89(3)	2.055(7)	2.22(2)
Powder X-Ray[9]	1*	2.07(7)	2.6(1)

* was unrefined set to unity.

4.8. Comparison of the Different Refinements

Bond Lengths in the Complex Cation

When comparing the Cu–N distances throughout the different refinements (Table 4.10), it is evident that the axial Cu–N distances vary strongly. This also applies, to a lesser extent, to the equatorial Cu–N distances. These strong deviations advocate a high degree of structural freedom within the complex environment. No clear correlation between the ammonia occupancy and the bond distances can be drawn, however, and further study using direct probes of the coordination environment will be indispensable to clarify the nature and extent of the structural variations. The different samples do differ slightly in their preparation route and this may have an effect on the exact chemical environment and hence on the structural situation.

Ammonia deficiency

The main difference arising from the different analyses from a practical point of view is in the occupation of the axial site of the complex cation (Table 4.10). While the occupation in the single crystal was refined as 89(3) %, the value from the powder diffraction was only 68(2) % while the neutron refinement yielded an occupancy of 67.3(3) %. It is notable that the two powder samples prepared in a similar way exhibit the same non-stoichiometric behaviour while the single crystal sample, prepared from aqueous solution under ammonia flow, shows a significantly lower level of ammonia deficiency. It is therefore likely that the synthesis route has an important impact on the chemical composition of the product.

The uptake into the sample characterised by powder X-ray diffraction was also monitored gravimetrically (section 4.3.1). The gravimetrically obtained degree of conversion (95.6(7) %) is higher than the conversion degree calculated on the basis of the Rietveld refinement (89.2(5) %) but this may be caused by a small loss during the X-ray sample preparation once the sample was removed from the saturated ammonia atmosphere.

Unit Cell Parameters

With respect to the cell parameters, the values obtained from powder diffraction can be assumed to be more precise than those from the single crystal analysis. This is firstly due to the different methods and the fact, that the zero position of a powder diffractometer can be determined with a much higher degree of freedom, but secondly also due to the nature of the different samples. While the analysed single crystal used in the previously presented analysis contained few crystallites with partly overlapping reflections and hence a degree of uncertainty in the exact peak position, this problem does not exist in the powder diffraction experiment. Even if the cell parameters from one crystallite to another differ significantly, such behaviour would express itself in the profile of the peaks. If only one of the cell parameters is affected, a subset of reflections would show a different peak broadening to the others, while all peaks would be broadened if the cells are isotropically different from each other. The peak position however could still be determined without major uncertainty, especially in cases of high symmetry patterns, where overlapping peaks do not pose a major problem. Neither anisotropic peak broadening nor a particularly strong isotropic peak broadening was however found in this analysis and it must therefore be assumed that the difference in cell parameters between the powder diffraction experiment and the single crystal experiment is primarily caused by the difference in the exact chemical composition of the two compounds measured.

4.9. On the nature of the NH_3 deficiency

The deviations of the different crystal structure refinements (Table 4.11*) and the remarkable elongation of thermal ellipsoids of Cu when refined anisotropically raise the question of the true complex formation situation in the the pseudo hexammine compounds. It is manifest throughout all analyses, gravimetric and crystallographic, that the compound does indeed not form as the stoichiometric hexammine compound but instead as a sub-stoichiometric compound with a somewhat variable ammonia content. This observation is in fact substantiated by older publications in which the hexammine copper halides are described as being very unstable and prone to ammonia loss at room temperature.[3,24] It is not the case that the compounds here can be classified as stoichiometric pentammine complexes, however, as earlier reports would propose.[2] Given the compounds do not contain a stoichiometric number of ligands, more than one coordination environment must co-exist in the structure. It is this nature of more than one coordination environment, which makes the crystallographic analysis cumbersome and leads to unreliable Cu–N coordination distances.

---

*It is remarkable that the main differences between the different structures are manifested in the distances between two neighbouring axial ammonia molecules (N2) and that this distance seems to roughly coincide with the occupancy: the more ammonia on the site, the further neighbouring molecules are away.

Table 4.11.: Comparison of the inter-molecular distances and angles in $[Cu(NH_3)_6]Cl_2$ as determined by single crystal, powder X-ray and neutron diffraction. The distances in the table are the respective shortest distances in the structure.

	Single Crystal	**Powder**	**Neutron**
Refined NH_3 cont.	5.7(2)	5.35(2)	5.35(3)
Cu–Cl /Å	4.3451(4)	4.3418(1)	4.3239(1)
Cl–N_1 /Å	3.552(4)	3.537(7)	3.509(1)
Cl–N_2 /Å	3.613(1)	3.6468(2)	3.6331(2)
Cl–N_1–Cu	98.0(1) /°	99.0(1)	97.6(1)
Cl–N_2–Cu	93.1(1) /°	89.3(1)	90.9(1)
N_1–N_1 /Å	4.310(7)	4.43(1)	4.288(2)
N_2–N_2 /Å	5.23(3)	4.62(2)	4.81(1)
N_1–N_2 /Å	4.02(1)	3.89(1)	3.870(5)

A molecular structure optimisation using NWChem[25,26] for the haxammine and pentammine copper complex cations was performed to elucidate likely complex configurations. In order to facilitate the convergence by applyinge symmetry restrictions, the hexammine was restricted to have orthogonal N–Cu–N angles and the distances were grouped together: the equatorial distances in one subset and the axial bonds in another. The result of the structure optimisation (Figure 4.17 b) is in fact a Jahn-Teller distorted complex in which the axial ammonia molecules are over 0.3 Å further apart from the central Cu atom than the equatorial ligands. Such a strong distortion was not observed in the crystal structures themselves, which might be an effect of the crystal field or of the uncertainties in the crystal structures.

The structure optimisation for the pentammine complex was restricted in a similar way: the distances were grouped as above and the N_{axial}–Cu–$N_{equatorial}$ angle was grouped to effectively force the four equatorial ammonia molecules in one plane. The result of this optimisation (Figure 4.17 a) reveals that the Cu atom is lifted out of the plane towards

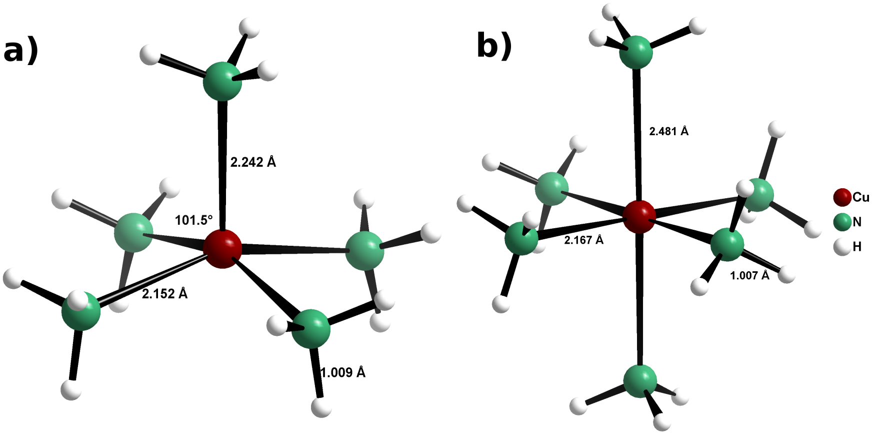

Figure 4.17.: Optimised structures for a) $[Cu(NH_3)_5]^{2+}$ and b) $[Cu(NH_3)_6]^{2+}$ in vacuum. The bond distances are given in Å.

the axial ligand. The copper atom is displaced 0.4 Å from the equatorial plane leading to a N_{axial}–Cu–$N_{equatorial}$ angle of 101.5°. It has to be noted that the comparably short Cu–N_{axial} distance is not unexpected as a square-planar coordination is not Jahn-Teller distorted because its ligand field is not degenerate. The postulate of a pentammine complex in which the Cu atom is raised from the equatorial plane is however consistent with the observation of thermal ellipsoids for the Cu atoms being elongated towards the axial ammine ligands. The anisotropic refinement was possible for the single crystal data and although the elongation is not very strong here (probably because the complex contains much more ammonia than those refinements from powder data), it is still observable.

In order to underpin this hypothesis of two different competing coordination environments on the complex position, more direct probes of the local coordination have to be taken into account, as crystallography averages both over time and space. The most straightforward techniques for the study of the local environment are spectroscopic studies and both the vibrational and electronic spectra of the compounds were measured to test the hypothesis.

Table 4.12.: IR band attribution for $[Cu(NH_3)_{6\text{-}x}]Cl_2$ in comparison with literature values.

Mode	$[Cu(NH_3)_{6\text{-}x}]Cl_2$	$Cu(NH_3)_6]F_2$ [28]	$[Cu(NH_3)_5]Cl_2$ [2]
$\nu_a(NH_3)$	3302(2)	3300	
$\nu_s(NH_3)$	3199(2)	3240	
$\nu_s(NH_3)$	3158(2)	3160	
$\delta_a(HNH)$	1604(2)	1600	1608
$\delta_s(HNH)$	1224(2)	1270	1225
$\delta_s(HNH)$	1081(2)	not observed	1087
$\rho(NH_3)$	726(2)	700	740

4.9.1. Mid IR spectroscopy

Mid infrared spectroscopy allows the direct measurement of molecular vibrations and in this case, the vibrational modes of the ammonia molecules. The bands in the measured spectrum (Figure 4.18) are all attributable to the vibration modes of the ammonia ligands (Table 4.12) and show little deviation from the literature values. The N–H vibration modes are reportedly not very sensitive to the complex coordination environment with the prominent exemption of the symmetric deformation mode.[27] This mode is in fact split in the spectrum measured, a feature which is observed in the pentammine compounds but not the hexammine compounds.[2] The band at 1087 cm^{-1} could be simply due to the symmetry lowering of the complex coordination but could also be interpreted as supplementary mode due to more than one coordination environment. Given the analyses performed herein, it is questionable whether the premise of Tomlinson and Hathaway[2] to assume stoichiometric hexammine and pentammine complexes of copper compounds is valid or whether the reported “pentammine” compound could be rather non-stoichiometric $[Cu(NH_3)_{6\text{-}x}]Cl_2$ with x being close to unity.

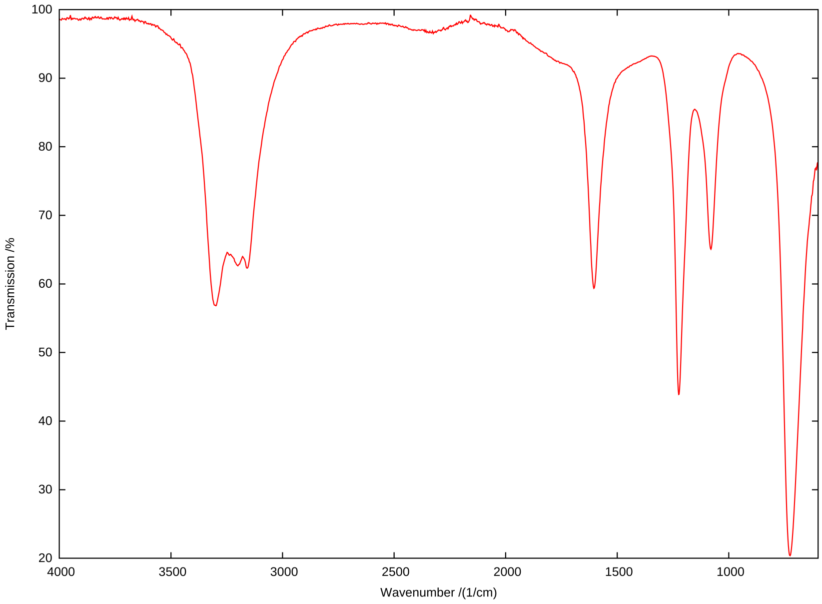

Figure 4.18.: ATR-IR spectrum of $[Cu(NH_3)_{6\text{-}x}]Cl_2$.

4.9.2. Far Infrared spectroscopy

Far Infrared spectroscopy gives a more direct insight into the coordination environment, as the metal-nitrogen vibrations can be observed directly. Conversely, the interpretation of the data is more complex as less reference data is available and peaks exhibit more overlap. In order to gather more information on the spectrum, it was deconvoluted using Gaussian functions to extract the peak positions (Figure 4.19, Table 4.13). The spectrum from 600 cm^{-1} to 150 cm^{-1} can be roughly divided into two regions: the peaks over ≈ 300 cm^{-1} can be attributed to the Cu–N stretching modes while the bands below 300 cm^{-1} are mainly stretching modes and lattice vibrations. Two strong Cu–N stretching modes can be found, one at 513.7 cm^{-1} and one at 403.2 cm^{-1}. This is consistent with the findings of Tomlinson and Hathaway on the pentammine copper chloride[2]. These two stretching modes can be explained with the two different Cu–N distances in the distorted complex which therefore have two different force constants. Regarding the shoulder of the lower energy band however, a third small band is apparent which may be due to a third Cu–N

Table 4.13.: Far infrared spectroscopy band fitting for $[Cu(NH_3)_{6\text{-}x}]Cl_2$.

$[Cu(NH_3)_{6\text{-}x}]Cl_2$	Relative Area	$[Cu(NH_3)_5]Cl_2$ [2]
513.7(6)	24.2	523 ν(Cu–N)
403.2(6)	26.7	405 ν(Cu–N)
367.6(6)	1	
253.0(6)	38.6	252 δ(N–Cu–N)
236.5(6)	8.8	
219.6(6)	15.3	
188.7(6)	55.3	

distance should exist. As the bond strength decreases with increasing bond length, the force constant of the vibrations equally decreases with increasing bond length leading to smaller wavenumbers for weaker bonds.[29] As a consequence of this principle, the band at 513 cm^{-1} can be attributed to the equatorial Cu–N stretching and no splitting would be expected in this peak as the equatorial Cu–N distances are comparably similar in the two complexes (Figure 4.17). The axial Cu–N distances are however considerably different for the two complex environments meaning a superposition would contain bonds with different force constants causing shifted FIR absorption. The interpretation of the region below 150 cm^{-1} is difficult, but the appearance of more bands than mentioned in the literature[2] may be taken as a hint for more than one coordination environment.

4.9.3. Further analyses and Future work

In order to clarify the nature of the Cu^{II} coordination environment in the non-stoichiometric hexammine copper chloride compounds conclusively, more direct information on the Cu-coordination has to be gathered.

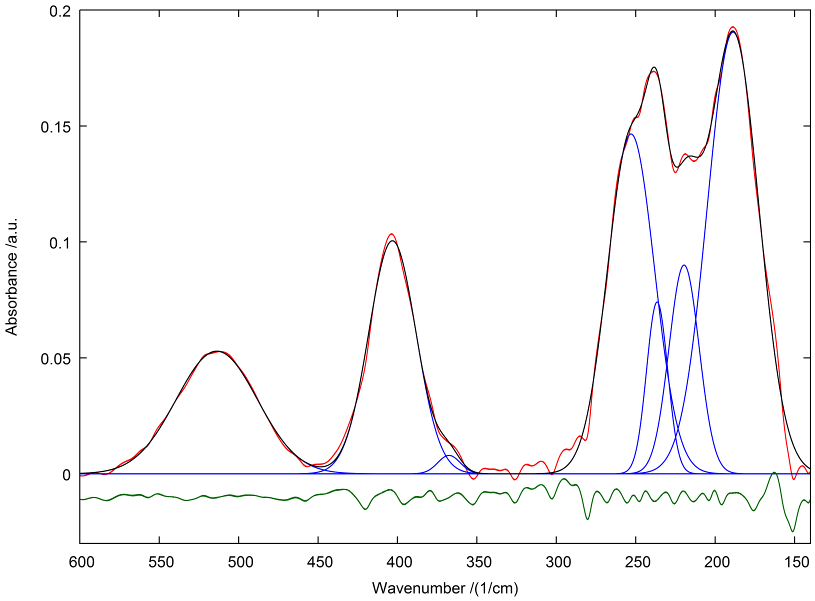

Figure 4.19.: ATR far IR spectrum of $[Cu(NH_3)_{6\text{-}x}]Cl_2$ (red) with a Gaussian fit (individual peaks: blue; overall function: black). The difference between measured and fitted pattern is given in green (shifted from zero for visibility reasons).

Inelastic neutron scattering could be one of the possible techniques for this purpose. Due to the low cross section of neutron scattering, this technique makes it possible to study the vibrations inside the solid even under ammonia atmosphere as $NH_{3(g)}$ only contributes very little to the scattering. Through this, a true study of the consequences of ammonia deficiency may be possible. Shortly before the writing of this thesis, a sample spectrum for $[Cu(NH_3)_{6\text{-}x}]Cl_2$ was taken at 30 K in order to assess the feasibility of such studies (Figure 4.20). While the resolution of the technique does not allow studies of the NH_3 modes in the higher energy region, the transitions in the lower energy region are well resolved. Very interesting is the splitting of the NH_3 rocking mode at $\approx$ 700 cm^{-1} into two groups of bands. This band splitting could be due to the different ammonia sites with different bond strengths. This effect may also be enhanced by the lower symmetry at low temperatures but a more detailed analysis has to be done to underline this point. It is however of great interest to have a closer look into the low energy region and to correlate the measured Inelastic neutron scattering to the FIR spectrum.

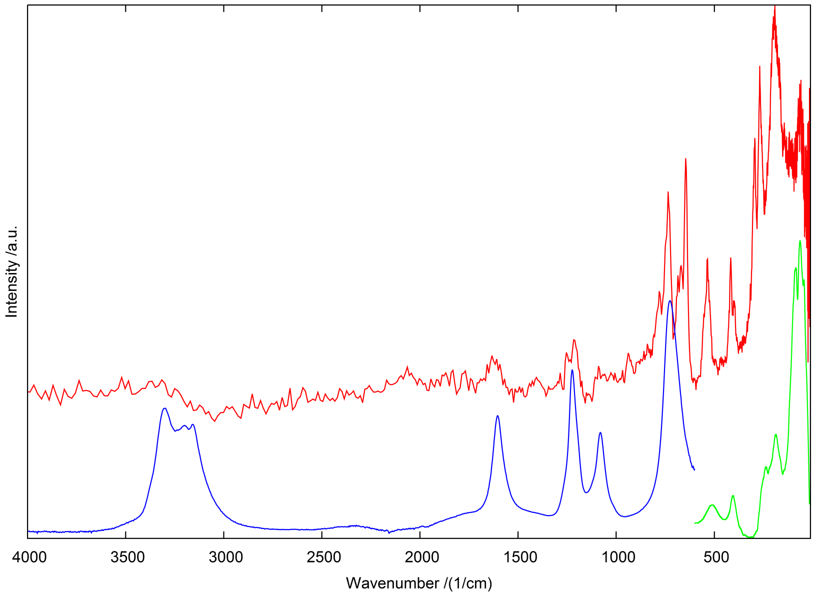

Figure 4.20.: Inelastic neutron scattering spectrum for $[Cu(NH_3)_{6-x}]Cl_2$ at 30 K (red) together with ATR-MIR (blue) and ATR-FIR (green) spectra.

The direct comparison of the INS data with the infrared spectra (Figures 4.20, 4.21, Table 4.14) reveals a good degree of similarity with the peak shift probably attributable to the different measurement temperatures. Given further interpretation of the INS spectrum, this preliminary results demonstrates the feasibility of further *in situ* experiments where the coordination environment could for instance be tested as a function of the temperature.

Table 4.14.: INS band fitting for $[Cu(NH_3)_{6-x}]Cl_2$ at 30 K.

INS /cm^{-1}	FIR /cm^{-1}	ΔINS-FIR /cm^{-1}
534(5)	513.7(6)	20
416(4)	403.2(6)	13
399(4)	367.6(6)	31
295(3)	253.0(6)	42
268(3)	236.5(6)	31
	219.6(6)	
194(2)	188.7(6)	

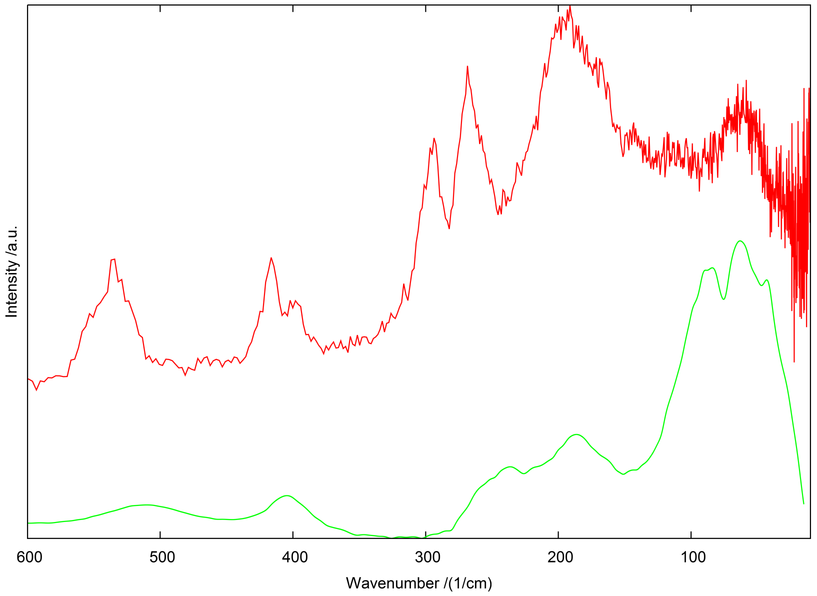

Figure 4.21.: Inelastic neutron scattering for $[Cu(NH_3)_{6\text{-}x}]Cl_2$ at 30 K (red) together with ATR-MIR (blue) and ATR-FIR (green).

4.10. Cubic $[Cu(NH_3)_6]X_2$ — Loss of Jahn-Teller distortion?

Examples where Cu^{II} exhibits a regular octahedral coordination in the solid state can mostly be explained by either dynamic rearrangements or static disorder of the complexes that consequently appear as regular octahedra.[30] However, use of local structure probes on many of these apparent regular octahedral coordination complexes has revealed a distorted environment along with a crystallographic distortion.[31] Genuine octahedral coordination of Cu atoms would lead to a forced degeneracy of the d-orbitals, which is normally far from the electronically ideal orbital splitting.[32,33]

$[Cu(NH_3)_6]Cl_2$, similar to many other Cu^{II} complexes, forms a distorted complex cation structure leading to crystallisation in the tetragonal space group $F4/mmm$ with two cell axes elongated and one compressed,[9] unlike other hexammine complexes such as $[Ni(NH_3)_6]Cl_2$ or $[Mn(NH_3)_6]Cl_2$ which crystallize in the cubic space group $Fm\bar{3}m$.[34–36] $F4/mmm$ is a non-standard setting of space group $I4/mmm$ but the former is however used in the following discussion to facilitate the comparison with the cubic cell. Similar cubic phases for the pentammine copper salts of bulkier anions $[Cu(NH_3)_5]X_2$ X = Br, I, (ClO_4), (BF_4) have previously been reported in the literature.[2,37] Cubic-to-tetragonal phase transition temperatures for such complexes can be partly as low as 142 K (e.g. for $[Cu(NH_3)_5](ClO_4)_2$)[38] where the higher symmetry lattice is stabilized by the bulkier anions and their dynamic reorientation. The results presented in section 4.3.1, however, do not match the previously reported cubic phase for $[Cu(NH_3)_6]Br_2$,[39] $[Cu(NH_3)_{6\text{-x}}]Br_2$ appeared as tetragonal phase in all our experiments at ambient temperature. It might be that the previously reported results were obtained at slightly higher “ambient” temperatures with the consequence that the structure was determine above a tetragonal-cubic phase transition.

4.10.1. *In-situ* observations under ammonia pressure

Unexpectedly, a tetragonal-to-cubic phase transformation for $[Cu(NH_3)_{6\text{-x}}]Cl_2$ was observed during an *in-situ* study of the ammonia uptake behaviour of metal halides on beamline I11 at the Diamond Light Source Synchrotron Facility. When ammoniating the sample at 253 K, the tetragonal phase formed as expected but subsequent heating ($4\ K\cdot min^{-1}$) resulted in the phase transformation from $F4/mmm$ to $Fm\bar{3}m$ at $\approx$350 K (Figure 4.22). This behaviour is explained by a *translationengleiche* increase in symmetry in the $F4/mmm$ – $Fm\bar{3}m$ subgroup-group relationship. The cubic phase remained stable up to 385 K above which the diammine structure was formed. A second sample was ammoniated in the beam at 353 K. This sample directly formed the cubic phase and upon

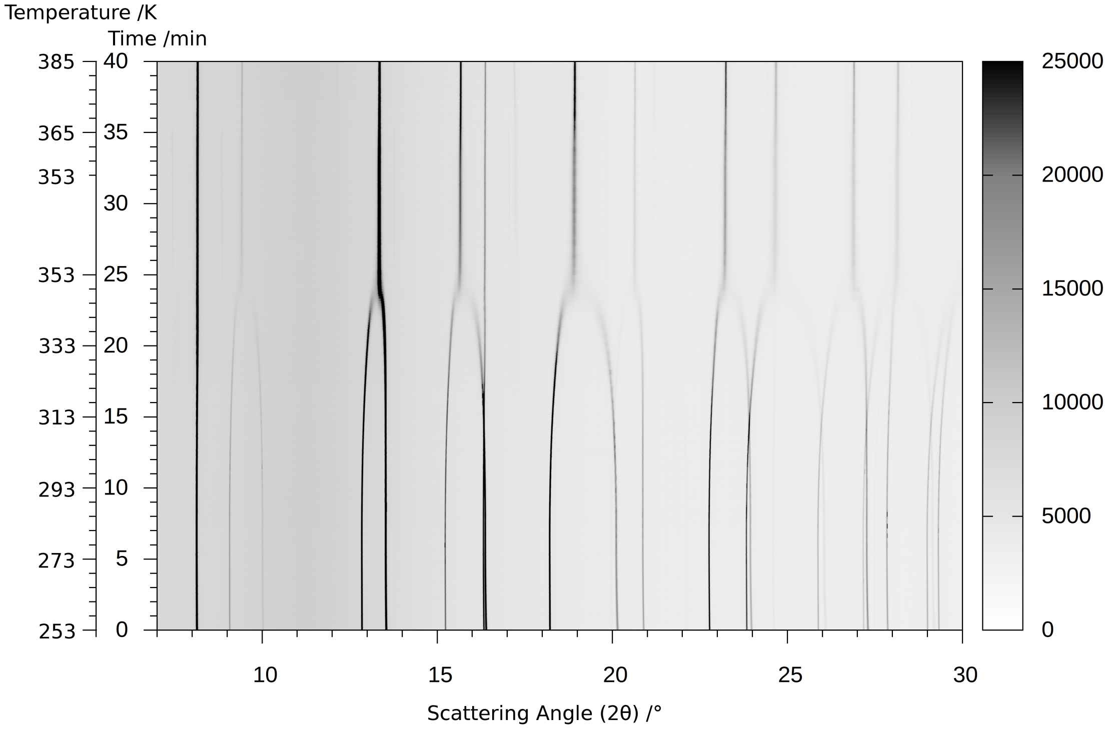

Figure 4.22.: Time resolved diffraction of $[Cu(NH_3)_6]Cl_2$ as a function of temperature during the heating process under ammonia pressure.

cooling to room temperature (–2 K·min^{-1}), the opposite phase transition from $Fm\bar{3}m$ to $F4/mmm$ proceeded at ≈330 K (Figure 4.23).

Refinement of the powder X-ray diffraction pattern of the cubic phase formed at 353 K was performed using Jana2006[1] to reveal the structure of the compound. Due to the experimental setup used for *in-situ* measurements in this experiment (*i.e.* the use of a position sensitive detector to allow time-resolved measurements), the diffraction pattern peak profile was not ideal for Rietveld refinements and no convergence could be reached when refining profile and phase parameters simultaneously. However, by doing a preliminary Le Bail fitting of the pattern and the subsequent fixing of all profile parameters apart from the background and scaling parameters, the structural model obtained by solving the structure with Superflip[40] was successfully refined and the

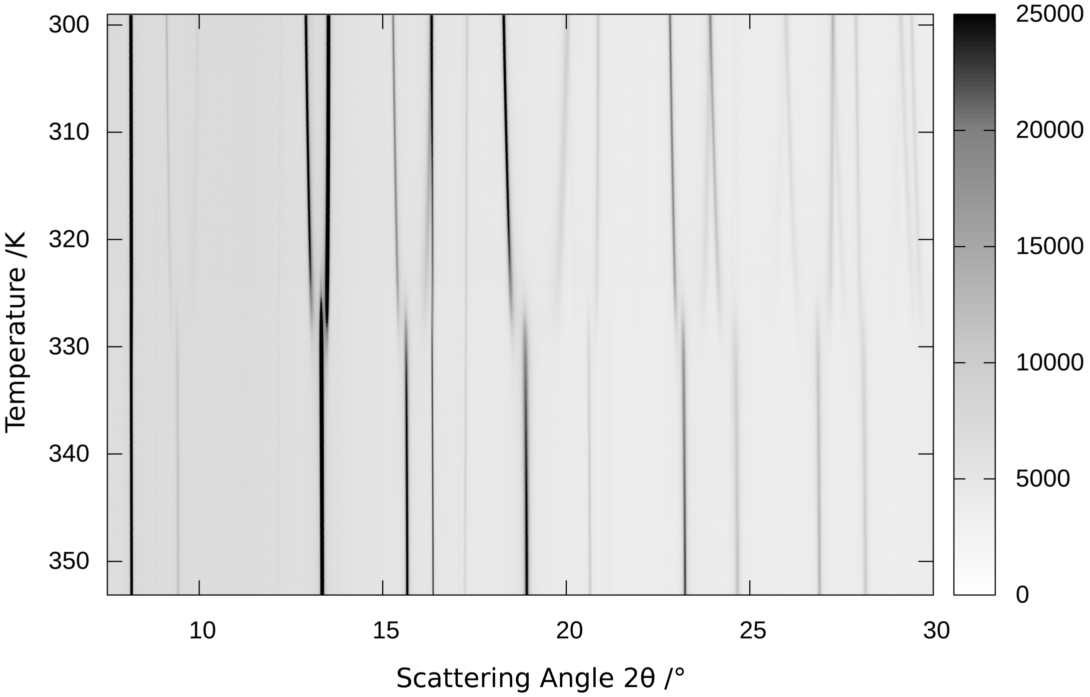

Figure 4.23.: Time resolved diffraction of $[Cu(NH_3)_6]Cl_2$ as a function of temperature during the cooling process under ammonia pressure.

refinement converged smoothly. (Figures 4.24 and 4.25, Table 4.15). A small CuO[41] impurity in the starting material was found to be present. Due to its low volumetric ratio (< 5 %) and its low crystallinity a refinement was not possible and it was omitted in the calculations (i.e. its phase ratio was set to zero, the peak positions are nevertheless shown in Figure 4.24).

$[Cu(NH_3)_{6\text{-}x}]Cl_2$ crystallises herein in the K_2PtCl_2 structure type, isostructural to the non-JT distorted analogues. The refined cell parameter of $a = 10.0425(5)$ Å and the refined Cu–N distance $d_{\text{Cu–N}} = 2.084(3)$ Å are close to the values expected for the analogous hexammine compounds (for $[Ni(NH_3)_6]Cl_2$: $a = 10.0800(1)$ Å, $d_{\text{Ni–N}} = 2.142(2)$ Å, see section 3.4). It was possible to refine a deficit on the ammonia site which is only occupied by 73.3(5) % leading to an overall composition of $[Cu(NH_3)_{4.40(3)}]Cl_2$. It is important to mention the ellipsoids of nitrogen are not elongated in the Cu–N bonding direction but

Table 4.15.: Refinement results for cubic and tetragonal hexammine copper chloride.

Temperature	**353 K**	**298 K**
Formula	$[Cu(NH_3)_{4.40(3)}]Cl_2$	$[Cu(NH_3)_{5.58(1)}]Cl_2$
Crystal system	cubic	tetragonal
Space group	$Fm\bar{3}m$	$F4/mmm$
***a*,*b* /Å**	10.0425(5)	10.3857(5)
***c* /Å**	10.0425(5)	9.500(1)
Volume /Å^3	1012.8(3)	1024.7(3)
Z	4	
Calculated Density, ρ_x /g·cm^{-3}	1.373	1.534
R_p; wR_p	0.037; 0.058	0.035; 0.051
Goof	3.56	3.22
R_{obs} ; wR_2 **(all)**	0.070; 0.066	0.078; 0.095

are stretched perpendicular to it. The refined structure from the powder pattern obtained at 295 K from a sample cooled on the diffractometer, formed in space group $F4/mmm$ (Table 4.15). Although the refinement suffers from the same drawbacks as the one for the cubic phase, a reasonable model could be obtained in which the $[Cu(NH_3)_{6-x}]^{2+}$ complex cation is strongly JT-distorted manifested by a strong anisotropy in the formerly equal cell parameters. When refining the ammonia occupation on the axial site (a simultaneous refinement for the occupancy on both nitrogen sites was impossible due to the strong correlation of both parameters), a much higher NH_3 content was found than at 353 K. Again, the shapes of the ellipsoids in the refinement are remarkable as they exhibit a strong elongation parallel to the Cu–N vector on the axial sites. This is attributed to the high degree of freedom in the Cu–N bond-length due to the non-stoichiometric ammonia content.

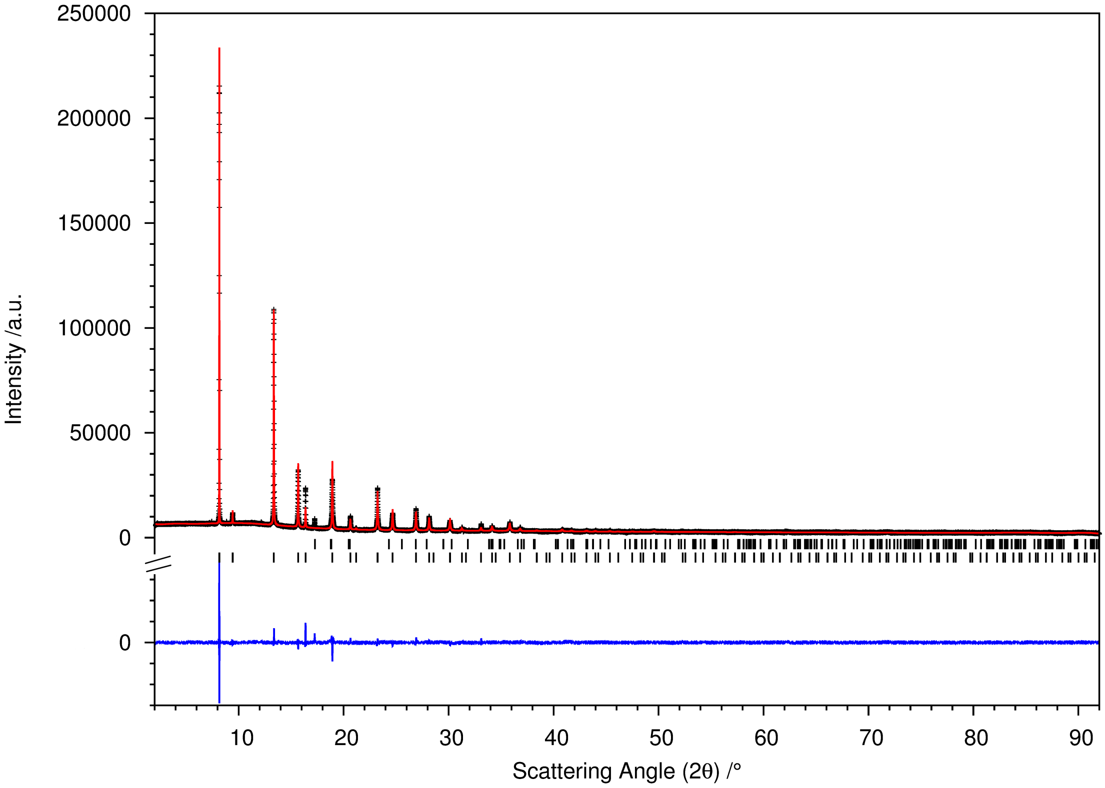

Figure 4.24.: Comparison of the observed (black crosses) and calculated patterns (red line) from the Rietveld refinement against PXD data for $[Cu(NH_3)_{6\text{-}x}]Cl_2$ at 353 K. The blue line represents the difference profile ($I_{obs} - I_{calc}$) and the black tick marks indicate the theoretical reflection positions for $[Cu(NH_3)_{6\text{-}x}]Cl_2$ ($Fm\bar{3}m$, bottom) and CuO (top).

4.10.2. *Ab-initio* calculations and energy surface of the ligand distances

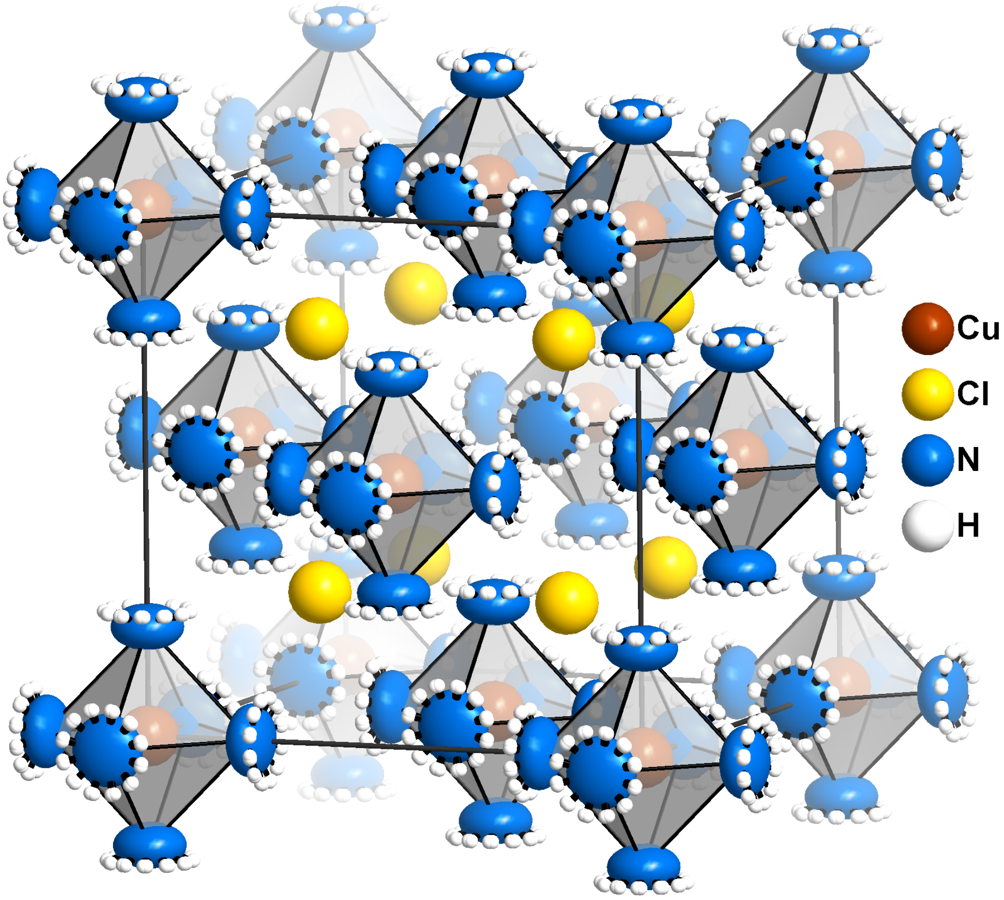

Figure 4.25.: Representation of the unit cell of $[Cu(NH_3)_{6\text{-}x}]Cl_2$. All atoms, except the hydrogen atoms, are represented by their ellipsoids of 90 % probability. The hydrogen atoms are represented as generic spheres. Copper, chlorine, nitrogen and hydrogen atoms are shown in wine, gold, blue and white, respectively.

In order to investigate the nature of the cubic phase and the reason behind the apparent loss of JT distortion, we performed total energy calculations on the DFT-GGA level using the ABINIT code.[42–44] To reduce the complexity of this preliminary analysis, calculations in this work were restricted to the stoichiometric hexammine, pentammine and tetrammine phases (the latter with vacancies on the axial site). For these three configurations, we calculated the energy surfaces with varying M-N distances on both the contracted equatorial site (a) as well as the axial site (b) (for definitions of (a) and (b), see Figure 4.26).

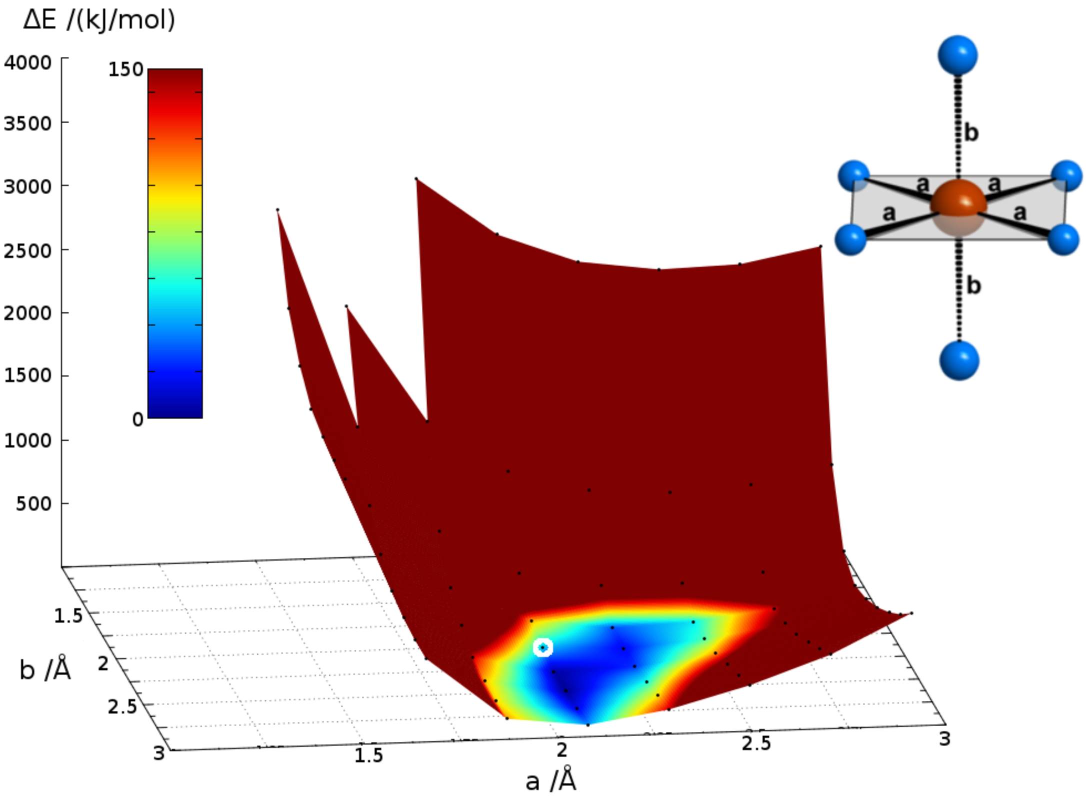

Figure 4.26.: Normalized total energy plot for $[Cu(NH_3)_6]Cl_2$ against the Cu–N distances on the two crystallographically independent sites (inset). The white circle indicates the observed Cu–N distance.

The optimisation of the structures of these complexes was not performed as the chosen models were idealised. The calculated energy surface for $[Cu(NH_3)_6]Cl_2$ (Figure 4.26) produced an equilibrium configuration with an elongated JT distortion with $d_{\text{Cu–N(a)}} \approx$ 2.08 Å and $d_{\text{Cu–N(b)}} \approx$ 2.55 Å. This finding is in agreement with the crystal structure obtained by Distler and Vaughan ($d_{\text{Cu–N(a)}}$ = 2.07(7) Å and $d_{\text{Cu–N(b)}}$ = 2.6(1) Å).[9] It must be noted that these previous experimental *M*–N distances are systematically too long due to the fact that Distler and Vaughan did not consider hydrogen positions. Another important finding from the energy surface calculation was that the surface had a second local minimum that corresponded to the contracted JT-structure in which the axial bonds were shorter than the equatorial bonds. Therefore, a static or dynamic overlay of the two structures would also appear as pseudo-cubic in the structure obtained experimentally from powder X-ray diffraction, which is averaged over both time and space. A dynamic disorder could, for instance, be obtained by the continuous rotation of the complex cation and, therefore, would be averaged over time, whereas a static disorder would be expressed in a different arrangement within the different complex positions leading to an averaging over space. Having considered the anisotropically refined temperature parameters in the crystal structure, it is concluded that neither of these types of distortions are observed here. One would expect that both static and dynamic distortion would result in strongly elongated thermal ellipsoids along the Cu–N bond direction due to the partial electron density distribution over two positions with different Cu–N bond lengths. Since the complete opposite is observed in this case, the tetragonal to cubic phase change likely has different origins. Comparing the stability regions for the hexammine and pentammine compounds (Figures 4.27), the observed Cu–N distance is found in the $[Cu(NH_3)_5]Cl_2$ stability region (Figure 4.28), which is also in closer agreement with the stoichiometry found by Rietveld refinement at 353 K; $[Cu(NH_3)_{4.40(3)}]Cl_2$.

4.10.3. Chemical stabilisation of non-JT distorted hexammine Cu^{II}

Another possibility of stabilising a cubic Cu ammine phase could be *via* the design of a phase where Cu ions share sites with a non-Jahn-Teller distorting metal cation. It was decided to use $MgCl_2$ as such a host due for several reasons: **1)** The hexammine compound $[Mg(NH_3)_6]Cl_2$ adopts the cubic K_2PtCl_6 structure type. **2)** Mg^{II} and Cu^{II} ions have a very similar ionic radius in six-fold coordination (0.72 Å and 0.73 Å).[45] **3)** Importantly, Mg and Cu have a quite different electron count (12 e$^-$ for Mg against 29 e$^-$ for Cu) which makes the atom distinction and quantification in X-ray diffraction much more reliable than for elements of more similar atomic number, as the scattering

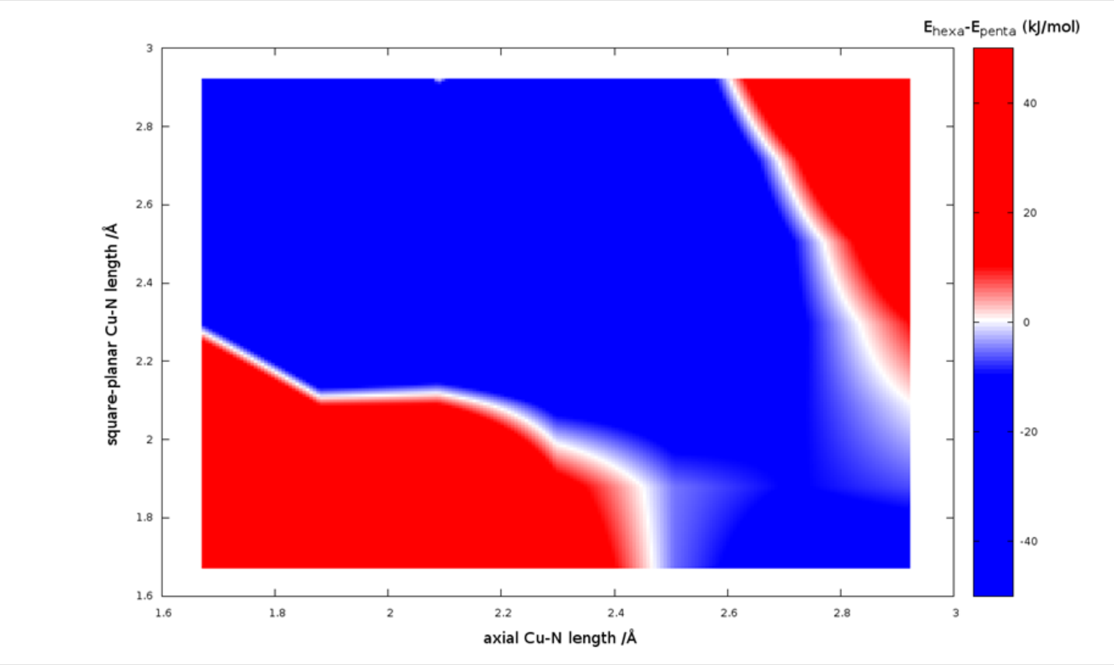

Figure 4.27.: Difference map for the total energies of $[Cu(NH_3)_6]Cl_2$ and $[Cu(NH_3)_5]Cl_2$. Blue areas signify more stability for the hexammine, red areas for the pentammine.

power strongly depends on the electron count of the elements. Finally and with regards to potential future work, Mg^{II} also has the great advantage of being a diamagnetic ion and hence would facilitate interpretation of magnetic behaviour on the paramagnetic Cu^{II} ions within the structure.

In order to synthesise the mixed metal hexammine, it was decided to start with a mix of the pure dihalides and then ammoniate the product as for the other samples. A mass ratio $CuCl_2$:$MgCl_2$ of 1:4 was chosen for the reaction, which corresponds to a metal composition of 15 at.-% of Cu and 85 at.-% of Mg. This ratio was chosen as (1) The predominant metal species should be the hosting non-Jahn-Teller distorted Mg halide but (2) Cu would be present in a high enough quantity to be easily detected by X-ray diffraction. An intimate mixture of $CuCl_2$ and $MgCl_2$ was produced by ball-milling the starting materials for 15 hours (details in the experimental section). The resulting product, a fine light ochre powder, did not exhibit a defined diffraction pattern preventing the

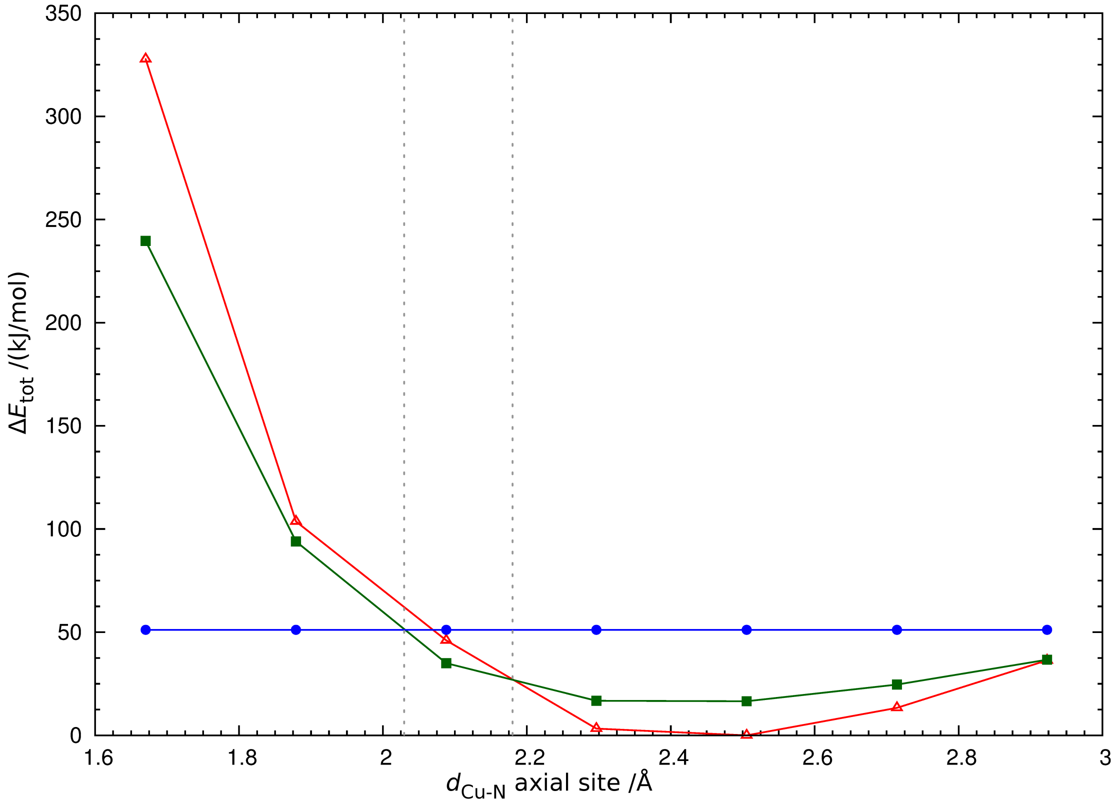

Figure 4.28.: Comparison of ΔE_{tot} (total energy difference between the calculation point and the global minimum of the calculation) for "$[Cu(NH_3)_6]Cl_2$" (red triangles), "$[Cu(NH_3)_5]Cl_2$" (green squares) and "$[Cu(NH_3)_4]Cl_2$" (blue circles) in dependence of the axial Cu–N distance. The grey dotted lines mark the region of lowest ΔE_{tot} for $[Cu(NH_3)_5]Cl_2$.

determination whether the two halides were simply physically mixed or formed a single ternary phase upon mixing. When exposing the mixed halides to a stream of ammonia for one hour at ambient conditions, however, the salts reacted quickly and formed a light blue reaction product which exhibited a good crystallinity and could be further analysed by powder X-ray diffraction.

Powder X-ray refinement

Three phases could be identified from the diffraction pattern: NH_4Cl,[†] tetragonal $[Cu(NH_3)_6]Cl_2$ and a major phase of cubic $[Mg,Cu(NH_3)_6]Cl_2$. Despite the presence of a small portion of tetragonal $[Cu(NH_3)_6]Cl_2$, it could be readily observed that the relative intensity of this phase could not account for 15 at.-% of the reaction product, especially given the higher scattering power of Cu mentioned above. It was hence decided to perform a Rietveld refinement in order to quantify the phase ratio and to determine the nature of the predominant cubic phase. Because the two minor phases NH_4Cl and $[Cu(NH_3)_6]Cl_2$ were of such low intensity compared to the cubic phase, they had to be treated specially. Their peak shapes were refined using only the angle independent G_w parameter and the atom positions were fixed as taken from the literature for NH_4Cl and from the single crystal structure presented in section 4.6 in the case of $[Cu(NH_3)_6]Cl_2$ (no hydrogen atoms were added in this structure and the occupancy of the axial nitrogen atom was set to 90 % in order to simplify the structure). The results of the refinement (Figure 4.29) are summarised in Table 4.16. As suggested from a simple visual examination, the refinement results confirm the strong predominance of the cubic phase constituting over 99 wt.-% of the sample while the two minor phases comprise ca. 0.5 wt.-%. Furthermore, the fit of the pattern could be significantly ameliorated when introducing a mixed (Mg,Cu) site. It can therefore be assumed that the cubic phase is in fact a pseudo-ternary phase containing both Cu and Mg ions.

[†] The appearance of NH_4Cl is commonly encountered in the synthesis of hexammine magnesium halides by reaction of the halides with ammonia.[46]

Table 4.16.: Refinement results for $[Mg,Cu(NH_3)_6]Cl_2$.

Formula	$[Mg,Cu(NH_3)_6]Cl_2$	$[Cu(NH_3)_6]Cl_2$	NH_4Cl
Crystal system	cubic	tetragonal	cubic
Space group	$Fm\bar{3}m$	$I4/mmm$	$Pm\bar{3}m$
a /Å	10.158(1)	7.260(8)	3.874(4)
c /Å	10.158(1)	9.35(2)	3.874(4)
Volume /Å^3	1048(1)	493.1(7)	58.1(2)
Z	4	2	1
Calculated Density, ρ_x **/g·cm^{-3}**	1.279	1.453	1.528
R_p; wR_p		0.020; 0.026	
Goof; X^2		1.79; 3.20	
R_{obs} ; wR_2 **(all)**	0.043; 0.053	0.089; 0.064	0.071; 0.071
Phase fraction /wt.-%	99.1(8)	0.4(2)	0.5(2)

The structure of $[Mg,Cu(NH_3)_6]Cl_2$

The refined cell parameter of the mixed phase $[Mg,Cu(NH_3)_6]Cl_2$ (a = 10.158(1) Å) is very similar to the reported crystal structure of pure $[Mg(NH_3)_6]Cl_2$ (a = 10.12258(3) Å).[11] This is not surprising, considering that the ionic radii of Cu and Mg are almost identical. The scattering of the inserted Cu ions is however distinct and allows the refinement of the occupancy of the metal site as 11(2) at.-% and 89(2) at.-% Cu and Mg respectively. This is in good agreement with the molar ratio of the starting mixture of $MgCl_2$ and $CuCl_2$ (85 at.-%:15 at.-%) The deficiency of Cu is accounted for by the tetragonal minor phase. While the overall structure of the compound is isostructural to many other examples of the same family (*e.g.* $[Ni(NH_3)_6]Cl_2$ as discussed in section 3.4) and therefore does not require detailed discussion, it is worth considering the effect of Cu substitution on the complex cation. While Jones and co-workers report a Mg–N distance of 2.161(2) Å for the pure hexammine magnesium chloride, the M–N distance found in $[Mg,Cu(NH_3)_6]Cl_2$ is 2.188(6) Å. It has also to be noted that the structure reported by

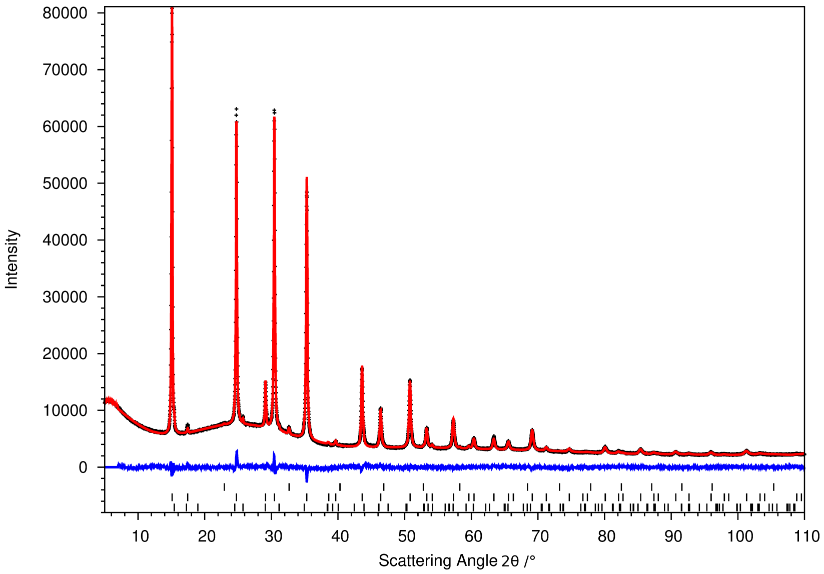

Figure 4.29.: Comparison of the observed (black crosses) and calculated patterns (red line) from the Rietveld refinement against PXD data for $[Mg,Cu(NH_3)_6]Cl_2$ and the accompanying side phases. The blue line represents the difference profile ($I_{obs} - I_{calc}$) and the black tick marks indicate the theoretical reflection positions for $[Cu(NH_3)_6]Cl_2$ ($I4/mmm$, bottom), $[Mg,Cu(NH_3)_6]Cl_2$ ($Fm\bar{3}m$, middle) and NH_4Cl (top).

Jones *et al.*[11] does not account for the hydrogen atoms in the ammonia moecule and therefore systematically overestimates the M–N bond length due to a shifting of the centre of electron density away from the the metal centre. The Cu–N distance for themetastable cubic $[Cu(NH_3)_{4.40(3)}]Cl_2$ phase is only 2.084(3) Å and therefore significantly shorter than that observed here. This discrepancy is most likely due to a combination of the reduced coordination number in $[Cu(NH_3)_{4.40(3)}]Cl_2$ and the Mg/Cu disorder. The refinement of anisotropic thermal ellipsoids for the nitrogen atoms does not lead to shapes elongated in the M–N bonding direction as expected for distorted complexes but to flattened shapes similar to those in the Ni analogues. While the inclusion of Cu^{II} guest ions into a host ammine structure is unlikely to lead to the formation of a better performing ammonia store, because of the reductive thermal decomposition of $[Cu(NH_3)_6]Cl_2$ to CuCl; this material is highly interesting from a structural point of view and the further study of the Mg/Cu hexammine halide solid solutions should enable a more detailed understanding of the complex coordination environments of Cu^{II} to be obtained (for instance by EXAFS, ESR or inelastic neutron scattering).

4.11. Conclusions

The effect of the Jahn-Teller distortion in the $CuCl_2$–NH_3 system became evident and the chemical consequences of this structural effect were studied. The uptake at ambient conditions, although being as rapid as in the case of nickel, led to the formation of a deficient phase as could be proved by gravimetric and X-ray studies. The thermal decomposition pathways of the hexammine copper halides proceed *via* tetrammine and diammine intermediates. The diammine salt does not decompose to the pure copper dihalide. This is an important drawback for the use of copper halides as ammonia store as it strongly impedes the recyclability of the storage material. The thermal analysis is nevertheless interesting from a chemical point of view as it further underlines the non-stoichiometric nature of the reaction product determining the amount of ammonia per equivalent of $CuCl_2$ in the range of 5.0-5.5 eq.

The crystal growth under controlled ammonia atmosphere presented in this chapter has proved its suitability for the growth of crystals of ammine compounds that could not be achieved by other methods, as was the case for $[Cu(NH_3)_{6\text{-x}}]Cl_2$. The structural work on this compound, by single crystal XRD and powder neutron diffraction has furthermore confirmed the prior findings on the non-stoichiometry of the ammoniated reaction product $[Cu(NH_3)_{6\text{-x}}]Cl_2$ with a variable stoichiometry depending on the synthesis method, the temperature and the post-reaction treatment. A surprisingly simple, partially ordered model for the deuterium arrangement on the equatorial site was found by neutron diffraction which showed two possible ammine arrangements related to each other through a mirror plane. The spectroscopic results presented in this chapter give rise to the presumption that the non-stoichiometric compound $[Cu(NH_3)_{6\text{-}x}]Cl_2$ may contain two distinct Cu^{II}-ion arrangements which are structurally similar but not equivalent. It is however indispensable to collect more detailed data on this in order to confirm the nature of the reaction products unambiguously.

When the tetragonal $[Cu(NH_3)_{6\text{-}x}]Cl_2$ phase is heated under an ammonia atmosphere, it undergoes a structural change into a cubic K_2PtCl_6-type structure in which the Jahn-Teller distortion is lifted and the Cu^{II} ions are surrounded by an apparent regular octahedral array of NH_3 molecules. It was possible to refine this structure from the *in situ* diffraction data confirming the structural type and an increased deficiency on the ammine site compared to the tetragonal structure. The analysis of the thermal ellipsoids suggested something other than a simple superposition of distorted octahedra in different orientations. Solid-state *ab-initio* calculation techniques were used to probe the nature of the coordination environment and it was found that a pentammine coordination is indeed more stable than the hexammine coordination for the experimentally observed Cu–N distance. This validates the assumption that the apparent octahedral coordination may be caused through an ammonia deficiency which allows a change in the coordination environment. The stabilisation of this octahedral Cu coordination could also be reached through the incorporation of Cu^{II} ions into a host material which exhibits the $Fm\bar{3}m$ aristotype structure, in the study presented herein, $[Mg(NH_3)_6]Cl_2$. Rietveld refinement of the reaction product confirmed the mixed cation site and the refined Mg and Cu contents are in excellent agreement with the expected values from the starting material stoichioemtry. This chemical substituted stabilisation of regularly octahedral coordinated Cu^{II} is of great importance as it would also allow the direct study of the Cu coordination environment by sensitive methods like electron paramagnetic resonance spectroscopy.

4.12. References

[1] V. Petříček, M. Dušek, L. Palatinus, *Z. Kristallogr. - Cryst. Mater.*, 2014, **229**, 345–352.

[2] A. A. G. Tomlinson, B. J. Hathaway, *J. Chem. Soc. A*, 1968, 1905–1909.

[3] B. J. Hathaway, A. A. G. Tomlinson, *Coord. Chem. Rev.*, 1970, **5**, 1–43.

[4] W. Biltz, E. Birk, *Z. Anorg. Allg. Chem.*, 1923, **127**, 34–42.

[5] R. F. Chaiken, D. J. Sibbett, J. E. Sutherland, D. K. Van de Mark, A. Wheeler, *J. Chem. Phys.*, 1962, **37**, 2311–2318.

[6] H. H. Glaeser, G. A. Lo, H. W. Dodgen, J. P. Hunt, *Inorg. Chem.*, 1965, **4**, 206–208.

[7] R. Eßmann, G. Kreiner, A. Niemann, D. Rechenbach, A. Schmieding, T. Sichla, U. Zachwieja, H. Jacobs, *Z. Anorg. Allg. Chem.*, 1996, **622**, 1161–1166.

[8] E. Mikuli, M. Liszka-Skoczylas, J. Hetmańczyk, J. Szklarzewicz, *J. Therm. Anal. Calorim.*, 2010, **102**, 889–897.

[9] T. M. Distler, P. A. Vaughan, *Inorg. Chem.*, 1967, **6**, 126–129.

[10] W. Biltz, *Z. Anorg. Allg. Chem.*, 1923, **130**, 93–139.

[11] M. O. Jones, D. M. Royse, P. P. Edwards, W. I. F. David, *Chem. Phys.*, 2013, **427**, 38–43.

[12] A. Leineweber, H. Jacobs, *J. Solid State Chem.*, 2000, **152**, 381 – 387.

[13] B. Morosin, *Acta Crystallogr. B*, 1976, **32**, 1237–1240.

[14] S. N. Bathia, C. J. O'Connor, R. L. Carlin, L. De Jongh, *J. Chem. Phys. Lett.*, 1977, **50**, 353–357.

[15] W. Biltz, H. Bröhan, W. Wein, *Z. Anorg. Allg. Chem.*, 1925, **148**, 207–216.

[16] E. A. Guggenheim, *Trans. Faraday Soc.*, 1937, **33**, 151–156.

[17] S. P. L. Sörensen, *Z. Anorg. Chem.*, 1894, **5**, 354–373.

[18] *Sheldrick, G. M. CELL_NOW, program for unit cell determination. University of Göttingen, Germany & Bruker AXS Inc, Madison (WI), USA (2005).*

[19] H. Kohlmann, R. O. Moyer Jr., Y. Hansen, K. Yvon, *J Solid State Chem.*, 2003, **174**, 35–43.

[20] B. Janik, J. M. Janik, J. A. Janik, *J. Raman Spectrosc.*, 1978, **7**, 297–302.

[21] A. Hoser, W. Joswig, W. Prandl, K. Vogt, *Mol. Phys.*, 1985, **56**, 853–869.

[22] A. Hoser, W. Prandl, P. Schiebel, G. Heger, *Z. Phys. B: Condens. Matter*, 1990, **81**, 259–263.

[23] V. F. Sears, *Neutron News*, 1992, **3**, 26–37.

[24] H. Elliott, B. J. Hathaway, *Inorg. Chem.*, 1966, **5**, 885–889.

[25] R. A. Kendall, E. Aprà, D. E. Bernholdt, E. J. Bylaska, M. Dupuis, G. I. Fann, R. J. Harrison, J. Ju, J. A. Nichols, J. Nieplocha, et al., *Comput. Phys. Commun.*, 2000, **128**, 260–283.

[26] M. Valiev, E. J. Bylaska, N. Govind, K. Kowalski, T. P. Straatsma, H. J. Van Dam, D. Wang, J. Nieplocha, E. Apra, T. L. Windus, et al., *Comput. Phys. Commun.*, 2010, **181**, 1477–1489.

[27] R. Eßmann, *J. Mol. Struct.*, 1995, **356**, 201 – 206.

[28] K. C. Patil, E. A. Secco, *Can. J. Chem.*, 1972, **50**, 567–573.

[29] A. Domenicano, I. Hargittai, *Strength from weakness: structural consequences of weak interactions in molecules, supermolecules, and crystals*, *Vol. 68*, Springer Science & Business Media, 2002.

[30] M. A. Halcrow, *Dalton Trans.*, 2003, 4375–4384.

[31] I. Persson, P. Persson, M. Sandström, A.-S. Ullström, *J. Chem. Soc., Dalton Trans.*, 2002, 1256–1265.

[32] H. A. Jahn, E. Teller in *Proceedings of the Royal Society of London A: Mathematical, Physical and Engineering Sciences*, The Royal Society, . 220–235.

[33] R. J. Deeth, L. J. Hearnshaw, *Dalton Trans.*, 2006, 1092–1100.

[34] R. Z. Sørensen, J. S. Hummelshøj, A. Klerke, J. B. Reves, T. Vegge, J. K. Nørskov, C. H. Christensen, *J. Am. Chem. Soc.*, 2008, **130**, 8660–8668.

[35] J. Breternitz, T. K. A. Hoang, D. H. Gregory, *Acta Crystallogr. A*, 2013, **69**, s580.

[36] H. Reardon, J. M. Hanlon, M. Grant, I. Fullbrook, D. H. Gregory, *Crystals*, 2012, **2**, 193–212.

[37] A. Migdał-Mikuli, E. Mikuli, Ł. Hetmańczyk, I. Natkaniec, E. Ściesińska, J. Ściesiński, S. Wróbel, *Chem. Phys.*, 2005, **317**, 188–197.

[38] L. Piekara-Sady, W. Bednarski, *J. Mol. Struct.*, 2003, **655**, 1–6.

[39] G. Peyronel, *Gazz. Chim. Ital.*, 1941, **71**, 363–375.

[40] L. Palatinus, G. Chapuis, *J. Appl. Crystallogr.*, 2007, **40**, 786–790.

[41] S. Åsbrink, L.-J. Norrby, *Acta Crystallogr. B*, 1970, **26**, 8–15.

[42] *The ABINIT code is a common project of the Université Catholique de Louvain, Corning Incorporated, and other contributors (URL http://www.abinit.org).*

[43] X. Gonze, G.-M. Rignanese, R. Caracas, *Z. Kristallogr.*, 2005, **220**, 458–472.

[44] X. Gonze, B. Amadon, P.-M. Anglade, J.-M. Beuken, F. Bottin, P. Boulanger, F. Bruneval, D. Caliste, R. Caracas, M. Cote, et al., *Comput. Phys. Commun.*, 2009, **180**, 2582–2615.

[45] R. D. Shannon, *Acta Crystallogr. A*, 1976, **32**, 751–767.

[46] J. M. Hanlon, Ph.D. thesis, University of Glasgow, 2013.

5. Metal nitrate ammines - A diffraction and spectroscopy study of ionic and ligand nitrate anions

5.1. Introduction

The study of the ammine nitrates is of some structural interest as this class of compounds does not only possess the structural effects of the disordered ammine ligands but is also interesting due to the molecular anion. The three examples discussed in this chapter show the remarkable ability of the nitrate anion to either act as a purely ionic anion or to enter into the ligand sphere and form directed bonds. Besides the structural elucidation of these compounds, the analysis of their vibrational spectra is most interesting as it proves to be a very efficient probe of the coordination environment. The effect of ammonia on hydrated salts is probed for the nickel nitrate system in order to test the effect of hydrate impurities in potential ammine based ammonia stores. Furthermore, it was possible for the first time to solve and refine the crystal structure of diammine nickel nitrate from powder data, a compound which exhibits an unprecedented structure type.

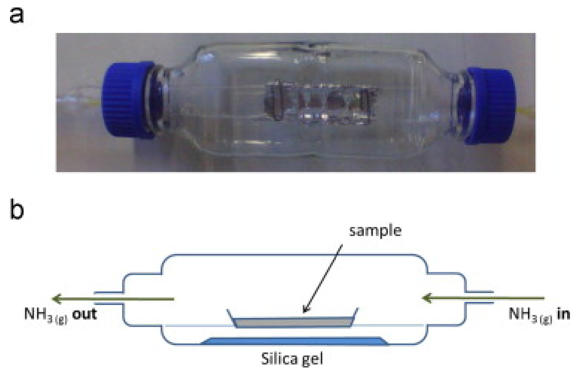

Figure 5.1.: Photograph (a) and schematic representation (b) of the reactor employed for the reaction of $[Ni(H_2O)_6](NO_3)_2$ with NH_3.[1]

5.2. Experimental

5.2.1. Reaction of $[Ni(H_2O)_6](NO_3)_2$with NH_3

$[Ni(H_2O)_6](NO_3)_2$ (99 %, BDH) was exposed to a stream of ammonia for 2 hours in a specially adapted reactor (Figure 5.1). The drying gel was added to the reaction to reduce water vapours in the reactor to a minimum. The drying gel was kept in a drying oven at 150 °C before the use to ensure that it was water-free at the start of the reaction.

5.2.2. Synthesis of Diammine Nickel Nitrate

$[Ni(NH_3)_6](NO_3)_2$ synthesised as above was heated to 200 °C under dynamic vacuum ($\approx$ 0.01 bar) for 2 hours. The product changed its colour from violet to green and the propagation of the reaction could be easily detected on this basis.

Single Crystal Experiments

The single crystal experiments for $[Ni(NH_3)_6](NO_3)_2$ and $Cu(NH_3)_4(NO_3)_2$ were conducted on samples grown by controlled evaporation as described in section 4.2.3.

5.3. Ligand Exchange Reaction in $[Ni(H_2O)_6](NO_3)_2$ + NH_3[1,2]

An important question when dealing with metal salts as ammonia storage materials is the impact of their moisture sensitivity on ammonia storage capacity. When exposed to moist air, the metal di-halides pick up water and form hydrate complexes. One of the most moisture sensitive salts is nickel nitrate which forms the hexahydrate $[Ni(H_2O)_6](NO_3)_2$. The commercial starting material (BDH, 99 %) was received as large crystals, which showed an extreme preferred orientation in the [001] direction of the triclinic cell (Figure 5.2). Considering the fact that the only deposited single crystal measurement is over 40 years old,[3] a redetermination of the structure at room temperature and the first structural determination at 100 K were performed (Table 5.1). The refinements at 100 K and 295 K revealed that the compound does not undergo a low temperature phase transition, as was postulated by Bigoli *et al.*,[3] above 100 K but remains in the $P\bar{1}$ structure type. The atomic positions between the two measurements deviate only very little (tables 5.2 and 5.3) and the thermal displacement parameters follow the expected trend to decrease with decreasing temperature. As both structures are similar to each other, only the values for the room temperature measurement are cited in the following text, and the values for 100 K may be obtained in the appendix (section A.3.1).

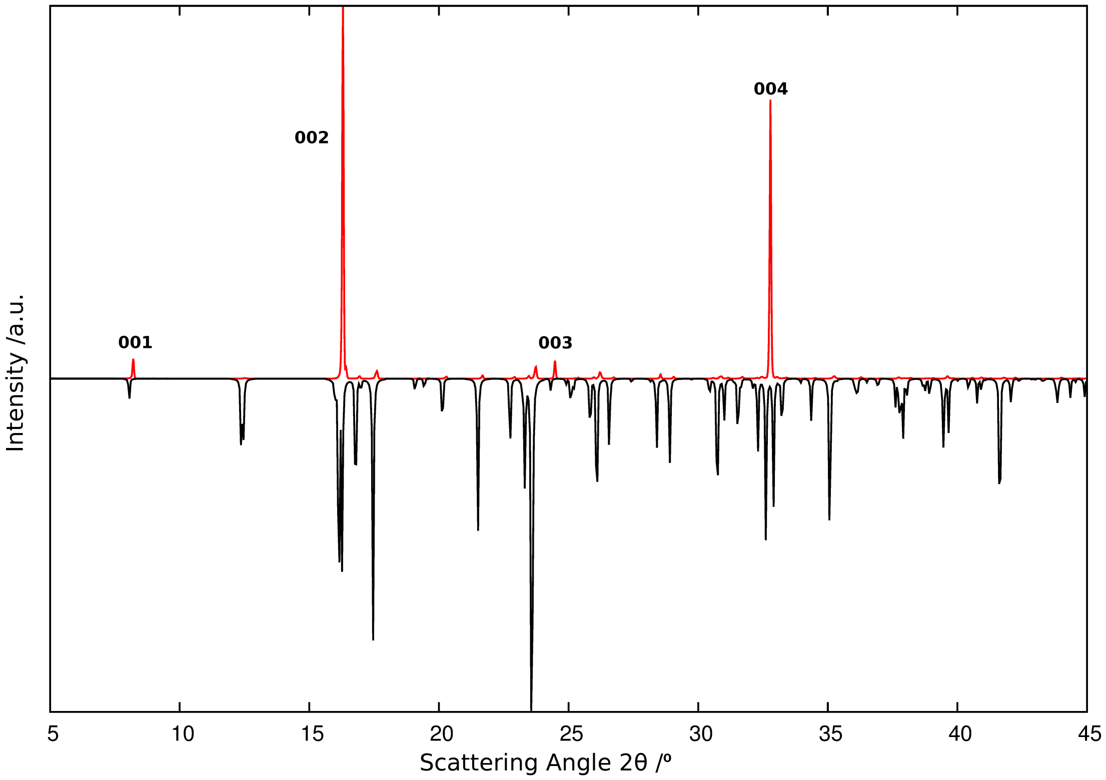

Figure 5.2.: Comparison of the powder pattern of $[Ni(H_2O)_6](NO_3)_2$ (red line) with the calculated powder pattern (negative, black line).[1] The peaks of the preferred orientation in the measured cell are marked.

5.3.1. Crystal structure of $[Ni(H_2O)_6](NO_3)_2$

The structure of $[Ni(H_2O)_6](NO_3)_2$ consists of isolated $[Ni(H_2O)_6]^{2+}$ octahedra and nitrate counter-anions (Figure 5.3). Despite the fact that, due to the low symmetry, all water ligands in the complex cation are crystallographically inequivalent (Figure 5.4), they form a distorted octahedral coordination with Ni–O distances ranging from 2.017(2) Å to 2.088(2) Å and ∢O–Ni–O angles in the range of 85.66(7)° to 93.18(6)° with the arithmetic mean being 90.00(6)° . This small distortion has a consequence that the perfect octahedral molecule symmetry O_h is broken in the complex cation. As the deviations from the ideal octahedral coordination are comparably small, however, the complex cation can still be regarded a approximately octahedral. The nitrate anion has an idealised molecular

Table 5.1.: Results of the structure determination for the single crystal analysis of $[Ni(H_2O)_6](NO_3)_2$ at 100 K and 295 K.

	295 K	**100 K**
Sum formula	$H_{12}N_2O_{12}Ni$	
Space Group	$P\bar{1}$	
a /Å	5.8056(2)	5.7531(3)
b /Å	7.7023(3)	7.6604(4)
c /Å	11.6864(4)	11.4876(6)
α /°	105.841(2)	106.347(2)
β /°	98.451(2)	98.450(2)
γ /°	102.203(2)	101.538(2)
V /Å^3	479.59(3)	464.73(4)
Measurement range	$-8 \leq h \leq 7$	$-10 \leq h \leq 14$
	$-10 \leq k \leq 10$	$-18 \leq k \leq 10$
	$-16 \leq l \leq 16$	$-24 \leq l \leq 27$
Measured Reflections	12115	32234
Independent Reflections ($I > 2\sigma$)	2786 (2691)	13670 (12467)
R_{int}	0.059	0.057
R_1 [$F_o^2 > 2\sigma$]	0.034	0.039
wR_2 all F_o^2	0.096	0.103
Parameters (Restraints)	186 (12)	185 (12)
$Goof$	1.14	1.06
$\Delta\rho$ [max, min] /(e^-/Å^3)	0.76, –0.40	2.26; –1.12

symmetry of D_{3h}. However, the N–O distances deviate slightly ranging from 1.238(3) Å to 1.259(2) Å around N1 and from 1.239(3) Å to 1.255(4) Å around N2. The ∢O–N–O angles deviate slightly (118.7(2)° – 121.1(2)° , both around N1) from the ideal value of 120° and also no remarkable deviation of the nitrate anions from the planar configuration can be observed. The distances of the nitrogen atoms from the plane described by the oxygen atoms is only 0.003(2) Å for N1 and 0.010(2) Å for N2. These values are still much smaller than the vibrational displacements and the anion can be taken as planar. It

Table 5.2.: Atomic positions and equivalent isotropic displacement parameters for $[Ni(H_2O)_6](NO_3)_2$ at 100 K

Atom Site	X	Y	Z	$U_{\mathrm{iso}}/U_{\mathrm{eq}}$ /Å^2
Ni1	0.67251(2)	0.23239(2)	0.23239(2)	0.00574(2)
O1	0.59814(9)	0.36829(4)	0.36829(4)	0.00975(5)
O2	0.30943(7)	0.14528(4)	0.14528(4)	0.00867(5)
O3	0.75154(8)	0.10307(4)	0.10307(4)	0.00920(5)
O4	0.63467(8)	0.35305(5)	0.35305(5)	0.00979(5)
O5	1.04304(8)	0.31494(4)	0.31494(4)	0.00931(5)
O6	0.72217(8)	0.12390(5)	0.12390(5)	0.01006(5)
H11	0.672(4)	0.371(3)	0.371(3)	0.030(6)
H12	0.646(4)	0.4342(15)	0.4342(15)	0.023(5)
H21	0.221(4)	0.181(2)	0.181(2)	0.032(6)
H22	0.262(4)	0.133(2)	0.133(2)	0.025(6)
H31	0.720(4)	0.0320(12)	0.0320(12)	0.021(5)
H32	0.689(4)	0.103(2)	0.103(2)	0.024(5)
H41	0.499(2)	0.350(2)	0.350(2)	0.021(5)
H42	0.715(4)	0.366(2)	0.366(2)	0.026(5)
H51	1.112(6)	0.333(3)	0.333(3)	0.053(9)
H52	1.076(5)	0.3843(15)	0.3843(15)	0.038(7)
H61	0.663(5)	0.128(3)	0.128(3)	0.039(7)
H62	0.856(2)	0.121(2)	0.121(2)	0.021(5)
O11	0.20807(9)	0.12333(6)	0.12333(6)	0.01235(6)
O12	0.52024(9)	0.13714(6)	0.13714(6)	0.01305(7)
O13	0.15867(9)	0.12317(5)	0.12317(5)	0.01109(6)
N1	0.29363(9)	0.12761(5)	0.12761(5)	0.00833(5)
O21	0.21457(10)	0.39246(5)	0.39246(5)	0.01217(6)
O22	0.15359(10)	0.36954(5)	0.36954(5)	0.01250(6)
O23	-0.13077(10)	0.41090(6)	0.41090(6)	0.01395(7)
N2	0.08050(9)	0.39026(4)	0.39026(4)	0.00886(5)

must be noted that the length of the N–O bonds in the nitrate anions can be seen to arise as a consequence of the different hydrogen bonding environments of the oxygen atoms (Figure 5.5). Longer N–O bonds can be observed for oxygen atoms with shorter or more numerous hydrogen contacts and shorter N–O bonds can be observed in the inverse case.

Table 5.3.: Atomic positions and equivalent isotropic displacement parameters for $[Ni(H_2O)_6](NO_3)_2$ at 295 K

Atom Site	X	Y	Z	$U_{\mathrm{iso}}/U_{\mathrm{eq}}$ /Å^2
Ni1	0.67198(4)	0.23252(2)	0.23252(2)	0.01920(12)
O1	0.5956(3)	0.36545(15)	0.36545(15)	0.0295(3)
O2	0.3112(3)	0.14399(14)	0.14399(14)	0.0254(3)
O3	0.7514(3)	0.10494(14)	0.10494(14)	0.0269(3)
O4	0.6337(3)	0.34917(15)	0.34917(15)	0.0294(3)
O5	1.0394(3)	0.31464(15)	0.31464(15)	0.0293(3)
O6	0.7223(3)	0.12634(16)	0.12634(16)	0.0302(3)
H11	0.669(6)	0.368(3)	0.368(3)	0.044(9)
H12	0.638(6)	0.4318(18)	0.4318(18)	0.044(9)
H21	0.260(6)	0.139(3)	0.139(3)	0.046(9)
H22	0.215(5)	0.177(3)	0.177(3)	0.047(9)
H31	0.698(6)	0.107(3)	0.107(3)	0.045(9)
H32	0.725(6)	0.0359(15)	0.0359(15)	0.036(8)
H41	0.502(3)	0.355(3)	0.355(3)	0.037(8)
H42	0.699(7)	0.362(4)	0.362(4)	0.060(11)
H51	1.106(7)	0.327(4)	0.327(4)	0.061(12)
H52	1.071(7)	0.376(2)	0.376(2)	0.062(11)
H61	0.856(3)	0.121(3)	0.121(3)	0.043(9)
H62	0.667(7)	0.132(4)	0.132(4)	0.055(10)
O11	0.2081(3)	0.12394(19)	0.12394(19)	0.0380(4)
O12	0.5195(3)	0.1354(2)	0.1354(2)	0.0413(4)
O13	0.1637(3)	0.12322(16)	0.12322(16)	0.0341(4)
N1	0.2957(3)	0.12718(15)	0.12718(15)	0.0257(3)
O21	0.2137(4)	0.39635(16)	0.39635(16)	0.0392(4)
O22	0.1528(4)	0.37056(18)	0.37056(18)	0.0415(4)
O23	-0.1306(4)	0.4096(2)	0.4096(2)	0.0486(5)
N2	0.0785(4)	0.39121(16)	0.39121(16)	0.0291(4)

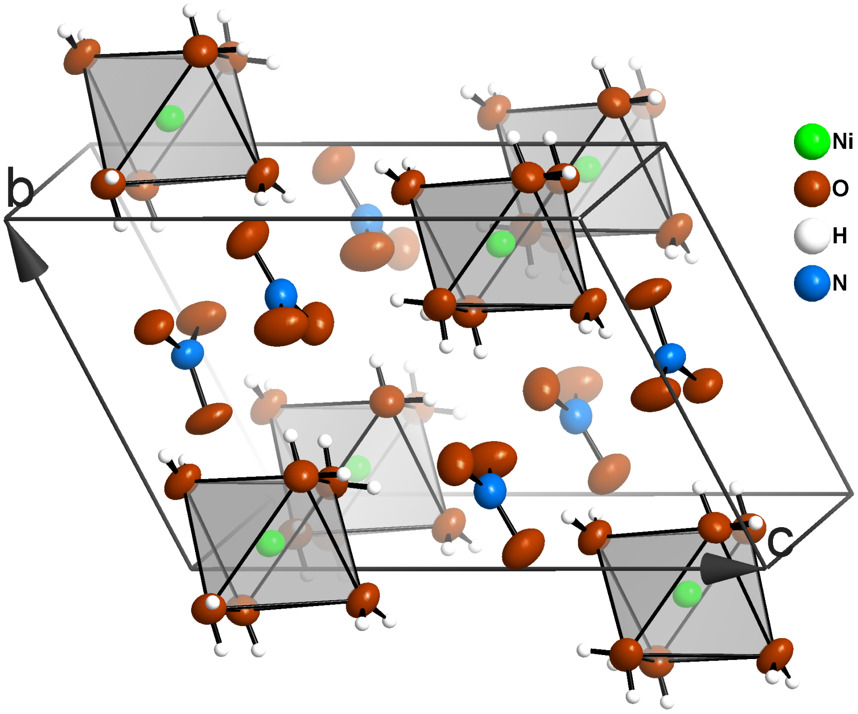

Figure 5.3.: Image of the unit cell of $[Ni(H_2O)_6](NO_3)_2$. The atoms are represented by their thermal ellipsoids at the 70 % probability level at RT apart from H atoms which are shown as spheres (blue: nitrogen, green: nickel, red: oxygen, white: hydrogen). The complex cations are represented as octahedra.[1]

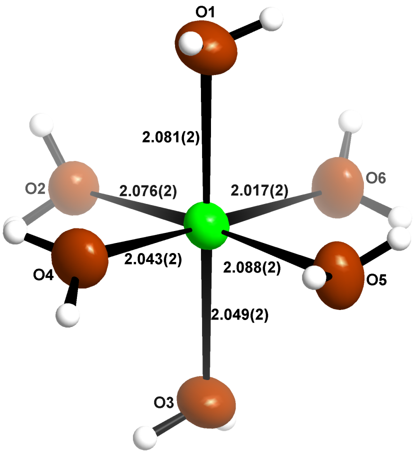

Figure 5.4.: Representation of the complex cation $[Ni(H_2O)_6]^{2+}$ in $[Ni(H_2O)_6](NO_3)_2$. The distances of the Ni–O bonds are given in Å.[1]

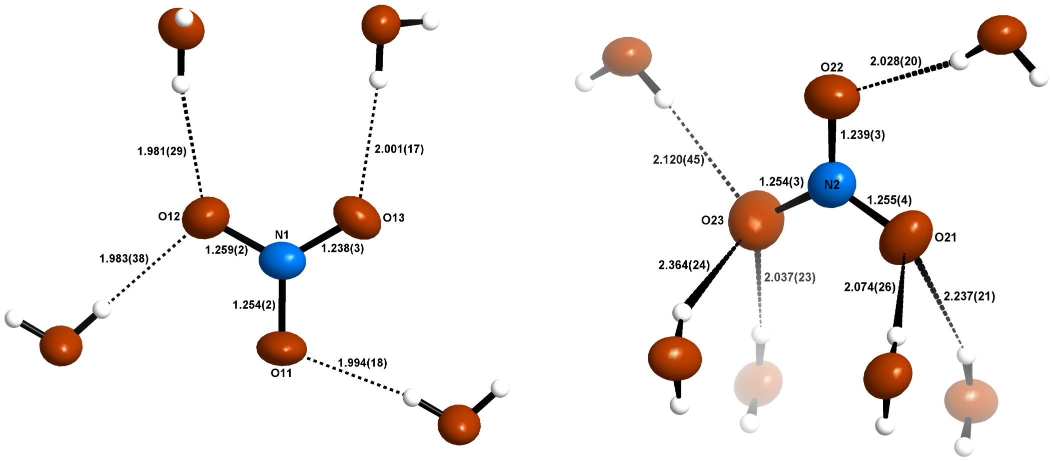

Figure 5.5.: Representation of the hydrogen-bonding environment around the two crystallographically independent nitrate anions in $[Ni(H_2O)_6](NO_3)_2$. The H–O distances are given in Å.[1]

5.3.2. Reaction of $[Ni(H_2O)_6](NO_3)_2$ with gaseous NH_3

The most important question to be answered by this experiment in terms of ammonia storage materials, was to determine if water impurities in metal salts have an impact on the storage performance, for instance through a de-activation of the storage material. Water is clearly a suitable ligand in transition metal complexes as can be shown by the example of $[Ni(H_2O)_6](NO_3)_2$ where the central nickel cation is surrounded octahedrally by water molecules. Ammonia is a stronger ligand than water according to the spectrochemical series[4,5] and the replacement of water for ammonia in aqueous solutions is a well established fact (dating back to the first reported complex formation by Libavius[6]) and the basis for the synthesis of ammine complex from aqueous solutions (see also section 4.5).

In order to test whether the same principle applies in the solid state and how this would affect the product, $[Ni(H_2O)_6](NO_3)_2$ was chosen as an exemplary case. The dark green crystals of $[Ni(H_2O)_6](NO_3)_2$ were brought into the reactor (detailed description of the setup in section 5.2.1) and reacted with ammonia gas for 2 hours. Very quickly after the start of the ammonia dosing, it could be observed how the crystal surfaces lost their gloss and became opaque. The reaction compound changed its colour over the course of the reaction from green to purple-blue. The reaction vessel also contained silica gel as a drying agent that was used to remove water from the gas phase more efficiently and yield an ostensibly dry product. Silica gel did however not influence the reaction directly, which took place in a control experiment without drying gas as well, but it facilitated the removal of water from the reaction and hence allowed a quicker reaction and dry product recovery. A colour change from blue to brown could be observed for the silica gel during the reaction which was attributed to the reaction of the Co-based indicator with ammonia but does not appear to have affected the drying gels water uptake capabilities for the above mentioned reasons.

The first remarkable observation was the apparent crystallinity of the product, as could be proven by subsequent SEM experiments (Figure 5.6). Although the crystals are well faceted and up to ≈ 50 µm across, it was not possible to collect a crystal suitable for single crystal X-ray diffraction. In fact, the crystals were highly intergrown and could not be separated. It was however possible to record a powder pattern of the reaction product which showed two main points: (1) The product is indeed very crystalline as manifested by the high diffraction intensity (compared to the background level) and the clearly defined crystal faces and (2) All the peaks could be indexed to the known cell of $[Ni(NH_3)_6](NO_3)_2$ (Figure 5.9).

The clean X-ray pattern and the possibility to assign the observed IR bands completely demonstrates the formation of a single phase product, that neither ostensibly nor spectroscopically shows any obvious signs of water impurities. One has to bear in mind that X-ray diffraction (especially powder diffraction) is incapable of determining the difference between isoelectronic water and ammonia as both have only very slight differences in electron distribution.

The MIR spectrum (Figure 5.7, Table 5.4) exhibits bands that can be attributed to the vibrational modes of the nitrate anion as well as to the vibrational modes of the ammonia molecules. The latter are in agreement with the bands observed in the halides and to those described by Viltange[7]. Besides the strongest bands attributed in Table 5.4, some smaller bands can be found. These are weak fundamental modes of the nitrate anion (in-plane bending: ν_4 = 713 cm^{-1}), symmetric stretch: ν_1 = 1048 cm^{-1}) and combination

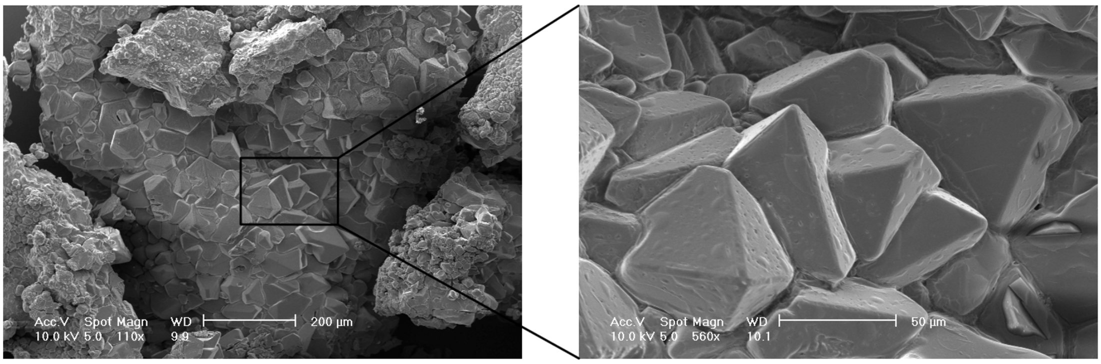

Figure 5.6.: SEM images of $[Ni(NH_3)_6](NO_3)_2$ crystals grown from the reaction between $[Ni(H_2O)_6](NO_3)_2$ and NH_3 gas.[2]

modes ($\nu_1 + \nu_4$ = 1757 cm^{-1}, $\nu_1 + \nu_3$ = 2386 cm^{-1}). While the in-plane bending mode is largely covered by the very intense NH_3 rocking mode and therefore only appears as a small side-peak, the symmetric stretching mode of the nitrate anion is IR inactive because the dipole moment does not change during the vibration. The very small intensity of this mode could be attributed to a fluxional breaking of the D_{3h} molecular symmetry through the formation of hydrogen bonds. Its combination modes $\nu_1 + \nu_4$ and $\nu_1 + \nu_4$ are however not symmetry forbidden and do allow a closer interpretation of the bonding situation of the complexes. The fact, that both appear as single peak and none of the fundamental modes are split together with the very low intensity of the symmetric stretching mode suggest that the nitrate anion in this compound perfectly adopts the D_{3h} symmetry of the molecule. This signals the absence of significant directed bonding of the nitrate ion and hence proves the purely ionic nature of the nitrate anion.

5.3.3. Crystal structure of $[Ni(NH_3)_6](NO_3)_2$

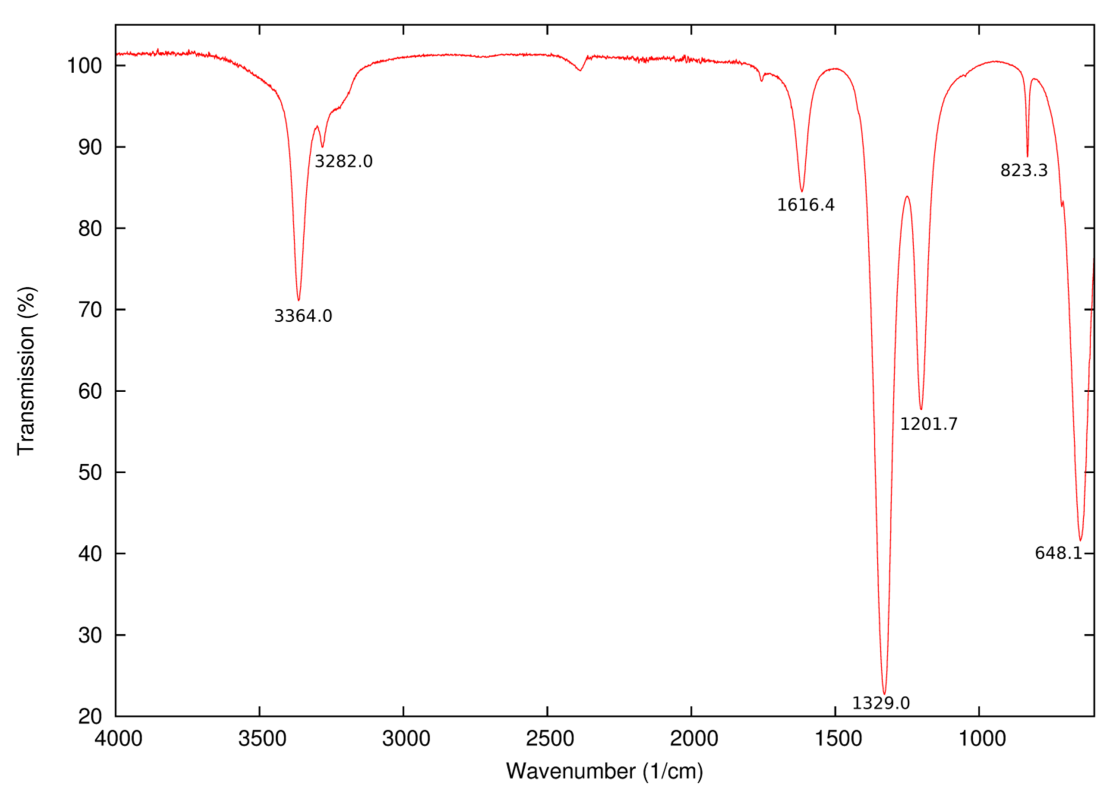

Figure 5.7.: ATR-FTIR plot of $[Ni(NH_3)_6](NO_3)_2$ crystals grown from the reaction between $[Ni(H_2O)_6](NO_3)_2$ and NH_3 gas. The wavenumbers of the peak maxima are annotated on the spectrum.[1]

Table 5.4.: Assignment of the strongest IR bands for $[Ni(NH_3)_6](NO_3)_2$.

Wavenumber /cm^{-1}	Band intensity/shape	Wavenumber from reference[7] /cm^{-1}	Band
3364(2)	strong	3325	$\nu_{as}(NH_3)$
3282(2)	weak	3260	$\nu_s(NH_3)$
1616(2)	medium	1598	$\delta_a(HNH)$
1329(2)	very strong	1350	$\nu_3(NO_3)$
1202(2)	strong	1180	$\delta_s(HNH)$
823(2)	shoulder	837	$\nu_2(NO_3)$
648(2)	very strong	674	$\rho_r(NH_3)$

After indexing the powder pattern of the ammoniation product and obtaining cell parameters in good agreement with $[Ni(NH_3)_6](NO_3)_2$,[8] the structure was refined using the Rietveld method (Figure 5.8, Tables 5.5, 5.6, 5.7). The initial model for the refinement was obtained from a structure solution using Superflip[9] which was subsequently compared to the structure previously reported in order to minimise the risk of a wrong solution. The cell parameter for hexa-ammine nickel nitrate (a=10.8738(6) Å) is larger than that of the corresponding chloride and bromide analogue but slightly smaller than for the iodide compound (see section 3.4).

$[Ni(NH_3)_6](NO_3)_2$ crystallises isostructurally to the hexa-ammine nickel halides in the cubic space-group $Fm\bar{3}m$. Analogous to the halides, $[Ni(NH_3)_6](NO_3)_2$ is composed of isolated $[Ni(NH_3)_6]^{2+}$ cations and surrounding $(NO_3)^-$ anions which are arranged in a fluorite-type derived structure. The cations are surrounded by eight nearest-neighbour anions arranged as a cube while the anions are tetrahedrally surrounded by four nearest neighbour cations (Figure 5.9).

The complex cations $[Ni(NH_3)_6]^{2+}$ are comparable to those in the halides but the Ni–N bonding distances are slightly longer in the halides (2.142(2) Å for $[Ni(NH_3)_6]Cl_2$) than

Table 5.5.: Crystallographic data for $[Ni(NH_3)_6](NO_3)_2$

Sum formula	$H_{18}N_8O_6Ni$
Crystal System	Cubic
Space Group	$Fm\bar{3}m$
a / Å	10.8738(6)
V /Å^3	1285.73(7)
Z	4
Calculated Density, ρ_x /g·cm^{-3}	1.471
R_p; wR_p	0.025; 0.033
Goof; X^2	1.03; 1.06
R_{obs}; wR_2(all)	0.018; 0.020

Table 5.6.: Refined atom parameters for $[Ni(NH_3)_6](NO_3)_2$

Atom Site	X	Y	Z	U_{iso}/U_{eq} /Å^2	SOF	Site multiplicity
Ni1	0	0	0	0.083(2)	1	4
N2	0.25	0.25	0.25	0.118(14)	1	8
N1	0.1890(7)	0	0	0.103(4)	1	24
O1	0.6932(5)	0.1932(5)	0.1932(5)	0.223(4)	0.75	32
H1n1	0.2488*	-0.0502*	-0.0502*	0.124*	0.75	96

* Positioned using a riding model

those found in the nitrate analogue (2.050(8) Å. This may be caused by the disorder of the nitrate anion preventing the formation of stable N–O$\cdots$H–N hydrogen bonds (compare discussion in section 3.4.1). It is however necessary to mention that this derivation must not be overestimated as it may also be a consequence of the relatively low resolution of the refined pattern (due to its strong attenuation).

Crystallographic description of the nitrate anions

The shape of the nitrate anions from diffraction experiments in $[Ni(NH_3)_6](NO_3)_2$ has been a topic for discussions in the past and different models have been proposed as a result.[8,10] This is due to the clash of the three-fold molecular symmetry of the nitrate anion (D_{3h} symmetry) and the higher symmetry of the crystallographic site. The nitrogen

Table 5.7.: Anisotropic displacement parameters in $[Ni(NH_3)_6](NO_3)_2$ in Å^2

Atom Site	U^{11}	U^{22}	U^{33}	U^{12}	U^{13}	U^{23}
N1	0.074(6)	0.118(8)	0.118(8)	0	0	0
O1	0.223(8)	0.223(8)	0.223(8)	-0.071(5)	-0.071(5)	-0.071(5)

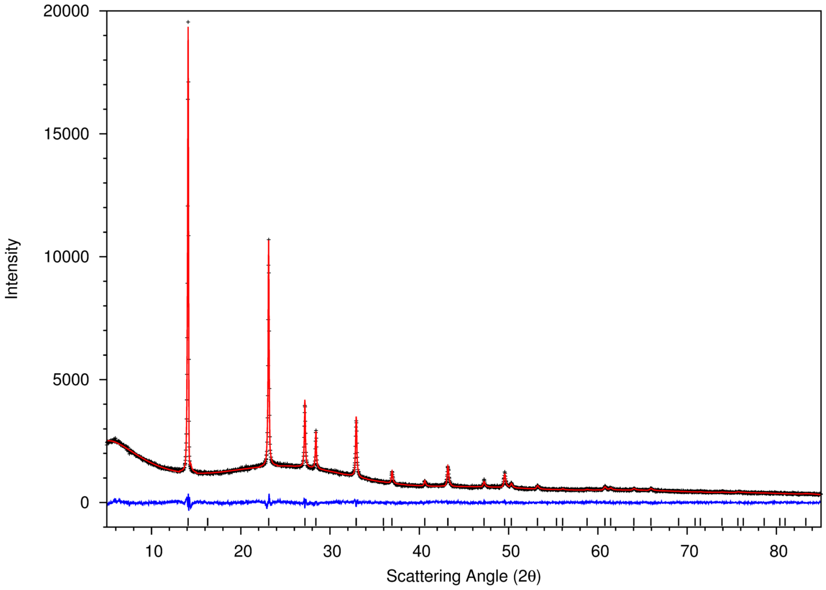

Figure 5.8.: Rietveld refinement results for $[Ni(NH_3)_6](NO_3)_2$ grown from the reaction between $[Ni(H_2O)_6](NO_3)_2$ and NH_3. The measured x-ray pattern (black crosses), the calculated pattern (red lines) and the difference profile ($I_{obs} - I_{calc}$, blue line) are given together with the theoretical reflection positions (black sticks).

atom within the nitrate anion lies on the special position ($^1/_4$,$^1/_4$,$^1/_4$). This is also the position of the halide anions in the analogous halide structures. The position of the oxygen atoms around the nitrogen atom is less evident. The structure solution for the powder data resulted in an oxygen position lying on the vector between the nickel position (at the origin) and the nitrate nitrogen position. This site has however a multiplicity of 32. The main consequence of this distribution in the unit cell is the formation of a tetrahedral shape for the nitrate anions which clearly clashes with the charge of the anion, the count of oxygen atoms in the anion and the shape known from numerous measurements and simulations. The problems of charge and oxygen count could be overcome by setting the occupation factor of the oxygen site to ¾ instead of 1, assuming that only 3 of the four positions are occupied and that the anion is distorted over the available positions. This is however unsatisfactory because no configuration of the nitrate anion distorted over these sites can fulfil the trigonal planar shape of the nitrate anion (D_{3h}). The apparent distortion

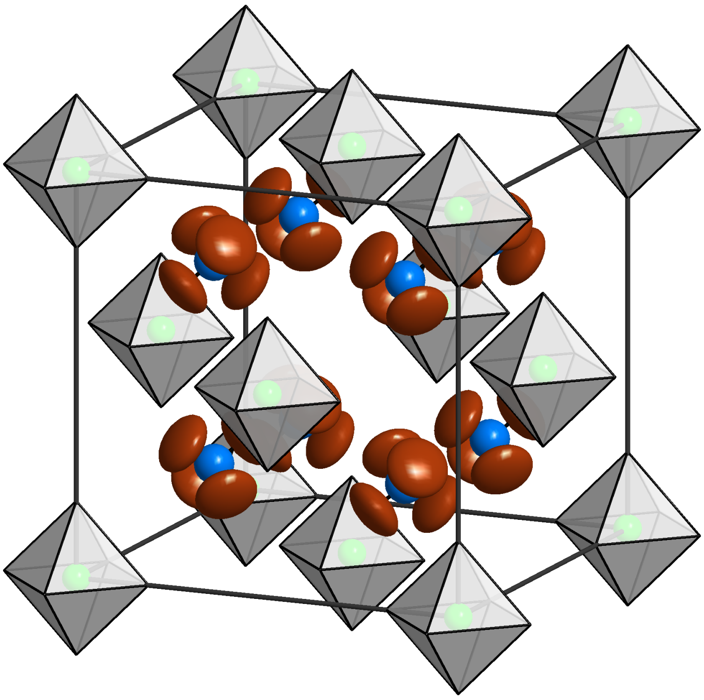

Figure 5.9.: Representation of the unit cell of $[Ni(NH_3)_6](NO_3)_2$. The atoms are denoted by their thermal ellipsoids at the 50 % probability level (blue: nitrogen, green: nickel, red: oxygen). The complex cations are represented as octahedra with the hydrogen positions omitted for clarity.[1]

from the planar shape includes a change of the ∢O–N–O angles from 120° to 109.5°. This arrangement is therefore described with a C_{3v} molecular symmetry. Also the distance between the nitrogen atom and the oxygen atom refined with this model (1.068(6) Å) is considerably smaller than in comparable reference materials (≈ 1.24 Å).[11]

Riou *et al.* proposed an explanation of the anion shape from single crystal data by distorting the oxygen atoms from the special position on the tetrahedral symmetry (multiplicity of 32) onto a general position (multiplicity of 96) off the $\langle 111 \rangle$ vectors.[8] This necessitates a further reduction of the occupancy from 0.75 in the purely tetrahedral model to 0.25 in this model. Although the Riou *et al.* model tackles the problem of the clash of molecular symmetry and crystallographic symmetry with ∢O–N–O angles much closer to 120° and nearly flat arrangements, no completely flat anion configuration can be produced using these oxygen positions. Also, although the N–O distances of 1.19(2) Å are longer than those in this work, they are still shorter than expected from comparable reference materials (≈ 1.24 Å).[11]

Hoser and co-workers used neutron diffraction to derive two different models to explain the distortion in the nitrate anions.[10] The first model is based on a static Frenkel type distortion which can be described using a finite number of supplementary oxygen positions in order to get a realistic model. The second model derived by Hoser *et al.* is based on the use of a dynamical distortion model where the molecular model is de-coupled from specific crystallographic positions and described with a volume of likely positions. The comparison of both models as applied by Hoser resulted in the dynamic model as more realistic because the refined N–O distances were closer to the expected value in the latter model.

None of thee above mentioned models could be employed successfully in this refinement as the Powder data refinement is much more limited in terms of reciprocal space coverage and through the merging of the 3-dimensional diffraction information into one dimension and therefore typically yields lower resolutions than single crystal analyses. It is most likely that the different refinements presented above are different descriptions of the same dynamic distortion of the nitrate anion and that the observation through time and space averaged diffraction is not the optimal method to obtain a realistic view.

5.3.4. Crystal Growth *via In-Situ* Solvation

The growth mechanism for the reaction presented herein is perhaps unconventional. Commonly, gas-solid reactions, especially at ambient conditions, result in the formation

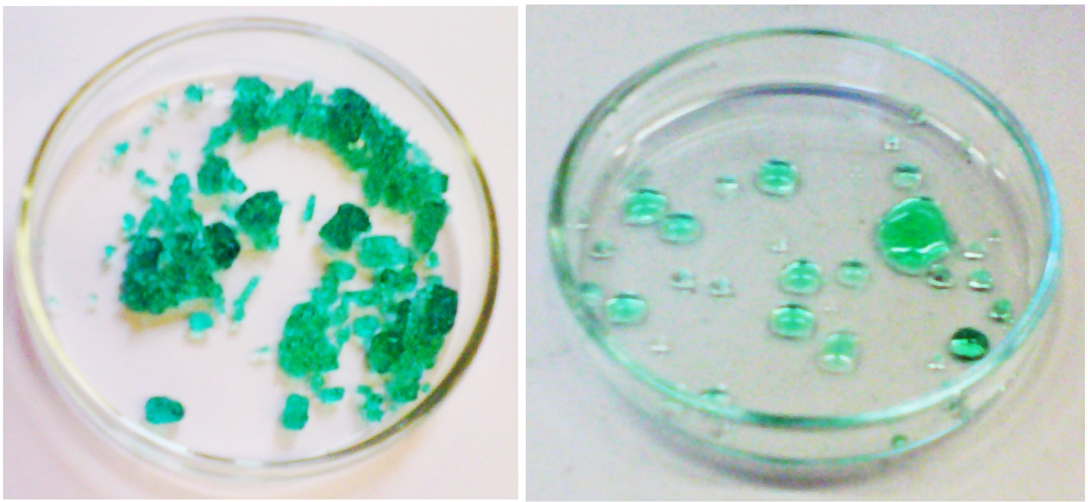

Figure 5.10.: Photographs of $[Ni(H_2O)_6](NO_3)_2$ freshly put in air (left) and after ≈30 minutes (right)

of small crystallites and strongly dispersed powder samples (compare also with section 3.4). The case in the reaction of $[Ni(H_2O)_6](NO_3)_2$ with ammonia is quite different. The large crystallites formed during the reaction (Figure 5.6) are well formed and mostly octahedrally shaped. Such a growth behaviour cannot be explained easily from a rapid gas-solid reaction. A crystal growth medium could be water, which would then result in crystal growth from solution. However, the visually dry product would not necessarily indicate this.

An important consideration is that nickel nitrate hexahydrate, although nominally fully coordinated with ligand water, is strongly hygroscopic. The nitrate hydrate forms a green solution within ≈30 minutes (Figure 5.10). A similar phenomenon can be assumed during the reaction of $[Ni(H_2O)_6](NO_3)_2$ with NH_3. Upon introduction of the ammonia gas, ligated water will be replaced by ammonia since that it is both a stronger ligand than water and the gas has a higher partial pressure than water in the system. Departing water does not leave the proximity of the solid as water vapour but acts as a solvent for remaining $[Ni(H_2O)_6](NO_3)_2$. This aqueous system is now able to dissolve more ammonia and enhance the formation (and crystallisation) of $[Ni(NH_3)_6](NO_3)_2$. This is in fact also enhanced by the fact that $[Ni(NH_3)_6](NO_3)_2$ is less soluble in water than $[Ni(H_2O)_6](NO_3)_2$.* It should be noted, however, that the water evaporates after the reaction and leaves the product both visually dry and without signs of water in the FTIR spectrum(Figure 5.7 and Table 5.4). The role of water in this reaction mechanism can therefore be best described as *in-situ* solvent.

5.4. The Crystal structure of $[Ni(NH_3)_6](NO_3)_2$ at 200 K and 100 K

The data in this section was obtained from single crystal diffraction on crystals grown under controlled ammonia atmosphere. See section 4.2.3 for details on the method.

The fact that the structure of $[Ni(NH_3)_6](NO_3)_2$ has more than one low temperature phase has been well established using different methods.[12–16] Between three[12,14] and four[15] phases have in fact been observed in prior measurements. Here, the room temperature $Fm\bar{3}m$ structure will be called *phase I* while the low temperature structure refined at 200 K and 100 K will be referred to as *phase II*. This complex phase behaviour is in fact not surprising as both the rotation of the nitrate anions as well as the rotation of the ammonia molecules in the high temperature structure are caused by the thermal activation of the solid and hence would be inhibited when cooling down. Considering the relative masses of the two groups as a simple comparison for the ease of the individual rotations (neglecting further influences such as intermolecular interactions and rotation

---

* This behaviour can be easily shown by a simple experiment as encountered during the single crystal growth. When a saturated solution of $[Ni(H_2O)_6](NO_3)_2$ is treated with gaseous NH_3, a purple precipitate of $[Ni(NH_3)_6](NO_3)_2$ appeared immediately.

Table 5.8.: Refinement summary for the single crystal analysis of $[Ni(NH_3)_6](NO_3)_2$ at 200 K and 100 K.

Sum formula	$H_{18}N_8NiO_6$	
Temperature	200 K	100 K
Space Group	$Pa\bar{3}$	
a /Å	10.664(2)	10.579(2)
V /Å^3	1212.7(8)	1184.0(5)
Measurement range	$-11 \leq h \leq 12$	$-11 \leq h \leq 12$
	$-12 \leq k \leq 12$	$-12 \leq k \leq 9$
	$-12 \leq l \leq 10$	$-12 \leq l \leq 12$
Measured Reflections	3274	5329
Independent Reflections ($I > 2\sigma$)	392(290)	381(290)
R_{int}, R_σ	0.079; 0.053	0.100; 0.039
R_1 $[F_o^2 > 2\sigma]$	0.041	0.044
wR_2 all F_o^2	0.114	0.123
Parameters	25	24
$Goof$	1.102	1.132
$\Delta\rho$ [max, min] /(e^-/Å^3)	0.39;–0.45	0.47;–0.71

barriers), it is further easily understandable that the nitrate anion rotation is likely to be frozen before the ammonia ligand rotation. Although the crystal structure of phase II was first described by S. H. Yü in 1942,[17] and a Rietveld refinement from neutron data was subsequently published by Andresen *et al.*,[15] no definitive crystal structure refinement including thermal parameters and fit indices has been published in the literature and it was hence decided to measure the single crystal structure at low temperatures if possible. The article of Yü is also interesting in that this is probably one of the earliest descriptions of structures solved from twinned crystals.[17] It can be stated that the structures in the measurements at 200 K and 100 K are similar to each other and therefore demonstrate the stability of phase II at least in a temperature window from 100 K – 200 K.

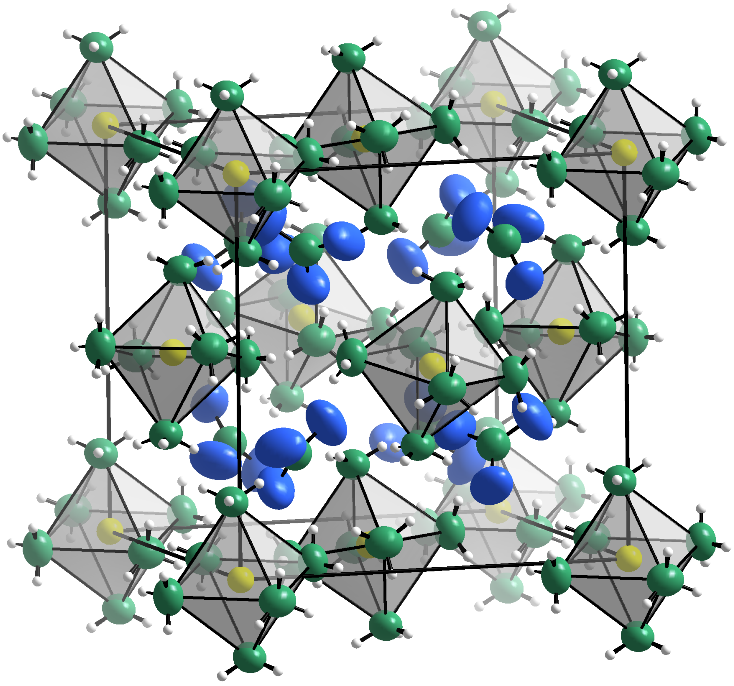

Figure 5.11.: Representation of the unit cell of $[Ni(NH_3)_6](NO_3)_2$ at 100 K with the atoms, apart from H, being represented by their probability ellipsoids at 90 %. H is represented by a ball of generic radius. The atoms are represented by the following colours: Ni: yellow; N: dark green; O: blue; H: white

The transition from phase I (the room temperature $Fm\bar{3}m$ structure, see section 5.3.2) to phase II (the $Pa\bar{3}$ structure presented in this section) proceeds with the development of a number of supplementary peaks and hence a lowering in the translational symmetry. When indexing the data, a cubic cell of similar dimensions to phase I (bearing the differences in measurement temperature in mind) can be found. The lowering of symmetry is hence most likely a *translationengleiche* transformation into a subgroup of the parent $Fm\bar{3}m$ symmetry. Due to the fact that no single crystal without twinning could be measured at 200 K and 100 K, the attribution of the space group presented some problems and a run of the routine tools (Bruker XPrep, Jana2006) did not give a sensible solution. However, as the space group of the low temperature cell has been described as $Pa\bar{3}$,[15,17] it was chosen to use this space group as a starting point for the crystal structure analysis. The structure was subsequently solved with direct methods (using SHELXS2013) during which all atoms apart from hydrogen could be located. The structure was then refined with SHELXL2013 and the hydrogen atoms were subsequently added to the structure (Table 5.8). In order to fit a physically sound model, the hydrogen atoms were constrained to the nitrogen atom of the ammonia molecule as described below. The measurements at the two temperatures were treated slightly differently due to the fact that the thermal excitation of the ammonia rotation is strongly influenced by the measurement temperature. At both temperatures, the hydrogen atoms were constrained to a tetrahedral shape with the nitrogen in the centre of the tetrahedron and the neighbouring Ni atom as fourth corner of the tetrahedron. The displacement parameters of the hydrogen atoms were fixed to equal values of 1.5 times the equivalent thermal displacement parameter of the nitrogen atom. Only the N–H distance was refined freely in the 200 K measurement and the hydrogen positions were taken as calculated by SHELXL (with a HFIX 134 command). As a modification to this model, the ammonia molecule was free to rotate (SHELXL command HFIX 137) in the 100 K refinement and hence yielded a refined ammonia molecule orientation. As the 200 K and 100 K structures do not vary, only the values of the 100 K structures are given in the following text and this structure is discussed in detail. The atom positions and equivalent displacement parameters at 100 K are given in Table 5.9 and a comparison of selected angles and distances in the 200 K and 100 K measurements may be found in Table 5.10.

The overall arrangement of the complex cations and anions in the phase II structure of $[Ni(NH_3)_6](NO_3)_2$ can still be understood as a CaF_2-type arrangement with eight nearest neighbour anions around the complex cation and a tetrahedral arrangement of complex cations around the anions (Figure 5.11). Also, the centres of gravity of the complex cation (the Ni atom at (0,0,0)) and the anion (the nitrate N atom at (0.2330(3),0.2330(3),0.2330(3)) $\approx$ (¼,¼,¼)) remain unshifted (or nearly in the case of the anion) as compared to phase I. The main differences to the structure of phase I

Table 5.9.: Atomic positions and isotropic displacement parameters for $[Ni(NH_3)_6](NO_3)_2$ at 100 K.

Atom Site	X	Y	Z	U_{iso}/U_{eq} /Å^2
Ni1	0	0	0	0.0197(5)
N1	-0.0301(4)	0.0281(4)	0.0281(4)	0.0317(9)
H1A	-0.0835	-0.0301	-0.0301	0.048
H1B	0.0432	0.0217	0.0217	0.048
H1C	-0.0626	0.1047	0.1047	0.048
N2	-0.2670(3)	0.2670(3)	0.2670(3)	0.0314(16)
O1	-0.3344(3)	0.1756(3)	0.1756(3)	0.0502(11)

however arise from the orientation of the ligands and anions within the structure. The anion herein is fully ordered and does not show the typical crystallographic disorder of the high temperature phase. In addition to this, the octahedral cation is slightly tilted away by 11.65(7)° from the perfect alignment of the octahedra in the $\{200\}$ planes.

The complex cation

The complex cation $[Ni(NH_3)_6]^{2+}$ itself retains most of the features present in phase I. The reduction in crystal symmetry does not force the cation into a perfectly octahedral shape and the refined N–Ni–N angles of neighbouring nitrogen atoms (*i.e.* cis-nitrogens)

Table 5.10.: Selected distances and angles for $[Ni(NH_3)_6](NO_3)_2$ at 200 K and 100 K.

	200 K	100 K
Ni–N_{NH_3}	2.134(3) Å	2.125(3) Å
N_{NO_3}–O	1.231(3) Å	1.238(3) Å
N_{NH_3}–Ni–N_{NH_3}, trans	180.0(2)°	180.0(3)°
N_{NH_3}–Ni–N_{NH_3}, cis	91.2(1)°	91.8(2)°
O–N_{NO_3}–O	119.992(9)	119.95(2)°

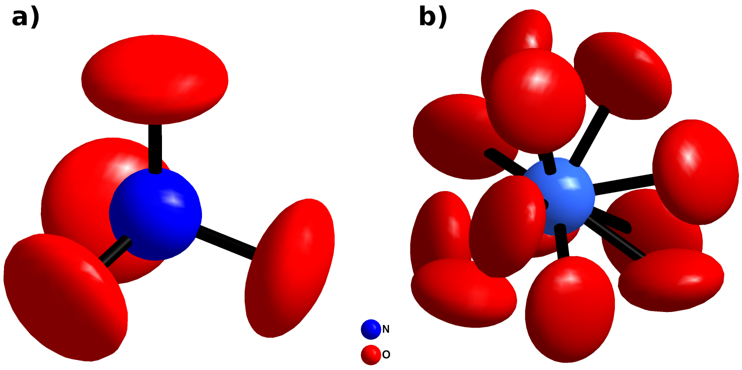

Figure 5.12.: Representation of the nitrate anion in $[Ni(NH_3)_6](NO_3)_2$ at room temperature as refined from powder data in section 5.3.2 (a) by Riou *et al.*[8] (b).

differ slightly from the ideal value of 90° with values of 88.3(2)° and 91.8(2)° respectively. This distortion of the octahedral angles is possible, because the nitrogen atoms are shifted away from the special positions on the $\langle 100 \rangle$ cell axes. The effect of this shift is that the 3-fold axes of the cubic symmetry along $\langle 100 \rangle$ are no longer aligned with the 3-fold axes of the octahedra (through the octahedral face centres) and hence cause a distortion of the angles from the ideal value. The Ni–N_{NH_3} distance is nevertheless constant in the complex environment (within the error) and has a value of 2.125(3) Å. The Ni–N distance found herein is considerably longer that the one refined from powder data at room temperature (2.050(8) Å, section 5.3.1) and lies more in the range of those found in the halide analogues (*e.g.* 2.142(2) Å for $[Ni(NH_3)_6]Cl_2$, section 3.4). This could be due to the ordering of the nitrate anion and therefore the establishment of stronger hydrogen bonding between the oxygen atoms of the nitrate anions and the hydrogen atoms of the ammonia ligands. The stronger hydrogen bonds may have an attractive effect on the ammonia ligands which consequently widens the coordination sphere of the complex cation.

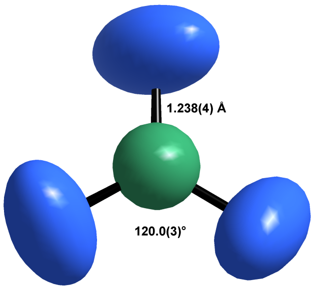

Figure 5.13.: Representation of the nitrate anion in $[Ni(NH_3)_6](NO_3)_2$ at 100 K with the atoms (N: turquoise, O: blue) being represented by the ellipsoids of 90 % probability. The bond lengths (top) and the O–N–O angle (bottom) are given.

The Structure of the Ordered Nitrate Anion

The most obvious difference in the low temperature structure as compared to phase I is the the complete ordering of the nitrate anions. While the nitrate anion in phase I is crystallographically distorted and has to be modelled with a partial occupancy model over multiple orientations (Figure 5.12, see section 5.3.2), the nitrate anion in the low temperature structure exist as almost flat triangular anions (Figure 5.13). In fact, the dihedral angle N–N–N–O differs from a completely flat arrangement by 2.5(3)°. These deviations are however within the range of the thermal displacements as refined from the structure and the significance of the refined atom positions should hence not be overestimated, *i.e.* the data presented herein does not allow the conclusion that the nitrate anion is non-planar. The N–O bond distance of 1.238(3) Å is consistent with the values found in other structures containing nitrate anions.[18,19]

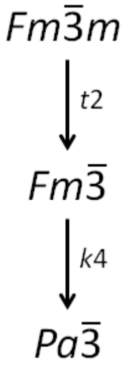

Figure 5.14.: Bärnighausen tree for the group-subgroup relationship between $Fm\bar{3}m$ and $Pa\bar{3}$.

5.5. Symmetry Comparison between phases I and II of $[Ni(NH_3)_6](NO_3)_2$

In order to rationalise the phase transition of $[Ni(NH_3)_6](NO_3)_2$ upon cooling, it is necessary to have a closer look at the different crystal symmetries involved. While the room-temperature structure crystallises in one of the highest symmetrical space groups ($Fm\bar{3}m$) with 192 defining symmetry operations, phase II in $Pa\bar{3}$ has dramatically lost symmetry and is only defined by 24 symmetry operations. The disappearance of two prominent symmetry elements can be identified when comparing the representations of phase I (section 5.3.2) and phase II (Figure 5.11): phase II lacks the four-fold axes along $\langle 1\ 0\ 0 \rangle$ and also lacks the face centering. The absence of these two symmetry elements, or more precisely their absence, already suggests that the symmetry relationship between $Fm\bar{3}m$ and $Pa\bar{3}$ is not a direct group-subgroup relationship. This is because the four-fold axis is a non-translational symmetry element and is hence lost during a *translationengleiche* symmetry descent while the loss of the face centering can be understood in terms of a volume increase in the respective reduced cell volume and is hence part of a *klassengleiche* symmetry descent.

Bearing the information above in mind, one finds a symmetry connection between $Fm\bar{3}m$ and $Pa\bar{3}$ *via* the intermediate space group $Fm\bar{3}$. This relationship can be rationalised in a Bärnighausen tree[20] in which the relationship between the parent structure and the hettotype is given in a graphical form (Figure 5.14). It has to be noted, though that the group-subgroup relationship *via* the intermediate space group $Fm\bar{3}$ does not suggest that a potential, non-observed intermediate structure in that space group must exist. On the contrary, both the reduction of the translational symmetry (the centering) and the reduction of the non-translational symmetry (the 4-fold axes) are necessary to allow the (crystallographically) distortion free tilting of the complex cations from the cell axes. The group-subgroup formalism however differentiates between non-translational symmetry reduction (*translationengleiche* symmetry reduction) and translational symmetry reduction (*klassengleiche* reduction) and hence the group-subgroup relationship between $Fm\bar{3}m$ and $Pa\bar{3}$ must consist of more than one step. Following the Bärnighausen tree for the symmetry descent, a *translationengleiche* symmetry reduction of index two is followed by a *klassengleiche* symmetry reduction of index four and the overall symmetry reductions is hence by a factor of $2 \cdot 4 = 8$. Comparing the symmetry operations in the two space groups, $192/24 = 8$ emphasises on the fact that the formalism has been applied correctly. The other important finding from the group-subgroup relationship is based on the fact that *translationengleiche* symmetry reductions are prone to cause twinning during a second order transition. The corresponding twin law must follow one of the non-translational symmetry elements lost during the symmetry reduction. The fact that both the 200 K and 100 K measurements contain a twin along one of the face diagonals $\langle 1\ 1\ 0 \rangle$ does indeed suggest that this twinning was caused during the phase transition.

A group-subgroup relationship is a prerequisite for a second-order phase transition according to Landau theory and the data herein could thus suggest such a second-order phase transition.[21,22] While the existence of a group-subgroup relationship is a good indicator, it is important to find other evidence for this, as a reconstructive first-order phase transition does not have to follow a group-subgroup relationship, but could do so. Further studies (e.g. careful thermodiffraction around the phase transition) would be needed to study the hysteresis in detail. The cell volume would need to be investigated as a function of temperature to give a definitive answer as to whether this phase transition is first or second order.

5.6. The structure of Diammine Nickel Nitrate

5.6.1. Structure Solution and Refinement

When hexammine nickel nitrate is heated to 200 °C under mild dynamic vacuum (≈ 0.01 bar), a chemical reaction is triggered in which the compound changes its colour from purple to green. The product of this reaction was measured by X-ray diffraction, but the pattern could not be matched with a known crystal structure. It was therefore decided to index the pattern from scratch in order to solve the structural nature of the product. The four indexing programs employed (Dicvol[23], Ito[24], Treor[25] and McMaille[26]) led to very similar results, yielding an orthorhombic cell with approximate cell parameters of 11.06 Å, 9.35 Å and 6.05 Å. The attribution of the three cell parameters was different amongst the different programs and basically depended on the arbitrary settings of the programs. It is to be kept in mind that these programs are able to determine probable vectors which could be the cell parameters but do not include a mechanism for the determination of space groups or any supplementary symmetry information and the attribution of the vectors to the different cell parameters therefore has to be somewhat arbitrary.

Based on the knowledge of the approximate cell vectors, however, it is possible to obtain further symmetry operations by the means of specialised programs. The procedure used in here is based on the symmetry determination algorithm in Jana2006.[27] Before the symmetry determination routine can be employed, a structure-less Le Bail fitting solely based on the approximate cell parameters (*i.e.* in space group $P1$) was performed to refine the cell parameters further and to determine the approximate intensities of the peaks. Due to the fact that the cell indexing programs unanimously yielded an orthorhombic cell setting, the angles were kept fixed at 90° during this refinement. As no further symmetry implications were made at this stage, the Le Bail fitting extracted intensity information on all possible peak positions. This subsequently allowed the determination of further translational symmetry, *i.e.* cell centerings, screw axes and glide planes by using the extracted intensity information for the determination of systematic absences. Due to the nature of powder diffraction where the 3-dimensional diffraction information is merged into only one dimension, no attribution of non-translational symmetry (mirror planes and rotation axes) is possible without a structural model, hence only a subset of possible space groups with the same translational symmetry can be identified.

It is therefore very beneficial for the solution of crystal structures from powder data to use the program Superflip[9] included into Jana2006. Superflip uses a charge flipping mechanism in superspace in order to determine the possible phase of the crystal structure and hence solve the structure. Superflip itself does not make use of any symmetry information during the phase determination but instead proposes a possible space group based on the information derived from the found electron density distribution. The set of information obtained both from the space group algorithm and the structure solution in Superflip resulted in the determination of the space group as $Pca2_1$. This non-centrosymmetric space group proved consistency at later stages of the refinement and the structure could be further refined in this space group. This furthermore allowed the exact determination of the cell parameters as the set of symmetries determined from the structure solution allowed the establishment of the structure in the standard setting. All atoms but the non-ligating oxygen atoms of the nitrate anions and the hydrogen atoms were found during the structure solution. The missing oxygen atoms could later be identified in the difference Fourier maps and the hydrogen atoms were constrained to the nitrogen atoms in order to give complete ammonia molecules.

Considering the low symmetry of the structure and the limited amount of information due to the nature of powder diffraction and the wavelength used, some constraints and restraints were used during the refinement in order to yield a reasonable and trustworthy structural model. All of these constraints and restraints are built upon the knowledge of the chemical nature of the compound and they were benchmarked against a completely unrestrained refinement in order to guarantee that the obtained fitting indices (Table 5.11) did not differ largely from those of an unrestrained refinement. The difference between constraints and restraints lies in their definition and the implications following from it. One variable is directly obtained from another variable through a mathematical operation in a constraint (and the overall numbers of variables is therefore reduced by one in the refinement). It is however noteworthy that the constrained parameter does not converge until it reaches the relative minimum for *all* formerly independent parameters and hence converges into an intermediate value of an independent refinement. A similar behaviour is reached through the use of restraints, but their implication is slightly different. The coupled parameters in restraints are still treated as individual variables during the refinement but their value is restricted to an expectation value within a certain tolerance of deviation. The expectation value in Jana2006 can be defined in two different ways: either by defining a numerical expectation value, or by grouping crystallographically independent values together in order to set them as equal. This latter method proved particularly useful within the refinement as bond lengths for chemically equivalent bonds

Table 5.11.: Crystallographic data for $[Ni(NH_3)_2](NO_3)_2$

Sum formula	$H_6N_4O_6Ni$
Crystal System	Orthorhombic
Space Group	$Pca2_1$
a / Å	11.0631(4)
b / Å	6.0456(3)
c / Å	9.3530(4)
V /Å^3	625.55(4)
Z	4
Calculated Density, ρ_x /g·cm^{-3}	2.3016
R_p; wR_p	0.044; 0.060
Goof	2.49
R_{obs}; wR_2(all)	0.034; 0.043
$\Delta\rho$ [max, min] /(e^-/Å^3)	0.40;–0.42

could be restrained to equal values. It is to be noted that this last feature does not exist in EXPGUI/GSAS[28] where parameters can only be restrained to concrete expectation values.

In order to yield reasonable refinements, the U_{iso} values of the ligands were constrained to unique values: both nitrogen atoms in the ammonia molecules were bound together[†], and the two crystallographically independent nitrate anions were bound as individual groups, *i.e.* one nitrate anion was defined to have the same displacement parameter for all four atoms. The distances and some of the angles within the compound were treated with restraints (with a relatively high tolerance) rather than constraints in order to allow for some structural flexibility and derivation from the ideal molecular structures. The restraints used were as following:

- the Ni–N distances should be approximately equal,
- the Ni–O distances should be approximately equal,

[†] By binding the two nitrogen atoms together, the hydrogen displacement parameters were also made equal as these were defined as 1.2 times the displacement parameters of the atom they were riding on.

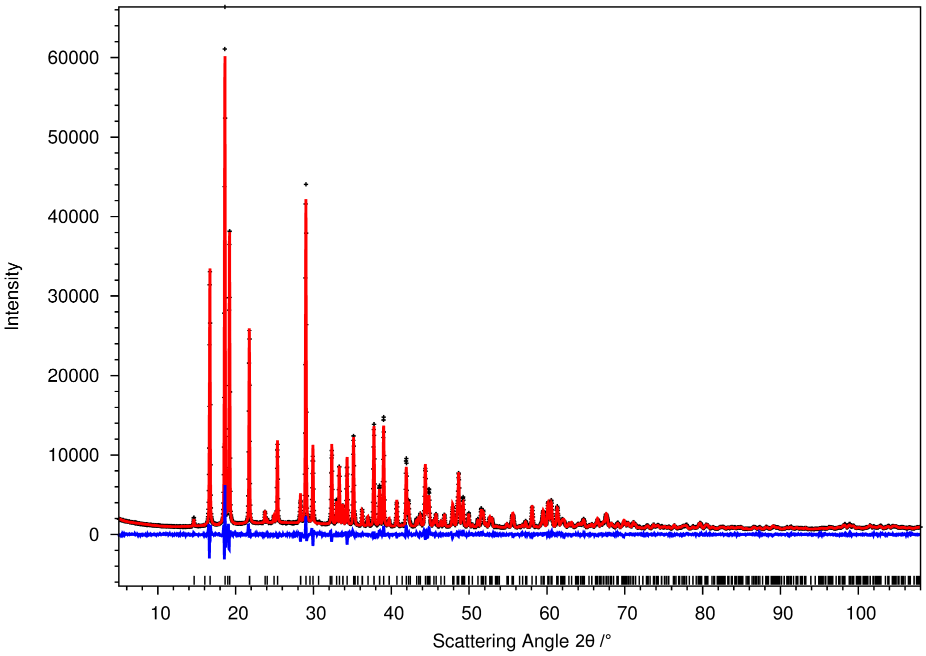

Figure 5.15.: Rietveld refinement results for $[Ni(NH_3)_2](NO_3)_2$. The measured X-ray pattern (black crosses), the calculated pattern (red lines) and the difference profile ($I_{obs} - I_{calc}$, blue line) are given together with the theoretical reflection positions (black sticks).

- the N–O distances in the individual nitrates should be approximately equal and
- the torsion angles of the nitrate anions should be approximately 180°.

This treatment resulted in a stable refinement with good refinement parameters (Table 5.11) and a good match between observed and calculated pattern (Figure 5.15), but more importantly in a chemically reasonable structure (Figure 5.16) which shall be the object of discussion in the next section.

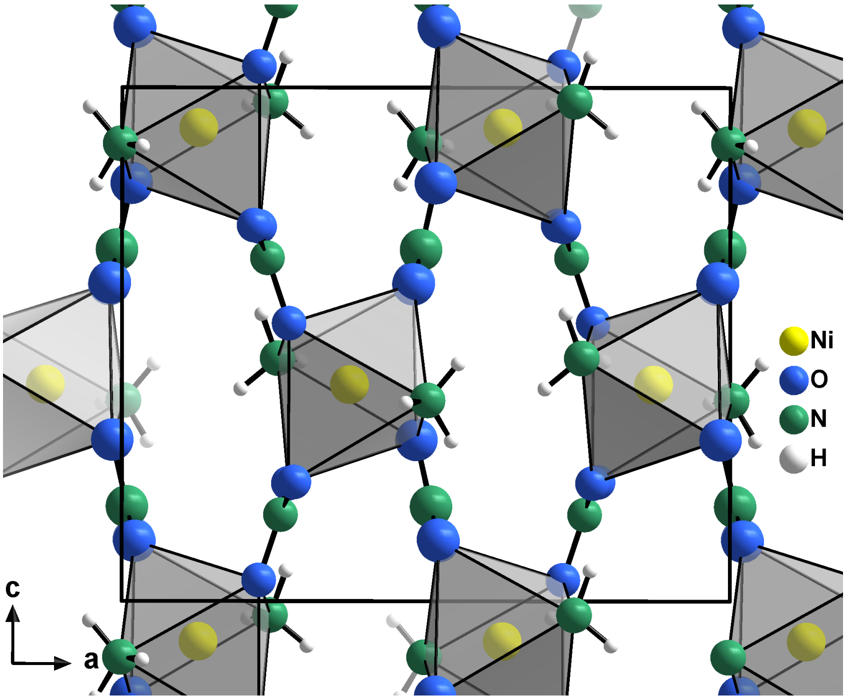

Figure 5.16.: Representation of the unit cell of $[Ni(NH_3)_2](NO_3)_2$ along the crystallographic *b*-axis. All atoms are represented by their ellipsoids of 90 % probability.

5.6.2. Description of the Crystal Structure

As pointed out in the last section, diammine nickel nitrate crystallises in the non-centrosymmetric space group $Pca2_1$ with the cell parameters as in Table 5.11. The structure is composed of a 3-dimensional network of $[Ni(NH_3)_2(NO_3)_{4/2}]$ octahedra which are linked through bridging nitrate anions. This structural type is somewhat unique as it forms the first structural evidence of bridging nitrate ions in an octahedral environment amongst ammine complexes. The only structures known so far in which nitrate anions are bridging metal ammine complexes are those of the diammines of copper and platinum which both form with the metals in square-planar coordination.[29,30] The copper and platinum diammine nitrates furthermore form layers of bridged square-planes (*i.e.* a 2D network) while this material consists of a 3-dimensional network.

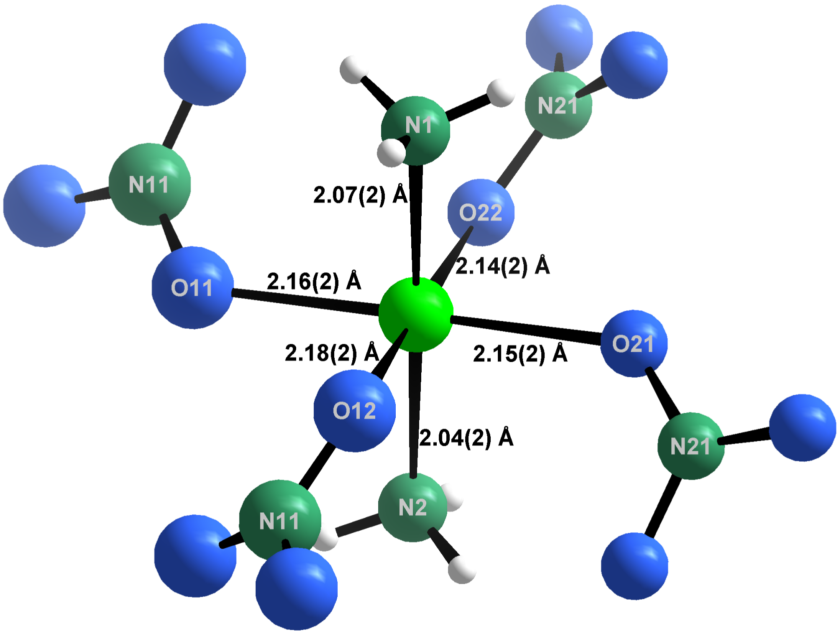

Figure 5.17.: Coordination sphere around Ni within the structure of $[Ni(NH_3)_2](NO_3)_2$. The Ni-ligand distances are given in Å.

The Ni coordination environment

All of the following analyses from the crystal structure suffer from the comparably large errors making most effects statistically insignificant. Further analyses, for instance from synchrotron data with higher d-spacing resolution will be needed to ensure the accuracy of these preliminary conclusions. A perfect octahedral coordination of Ni in $[Ni(NH_3)_2(NO_3)_{4/2}]$ is not expected as the complex consists of 2 different ligands (Figure 5.17). The ammonia ligands are accordingly closer to the Ni central atom (Ni–N 2.04(2) Å and 2.07(2) Å) as the nitrate ligands (Ni–O from 2.14(2) Å to 2.18(2) Å). The ligating nitrate anions form a square-plane around the central Ni atom hwile the ammonia ligands overcap the square-plane to form a pseudo-octahedron. The Ni–O and Ni–N bonding distances lie within the range of what is observed for the other compounds in this theses and the structure can therefore be regarded with some confidence.

The low overall symmetry of the crystal structure does not reflect all the symmetry elements of the (idealised) compressed octahedron with its 4-fold axis as the highest symmetry element and the angles within the coordination environment are therefore free to refine as they depend on the atom positions. The N–Ni–N angle of 174(1)° between the opposing ammonia ligands is most likely an effect of the hydrogen bonding between the ammonia molecules and the nitrate anions surrounding it (*e.g.* d(H3N2–O22) = 2.36 Å). This observation is also underlined by the small difference in the Ni–N bond lengths and the fact that restraining this angle to the ideal 180° would in fact result in a significantly worse fitting of the model. The O–Ni–O angles in the square-plane range from 85.7(7)° to 93.0(7)° and are therefore also distorted from the ideal value. The distortions and the deviations in the respective bond lengths are most likely a consequence of the nitrate anion arrangement, which bridge two complex octahedra and are therefore in a chemically anisotropic environment, causing a structurally anisotropic bonding situation. This anisotropic bonding situation is also reflected in the structure of the nitrate anions, where this effect has dramatic consequences for the symmetry of the anion and its vibrational modes.

5.6.3. Structure of the Nitrate Anions and Vibrational Analysis

The N–O bond length in both crystallographically independent nitrate anions maximises at ca. 1.24 Å (Figure 5.18), comparable to those in the ordered phase II of hexammine nickel nitrate (see previous section). The N–O bond lengths of the oxygen atoms not involved in ligand bonding to Ni atoms appear shorter than those involved in ligand bonding. Also, the angles between the bonding oxygen atoms O11–N11–O12 and O21–N21–O22 appear smaller than those with one non-ligating oxygen (Table 5.12). This may hint towards a symmetry breaking in the anion. However, this interpretation needs to be

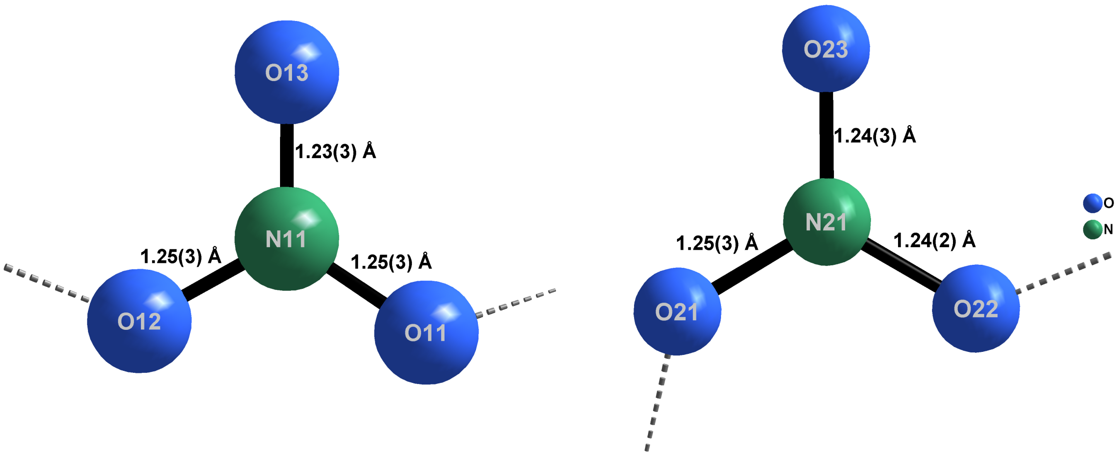

Figure 5.18.: The two crystallographically independent nitrate anions in the structure of $[Ni(NH_3)_2](NO_3)_2$. The N–O distances are given in Å.

treated with prudence as the differences in bonds and angles are within the range of the estimated standard derivation and therefore not statistically relevant. Instead of purely relying on the data obtained from diffraction on this question, a more direct probe of the bonding situation in the nitrate anions is needed to further clarify the bonding situation in this very compound.

The careful evaluation of spectroscopic data can be one way to clarify the bonding in these compounds. It has been suggested in the literature that the involvement of nitrate anions in ligand bonding leads to lower molecular symmetry of the anions[31] and therefore provokes the appearance of supplementary bands in the vibrational spectra.[32]

Table 5.12.: Comparison of the O–N–O angles in the nitrate groups of $Ni(NO_3)_2 \cdot 2\,NH_3$

Atoms	Angle
O11–N11–O12	117(2)°
O11–N11–O13	124(2)°
O12–N11–O13	119(2)°
O21–N21–O22	119(2)°
O21–N21–O23	121(2)°
O22–N21–O23	120(2)°

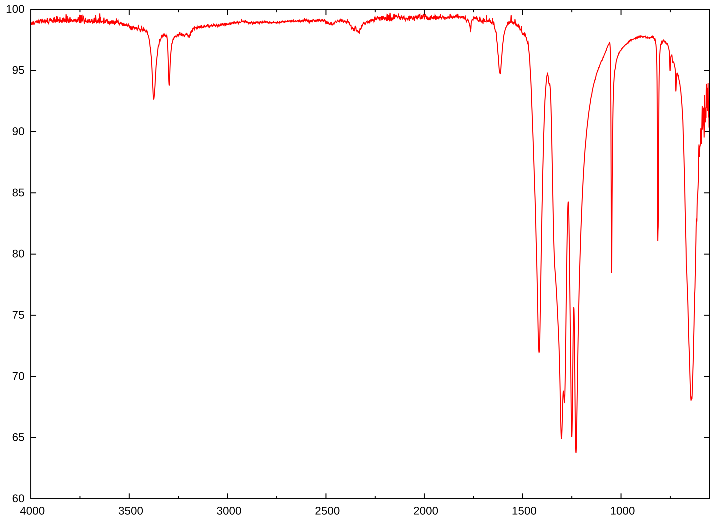

Figure 5.19.: Infrared spectrum for diammine nickel nitrate.

The examination of the IR spectrum (Figure 5.19) of $Ni(NH_3)_2(NO_3)_2$ was used to clarify the bonding situation. Although the spectrum appears considerably more complicated than those of the ammine halides, all bands could be assigned to the ammonia or nitrate groups (Table 5.13). The ammonia bands are similar to those observed for the diammine nickel chloride and underline again that the N–H bands are relatively independent of the ligand environment. One notable exception is the symmetric deformation band, which appears with two strong maxima close to each other. This is in stark contrast to the situation in the diammines where only one very strong peak is observed and the other bands attributed to symmetric deformations appear much smaller. This band splitting may coincide with the chemical inequvalence of the two ammonia ligands as it is probably arises from the splitting of the very strong NH_3 deformation band.

The nitrate bands exhibit clear signs of the symmetry reduction expected for covalently bonded nitrate anions. The band at 1048 cm^{-1} is attributed to the symmetric stretching $(\nu_1)^‡$ of the nitrate anion. The appearance of this band is important since the mode is

---

‡The notation of the different NO_3 modes is based on that used by Curtis and Curtis[32].

Table 5.13.: Assignment of the IR bands in the spectrum of $Ni(NO_3)_2 \cdot 2\,NH_3$.

Wavenumber /cm^{-1}	Band attribution	Reference wavenumber	
$Ni(NO_3)_2 \cdot 2\,NH_3$		$Ni(en)_2(NO_3)_2$[32]	$Ni(NH_3)_2Cl_2$
3375(2)	$\nu_a(NH_3)$		3346(2)
3296(2)	$\nu_s(NH_3)$		3265(2)
3195(2)	$2\delta_a(HNH)$		3167(2)
2475(2)	$\nu_1 + \nu_3(NO_3)$	2455	
2330(2)	$\nu_1 + \nu_3(NO_3)$	2320	
1765(2)	$\nu_1 + \nu_4(NO_3)$	1762, 1741	
1616(2)	$\delta_a(HNH)$		1607(2)
1417(2)	$\nu_3(NO_3)$	1420	
1303(2)	$\nu_3(NO_3)$	1303	
1250(2)	$\delta_s(HNH)$		1281(2)
1229(2)	$\delta_s(HNH)$		1239(2)
1048(2)	$\nu_1(NO_3)$	1033,1034	
812(2)	$\nu_2(NO_3)$	818	
751(2)	$\nu_4(NO_3)$	728	
721(2)	$\nu_4(NO_3)$	708	
643(2)	$\rho(NH_3)$		675(2)

IR inactive for the ideal D_{3h} symmetry of the nitrate anion because the dipole moment remains unchanged. If the symmetry is reduced by losing the three-fold rotation axis (i.e. C_{2v} or C_s), this mode becomes IR active as the stretching of the three N–O bonds are no longer equivalent and hence contribute differently to this mode. This results in an overall change of the dipole moment during this mode, which makes it IR active. Two other degenerate vibration modes in the D_{3h} symmetry, the asymmetric stretching mode (ν_3) and the in-plane bending mode (ν_4), lose their degeneracy and are observed as split bands in the IR spectrum of $Ni(NO_3)_2 \cdot 2\,NH_3$. Together with the last fundamental vibration mode, the out-of-plane deformation (ν_2), two sets of combination modes appear in the spectrum, both of which are split into two peaks. The separation between the two peaks attributed to the $\nu_1 + \nu_3$ mode of 145 cm^{-1} is slightly greater than that of the fundamental ν_3 mode of 114 cm^{-1}. This is most likely an effect of the very small band intensity of the combination bands, especially considering their relative breadth. The second combination band $\nu_1 + \nu_4$ does not appear split in the spectrum (a feature which is also observed in $Ni(NO_3)_2 \cdot 2\,H_2O$)[33] and is probably an effect of the bridging nature of the ligand. This is probably also due to the low intensity of the underlying fundamental mode ν_4 which is the weakest of the fundamental modes.

5.7. The Structure of $Cu(NH_3)_4(NO_3)_2$

5.7.1. Structure Refinement

Conventionally, $[Cu(NH_3)_4](NO_3)_2$ is produced by crystallisation based on an ethanol/water solvent mixing either by slowly pouring ethanol into water[34] or by solvent migration.[35] The intrinsic problem of these methods is the lower saturation level of ammonia in the solution as opposed to that in a pure aqueous solution, This could provoke the formation of a complex containing less than the maximum amount of ammonia. Using the method described herein guarantees the ammonia saturation of the solution at all times during the crystallisation, and should therefore lead to the formation of the highest ammoniated product obtainable at ambient conditions. Using $Cu(NO_3)_2 \cdot 2.5H_2O$ as the starting material for the reaction, crystals of the tetrammine $Cu(NH_3)_4(NO_3)_2$ were obtained as the end-product. $Cu(NH_3)_4(NO_3)_2$ crystallises in blue-violet platelets up to several centimetres in edge lengths after several days (Figure 4.11) of evaporation (reactions were normally left over the weekend after which the crystals could be observed).

The question of the space group of this compound has been the subject of discussion in the past. The discussion was concerned, whether the non-centrosymmetric space group *Pnn*2[36] or the centrosymmetric *Pnnm*[34] would apply. The non-centrosymmetric space group proposed by Karovicova and Mad'ar[36] is not based on a full structure determination, while the centrosymmetric spacegroup *Pnnm* allowed Morosin to solve and refine the crystal structure. Chukanov and co-workers[37] did nevertheless refine the structure of naturally occurring tetrammine copper nitrate (shilovite) in the non-centrosymmetric spacegroup *Pnn*2 based on *E* statistics[38] of the single crystal determination. The authors did however describe the mineral as "imperfect, thick tabular to equant crystals"[37], a fact which is of high importance when regarding *E* statistics as they can be easily yield unreasonable values through imperfections in the crystal or the measurement. Moreover, Chukanov *et al.* state that "The only difference is in the arrangement of H atoms of [sic] NH_3 groups which leads to the non-centrosymmetric space group in the case of shilovite."[37] This has however to be treated with great prudence as Chukanov *et al.* used a riding model for the hydrogen positions, a model which is adapted to the given crystal structure and can therefore hardly be taken as a decisive parameter for space group assignment. With the above in mind, no clear evidence for a non-centrosymmetric spacegroup could be found and it was therefore decided to use the orthorhombic spacegroup *Pnnm* as described by Morosin.[34]

5.7.2. Description of the Crystal Structure

The structure of $[Cu(NH_3)_4](NO_3)_2$ contains 8 formula units per unit cell (Figure 5.20, Table 5.14). The structure is essentially constructed from $[Cu(NH_3)_4]^{2+}$ cations and surrounding nitrate anions (Figure 5.20). The unit cell contains two crystallographically independent cations and four crystallographically independent nitrate anions (Table 5.15).

Table 5.14.: Refinement summary for the single crystal analysis of $[Cu(NH_3)_4](NO_3)_2$ at 295 K.

Sum formula	$CuH_{12}N_6O_6$
Space Group	*Pnnm*
a /Å	10.845(2)
b /Å	23.732(3)
c /Å	6.910(1)
V /Å^3	1778.4(4)
Measurement range	$-12 \leq h \leq 12$
	$-24 \leq k \leq 26$
	$-7 \leq l \leq 7$
Measured Reflections	8722
Independent Reflections ($I > 2\sigma$)	1530(1120)
R_{int}	0.071
R_1 [$F_o^2 > 2\sigma$]	0.054
wR_2 all F_o^2	0.135
Parameters	153
$Goof$	1.11
$\Delta\rho$ [max, min] /(e^-/Å^3)	0.94;–0.58

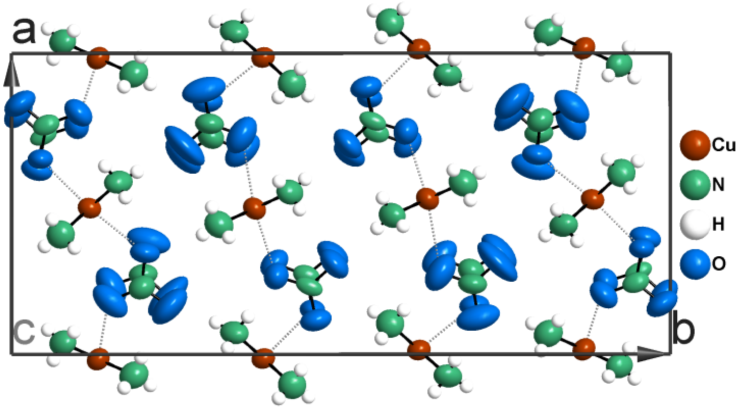

Figure 5.20.: Representation of the unit cell of $[Cu(NH_3)_4](NO_3)_2$ along the crystallographic c-axis. All atoms are represented by their ellipsoids of 90 % probability. The shortest Cu–O distances, which correspond to the poles of the distorted coordination octahedra are represented by dotted lines. Cu, N, H, and O are given in wine, green, white and blue respectively.

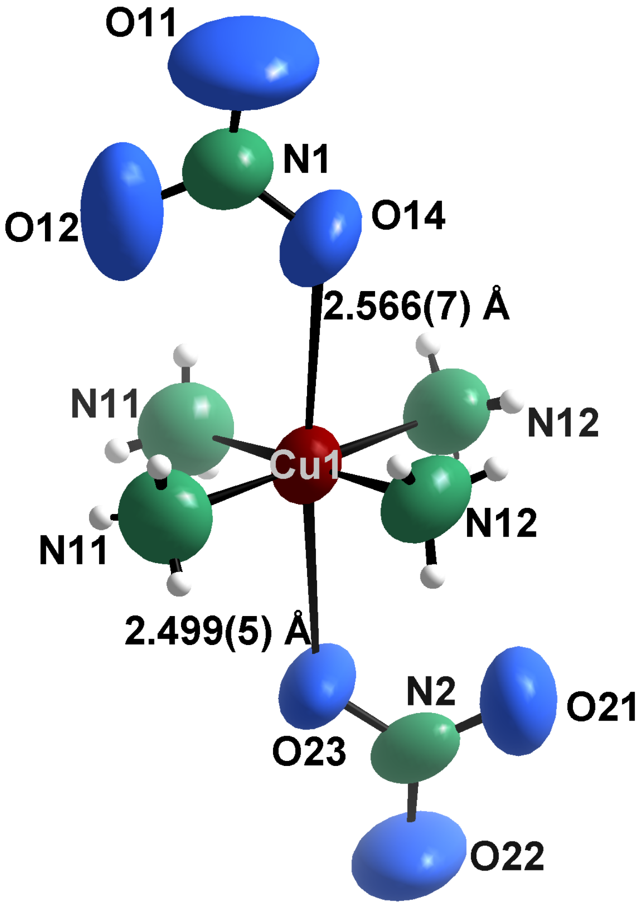

Figure 5.21.: Coordination sphere around Cu1 within the structure of $[Cu(NH_3)_4](NO_3)_2$. The Cu–O distances are given in Å.

While the different cations and anions are crystallographically independent, they only differ slightly in the bond lengths and angles (see section A.3.5 in the appendix) and can therefore be regarded as chemically equivalent.

It is interesting that the nitrate system shows the preference to form the tetrammine structure while the chloride system under the same conditions yields the formation of the hexammine (section 4.6). The amount of ligand during the reaction however should not be limited as the slow evaporation under ammonia atmosphere guarantees a saturated aqueous ammonia solution at any point during the crystal growth. In fact, when looking more closely at the coordination environment of the Cu central atoms (Figure 5.21 for

Cu1), one finds that the nitrate anions surrounding the [Cu(NH_3)$_4$] square-planes are aligned in a way that allows one oxygen atom per nitrate anion to enter the coordination sphere of the Cu central atom. These oxygen atoms are however over 2.49 Å away from the central atom (the equatorial Cu–N distances are much shorter and range from 2.012(5) Å to 2.017(4) Å) and hence complete the coordination of the Cu atoms to a strongly pseudo-Jahn-Teller distorted square-planar bi-pyramid (*i.e.* axially elongated octahedron). The shortest bond length of 2.49 Å corresponds to a bond valence parameter of 0.10 (R_0 = 1.649 Å, b = 0.37) and therefore indicates weak interactions between the central atom and the ligand. Also, the thermal ellipsoids of the ligating oxygen atoms in the nitrate anions are smaller than the non-ligated oxygen atoms (e.g. by 1/3 for O14 compared to O11 and O12, Figure 5.21 and Table 5.15) suggesting that the ligand oxygen atoms have a exhibit less liberation movement than the unbound oxygen atoms.

Although the nitrate anion is a rather weak ligand, as can be deduced from its position in the spectrochemical series,[4,5] it is preferred over the much stronger ammine ligand in this compounds. It is interesting to compare this result to hexammine copper chloride as the chloride anion would be a potential ligand as well, but is even weaker than the nitrate anion (and in fact enters the ligand sphere when ammonia is lacking in the lower ammines).

Table 5.15.: Atomic positions and isotropic displacement parameters in $[Cu(NH_3)_4](NO_3)_2$

Atom Site	X	Y	Z	U_{iso}/U_{eq} /Å^2
Cu1	0.48606(8)	0.11811(4)	0	0.0285(3)
N11	0.3983(4)	0.07441(19)	0.2084(7)	0.0415(14)
H11A	0.353(3)	0.0950(9)	0.267(4)	0.062
H11B	0.4478(19)	0.0613(16)	0.281(4)	0.062
H11C	0.359(3)	0.0497(14)	0.160(2)	0.062
N12	0.5721(4)	0.16205(19)	0.2102(7)	0.0396(13)
H12A	0.625(3)	0.1417(9)	0.263(5)	0.059
H12B	0.521(2)	0.1723(16)	0.293(4)	0.059
H12C	0.606(3)	0.1903(13)	0.162(2)	0.059
Cu2	0.98406(8)	0.13135(4)	0.5	0.0309(3)
N21	1.0386(4)	0.07759(18)	0.2911(7)	0.0388(13)
H21A	0.981(2)	0.0631(15)	0.246(5)	0.058
H21B	1.082(4)	0.0547(13)	0.336(2)	0.058
H21C	1.074(4)	0.0941(7)	0.211(4)	0.058
N22	0.9315(4)	0.1854(2)	0.2916(7)	0.0444(15)
H22A	0.889(4)	0.1704(8)	0.221(5)	0.067
H22B	0.988(2)	0.1962(16)	0.238(5)	0.067
H22C	0.898(4)	0.2102(14)	0.337(2)	0.067
N1	0.2226(6)	0.1976(3)	0	0.0396(19)
O11	0.1598(7)	0.2396(3)	0	0.094(3)
O12	0.1771(6)	0.1495(3)	0	0.063(2)
O14	0.3374(5)	0.2022(3)	0	0.0525(18)
N2	0.7619(6)	0.0526(3)	0	0.0268(15)
O21	0.8026(5)	0.1013(3)	0	0.0512(17)
O22	0.8331(6)	0.0127(3)	0	0.074(2)
O23	0.6489(5)	0.0436(2)	0	0.0534(19)
N3	0.7253(5)	0.0483(3)	0.5	0.0233(15)
O31	0.6134(5)	0.0381(3)	0.5	0.0519(17)
O32	0.7596(5)	0.0986(2)	0.5	0.0552(18)
O33	0.8005(6)	0.0103(3)	0.5	0.066(2)
N4	0.2660(6)	0.1996(3)	0.5	0.0390(19)
O41	0.3777(6)	0.2081(3)	0.5	0.067(2)
O42	0.2284(7)	0.1509(3)	0.5	0.075(2)
O43	0.1928(8)	0.2374(4)	0.5	0.107(4)

Table 5.16.: Atomic positions and isotropic displacement parameters in $[Cu(NH_3)_4](NO_3)_2$ in Å^2

Atom Site	U^{11}	U^{22}	U^{33}	U^{12}	U^{13}	U^{23}
Cu1	0.0224(5)	0.0293(6)	0.0337(6)	-0.0023(4)	0	0
N11	0.042(3)	0.042(3)	0.041(3)	0.000(2)	0.004(2)	0.002(3)
N12	0.028(2)	0.043(3)	0.047(3)	0.002(2)	-0.006(2)	-0.007(3)
Cu2	0.0263(5)	0.0278(6)	0.0386(6)	0.0039(4)	0	0
N21	0.033(2)	0.038(3)	0.045(3)	0.002(2)	0.001(2)	-0.008(2)
N22	0.040(3)	0.045(3)	0.049(4)	0.005(2)	0.001(2)	-0.001(3)
N1	0.031(4)	0.037(5)	0.051(6)	0.005(3)	0	0
O11	0.069(5)	0.066(5)	0.147(9)	0.038(4)	0	0
O12	0.058(4)	0.064(5)	0.069(5)	-0.029(4)	0	0
O14	0.023(3)	0.048(4)	0.087(5)	-0.003(3)	0	0
N2	0.023(3)	0.038(4)	0.019(4)	0.007(3)	0	0
O21	0.040(3)	0.041(4)	0.073(5)	-0.013(3)	0	0
O22	0.037(4)	0.051(5)	0.133(8)	0.018(3)	0	0
O23	0.020(3)	0.034(4)	0.106(6)	0.001(2)	0	0
N3	0.020(3)	0.037(4)	0.013(4)	0.009(3)	0	0
O31	0.026(3)	0.052(4)	0.077(5)	-0.007(3)	0	0
O32	0.038(3)	0.032(4)	0.095(6)	-0.003(3)	0	0
O33	0.046(4)	0.043(4)	0.110(6)	0.018(3)	0	0
N4	0.022(4)	0.044(5)	0.050(6)	0.002(3)	0	0
O41	0.038(4)	0.099(6)	0.066(5)	-0.019(4)	0	0
O42	0.071(5)	0.050(5)	0.103(7)	-0.024(4)	0	0
O43	0.085(6)	0.085(6)	0.150(10)	0.060(5)	0	0

5.7.3. Vibrational Analysis

Similar to the discussion in the previous section, IR spectroscopy can be used to study the exact symmetry of the nitrate anion and therefore the influence of a possible covalent Cu–O bond formation. Chukanov *et al.* previously obtained an IR spectrum of shilovite,[37] but this appears to be contaminated with other compounds, most likely water, as all of the bands appear shifted from the ammines and nitrates here,§ while the bands appear in close agreement with the other ammine nitrates in this thesis (Table 5.17). The IR spectrum in this work shows the characteristic bands for ammine and nitrate groups (Figure 5.22). The small shift of the N–H stretching band (3341 cm^{-1} for ν_a) in comparison to diammine nickel nitrate (3375 cm^{-1}) is most probably a consequence of the shorter Cu–N bond, which causes a weakening of the N–H bond. The symmetric ammonia deformation band appears with a shoulder in the copper compound signifying the chemical independence of the two crystallographically independent ammonia molecules, although this phenomenon is much less distinct than in the diammine nickel nitrate.

Similar to the situation in $Ni(NO_3)_2 \cdot 2\,NH_3$, the appearance of a sharp band at 1050 cm^{-1} signifies the symmetry breaking and deviation from ideal nitrate D_{3h} symmetry. Each nitrate anion in the copper tetrammine could only serve as monodentate ligand and symmetry lowering suggests the formation of such ligand interactions. Another important feature in the IR spectrum of $[Cu(NH_3)_4](NO_3)_2$ is the quadruply split ν_3 band. This is most likely a consequence of the four crystallographically independent nitrate anions. While the $\nu_1 + \nu_4$ combination band in $Ni(NO_3)_2 \cdot 2\,NH_3$ is not split, it is split in the case of tetrammine copper nitrate. This splitting is indeed a feature which is often observed

---

§One striking example for this is the strong stretching vibration at 3472 cm^{-1} which is more likely to be an O–H stretching mode than a N–H stretching mode.[39] The ammonia stretching modes (normally strong in the analyses in this thesis) appear as small side peaks below the main peak. The high wavenumber shoulder at 3620 cm^{-1} could in fact even be an hydroxide O–H stretch.[40]

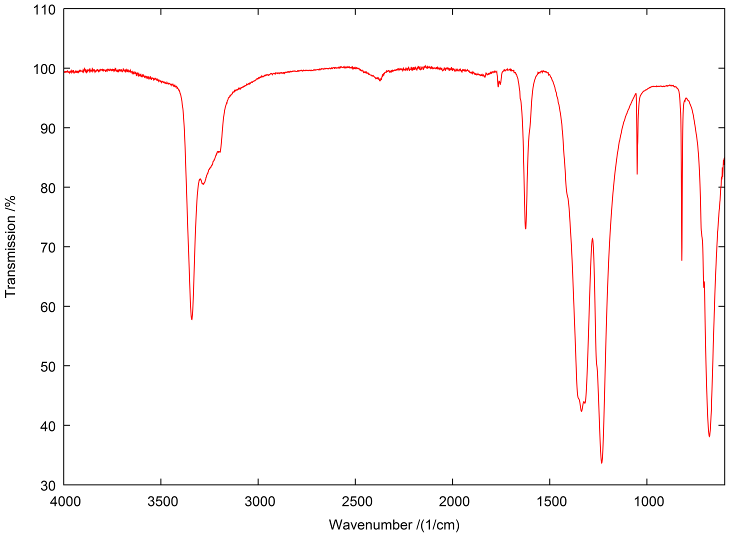

Figure 5.22.: Infrared spectrum for tetrammine copper nitrate.

for ligating nitrate anions[33] and further underlines the finding of a real Cu–N ligand interaction. The fact that the other distinct combination band $\nu_1 + \nu_3$ cannot be separated into individual peaks is most likely due to the fact that the individual peaks are hidden under the pronounced shoulder of the weak main peak.

5.8. Conclusions

It could be demonstrated that water as ligand molecule in $[Ni(H_2O)_6](NO_3)_2$ is easily replaced by ammonia to form the hexammine compound. This finding suggests that water impurities in ammine based ammonia storage materials may not be of great importance because they would get lost during the ammonia loading of the storage material. In addition, the first full structural characterisation of phase II of hexammine nickel nitrate could be presented in this work including a conclusive analysis of the symmetry relationship between the two phases in the system. The structure of diammine nickel nitrate was solved and refined from powder data. Its structure forms the first known member of a

Table 5.17.: Attribution of the IR bands of $Ni(NO_3)_2 \cdot 2\,NH_3$.

Wavenumber /cm^{-1}	Band attribution	Reference wavenumber	
$[Cu(NH_3)_4](NO_3)_2$		$Ni(NO_3)_2 \cdot 2\,NH_3$	$Ni(NH_3)_2Cl_2$
3341(2)	$\nu_a(NH_3)$	3375(2)	3346(2)
3283(2)	$\nu_s(NH_3)$	3296(2)	3265(2)
3196(2)	$2\delta_a(HNH)$	3195(2)	3167(2)
2373(2)	$\nu_1 + \nu_3(NO_3)$	2475(2)	
1765(2)	$\nu_1 + \nu_4(NO_3)$	1765(2)	
1755(2)	$\nu_1 + \nu_4(NO_3)$	1765(2)	
1624(2)	$\delta_a(HNH)$	1616(2)	1607(2)
1412(2)	$\nu_3(NO_3)$	1417(2)	
1355(2)	$\nu_3(NO_3)$	1303(2)	
1338(2)	$\nu_3(NO_3)$	1303(2)	
1319(2)	$\nu_3(NO_3)$	1303(2)	
1258(2)	$\delta_s(HNH)$	1250(2)	1281(2)
1233(2)	$\delta_s(HNH)$	1229(2)	1239(2)
1050(2)	$\nu_1(NO_3)$	1048(2),1034(2)	
821(2)	$\nu_2(NO_3)$	812(2)	
720(2)	$\nu_4(NO_3)$	751(2)	
708(2)	$\nu_4(NO_3)$	721(2)	
679(2)	$\rho(NH_3)$	643(2)	675(2)

new structure-type, as no other octahedral ammine nitrates in which the nitrate anion is located in the ligand sphere are known in the solid state. The participation of the nitrate anion in the coordination sphere of $Cu(NH_3)_4(NO_3)_2$ is somewhat debatable from the crystal structure, as the nitrate anions are positioned above and below the square-planar arrangement of ammine ligands with a relatively large distance to the central Cu ion. This compound was synthesised using the crystal growth method under controlled atmosphere which should guarantee the highest possible coordination of the final product due to the constantly saturated ammonia solution employed.

Due to nitrate symmetry breaking, IR spectroscopy is a very sensitive tool for detecting whether the counter ions are involved in coordination bonding or not. The three examples presented in this chapter suggest three different types of nitrate bonding: $[Ni(NH_3)_6](NO_3)_2$ contains purely ionic nitrate anions that are in the perfect D_{3h} molecular symmetry. The situation in $Cu(NH_3)_4(NO_3)_2$ is however different as the D_{3h} symmetry is clearly broken indicating that the nitrate anions interact with the central Cu ion. This symmetry breaking is also evident in diammine nickel nitrate but while the nitrate anions bind to only one Cu ion in $Cu(NH_3)_4(NO_3)_2$, the nitrate ions in $Ni(NH_3)_2(NO_3)_2$ bridge two Ni ions building up a 3D network of interlinked octahedra.

5.9. References

[1] J. Breternitz, L. J. Farrugia, A. Godula-Jopek, S. Saremi-Yarahmadi, I. E. Malka, T. K. A. Hoang, D. H. Gregory, *J. Cryst. Growth*, 2015, **422**, 1–6.

[2] J. Breternitz, L. J. Farrugia, A. Godula-Jopek, D. H. Gregory, *Z. Anorg. Allg. Chem.*, 2014, **640**, 2326.

[3] F. Bigoli, A. Braibanti, A. Tiripicchio, M. T. Camellini, *Acta Crystallogr. B*, 1971, **27**, 1427–1434.

[4] R. Tsuchida, *Bull. Chem. Soc. Jpn.*, 1938, **13**, 388–400.

[5] R. Tsuchida, *Bull. Chem. Soc. Jpn.*, 1938, **13**, 436–450.

[6] B. Weber, *Koordinationschemie: Grundlagen und aktuelle Trends*, Springer-Verlag, 2014, chapter Was Sind Komplexe?, . 3 ff.

[7] M. Viltange, *Microchim. Acta*, 1965, **53**, 609–620.

[8] A. Riou, Y. Cudennec, Y. Gerault, A. Lecerf, *C. R. Acad. Sci., Ser. IIb: Mec., Phys., Chim., Astron.*, 1996, **322**, 247–253.

[9] L. Palatinus, G. Chapuis, *J. Appl. Crystallogr.*, 2007, **40**, 786–790.

[10] A. Hoser, W. Joswig, W. Prandl, K. Vogt, *Mol. Phys.*, 1985, **56**, 853–869.

[11] A. Leclaire, *J. Solid State Chem.*, 1979, **28**, 235–244.

[12] E. A. Long, F. C. Toettcher, *J. Am. Chem. Soc.*, 1942, **64**, 629–632.

[13] S. Isotani, W. Sano, J. A. Ochi, *J. Phys. Chem. Solids*, 1975, **36**, 95–98.

[14] S. Hodorowicz, J. Czerwonka, J. M. Janik, J. A. Janik, *Physica B+C*, 1981, **111**, 155–159.

[15] A. F. Andresen, H. Fjellvåg, J. A. Janik, J. Mayer, J. Ściesiński, J. M. Janik, A. Migdał-Mikuli, E. Mikuli, M. Rachwalska, T. Stanek, *Physica B+C*, 1986, **138**, 295–304.

[16] Z. Trybuła, J. Stankowski, *Physica B: Condens. Matter*, 1988, **154**, 87–92.

[17] S. H. Yü, *Nature*, 1942, **150**, 347–349.

[18] J. K. Nimmo, B. W. Lucas, *Acta Crystallogr. B*, 1976, **32**, 1968–1971.

[19] Y. Laligant, G. Ferey, A. Le Bail, *Mater. Res. Bull.*, 1991, **26**, 269 – 275.

[20] H. Bärnighausen, *MATCH Comm. Math. Chem*, 1980, **9**, 139–175.

[21] U. Müller, *Z. Anorg. Allg. Chem.*, 2004, **630**, 1519–1537.

[22] U. Müller, *Symmetry relationships between crystal structures: applications of crystallographic group theory in crystal chemistry*, Oxford University Press, 2013.

[23] A. Boultif, D. Louër, *J. Appl. Crystallogr.*, 1991, **24**, 987–993.

[24] J. W. Visser, *J. Appl. Crystallogr.*, 1969, **2**, 89–95.

[25] P.-E. Werner, L. Eriksson, M. Westdahl, *J. Appl. Crystallogr.*, 1985, **18**, 367–370.

[26] A. Le Bail, *Powder Diffr.*, 2004, **19**, 249–254.

[27] V. Petříček, M. Dušek, L. Palatinus, *Z. Kristallogr. - Cryst. Mater.*, 2014, **229**, 345–352.

[28] B. H. Toby, *J. Appl. Crystallogr.*, 2001, **34**, 210–213.

[29] S. I. Troyanov, I. V. Morozov, K. O. Znamenkov, Y. M. Korenev, *Russ. J. Inorg. Chem.*, 1996, **41**, 1411–1418.

[30] B. Lippert, C. Lock, B. Rosenberg, M. Zvagulis, *Inorg. Chem.*, 1977, **16**, 1525–1529.

[31] C. C. Addison, N. Logan, S. C. Wallwork, C. D. Garner, *Q. Rev., Chem. Soc.*, 1971, **25**, 289–322.

[32] N. F. Curtis, Y. M. Curtis, *Inorg. Chem.*, 1965, **4**, 804–809.

[33] A. B. P. Lever, E. Mantovani, B. S. Ramaswamy, *Can. J. Chem.*, 1971, **49**, 1957–1964.

[34] B. Morosin, *Acta Crystallogr. B*, 1976, **32**, 1237–1240.

[35] S. N. Bathia, C. J. O'Connor, R. L. Carlin, L. De Jongh, *J. Chem. Phys. Lett.*, 1977, **50**, 353–357.

[36] M. Karovičová, J. Maďar, *Czech. J. Phys.*, 1960, **10**, 258–258.

[37] N. V. Chukanov, S. N. Britvin, G. Möhn, I. V. Pekov, N. V. Zubkova, F. Nestola, A. V. Kasatkin, M. Dini, *Mineral. Mag.*, 2015, **79**, 613–623.

[38] I. L. Karle, K. S. Dragonette, S. A. Brenner, *Acta Crystallogr.*, 1965, **19**, 713–716.

[39] F. Agulló-Rueda, J. M. Calleja, M. Martini, G. Spinolo, F. Cariati, *J. Raman Spectrosc.*, 1987, **18**, 485–491.

[40] E. F. De Oliveira, Y. Hase, *Vib. Spectrosc.*, 2003, **31**, 19–24.

6. Conclusions and Outlook

The work presented in this thesis has established that $NiCl_2$ is a promising ammonia store. It takes up gaseous ammonia at ambient conditions readily and releases it at mild temperatures upon heating. The thermal decomposition of $[Ni(NH_3)_6]Cl_2$ and its higher halide analogues were studied and the activation energies of the different steps were extracted using the Kissinger method. Furthermore, it was shown that $[Ni(NH_3)_6]Cl_2$ releases ammonia slowly when exposed to moist air, adding a safety relevant feature to the systems overall performance. The decomposition product of the reaction of $[Ni(NH_3)_6]Cl_2$ in moist air was identified as $(NH_4)_2[NiCl_4(NH_3,H_2O)_2]$ by structure solution from powder X-ray diffraction and the reaction pathway of the hexammine degradation could be elucidated using a combination of chemical analyses and crystallographic information.

$[Cu(NH_3)_6]Cl_2$ exhibits a Jahn-Teller distorted type of the K_2PtCl_6 structure type common for hexammine metal halides. Furthermore, the use of different methods (gravimetric uptake and thermal release experiments and diffraction experiments) revealed a non-stoichiometric ammonia deficit in the complex cation. Thermal decomposition of $[Cu(NH_3)_6]Cl_2$ and its bromide analogue were performed and the activation energies of the different decomposition steps were extracted. The thermal decomposition did not stop at the copper dihalide compounds but a larger weight loss was observed. This behaviour makes this material not recyclable at the full ammonia capacity and therefore impedes its usability as an ammonia store. The structural features related to the Jahn-Teller distortion were further analysed using powder neutron diffraction and single crystal diffraction. The latter was performed on crystals grown in a novel process, where slow evaporation from aqueous solution was performed under an ammonia atmosphere. All data collected consistently suggested a non-stoichiometric ammonia occupancy and some efforts were made to explain the complex cation, probably a superposition of hexammine and pentammine copper ions. Further analyses using direct probes for the coordination environment (*e.g.* EXAFS, EPR, INS) will help to draw a clearer picture of the concrete situation in the complex. When heating tetragonal "$[Cu(NH_3)_6]Cl_2$" under an ammonia atmosphere, it undergoes a phase transition to the cubic K_2PtCl_6 structure type without apparent JT distortion. This reversible process was observed by *in situ* X-ray diffraction and the nature of the complex cation was probed using powder diffraction refinement and computational methods. Direct complex coordination methods will be also beneficial to elucidate the exact complex environment in this compound. A comparable JT suppression was observed in the mixed $[Mg,Cu(NH_3)_6]Cl_2$ phase. This compound was synthesised and structurally characterised using powder X-ray refinements and it may facilitate the measurement of spectroscopic data on the complex compounds.

The quick ligand exchange reaction between solid $[Ni(H_2O)_6](NO_3)_2$ and ammonia gas yielded the formation of hexammine nickel nitrate within two hours. The product grows in large crystals, which can be explained by an *in situ* solvation effect. The structure of the starting material was refined at both room temperature and 100 K using single crystal diffraction and the reaction product was characterised using powder X-ray diffraction. The structure of the low temperature phase of $[Ni(NH_3)_6](NO_3)_2$ was measured and refined using single crystal diffraction at 200 K and 100 K. The symmetry descent between the high and low temperature phases was rationalised using symmetry relationships making a second order phase transition process plausible. The structure of diammine nickel chloride was solved and refined using powder data. The compound forms a new structure type and is so far the only known example of octahedrally coordinated bridging nitrate anions in a diammine metal nitrate. $Cu(NH_3)_4(NO_3)_2$ was characterised using single crystal X-ray diffraction. The infrared spectra (IR) of the three compounds above were examined and revealed interesting insights into the bonding situation of the nitrate anion. While $[Ni(NH_3)_6](NO_3)_2$ possesses purely ionic nitrate anions in D_{3h} symmetry, the appearance of further bands in the IR of $Ni(NH_3)_2(NO_3)_2$ and $Cu(NH_3)_4(NO_3)_2$ suggested a symmetry reduction of the nitrate anions through the formation of ligand bonding. IR therefore proves its suitability for the exact detection of the bonding situation in such compounds.

The proof-of-concept studies for $NiCl_2$ as an ammonia store are very promising and future research directions should point to the development of prototype ammonia stores based on this technology. An important factor for the thermal decomposition is the ammonia partial pressure over the sample and it will be of importance to carefully consider this in a realistic storage system. Despite its limited usability as an ammonia store, the further study of the $CuCl_2$–NH_3 promises new insights into the JT distortion in solids and in the stability of metal ammine salts under different conditions. Furthermore, their potential could be used in a mixed cation material to tune its storage properties.

A. Appendices

A.1. Appendix for 3. Nickel Halides as Promising Ammonia Stores

A.1.1. Tables for $[Ni(NH_3)_6]Cl_2$

Table A.1.: Atom positions and displacement parameters in $[Ni(NH_3)_6]Cl_2$.

Atom Site	X	Y	Z	U_{iso}/U_{eq} Å^2
Ni1	0	0	0	0.0237(6)
Cl1	0.25	0.25	0.25	0.0349(7)
N1	0.21249(16)	0	0	0.0475(9)
H1n1	0.241265	–0.078158	0.022648	0.057
H2n1	0.241265	0.019465	–0.079011	0.057
H3n1	0.241265	0.058693	0.056363	0.057

Table A.2.: Anisotropic displacement parameters for $[Ni(NH_3)_6]Cl_2$ in Å^2.

Atom Site	U^{11}	U^{22}	U^{33}	U^{12}	U^{13}	U^{23}
N1	0.0332(18)	0.0546(15)	0.0546(15)	0	0	0

Table A.3.: Atomic distances in $[Ni(NH_3)_6]Cl_2$.

Atom Site 1	Atom Site 2	Distance /Å
Ni1	N1	2.1420(16)
N1	H1n1	0.87
N1	H2n1	0.87
N1	H3n1	0.87

Table A.4.: Selected angles in $[Ni(NH_3)_6]Cl_2$.

Atom Site 1	Atom Site 2	Atom Site 3	Angle /°
N1	Ni1	N1	180.0(5)
N1	Ni1	N1	90
Ni1	N1	H1n1	109.47
Ni1	N1	H2n1	109.47
Ni1	N1	H3n1	109.47

A.1.2. Tables for $[Ni(NH_3)_6]Br_2$

Table A.5.: Atom positions and displacement parameters in $[Ni(NH_3)_6]Br_2$.

Atom Site	X	Y	Z	U_{iso}/U_{eq} /Å^2
Br1	0.25	0.25	0.25	0.0369(5)
Ni1	0	0	0	0.0258(6)
N1	0.20758(18)	0	0	0.0460(12)
H1n1	0.235513	–0.075712	0.02255	0.0552
H2n1	0.235513	0.018327	–0.076844	0.0552
H3n1	0.235513	0.057385	0.054294	0.0552

Table A.6.: Anisotropic displacement parameters in $[Ni(NH_3)_6]Br_2$ in Å^2.

Atom Site	U^{11}	U^{22}	U^{33}	U^{12}	U^{13}	U^{23}
N1	0.037(3)	0.0507(17)	0.0507(17)	0	0	0

Table A.7.: Atomic distances in $[Ni(NH_3)_6]Br_2$.

Atom Site 1	Atom Site 2	Distance /Å
Br1	N1	3.6973(2)
Ni1	N1	2.1553(19)
N1	H1n1	0.87
N1	H2n1	0.87
N1	H3n1	0.87

Table A.8.: Selected angles in $[Ni(NH_3)_6]Br_2$.

Atom Site 1	Atom Site 2	Atom Site 3	Angle /°
N1	Ni1	N1	90
N1	Ni1	N1	180.0(5)
Ni1	N1	H1n1	109.47
Ni1	N1	H2n1	109.47 Ni1
N1	H3n1	109.47	

A.1.3. Tables for $[Ni(NH_3)_6]I_2$

Table A.9.: Atom positions and displacement parameters in $[Ni(NH_3)_6]I_2$.

Atom Site	X	Y	Z	$U_{\mathrm{iso}}/U_{\mathrm{eq}}$ /Å^2
I1	0.25	0.25	0.25	0.0362(8)
Ni1	0	0	0	0.0173(15)
N1	0.1987(4)	0	0	0.063(4)
H1n1	0.225309	–0.07497	0.006068	0.0759
H2n1	0.225309	0.03223	–0.06796	0.0759
H3n1	0.225309	0.04274	0.061892	0.0759

Table A.10.: Anisotropic displacement parameters in $[Ni(NH_3)_6]I_2$ in Å^2.

Atom Site	U^{11}	U^{22}	U^{33}	U^{12}	U^{13}	U^{23}
N1	0.097(9)	0.047(4)	0.047(4)	0	0	0

Table A.11.: Atomic distances in $[Ni(NH_3)_6]I_2$.

Atom Site 1	Atom Site 2	Distance /Å
I1	N1	3.8960(7)
Ni1	N1	2.167(5)
N1	H1n1	0.87
N1	H2n1	0.87
N1	H3n1	0.87

Table A.12.: Selected angles in $[Ni(NH_3)_6]I_2$.

Atom Site 1	Atom Site 2	Atom Site 3	Angle /°
N1	Ni1	N1	90
N1	Ni1	N1	180.0(5)
Ni1	N1	H1n1	109.47
Ni1	N1	H2n1	109.47
Ni1	N1	H3n1	109.47

A.1.4. Thermal analyses of $[Ni(NH_3)_6]Cl_2$

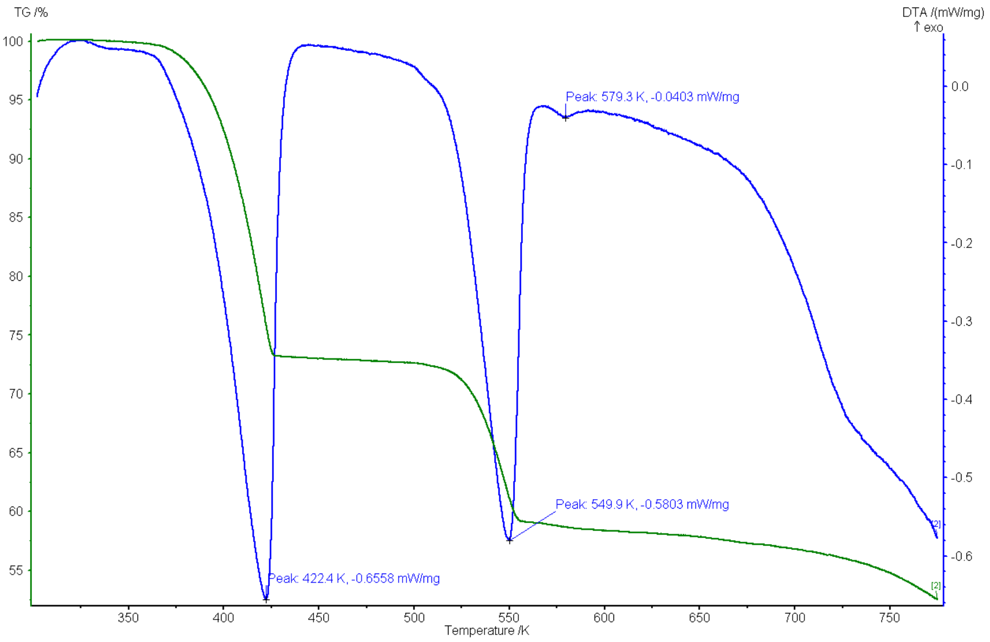

Figure A.1.: STA of $[Ni(NH_3)_6]Cl_2$ at 2 K/min. TG: green, DTA: blue

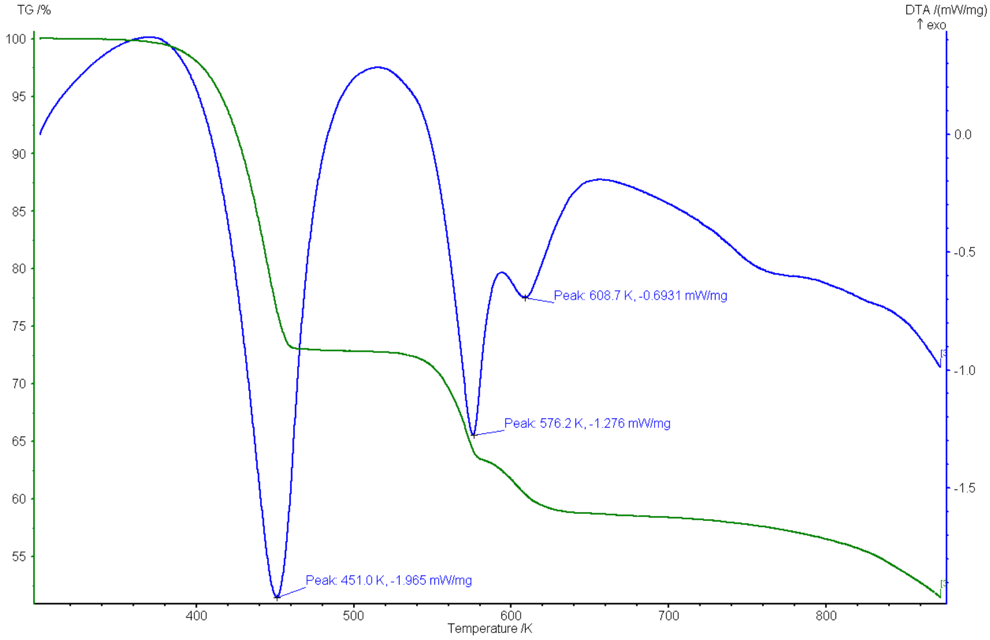

Figure A.2.: STA of $[Ni(NH_3)_6]Cl_2$ at 10 K/min. TG: green, DTA: blue

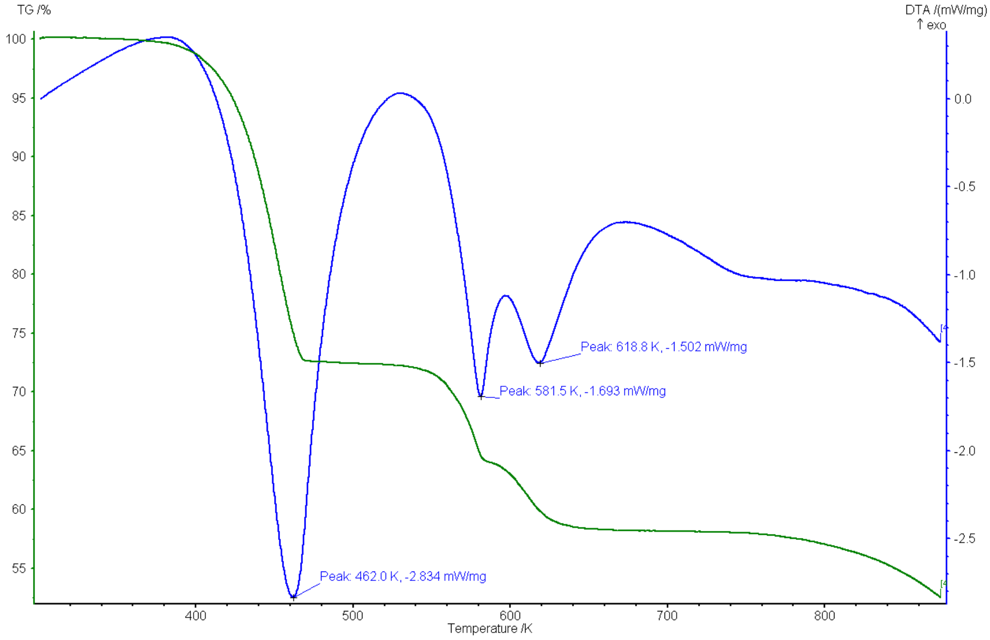

Figure A.3.: STA of $[Ni(NH_3)_6]Cl_2$ at 15 K/min. TG: green, DTA: blue

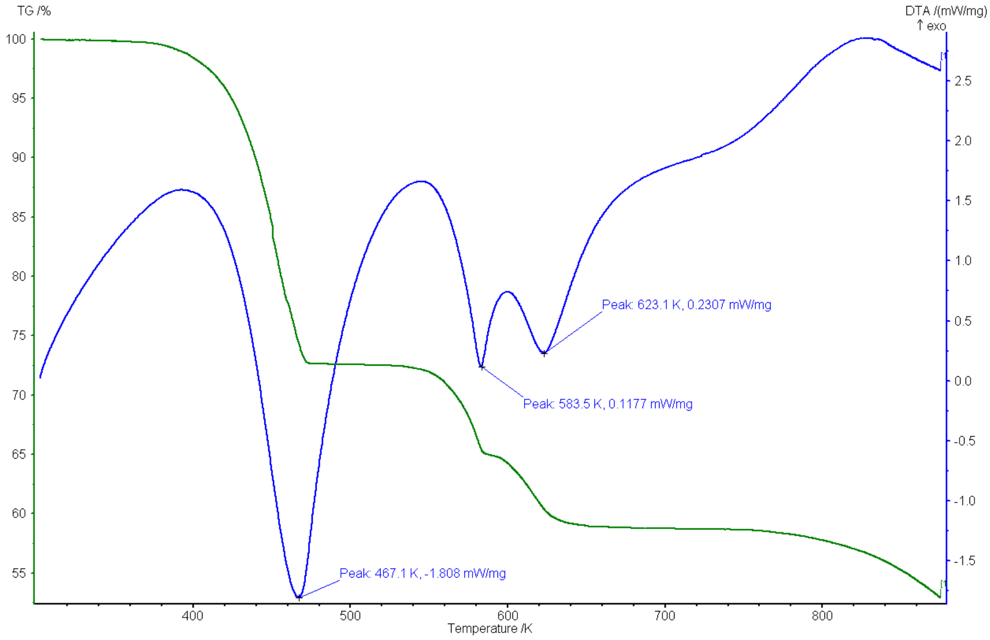

Figure A.4.: STA of $[Ni(NH_3)_6]Cl_2$ at 20 K/min. TG: green, DTA: blue

A.1.5. Thermal analyses of $[Ni(NH_3)_6]Br_2$

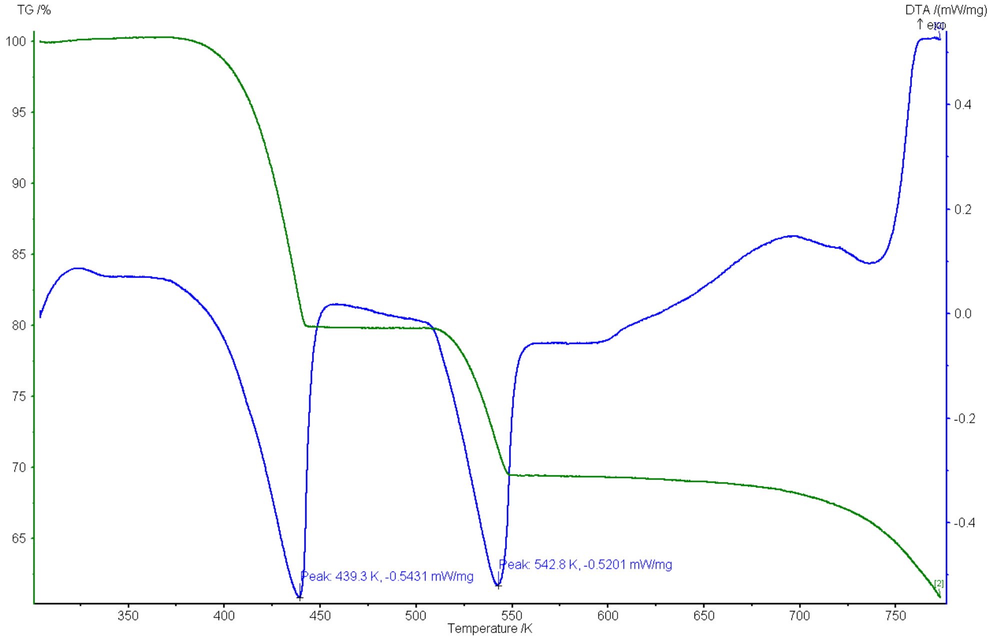

Figure A.5.: STA of $[Ni(NH_3)_6]Br_2$ at 2 K/min. TG: green, DTA: blue

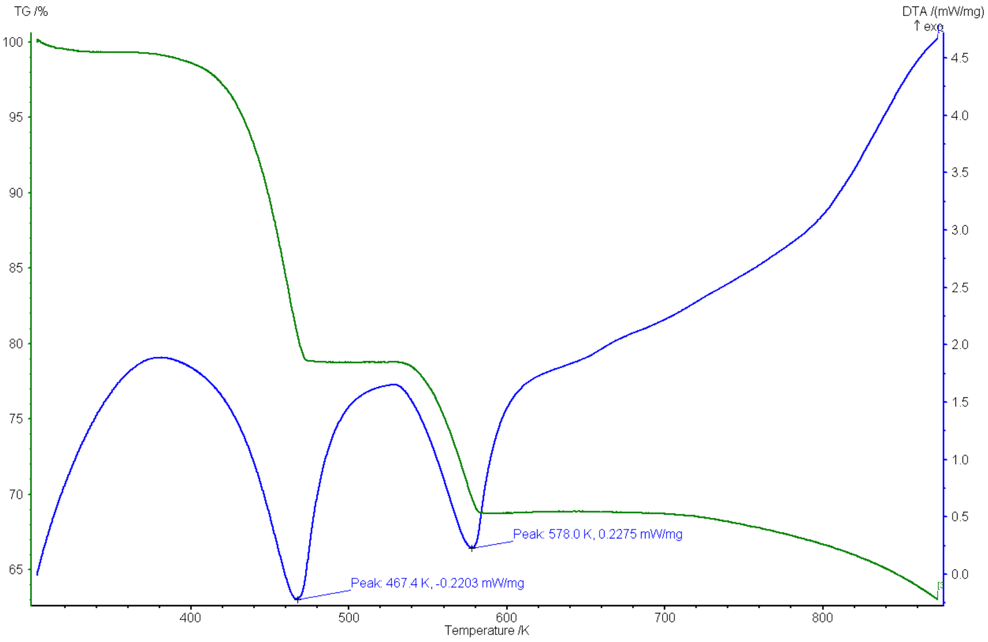

Figure A.6.: STA of $[Ni(NH_3)_6]Br_2$ at 10 K/min. TG: green, DTA: blue

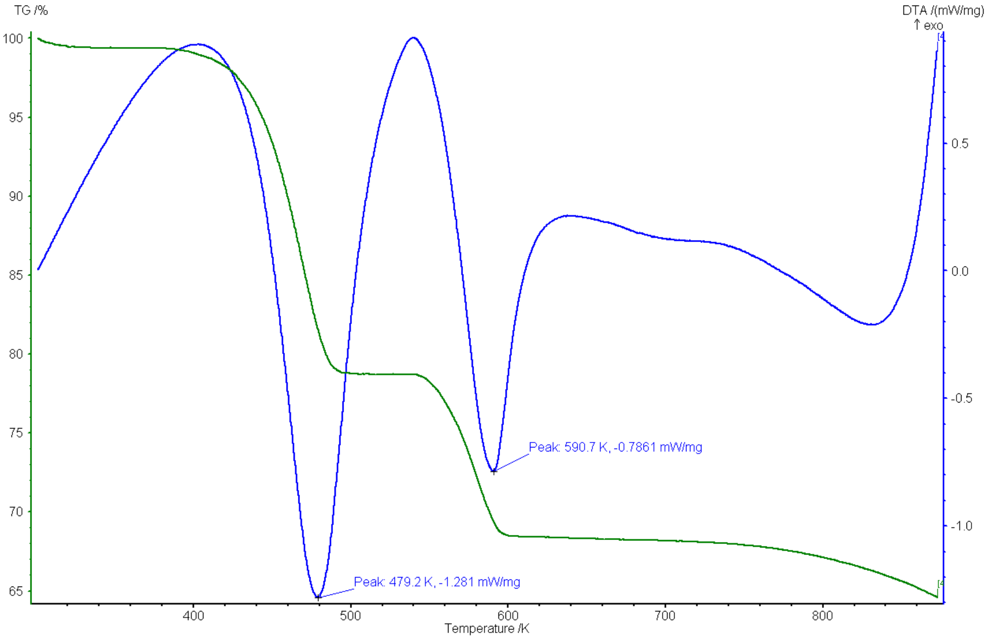

Figure A.7.: STA of $[Ni(NH_3)_6]Br_2$ at 15 K/min. TG: green, DTA: blue

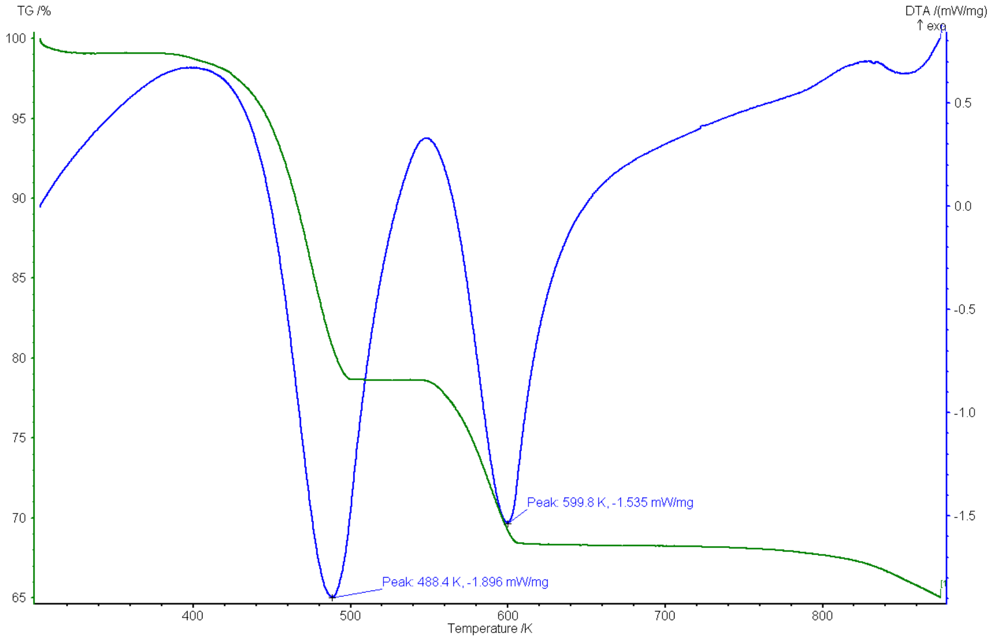

Figure A.8.: STA of $[Ni(NH_3)_6]Br_2$ at 20 K/min. TG: green, DTA: blue

A.1.6. Thermal analyses of $[Ni(NH_3)_6]I_2$

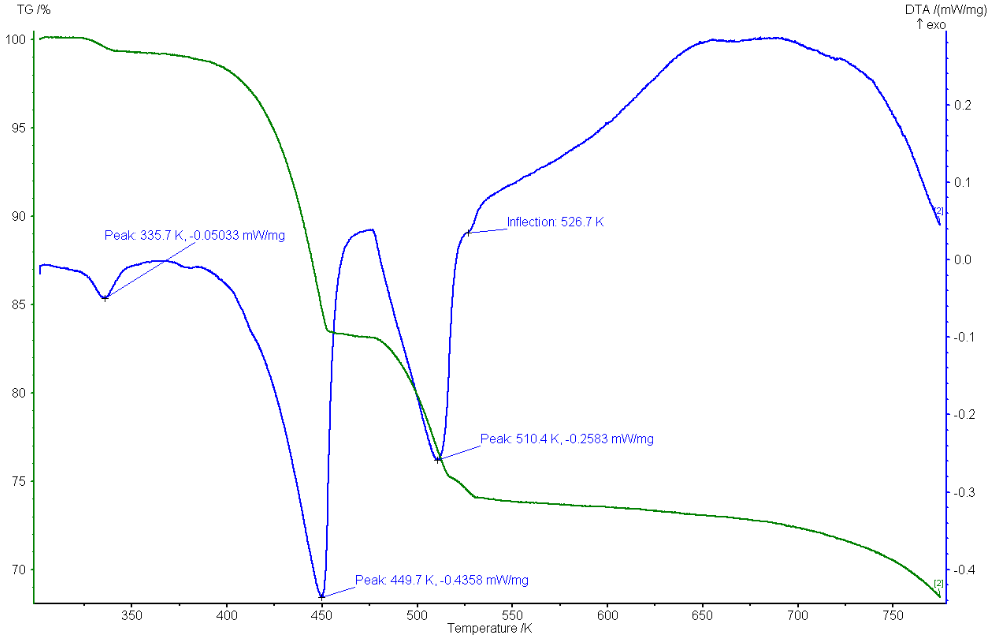

Figure A.9.: STA of $[Ni(NH_3)_6]I_2$ at 2 K/min. TG: green, DTA: blue

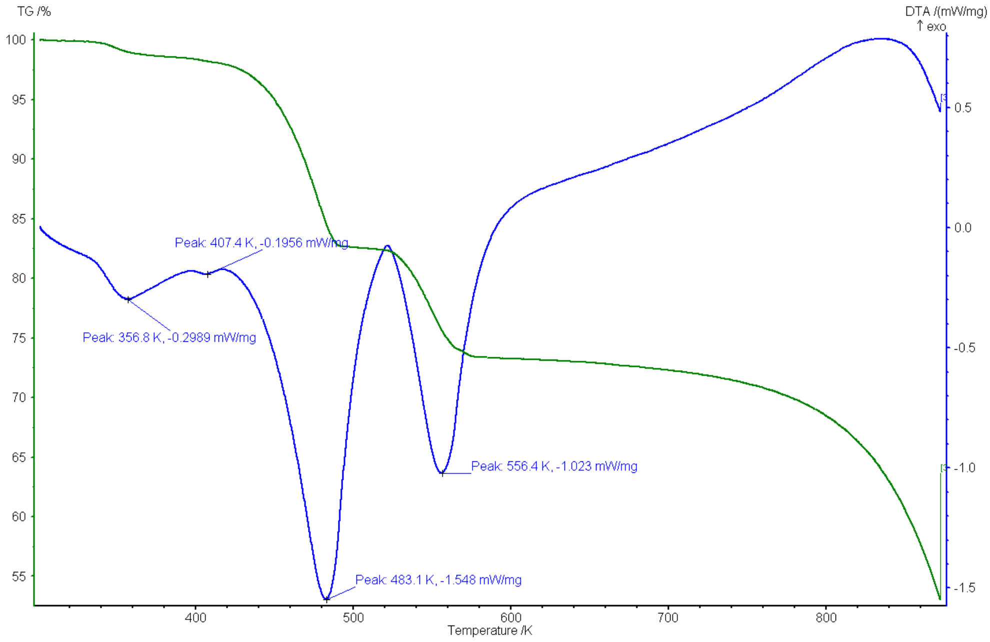

Figure A.10.: STA of $[Ni(NH_3)_6]I_2$ at 10 K/min. TG: green, DTA: blue

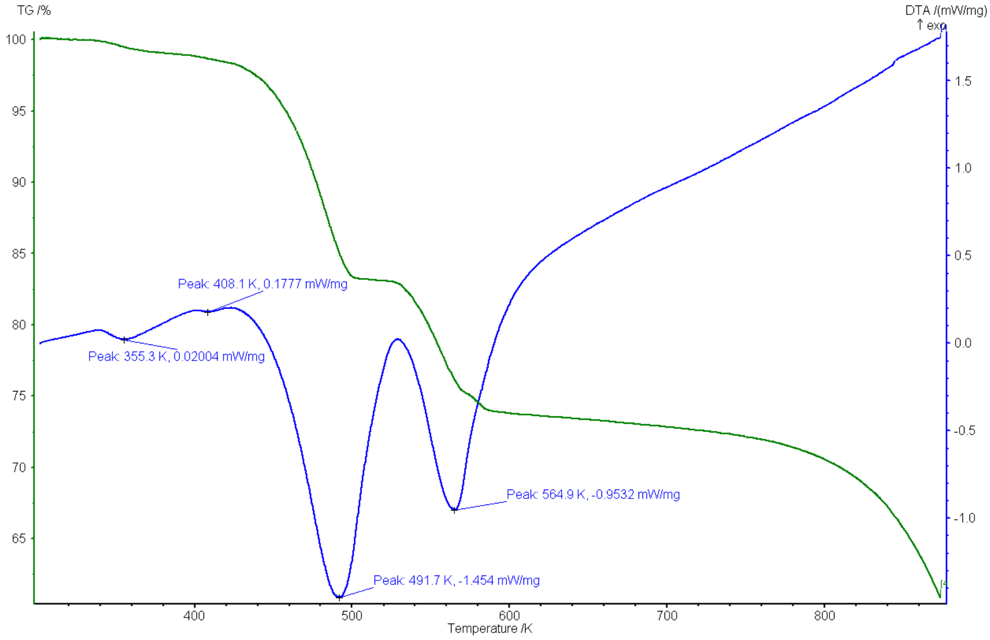

Figure A.11.: STA of $[Ni(NH_3)_6]I_2$ at 15 K/min. TG: green, DTA: blue

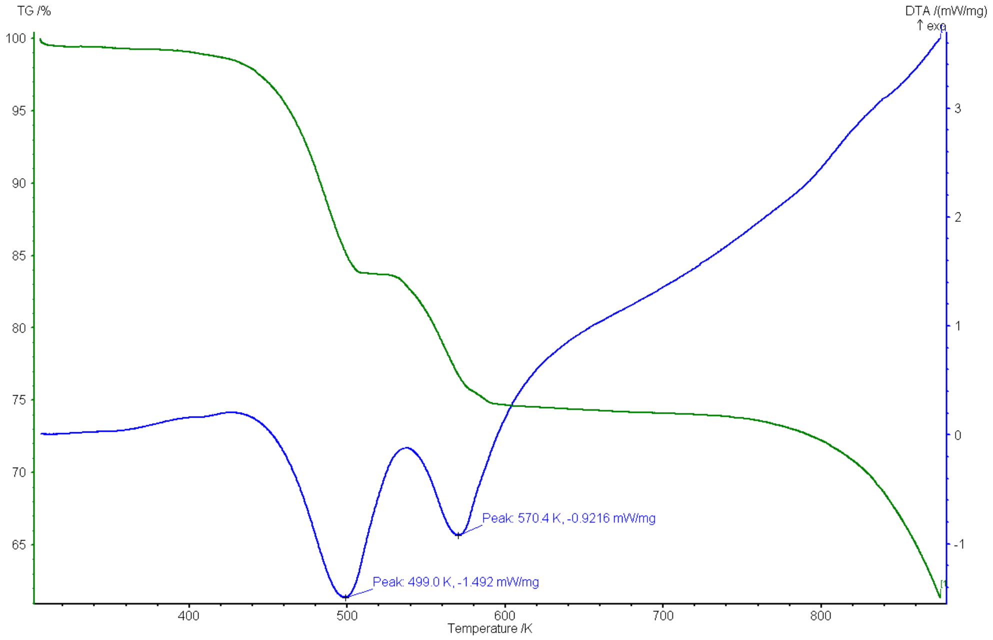

Figure A.12.: STA of $[Ni(NH_3)_6]I_2$ at 20 K/min. TG: green, DTA: blue

A.1.7. *In Situ* XRD of $[Ni(NH_3)_6]X_2$ (X = Br, I)

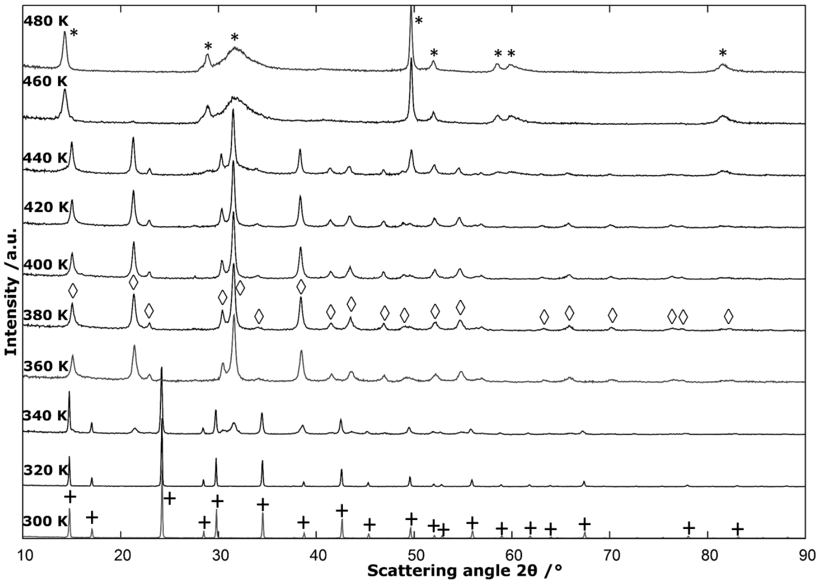

Figure A.13.: Variable temperature *in-situ* PXD patterns of the thermal decomposition of $[Ni(NH_3)_6]Br_2$. The measured temperature steps are given. The phases are indicated as follows: $[Ni(NH_3)_6]Br_2$: plusses, $Ni(NH_3)_2Br_2$: diamonds and $NiBr_2$: asterisks.

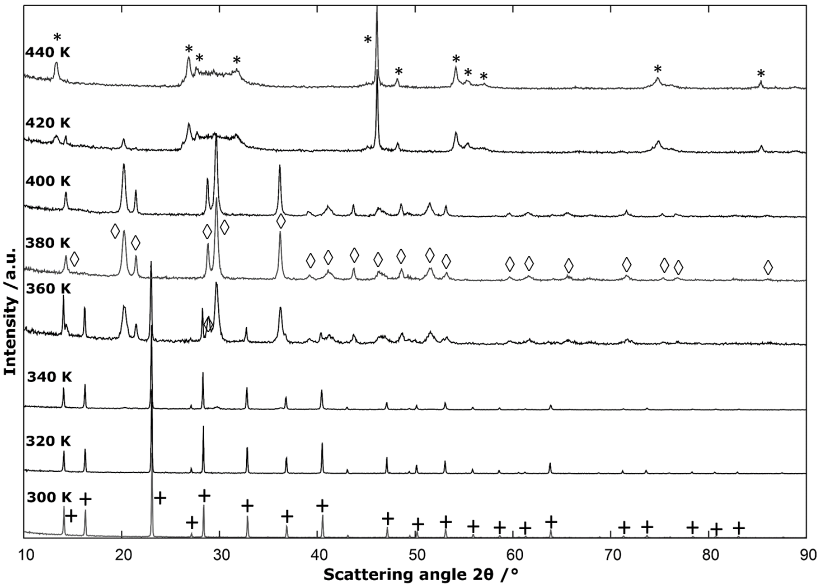

Figure A.14.: Variable temperature *in-situ* PXD patterns of the thermal decomposition of $[Ni(NH_3)_6]I_2$. The measured temperature steps are given. The phases are indicated as follows: $[Ni(NH_3)_6]I_2$: plusses, $Ni(NH_3)_2I_2$: diamonds and NiI_2: asterisks.

A.1.8. Tables for $NiCl_2 \cdot 2NH_3$

Table A.13.: Atom positions and displacement parameters in $Ni(NH_3)_2Cl_2$ at 373 K.

Atom Site	X	Y	Z	U_{iso}/U_{eq} /Å^2
Ni1	0	0	0	0.0317
Cl1	0.2226(7)	0	0.5	0.0317
N1	0	0.2541(14)	0	0.0317
H1n1	0.084453	0.290217	0.125921	0.038
H2n1	0.007808	0.290217	–0.222366	0.038
H3n1	–0.092261	0.290217	0.096445	0.038

Table A.14.: Atomic distances in $Ni(NH_3)_2Cl_2$ at 373 K.

Atom Site 1	Atom Site 2	Distance /Å
Ni1	Cl1	2.562(4)
Ni1	N1	2.040(11)
N1	H1n1	0.87

Table A.15.: Selected angles in $Ni(NH_3)_2Cl_2$

Atom Site 1	Atom Site 2	Atom Site 3	Angle /°
Cl1	Ni1	Cl1	91.74(14)
Cl1	Ni1	Cl1	88.26(14)
Cl1	Ni1	Cl1	180.0(5)
N1	Ni1	N1	180.0(5)
H1n1	N1	H1n1	141.06
H1n1	N1	H1n1	64.33
H1n1	N1	H2n1	109.47

A.1.9. Tables for $NiBr_2{\cdot}2NH_3$

Table A.16.: Atom positions and displacement parameters in $Ni(NH_3)_2Br_2$ at 373 K.

Atom Site	X	Y	Z	U_{iso}/U_{eq} /Å^2
Ni1	0	0	0	0.032(4)
Br1	0.2298(4)	0	0.5	0.0168(17)
N1	0	0.2677(18)	0	0.013(6)
H1n1	–0.011118	0.302569	0.210693	0.0151
H2n1	0.090621	0.302569	–0.084693	0.0151
H3n1	–0.079504	0.302569	–0.125999	0.0151

Table A.17.: Atomic distances in $Ni(NH_3)_2Br_2$ at 373 K.

Atom Site 1	Atom Site 2	Distance /Å
Ni1	Br1	2.716(3)
Ni1	N1	2.229(15)
N1	H1n1	0.87

Table A.18.: Selected angles in $Ni(NH_3)_2Br_2$ at 373 K.

Atom Site 1	Atom Site 2	Atom Site 3	Angle /°
Br1	Ni1	Br1	90.82(8)
Br1	Ni1	Br1	89.18(8)
Br1	Ni1	Br1	180.0(5)
N1	Ni1	N1	180.0(5)
Ni1	Br1	N1	93.188(16)
Ni1	N1	H1n1	109.47
H1n1	N1	H2n1	109.47

A.1.10. Tables for $NiI_2{\cdot}2NH_3$

Table A.19.: Atom positions and displacement parameters in $Ni(NH_3)_2I_2$ at 393 K.

Atom Site	X	Y	Z	U_{iso}/U_{eq} /Å^2
Ni1	0	0	0	0.056(6)
I1	0.2374(5)	0	0.5	0.028(2)
N1	0	0.254(4)	0	0.053(9)
H1n1	–0.000671	0.28655	0.198043	0.0639
H2n1	0.081745	0.28655	–0.097797	0.0639
H3n1	–0.081073	0.28655	–0.100246	0.0639

Table A.20.: Atomic distances in $Ni(NH_3)_2I_2$ at 393 K.

Atom Site 1	Atom Site 2	Distance /Å
Ni1	I1	2.929(3)
Ni1	N1	2.23(3)
N1	H1n1	0.87
N1	H2n1	0.87
N1	H3n1	0.87

Table A.21.: Selected angles in $Ni(NH_3)_2I_2$ at 393 K.

Atom Site 1	Atom Site 2	Atom Site 3	Angle /°
I1	Ni1	N1	90
N1	Ni1	N1	180.0(5)
Ni1	N1	H1n1	109.47
Ni1	N1	H2n1	109.47
Ni1	N1	H3n1	109.47

A.1.11. Tables for $(NH_4)_2[NiCl_4(H_2O)(NH_3)]$

Table A.22.: Anisotropic displacement parameters in $(NH_4)_2[NiCl_4(H_2O)(NH_3)]$ in Å^2

Atom Site	U^{11}	U^{22}	U^{33}	U^{12}	U^{13}	U^{23}
O1	0.05(2)	0.05(2)	0.04(3)	0	0	0

A.2. Appendix for 4. Structural Effects Copper Halide Ammines

A.2.1. Tables for $[Cu(NH_3)_6]Cl_2$

Table A.23.: Selected distances in $(NH_4)_2[NiCl_4(H_2O)(NH_3)]$

Atom Site 1	Atom Site 2	Distance /Å
Ni1	Cl1	2.507(6)
Ni1	O1	2.06(3)
Cl1	N1	3.369(5)
O1	H1o1	0.832(16)
N1	H1n1	0.87(11)

Table A.24.: Selected angles in $(NH_4)_2[NiCl_4(H_2O)(NH_3)]$

Atom Site 1	Atom Site 2	Atom Site 3	Angle /°
Cl1	Ni1	Cl1	180.0(5)
Cl1	Ni1	Cl1	90.0(2)
Cl1	Ni1	O1	90
Ni1	Cl1	N1	93.66(16)
Ni1	O1	H1o1	121.4(18)
H1o1	O1	H1o1	117(4)
H1n1	N1	H1n1	109(9)

Table A.25.: Atom positions and displacement parameters in NH_4Cl

Atom Site	X	Y	Z	$U_{\mathrm{iso}}/U_{\mathrm{eq}}$ /Å^2
H1	0.146	0.146	0.146	0.0378
N1	0	0	0	0.02(5)
Cl1	0.5	0.5	0.5	0.05(3)

Table A.26.: Atom positions and displacement parameters in $[Cu(NH_3)_6]Cl_2$ from Rietveld Refinement.

Atom Site	X	Y	Z	$U_{\mathrm{iso}}/U_{\mathrm{eq}}$ /Å^2	SOF
Cu1	0	0	0	0.041(2)	1
Cl1	0	0.5	0.25	0.039(3)	1
N1	0.1964(12)	0.1964(12)	0	0.098(5)	1
N2	0	0	0.2550(14)	0.054(11)	0.676(16)
H1n2	0.090564	0.066686	0.28575	0.0652	0.085(2)
H2n2	–0.103034	0.045088	0.28575	0.0652	0.085(2)
H3n2	0.01247	–0.111774	0.28575	0.0687	0.085(2)
H1n1	0.224531	0.224531	–0.087005	0.1173	0.5
H2n1	0.155659	0.293403	0.043502	0.1173	0.25
H3n1	0.293403	0.155659	0.043502	0.1173	0.25

Table A.27.: Atomic distances in $[Cu(NH_3)_6]Cl_2$ from Rietveld Refinement.

Atom Site 1	Atom Site 2	Distance /Å
Cu1	N1	2.026(9)
Cu1	N2	2.404(14)
N1	H1n1	0.87
N1	H2n1	0.87
N1	H3n1	0.87
N2	H1n2	0.87
N2	H2n2	0.87
N2	H3n2	0.87

Table A.28.: Selected angles in $[Cu(NH_3)_6]Cl_2$ from Rietveld Refinement.

Atom Site 1	Atom Site 2	Atom Site 3	Angle /°
N1	Cu1	N1	180.0(5)
N1	Cu1	N1	90.0(4)
N1	Cu1	N1	90.0(4)
N1	Cu1	N2	90
N1	Cu1	N2	90
N2	Cu1	N2	180.0(5)
H1n1	N1	H1n1	141.06
H1n1	N1	H2n1	109.47
H1n1	N1	H2n1	56.25
H2n1	N1	H3n1	109.47
H1n2	N2	H2n2	109.47
H1n2	N2	H3n2	109.47
H2n2	N2	H3n2	109.47

A.2.2. Thermal analyses of $[Cu(NH_3)_6]Cl_2$

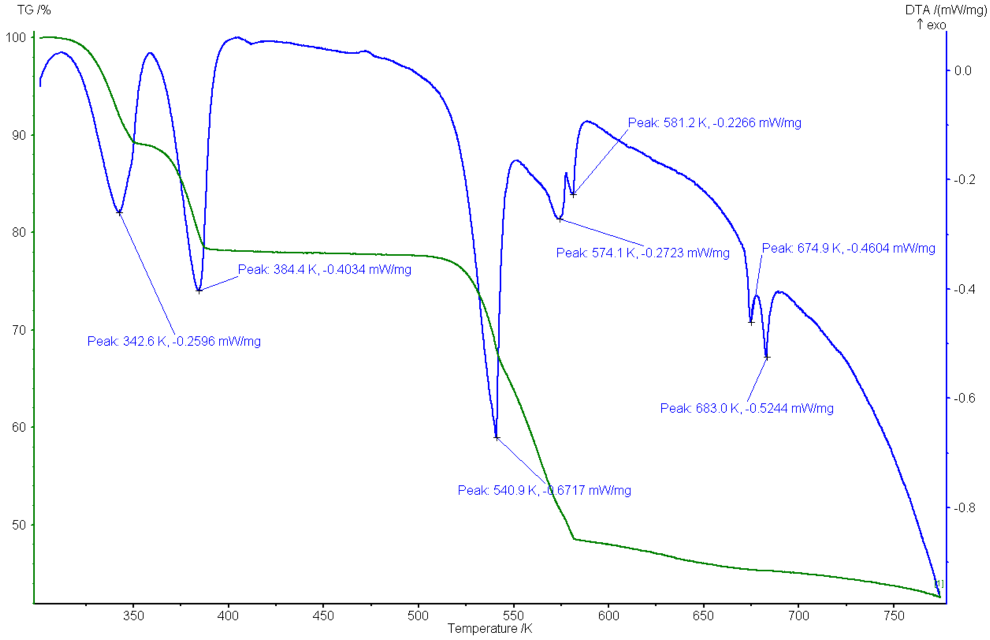

Figure A.15.: STA of $[Cu(NH_3)_6]Cl_2$ at 2 K/min. TG: green, DTA: blue

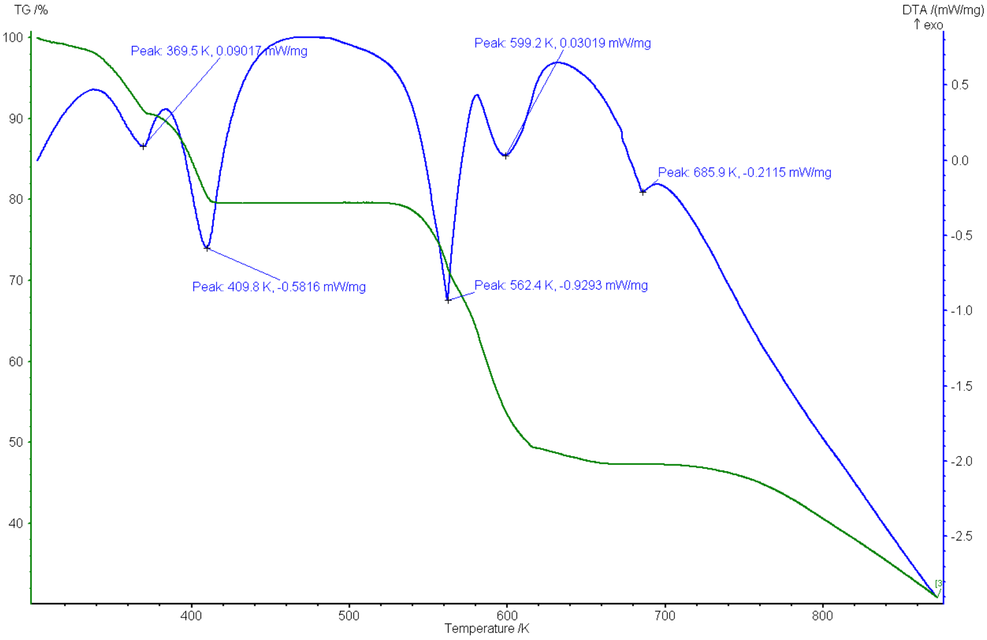

Figure A.16.: STA of $[Cu(NH_3)_6]Cl_2$ at 10 K/min. TG: green, DTA: blue

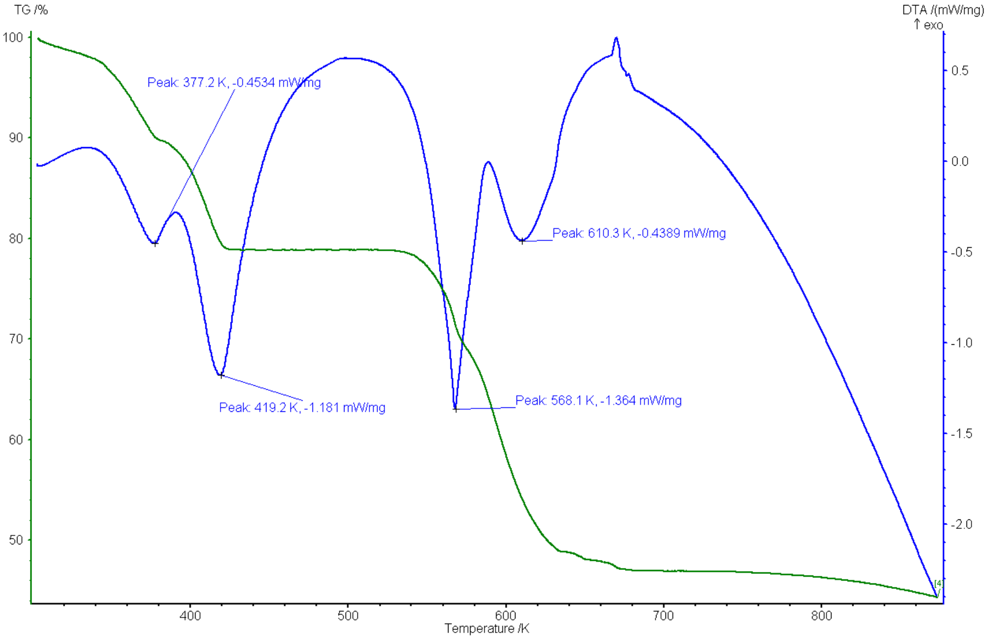

Figure A.17.: STA of $[Cu(NH_3)_6]Cl_2$ at 15 K/min. TG: green, DTA: blue

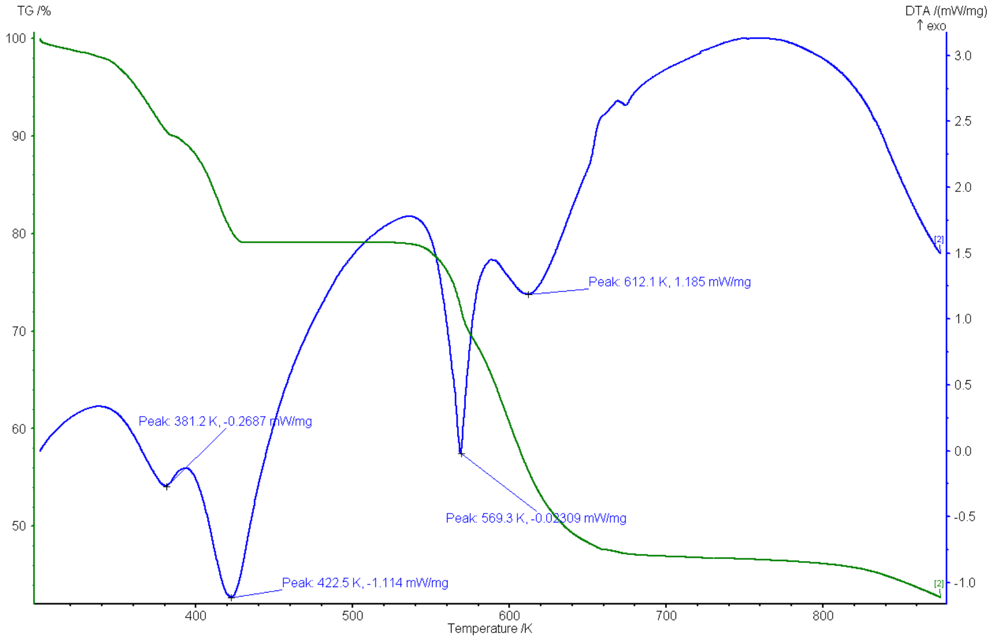

Figure A.18.: STA of $[Cu(NH_3)_6]Cl_2$ at 20 K/min. TG: green, DTA: blue

A.2.3. Thermal analyses of $[Cu(NH_3)_6]Br_2$

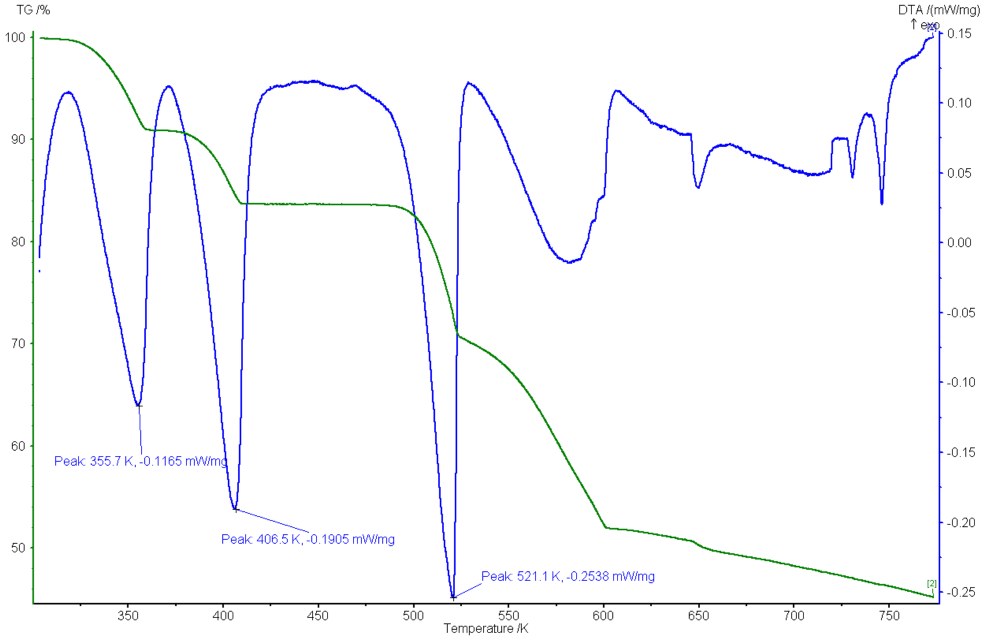

Figure A.19.: STA of $[Cu(NH_3)_6]Br_2$ at 2 K/min. TG: green, DTA: blue

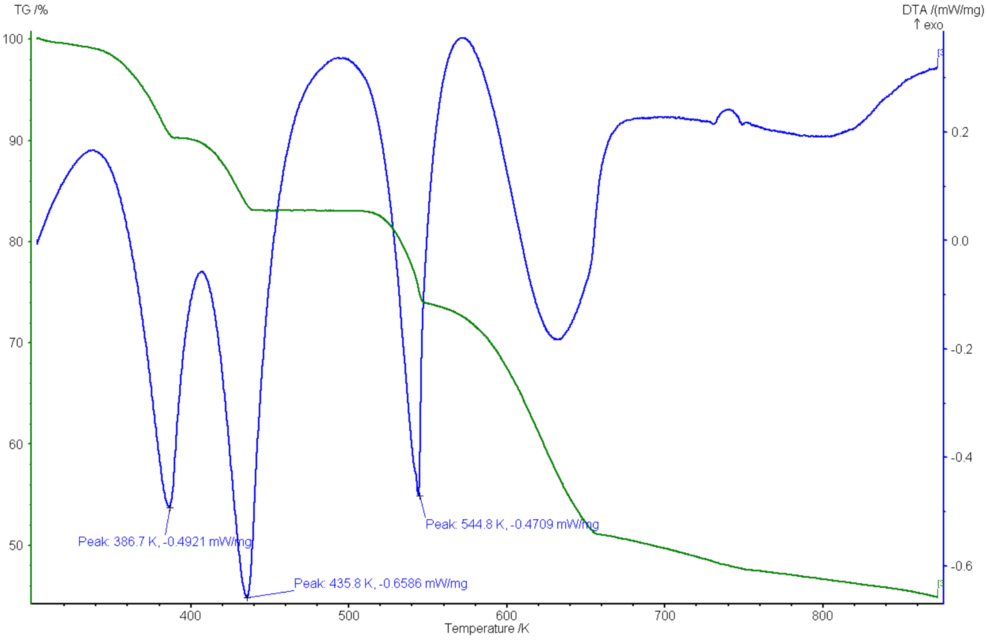

Figure A.20.: STA of $[Cu(NH_3)_6]Br_2$ at 10 K/min. TG: green, DTA: blue

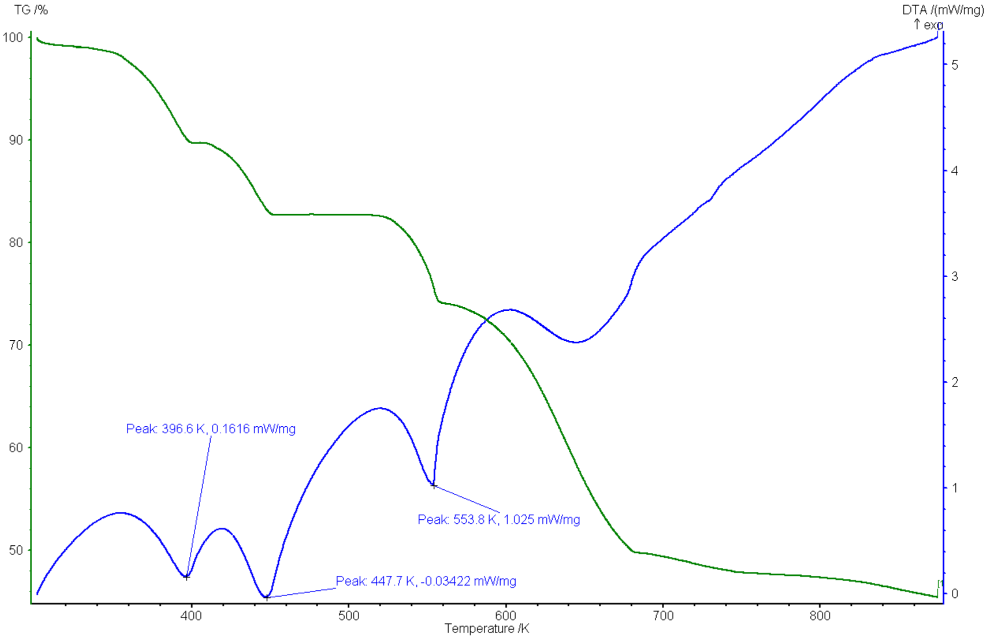

Figure A.21.: STA of $[Cu(NH_3)_6]Br_2$ at 20 K/min. TG: green, DTA: blue

A.2.4. Tables for the single crystal analysis of $[Cu(NH_3)_6]Cl_2$

A.2.5. Tables and Figures for $[Cu(ND_3)_6]Cl_2$

Table A.29.: Atomic distances in $[Cu(NH_3)_6]Cl_2$ as refined from single crystal analysis.

Atom Site 1	Atom Site 2	Distance /Å
Cu1	N1	2.055(7)
Cu1	N2	2.22(2)

Table A.30.: Selected angles in $[Cu(NH_3)_6]Cl_2$ as refined from single crystal analysis.

Atom Site 1	Atom Site 2	Atom Site 3	Angle /°
N1	Cu1	N1	180.0(4)
N1	Cu1	N1	90.0
N1	Cu1	N2	90.0
N2	Cu1	N2	180.0

Table A.31.: Atom positions and displacement parameters in $[\mathrm{Cu(ND_3)_6}]\mathrm{Cl_2}$.

Atom Site	X	Y	Z	$U_{\mathrm{iso}}/U_{\mathrm{eq}}$ /Å^2	SOF
Cu1	0	0	0	0.033(2)	1
Cl1	0	0.5	0.25	0.052(2)	1
N1	0.2055(2)	0.2055(2)	0	0.062(1)	1
N2	0	0	0.2416(8)	0.088(3)	0.673(3)
D1_2	0.2789(4)	0.1731(4)	0.0928(3)	0.0613(17)	0.465(4)
D2_1	0	0.1307(7)	0.2877(6)	0.103(4)	0.470(5)
D1_1	0.3343(7)	0.1423(7)	0	0.0613(17)	0.465(4)

Table A.32.: Atomic distances in $[\mathrm{Cu(ND_3)_6}]\mathrm{Cl_2}$.

Atom Site 1	Atom Site 2	Distance /Å
N1	D1_2	1.048(3)
N1	D1_1	1.042(5)
N2	D2_1	1.043(7)

Table A.33.: Selected angles in $[\mathrm{Cu(ND_3)_6}]\mathrm{Cl_2}$.

Atom Site 1	Atom Site 2	Atom Site 3	Angle /°
D$_2$	N1	D1$_2$	156.9(3)
D1_2	N1	D$_2$	112.5(3)
D1_2	N1	D$_2$	62.5(2)
D1_2	N1	D$_1$	115.1(2)
D1_2	N1	D$_1$	56.25(18)
D1_1	N1	D$_1$	141.5(4)
D2_1	N2	D$_1$	80.5(4)
D2_1	N2	D$_1$	132.1(10)

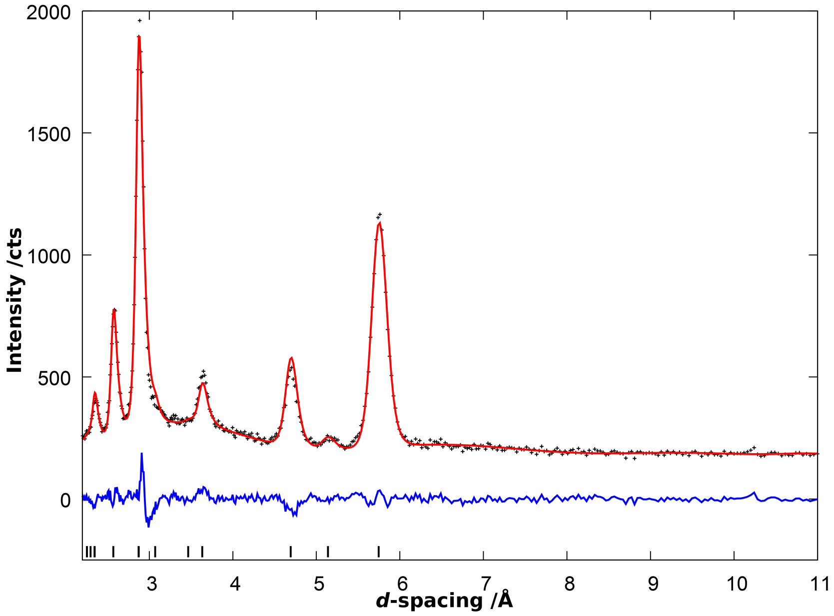

Figure A.22.: Comparison of the observed (black crosses) and calculated patterns (red line) from the Rietveld refinement against PND (detector bank 1) data for $[Cu(ND_3)_{6-x}]Cl_2$ at room temperature. The blue line represents the difference profile ($I_{obs} - I_{calc}$) and the black tick marks indicate the theoretical reflection positions.

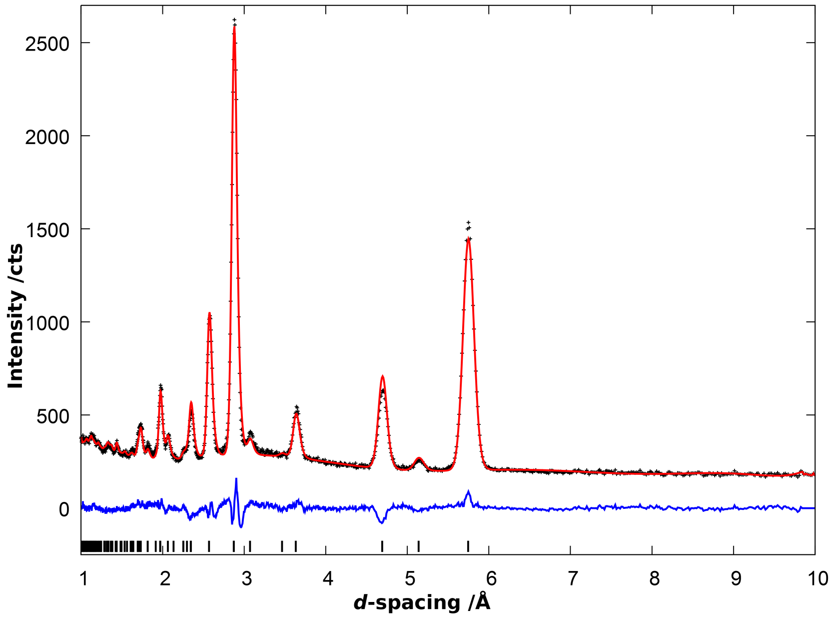

Figure A.23.: Comparison of the observed (black crosses) and calculated patterns (red line) from the Rietveld refinement against PND (detector bank 2) data for $[Cu(ND_3)_{6-x}]Cl_2$ at room temperature. The blue line represents the difference profile ($I_{obs} - I_{calc}$) and the black tick marks indicate the theoretical reflection positions.

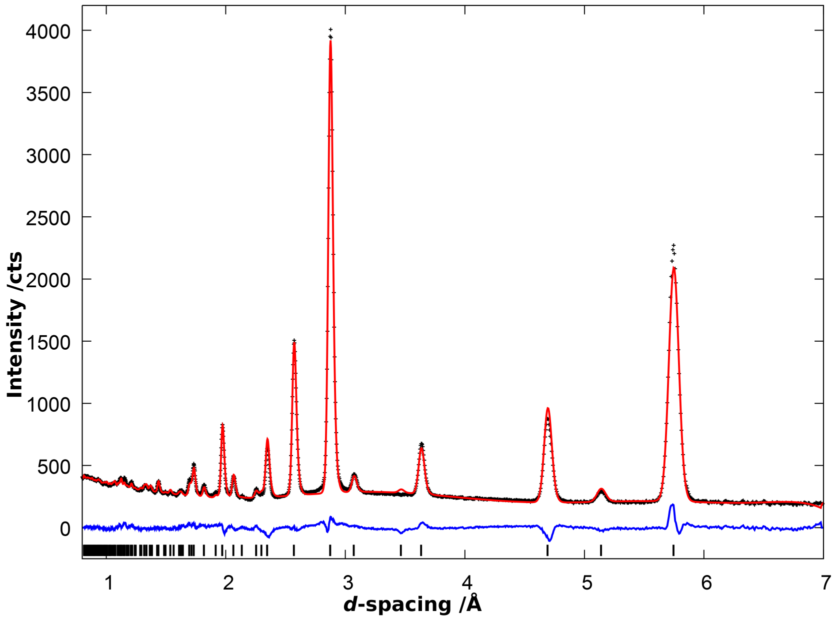

Figure A.24.: Comparison of the observed (black crosses) and calculated patterns (red line) from the Rietveld refinement against PND (detector bank 3) data for $[Cu(ND_3)_{6-x}]Cl_2$ at room temperature. The blue line represents the difference profile ($I_{obs} - I_{calc}$) and the black tick marks indicate the theoretical reflection positions.

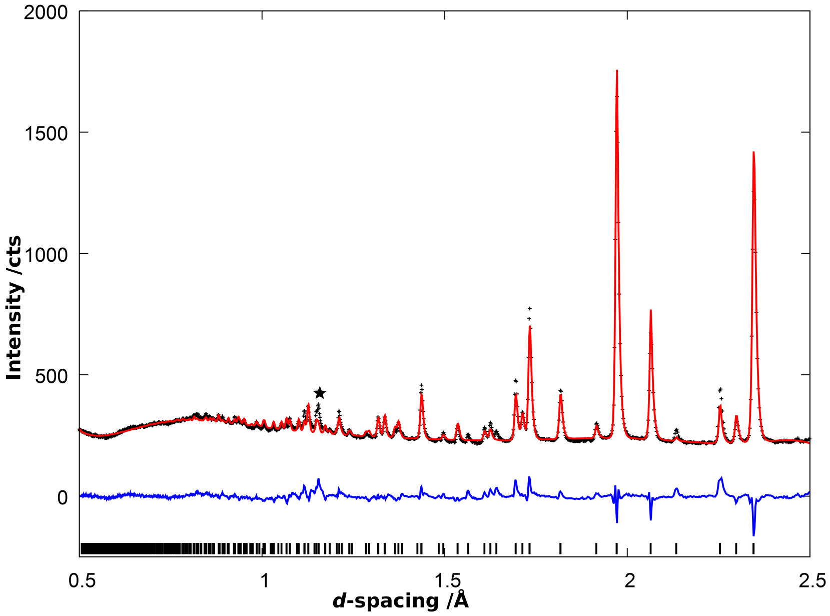

Figure A.25.: Comparison of the observed (black crosses) and calculated patterns (red line) from the Rietveld refinement against PND (detector bank 5) data for $[Cu(ND_3)_{6-x}]Cl_2$ at room temperature. The blue line represents the difference profile ($I_{obs} - I_{calc}$) and the black tick marks indicate the theoretical reflection positions.

A.2.6. Tables for cubic $[Cu(NH_3)_6]Cl_2$

Table A.34.: Atom positions and displacement parameters in cubic $[Cu(NH_3)_6]Cl_2$.

Atom Site	X	Y	Z	U_{iso}/U_{eq} /Å^2
Cu1	0	0	0	0.0547(6)
Cl1	0.25	0.25	0.25	0.0580(8)
N2	0.2075(3)	0	0	0.0622(19)
H1n2	0.236352	0.055709	0.05973	0.0747
H2n2	0.236352	−0.079582	0.01838	0.0747
H3n2	0.236352	0.023873	−0.07811	0.0747

Table A.35.: Anisotropic displacement parameters in cubic $[Cu(NH_3)_6]Cl_2$ in Å^2.

Atom Site	U^{11}	U^{22}	U^{33}	U^{12}	U^{13}	U^{23}
N2	0.031(4)	0.078(3)	0.078(3)	0	0	0

Table A.36.: Atomic distances in cubic $[Cu(NH_3)_6]Cl_2$.

Atom Site 1	Atom Site 2	Distance /Å
Cu1	N2	2.084(3)
N2	H1n2	0.87
N2	H2n2	0.87
N2	H3n2	0.87

Table A.37.: Selected angles in cubic $[Cu(NH_3)_6]Cl_2$.

Atom Site 1	Atom Site 2	Atom Site 3	Angle /°
N2	Cu1	N2	180.0(5)
N2	Cu1	N2	90
Cu1	N2	H1n2	109.47
Cu1	N2	H2n2	109.47
Cu1	N2	H3n2	109.47

A.2.7. Tables for $[Mg/Cu(NH_3)_6]Cl_2$

Table A.38.: Atom positions and displacement parameters in cubic $[Mg/Cu(NH_3)_6]Cl_2$.

Atom Site	X	Y	Z	U_{iso}/U_{eq} /Å^2
Cl1_2	0.25	0.25	0.25	0.053(3)
Mg1_2	0	0	0	0.027(4)
Cu1_2	0	0	0	0.027(4)
N1_2	0.2154(6)	0	0	0.077(5)
H1n1_2	0.243939	0.068161	0.043301	0.0925
H2n1_2	0.243939	−0.07158	0.037379	0.0925
H3n1_2	0.243939	0.003419	−0.080679	0.0925

Table A.39.: Atomic distances in cubic $[Mg/Cu(NH_3)_6]Cl_2$.

Atom Site 1	Atom Site 2	Distance /Å
Mg1_2	N1_2	2.188(6)
Cu1_2	N1_2	2.188(6)
N1_2	H1n1_2	0.87
N1_2	H2n1_2	0.87
N1_2	H3n1_2	0.87

Table A.40.: Selected angles in cubic $[Mg/Cu(NH_3)_6]Cl_2$.

Atom Site 1	Atom Site 2	Atom Site 3	Angle /°
N1_2	Mg1_2	N1_2	180.0(5)
Mg1_2	N1_2	H1n1_2	109.47
Mg1_2	N1_2	H2n1_2	109.47
Mg1_2	N1_2	H3n1_2	109.47

A.3. Appendix for 5. Metal nitrate ammines

A.3.1. Tables for $[Ni(H_2O)_6](NO_3)_2$

100 K

Table A.41.: Atom distances in $[Ni(H_2O)_6](NO_3)_2$ at 100 K

Atom Site 1	Atom Site 2	Distance /Å
Ni1	O6	2.0171(5)
Ni1	O3	2.0388(4)
Ni1	O4	2.0485(5)
Ni1	O2	2.0686(4)
Ni1	O1	2.0789(5)
Ni1	O5	2.0903(4)
O1	H11	0.802(12)
O1	H12	0.814(12)
O2	H21	0.809(12)
O2	H22	0.809(12)
O3	H31	0.801(12)
O3	H32	0.804(12)
O4	H41	0.799(12)
O4	H42	0.781(12)
O5	H51	0.802(12)
O5	H52	0.803(12)
O6	H61	0.800(12)
O6	H62	0.789(12)
O11	N1	1.2502(7)
O12	N1	1.2664(7)
O13	N1	1.2433(6)
O21	N2	1.2568(7)
O22	N2	1.2377(7)
O23	N2	1.2662(7)

Table A.42.: Anisotropic displacement parameters for $[Ni(H_2O)_6](NO_3)_2$ at 100 K in Å^2

Atom Site	U^{11}	U^{22}	U^{33}	U^{12}	U^{13}	U^{23}
Ni1	0.00582(2)	0.00496(2)	0.00651(2)	0.001180(10)	0.001190(10)	0.002120(10)
O1	0.01148(12)	0.00793(12)	0.00953(12)	0.00265(10)	0.00205(10)	0.00229(10)
O2	0.00748(10)	0.00778(12)	0.01064(12)	0.00157(9)	0.00168(9)	0.00318(9)
O3	0.01052(11)	0.00741(12)	0.00909(12)	0.00222(10)	0.00237(9)	0.00167(9)
O4	0.01054(11)	0.00904(13)	0.01147(13)	0.00279(10)	0.00277(10)	0.00550(10)
O5	0.00799(10)	0.00930(13)	0.01019(12)	0.00064(10)	0.00057(9)	0.00423(10)
O6	0.00981(11)	0.00988(13)	0.01324(14)	0.00286(10)	0.00378(10)	0.00704(11)
O11	0.01214(13)	0.00721(13)	0.01948(19)	0.00218(11)	0.00481(13)	0.00654(12)
O12	0.00980(12)	0.00946(14)	0.0204(2)	0.00128(11)	0.00394(13)	0.00597(13)
O13	0.01265(13)	0.00843(13)	0.01400(15)	0.00462(11)	0.00338(11)	0.00479(11)
N1	0.00998(12)	0.00646(12)	0.00920(13)	0.00202(10)	0.00269(10)	0.00327(10)
O21	0.01490(15)	0.01137(15)	0.01201(14)	0.00691(13)	0.00258(12)	0.00417(12)
O22	0.01514(15)	0.01035(14)	0.01518(16)	0.00394(13)	0.00616(13)	0.00706(13)
O23	0.01100(13)	0.01160(16)	0.0201(2)	0.00199(12)	0.00519(13)	0.00600(14)
N2	0.01065(12)	0.00838(13)	0.00821(12)	0.00298(11)	0.00222(10)	0.00317(10)

Table A.43.: Selected angles in Ni(H_2O)$_6$](NO_3)$_2$ at 100 K

Atom Site 1	Atom Site 2	Atom Site 3	Angle /°
O6	Ni1	O3	89.53(2)
O6	Ni1	O4	175.99(2)
O3	Ni1	O4	93.48(2)
O6	Ni1	O2	91.423(19)
O3	Ni1	O2	88.764(18)
O4	Ni1	O2	91.288(19)
O6	Ni1	O1	91.69(2)
O3	Ni1	O1	178.337(18)
O4	Ni1	O1	85.25(2)
O2	Ni1	O1	92.341(19)
O6	Ni1	O5	89.584(19)
O3	Ni1	O5	88.003(19)
O4	Ni1	O5	87.878(18)
O2	Ni1	O5	176.605(18)
O1	Ni1	O5	90.870(19)
Ni1	O1	H11	112(2)
Ni1	O1	H12	105.9(17)
H11	O1	H12	108(2)
Ni1	O2	H21	113.1(19)
Ni1	O2	H22	113.3(17)
H21	O2	H22	111(2)
Ni1	O3	H31	117.4(17)
Ni1	O3	H32	114.1(17)
H31	O3	H32	105(2)
Ni1	O4	H41	115.7(17)
Ni1	O4	H42	125.5(19)
H41	O4	H42	106(2)
Ni1	O5	H51	120(2)
Ni1	O5	H52	114.3(19)
H51	O5	H52	94(3)
Ni1	O6	H61	123(2)
Ni1	O6	H62	118.0(17)
H61	O6	H62	101(3)
O13	N1	O11	120.51(5)
O13	N1	O12	120.96(5)
O11	N1	O12	118.53(5)
O22	N2	O21	120.71(5)
O22	N2	O23	119.20(5)
O21	N2	O23	120.08(5)

295 K

Table A.44.: Selected distances in Ni(H_2O)$_6$](NO$_3$)$_2$ at 295 K

Atom Site 1	Atom Site 2	Distance /Å
Ni1	O6	2.0173(15)
Ni1	O4	2.0429(15)
Ni1	O3	2.0483(15)
Ni1	O2	2.0756(15)
Ni1	O1	2.0810(16)
Ni1	O5	2.0883(15)
O1	H11	0.783(15)
O1	H12	0.787(15)
O2	H21	0.783(15)
O2	H22	0.783(15)
O3	H31	0.793(15)
O3	H32	0.783(15)
O4	H41	0.779(15)
O4	H42	0.780(15)
O5	H51	0.781(15)
O5	H52	0.781(15)
O6	H61	0.783(15)
O6	H62	0.783(15)
O11	N1	1.254(2)
O12	N1	1.259(3)
O13	N1	1.239(2)
O21	N2	1.256(2)
O22	N2	1.239(3)
O23	N2	1.254(3)

Table A.45.: Anisotropic displacement parameters for $[Ni(H_2O)_6](NO_3)_2$ at 295 K in Å^2

Atom Site	U^{11}	U^{22}	U^{33}	U^{12}	U^{13}	U^{23}
Ni1	0.01903(16)	0.01734(15)	0.02156(16)	0.00437(9)	0.00412(9)	0.00712(10)
O1	0.0354(8)	0.0239(7)	0.0289(7)	0.0093(6)	0.0069(6)	0.0066(6)
O2	0.0210(7)	0.0237(7)	0.0319(7)	0.0057(5)	0.0056(5)	0.0098(6)
O3	0.0316(8)	0.0223(7)	0.0252(7)	0.0075(6)	0.0065(6)	0.0045(5)
O4	0.0327(8)	0.0281(7)	0.0334(8)	0.0100(6)	0.0094(6)	0.0166(6)
O5	0.0226(7)	0.0302(8)	0.0333(8)	0.0016(6)	0.0005(6)	0.0140(6)
O6	0.0284(8)	0.0298(7)	0.0414(8)	0.0101(6)	0.0123(6)	0.0215(7)
O11	0.0371(9)	0.0233(7)	0.0605(11)	0.0068(6)	0.0168(8)	0.0217(7)
O12	0.0309(8)	0.0298(8)	0.0658(12)	0.0059(7)	0.0141(8)	0.0189(8)
O13	0.0385(9)	0.0260(7)	0.0423(9)	0.0141(6)	0.0095(7)	0.0134(6)
N1	0.0314(8)	0.0214(7)	0.0249(7)	0.0054(6)	0.0080(6)	0.0086(6)
O21	0.0469(10)	0.0395(9)	0.0364(8)	0.0222(8)	0.0074(7)	0.0132(7)
O22	0.0522(11)	0.0365(9)	0.0472(10)	0.0158(8)	0.0215(8)	0.0229(8)
O23	0.0361(9)	0.0390(10)	0.0728(14)	0.0080(8)	0.0184(9)	0.0191(10)
N2	0.0346(9)	0.0289(8)	0.0251(8)	0.0105(7)	0.0064(7)	0.0087(6)

Table A.46.: Selected angles in Ni(H_2O)$_6$](NO_3)$_2$ at 295 K

Atom Site 1	Atom Site 2	Atom Site 3	Angle /°
O6	Ni1	O4	176.40(6)
O6	Ni1	O3	89.33(7)
O4	Ni1	O3	93.18(6)
O6	Ni1	O2	90.68(6)
O4	Ni1	O2	91.97(6)
O3	Ni1	O2	88.45(6)
O6	Ni1	O1	91.79(7)
O4	Ni1	O1	85.66(7)
O3	Ni1	O1	178.60(6)
O2	Ni1	O1	92.37(6)
O6	Ni1	O5	90.04(6)
O4	Ni1	O5	87.47(7)
O3	Ni1	O5	87.87(7)
O2	Ni1	O5	176.24(6)
O1	Ni1	O5	91.30(7)
Ni1	O1	H11	111(3)
Ni1	O1	H12	113(3)
H11	O1	H12	103(4)
Ni1	O2	H21	114(3)
Ni1	O2	H22	118(3)
H21	O2	H22	97(4)
Ni1	O3	H31	114(3)
Ni1	O3	H32	121(2)
H31	O3	H32	106(4)
Ni1	O4	H41	116(2)
Ni1	O4	H42	131(3)
H41	O4	H42	104(4)
Ni1	O5	H51	119(3)
Ni1	O5	H52	114(3)
H51	O5	H52	105(4)
Ni1	O6	H61	114(3)
Ni1	O6	H62	123(3)
H61	O6	H62	108(4)
O13	N1	O11	120.26(18)
O13	N1	O12	121.09(17)
O11	N1	O12	118.65(17)
O22	N2	O23	119.38(19)
O22	N2	O21	120.2(2)
O23	N2	O21	120.4(2)

A.3.2. Tables for $[Ni(NH_3)_6](NO_3)_2$ phase I

Table A.47.: Selected distances in $[Ni(NH_3)_6](NO_3)_2$

Atom Site 1	Atom Site 2	Distance /Å
Ni1	N1	2.050(8)
N2	O1	1.068(6)
N1	H1n1	0.87
H1n1	H1n1	0.9416

Table A.48.: Selected angles in $[Ni(NH_3)_6](NO_3)_2$

Atom Site 1	Atom Site 2	Atom Site 3	Angle /°
N1	Ni1	N1	90
N1	Ni1	N1	180.0(5)
O1	N2	O1	109.5(4)

A.3.3. Tables for $[Ni(NH_3)_6](NO_3)_2$ phase II

200 K

Table A.49.: Atomic positions and isotropic displacement parameters for $[Ni(NH_3)_6](NO_3)_2$ at 200 K.

Atom Site	X	Y	Z	U_{iso}/U_{eq} /Å^2
Ni1	0	0	0	0.0281(5)
N1	–0.0276(3)	0.1963(3)	0.0270(3)	0.0426(9)
H1A	–0.0541(7)	0.2264(7)	–0.0354(15)	0.064
H1B	0.0371(15)	0.2282(8)	0.0443(5)	0.064
H1C	–0.0760(12)	0.2071(4)	0.0821(14)	0.064
N2	–0.2660(3)	0.2340(3)	0.2660(3)	0.0404(15)
O1	–0.3310(3)	0.2061(3)	0.1748(3)	0.0710(11)

Table A.50.: Anisotropic displacement parameters for $[Ni(NH_3)_6](NO_3)_2$ at 200 K in Å^2.

Atom Site	U^{11}	U^{22}	U^{33}	U^{12}	U^{13}	U^{23}
N1	0.043(2)	0.0355(19)	0.050(2)	0.0015(17)	0.0008(15)	–0.0002(17)
N2	0.0404(15)	0.0404(15)	0.0404(15)	–0.0022(15)	0.0022(15)	0.0022(15)
O1	0.091(3)	0.059(2)	0.064(2)	–0.0071(18)	–0.031(2)	–0.0038(17)

Table A.51.: Selected atomic distances in $[Ni(NH_3)_6](NO_3)_2$ at 200 K.

Atom Site 1	Atom Site 2	Distance /Å
Ni1	N1	2.134(3)
N2	O1	1.231(3)

Table A.52.: Selected angles in $[Ni(NH_3)_6](NO_3)_2$ at 200 K.

Atom Site 1	Atom Site 2	Atom Site 3	Angle /°
N1	Ni1	N1	180.00(18)
N1	Ni1	N1	91.23(13)
N1	Ni1	N1	88.77(13)
O1	N2	O1	119.992(9)

100 K

Table A.53.: Anisotropic displacement parameters for $[Ni(NH_3)_6](NO_3)_2$ at 100 K in Å^2.

Atom Site	U^{11}	U^{22}	U^{33}	U^{12}	U^{13}	U^{23}
N1	0.030(2)	0.0257(19)	0.040(2)	-0.0008(18)	-0.0004(16)	-0.0013(18)
O1	0.062(2)	0.043(2)	0.046(2)	-0.0086(17)	-0.0207(19)	-0.0003(17)

Table A.54.: Selected atomic distances in $[Ni(NH_3)_6](NO_3)_2$ at 100 K.

Atom Site 1	Atom Site 2	Distance /Å
Ni1	N1	2.125(3)
N2	O1	1.238(3)

Table A.55.: Selected angles in $[Ni(NH_3)_6](NO_3)_2$ at 200 K.

Atom Site 1	Atom Site 2	Atom Site 3	Angle /°
N1	Ni1	N1	180.0(3)
N1	Ni1	N1	91.75(17)
N1	Ni1	N1	88.25(17)
O1	N2	O1	119.95(2)

A.3.4. Tables for $Ni(NO_3)_2{\cdot}2NH_3$

Table A.56.: Atomic positions and isotropic displacement parameters for $Ni(NO_3)_2 \cdot 2\,NH_3$.

Atom Site	X	Y	Z	$U_{\mathrm{iso}}/U_{\mathrm{eq}}$ /Å^2
Ni1	0.6258(3)	0.7264(8)	0.9216(7)	0.0200(14)
O22	0.726(2)	0.788(2)	0.7295(16)	0.016(4)
N11	0.4915(14)	0.498(4)	0.6842(19)	0.024(5)
O11	0.5157(17)	0.484(3)	0.814(2)	0.024(5)
N2	0.7439(15)	0.480(2)	0.973(3)	0.017(4)
O23	0.717(2)	1.143(3)	0.732(2)	0.016(4)
N1	0.4975(13)	0.972(3)	0.891(3)	0.017(4)
O21	0.7253(17)	0.970(3)	1.0411(19)	0.016(4)
O12	0.521(2)	0.679(3)	1.117(2)	0.024(5)
O13	0.480(2)	0.674(3)	0.620(2)	0.024(5)
N21	0.7390(14)	0.968(3)	0.6683(19)	0.016(4)
H1n2	0.707375	0.35266	0.966556	0.0207
H2n2	0.804645	0.482364	0.91358	0.0207
H3n2	0.77	0.49908	1.059447	0.0207
H1n1	0.533189	1.099758	0.88542	0.0207
H2n1	0.458166	0.946484	0.812051	0.0207
H3n1	0.447218	0.972236	0.962479	0.0207

Table A.57.: Selected distances for for $Ni(NO_3)_2 \cdot 2\,NH_3$.

Atom Site 1	Atom Site 2	Distance /Å
Ni1	O22	2.143(18)
Ni1	O11	2.155(18)
Ni1	N2	2.039(17)
Ni1	N1	2.073(16)
Ni1	O21	2.151(18)
Ni1	O12	2.18(2)
N11	O11	1.25(3)
N11	O12	1.24(3)
N11	O13	1.23(3)
N2	H1n2	0.87
N2	H2n2	0.87
N2	H3n2	0.87
O23	N21	1.24(2)
O21	N21	1.25(2)
N1	H1n1	0.87
N1	H2n1	0.87
N1	H3n1	0.87

Table A.58.: Selected angles for $Ni(NO_3)_2 \cdot 2\,NH_3$.

Atom Site 1	Atom Site 2	Atom Site 3	Angle /°
O22	Ni1	O11	91.1(7)
O22	Ni1	N2	89.5(9)
O22	Ni1	N1	96.6(10)
O22	Ni1	O21	93.0(7)
O22	Ni1	O12	177.5(7)
O11	Ni1	N2	88.5(7)
O11	Ni1	N1	92.1(7)
O11	Ni1	O21	175.7(7)
O11	Ni1	O12	90.1(7)
N2	Ni1	N1	173.9(12)
N2	Ni1	O21	92.9(8)
N2	Ni1	O12	92.6(10)
N1	Ni1	O21	86.2(8)
N1	Ni1	O12	81.3(10)
O21	Ni1	O12	85.7(7)
Ni1	O22	N21	126.8(14)
O11	N11	O12	117(2)
O11	N11	O13	124(2)
O12	N11	O13	119(2)
Ni1	N2	H1n2	109.47
Ni1	N2	H2n2	109.47
Ni1	N2	H3n2	109.47
Ni1	N1	H1n1	109.47
Ni1	N1	H2n1	109.47
Ni1	N1	H3n1	109.47
Ni1	O21	N21	130.6(13)
Ni1	O12	N11	126.5(16)
O22	N21	O23	120.3(18)
O22	N21	O21	118.7(17)
O23	N21	O21	121.0(17)

A.3.5. Tables for $[Cu(NH_3)_4](NO_3)_2$

Atom Site 1	Atom Site 2	Distance /Å
Cu1	N11	2.014(5)
Cu1	N12	2.017(4)
Cu2	N22	2.012(5)
Cu2	N21	2.015(4)
N1	O11	1.208(9)
N1	O12	1.245(9)
N1	O14	1.251(8)
N2	O22	1.221(8)
N2	O21	1.238(8)
N2	O23	1.245(8)
N3	O33	1.217(8)
N3	O31	1.237(8)
N3	O32	1.248(8)
N4	O43	1.197(9)
N4	O42	1.227(9)
N4	O41	1.228(9)

Atom Site 1	Atom Site 2	Atom Site 3	Angle /°
N11	Cu1	N11	91.3(3)
N11	Cu1	N12	88.27(19)
N11	Cu1	N12	179.35(19)
N11	Cu1	N12	179.35(19)
N11	Cu1	N12	88.27(19)
N12	Cu1	N12	92.1(3)
N22	Cu2	N22	91.4(3)
N22	Cu2	N21	88.53(19)
N22	Cu2	N21	179.35(18)
N22	Cu2	N21	179.35(18)
N22	Cu2	N21	88.53(19)
N21	Cu2	N21	91.5(3)
O11	N1	O12	122.3(8)
O11	N1	O14	119.3(8)
O12	N1	O14	118.4(7)
O22	N2	O21	119.9(7)
O22	N2	O23	119.3(7)
O21	N2	O23	120.8(6)
O33	N3	O31	120.8(7)
O33	N3	O32	120.6(6)
O31	N3	O32	118.6(6)
O43	N4	O42	119.1(8)
O43	N4	O41	122.1(9)
O42	N4	O41	118.8(8)